DEVELOPMENT OF THREE-DIMENSIONAL TURBULENT WALL JETS

By

HONGGUANG SUN, M. Eng.

A Thesis

Submitted to the School of Graduate Studies

in Partial Fulfilment of the Requirements

for the Degree

Doctor of Philosophy

McMaster University

DEVELOPMENT OF THREE-DIMENSIONAL TURBULENT WALL JETS

DOCTOR OF PHILOSOPHY (2002) McMaster University

(Mechanical Engineering) Hamilton, Ontario

TITLE: Development of Three-Dimensional Turbulent Wall Jets

AUTHOR: Hongguang Sun

B. Eng., Tsinghua University, China, 1987

M. Eng., China Academy of Railway Sciences, 1990

SUPERVISOR: Dr. Dan Ewing

NUMBER OF PAGES: xxiv, 207

TO

MY WIFE, ZHIMEI

Abstract

Detailed flow field measurements were performed to investigate the development of the three-dimensional wall jet, the effect of initial conditions on the development of wall jets and the evolution of the large-scale vortex structures that causes the large lateral growth rate in the flow. Single-point measurements in the wall jet exiting a contoured nozzle indicated that there were two regions in the intermediate field $10 \leq x/D \leq 40$. The flow underwent a significant change in the region $10 \leq x/D \leq 20$ as it adjusted to the wall. The changes of the profiles of the moments and the reorientation of the regions of the mean streamwise vorticity slowed down in the region beyond x/D=20 and were not apparent by x/D=40. The comparison of measurements of wall jets exiting the contoured nozzle and the fully developed long pipe indicated that changes in initial conditions do affect the jet half-widths and the decay of the maximum streamwise velocity through near and intermediate fields. The differences in growth rates of wall jets, profiles of moments and contours of the mean streamwise vorticity in the two jets were reduced in the region after x/D=10 and were not apparent in the region beyond x/D=20 - 30. Measurements of two-point, two-time correlation of the streamwise fluctuating velocity indicated that the large-scale vortex structures that consist two pair of horseshoe vortices in the flow continued to develop throughout the intermediate field. In particular, the inner vortex structures were induced towards the wall by the outer structures and the legs of the outer structures inclined relative to the streamwise direction as the flow evolved downstream.

Measurements also indicated that the flow below the outer region of the streamwise vorticity was laterally convected faster than the outer vortex structures.

Acknowledgements

I would like to express my sincere appreciation to my supervisor, Dr. Dan Ewing, for his guidance, support and encouragement through the course of this work. I benefit a lot from his inspiring and knowledgeable advice.

Special thanks go to Dr. William K. George and Chalmers University of Technology of Sweden. They provided me a great opportunity to learn the measurement skills. Dr. William K. George's hospitality during my stay in Sweden is always remembered.

The professors of my supervisory committee, Dr. Chan Y. Ching and Dr. Andrew N. Hrymak, are thanked for the time spent in reading the thesis and their many helpful suggestions.

The technical assistance of Mr. Joe Verhaeghe, Mr. Ron Lodewyks, Mr. Dave Schick and Mr. Andrew Buyers is greatly appreciated. I am also grateful to Mr. Nan Gao and Ms. Serena Goldstein for helping me to set up the experimental apparatus.

Finally, I would like to extend my gratitude to my family and friends for their support and understanding. Especially, I would like to thank my wife, Zhimei, for her love and encouragement. Without her this work would not have been possible.

Nomenclature

A	Cross area of the orifice, mm^2.
D	Nozzle diameter, mm.
d	Hot-wire diameter, mm.
E	Mean voltage from hot-wire anemometer, V.
F	Power spectrum of streamwise fluctuating velocity, m^2/s .
f	Frequency, Hz.
H	Height of square or rectangular orifice, mm.
h	Height of top edge of nozzle above the plate, mm.
k_1	Angular sensitivity of wire 1 in a cross-wire probe.
k_2	Angular sensitivity of wire 2 in a cross-wire probe.
l	Hot-wire length, mm.
Nu	Local Nusselt number.
R_{uu}	Correlation of the streamwise fluctuating velocity, m^2/s^2.
Re_{exit}	Reynolds number at the jet exit, $U_{exit}D/\nu$.
Q	Flow rate at the orifice exit, m^3/s.
St	Strouhal number, fD/U.
T	Length of blocks in spectrum calculation, s.
T_s	Hot-wire temperature in measurements, K.
T_f	Fluid temperature, K.
U	Local mean streamwise velocity, m/s.

U_{max}	Local maximum mean streamwise velocity, m/s.
U_{exit}	Average mean velocity at jet exit, $U_{exit} = Q/A$, m/s.
U_{eff1}	Mean effective velocity measured by wire 1, m/s.
U_{eff2}	Mean effective velocity measured by wire 2, m/s.
$\widetilde{u}_{eff1}$	Instantaneous effective velocity detected by wires 1, m/s.
$\widetilde{u}_{eff2}$	Instantaneous effective velocity detected by wires 2, m/s.
$\overline{u^2}$	Streamwise normal stress, m^2/s^2.
u'	Root mean square of streamwise fluctuating velocity, $u' = (\overline{u^2})^{1/2}$, m/s.
u_*	Streamwise friction velocity, m/s.
V	Local mean velocity normal to the plate, m/s.
$\overline{v^2}$	Vertical normal stress, m^2/s^2.
v'	Root mean square of vertical fluctuating velocity, $v' = (\overline{v^2})^{1/2}$, m/s.
W	Local mean lateral velocity, m/s.
$\overline{w^2}$	Lateral normal stress, m^2/s^2.
w'	Root mean square of lateral fluctuating velocity, $w' = (\overline{w^2})^{1/2}$, m/s.
w_*	Lateral friction velocity, m/s.
$\overline{uv}$	Reynolds shear stress, m^2/s^2.
$\overline{uw}$	Reynolds shear stress, m^2/s^2.
$\overline{vw}$	Reynolds shear stress, m^2/s^2.
x	Coordinate in streamwise direction, mm.
y	Coordinate in vertical direction, mm.
$y_{1/2}$	Vertical half-width of the three-dimensional wall jet, mm.
z	Coordinate in lateral direction, mm.
$z_{1/2}$	Lateral half-width of the three-dimensional wall jet, mm.
Ω_x	Mean streamwise vorticity, $1/s$.

ρ_{uu} Correlation coefficient of the streamwise fluctuating velocity.

η Vertical length scale of the inner layer in the wall jet, mm.

ν Kinematic viscosity, m^2/s.

θ Angle between wires 1 and 2 in the cross-wire probe, *degree*.

τ Time separation in correlation, s.

τ_l Integral time scale, s.

ϕ Angle between the instantaneous velocity vector and the wire. in the cross-wire probe, *degree*.

Contents

List of Tables

List of Figures

Chapter 1

Introduction

Wall jets formed when a jet travels parallel to a flat plate, occur in a number of industrial applications, such as cooling of gas turbine blade, forced air heating or automobile defrosters. Wall jets can generally be broken down into two-dimensional wall jets and three-dimensional wall jets. A two-dimensional wall jet is formed when a flow exits a long slot parallel to a plate as shown in figure 1.1 or when a coaxial jet flows over a cylinder. A three-dimensional wall jet is formed when a jet exits an orifice and flows over a wall, as shown in figure 1.2. It should be noted that even a jet that exits an orifice whose width is an order of magnitude larger than its height will quickly become a three-dimensional wall jet. There is currently considerable interest in the three-dimensional wall jet because the flow is of both practical interest and challenging to predict with current turbulent models [3, 4]. In particular, the anisotropic growth of the flow and the streamline curvature associated with the development of the lateral spread of the flow make the three-dimensional wall jet challenging to predict. Thus, there is interest in using the three-dimensional wall jet to test turbulent models because it includes these features in a flow with a relatively simple geometry.

The development of two-dimensional wall jets have been studied in number of investigations, including a recent study by George et al. [21] that reviewed the results

from many of previous studies. There have also been a number of investigations of three-dimensional wall jets [1, 13, 45, 48]. Many of these investigations have focused on different geometries so the investigation of the three-dimensional wall jet has not been studied as comprehensively as the two-dimensional wall jet.

As with most turbulent flows the development of the three-dimensional wall jet is divided into three regions: the near field, the intermediate field and the far field where the development of the flow is approximately self-similar. One of the notable features of the three-dimensional wall jet is the large anisotropy in the growth rates of the jet in the far field. For example, the growth rates in the far field of the wall jets exiting the round nozzles reported by a number of previous investigations are shown in table 1.1. It is clear that the growth rate in the lateral direction is 5 - 8 times larger than the growth rate in the vertical direction. This result is particularly interesting in that the growth rate in the lateral direction is approximately 3 times the value in the far field of a round jet [48], while the vertical growth rate is approximately half of the value of a round jet. Thus, the interaction between the jet and the wall acts to both enhance the lateral growth rate of the jet and suppress the vertical growth of the jet.

Launder and Rodi [35] argued that this large anisotropy in the growth rate was caused by the presence of two regions of counter rotating mean streamwise vorticity on each side of the jet centerline caused by the presence of intermittent large-scale structures. The formation and development of the large-scale structures in the near field of the wall jet exiting a round nozzle were investigated recently by Matsuda et al.[43] and Ewing and Pollard[16]. Ewing and Pollard proposed that the vortex rings formed at the jet exit deform to generate large-scale turbulent structures in the region $x/D \leq 10$ that eventually cause the large lateral growth rate in the flow. The lateral growth rate of the jet increases by a factor of more than 2 between 10 and 40 diameters downstream of the jet indicating that the large-scale structures are

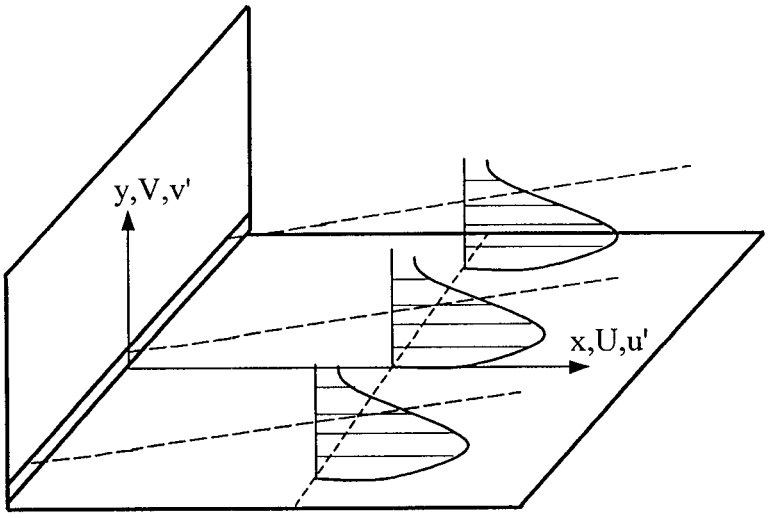

Figure 1.1: Schematic of the two-dimensional turbulent wall jet .

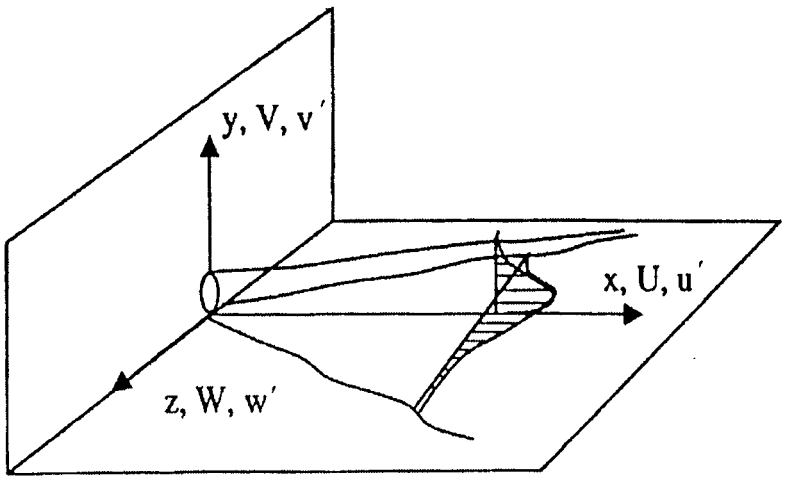

Figure 1.2: Schematic of the three-dimensional turbulent wall jet.

Investigation reference	Initial condition	Flow region x/D	$\frac{\partial y_{1/2}}{\partial x}$	$\frac{\partial z_{1/2}}{\partial x}$
Abrahamsson et al.[1]	Contoured nozzle with top-hat velocity profile	$50 \sim 90$	0.065	0.32
Davis and Winarto[13]	Contoured nozzle with top-hat velocity profile	$40 \sim 48$	0.037	0.32
Maslov et al.[42]	Contoured nozzle with top-hat velocity profile	$50 \sim 350$	0.056	0.30
Eriksson et al.[15]	Long pipe with fully developed pipe flow	$25 \sim 76$	0.055	0.27
Newman et al.[45]	Long pipe with fully developed pipe flow	$40 \sim 200$	0.052	0.28

Table 1.1: Growth rates reported for the far field of three-dimensional wall jets exiting round orifices.

still evolving over this region. The measurements of the mean streamwise vorticity at 15 diameters downstream of the jet reported by Iida and Matsuda [29] were very different from results proposed by Launder and Rodi [35] in the far field suggesting again the large-scale structures are evolving throughout the intermediate field. The development of the large-scale structures in this intermediate field that is of greatest interest in many practical applications has not been studied in detail and will be investigated here.

Measurements of the growth rates in three-dimensional wall jets exiting round orifices summarized in table 1.1 indicate that round jets with a top-hat velocity profile and a fully developed velocity profile produce different wall jets. In particular, the lateral growth rate of the wall jets exiting a round contoured nozzle were 10% – 15% larger than wall jets exiting a round fully developed pipe. Eriksson et al.[15] also reported that the presence of different size walls behind the nozzle affected the growth rate of the wall jet. The normal spread rate of the wall jet with a high wall behind the nozzle was approximately 20% smaller than that without a wall behind the nozzle. These results suggest that seemingly minor changes in the near field or initial conditions of the jet persist through the flow. It should be noted that the measurements of the jets exiting the contoured nozzle and the long pipe were performed in different facilities so it is not clear whether the difference of the growth rate observed for these flows were caused by differences in the initial conditions or the boundary conditions. The effect of the wall behind the nozzle was only examined qualitatively in different facilities so it would be useful to perform further quantitative measurements to understand the cause of the differences. Thus, the second objective of this investigation was to examine whether the changes in initial conditions and boundary conditions affect the development of three-dimensional wall jet. This was accomplished by performing a series of experiments where only one parameter was changed in each experiment. In particular, the effect of the change in initial conditions

was investigated by examining the development of the wall jets exiting a contoured nozzle and a long pipe. The facility was also designed so the effect of the presence of the wall behind the nozzle could be examined. The investigation of the effect of the initial and boundary conditions focussed on the development of the jet in the near and intermediate fields in order to examine how the differences develop and evolve downstream.

The development of the flow in the intermediate field should be examined by scaling the profiles using similarity variables to examine how the profiles evolve to the self-similar state. There have been a number of investigations that have shown the profiles measured in the far field of the jet are self-similar. However, none of these investigations have shown that the proposed similarity solutions are consistent with the governing equations for the three-dimensional wall jet. Thus, the first step in this investigation was to examine the Reynolds averaged governing equations in the far field of the three-dimensional wall jet in order to deduce the appropriate similarity solutions. The scales from these solutions were then used to scale the measurements in the intermediate field of the wall jet.

The results of this investigation are reported in five sections. The results from the previous investigations of the three-dimensional wall jet are initially reviewed and discussed. The experimental facilities and techniques used here are outlined and the accuracy of the reported measurements are discussed. The first order governing equations for the three-dimensional wall jet are then examined and the similarity solutions for the far field of the jet are developed. The predictions of this analysis are also compared with the measurements in the far field performed in this investigation. The effects of the initial conditions and boundary conditions on the development of the three-dimensional wall jet in near and intermediate fields are examined. Finally, the development of the large-scale structures in the intermediate field of the jet are examined.

Chapter 2

Literature Review

There have been a number of investigations that have examined the development of the three-dimensional wall jet and the large-scale turbulent structures that cause the highly anisotropic growth rate of the flow. A review of the early research was outlined by Launder and Rodi [35]. There has been a renewed interest in the three-dimensional wall jet because it includes the streamline curvature causing large anisotropy in the growth that make the flow challenging to predict with many standard turbulence models [3, 4]. This review will focus on the recent investigations of the three-dimensional wall jet while including the important results of the investigations reviewed by Lauder and Rodi [35].

An overview of the investigations in the far field are initially outlined. This is followed by a review of the investigations in the near and intermediate fields including both measurements of single-point moments and the large-scale vortex structures in the flow. The latter discussion focuses on the development of the jet exiting a round nozzle.

2.1 Development of the Three-Dimensional Wall Jet in the Far Field

The development of the three-dimensional wall jet has been studied for jets exiting a wide range of different orifices. This includes early investigations of the jet exiting a rectangular orifice with a width to height ratio of 10 by Viets and Sforza [67], the flow exiting a long pipe by Newman et al. [45] and later investigations of the flow exiting a range of different nozzle geometries by Rajaratnam et al. [52] and Padmanabham and Gowda [48]. In all cases, the investigations found that the mean streamwise velocity profiles were self-similar in the far field when they were scaled using the local maximum streamwise velocity and the jet half-widths. The development of the three-dimensional wall jet is generally characterized by examining the decay of the local maximum streamwise velocity and the evolution of the vertical and lateral half-widths of the jet, $y_{1/2}$ and $z_{1/2}$ respectively. In this flow, the vertical half-with, $y_{1/2}$, is defined as the distance along the jet centerline normal to the flat plate to the outer point where the streamwise velocity is half of the local maximum velocity. The lateral half-width, $z_{1/2}$, is the lateral distance between the jet centerline and the point where velocity is half of the maximum streamwise velocity at the same height as the maximum streamwise velocity point. The decay of the local maximum streamwise velocity and the growth rate of these length scales measured in the far field for a range of different investigations are summarized in table 2.1. Here, h is the distance from the top edge of the nozzle to the surface of the flat plate. In most cases it was found that the jet spread linearly in the far field. For example, Davis and Winarto [13] found that both vertical and lateral growth rate were constant in the region $x/D \geq 40$ for the wall jet exiting a contoured nozzle level to the wall and the values of $y_{1/2}$ and $z_{1/2}$ were 0.037 and 0.32 respectively. Maslov et al. [42] also performed measurements in the wall jet exiting a contoured nozzle with the top-hat velocity profile in the region

$50 \leq x/D \leq 350$ and found that the vertical and lateral growth rates appeared to be locally constant. They reported, however, that the vertical and lateral growth rates changed as the flow evolved downstream with values of 0.056 and 0.30 in the region $50 \leq x/D \leq 350$, and 0.057 and 0.31 in the region $150 \leq x/D \leq 350$.

Rajaratnam et al. [52] performed an extensive investigation to examine how the change in orifice geometry affected the development of the three-dimensional wall jet. They measured the flow fields in the wall jets exiting a circular orifice and a square orifice respectively and reported that the changes in the orifice geometry did not affect the decay of local maximum streamwise velocity, U_{max}/U_{exit}, in the region $x/\sqrt{A} > 60$, where A is the cross area of the orifice. They also found that the vertical half-width and the vertical growth rate shown in figure 2.1 were approximately the same in the region $x/D > 40$ or $x/H > 40$ for the wall jets exiting a circle orifice and a square orifice, where H is the height of the square orifice. The lateral length scale, $z'_{1/2}$, and the lateral growth rate of the wall jet exiting a circular orifice were, however, smaller than the jet exiting a square orifice in the region $x/D > 40$ or $x/H > 40$. It should be noted that Rajaratnam et al. [52] did not measure the lateral half-width defined as the width from the centerline to the half velocity point at the height of the the maximum velocity point. They instead characterized the lateral length scale of the jet, $z'_{1/2}$, at y/D=0.5 or y/H=0.5. Padmanabham and Gowda [48] later examined the development of wall jet exiting different orifices that were different segments of a circle shown in figures 2.2. They found that the change in the orifice geometry did not significantly affect the decay of the local maximum velocity (cf. table 2.1). They reported that the change of the orifice geometry did have significant effect on both the vertical and lateral growth rates of the three-dimensional wall jet. In particular, the lateral growth rate increased as the segment above the wall decreased.

Davis and Winarto[13] examined the effect of the orifice position on the development of the wall jet by adjusting the position of the contoured nozzle above the

Investigation	Nozzle geometry	Velocity profile	Region	Re_{exit} $(\frac{U_{exit}D}{\nu})$	$\frac{\partial y_{1/2}}{\partial x}$ $\frac{\partial z_{1/2}}{\partial x}$	$\frac{U_{max}}{U_{exit}}$
Padmanabham and Gowda[48]	Segment		x/h	95,400		
	h/D=0.23		50 ~ 120		0.040 0.250	$x^{-1.16}$
	h/D=0.50				0.049 0.245	$x^{-1.15}$
	h/D=0.80		20 ~ 100		0.043 0.215	$x^{-1.12}$
	h/D=1.00				0.045 0.216	$x^{-1.15}$
Davis and Winarto[13]	Contoured nozzle	Top-hat	x/D	170,000		
	h/D=1.0		40 ~ 48		0.037 0.32	
	h/D=1.5		40 ~ 56		0.036 0.33	
	h/D=2.5		48 ~ 64		0.039 0.29	
	h/D=4.5		48 ~ 56		0.046 0.23	
Maslov et al.[42]	Contoured nozzle	Top-hat	x/D	100,000		
			50 ~ 350		0.056 0.30	
			150 ~ 350		0.057 0.31	
Abrahamsson et al.[1]	Contoured nozzle	Top-hat	x/D 50 ~ 90	79,000	0.065 0.32	$x^{-1.29}$
Newman et al.[45]	Long pipe h/D=1.5	Fully developed	x/D 40 ~ 200	16,400	0.052 0.28	$x^{-1.0}$
Eriksson et al.[15]	Long pipe h/D=1.0	Fully developed	x/D 25 ~ 76.1	10,000	0.055 0.27	

Table 2.1: Growth rates in the far field of three-dimensional wall jets reported in previous investigations.

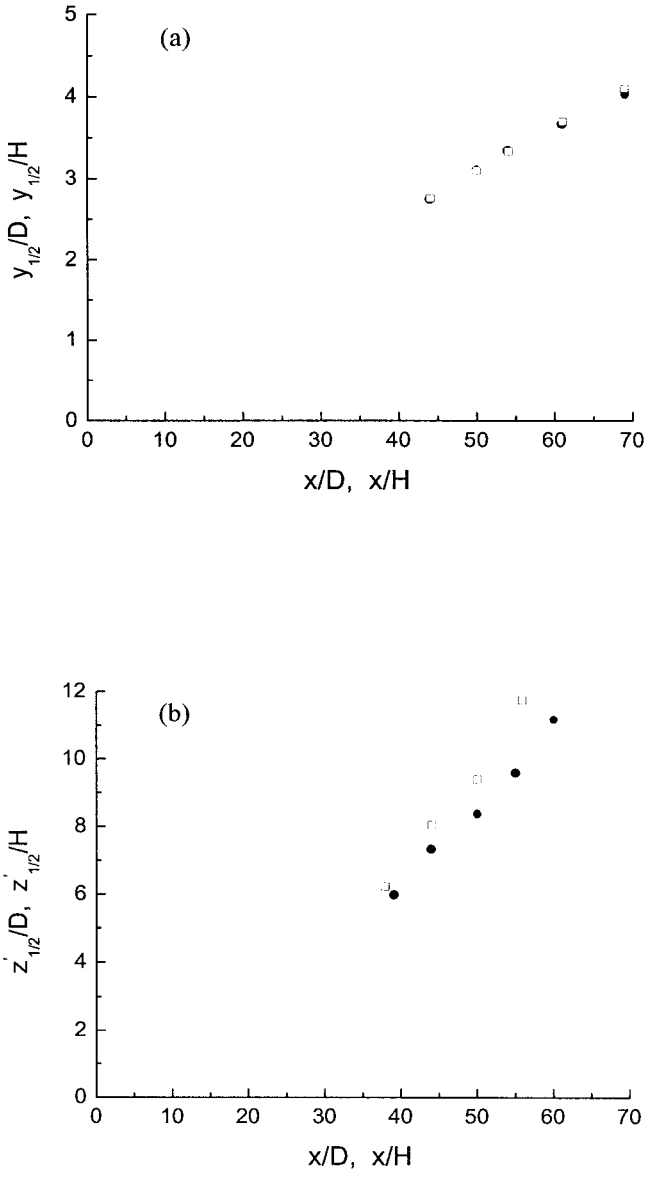

Figure 2.1: The development of (a) the vertical half-width and (b) the lateral length scale of wall jets exiting • a circular orifice and □ a square orifice reported by Rajaratnam [52].

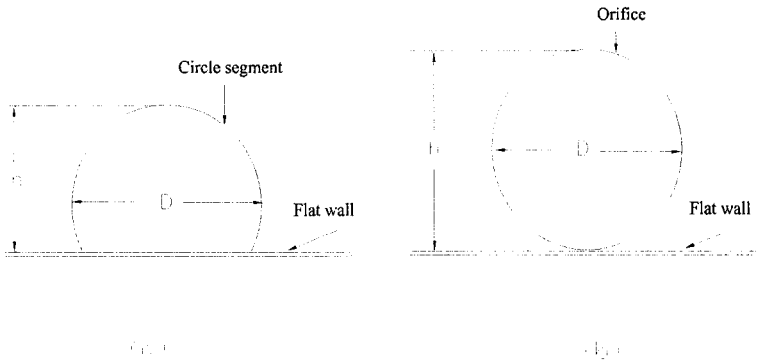

Figure 2.2: Schematic of the three-dimensional orifice configurations investigated by Padmanabham and Gowda[48].

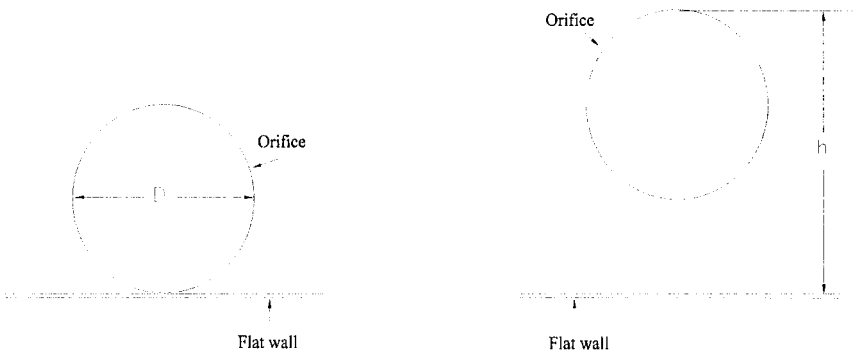

Figure 2.3: Schematic of the three-dimensional orifice configurations investigated by Davis and Winarto[13].

surface of the flat plate as shown in figure 2.3 while maintaining the other conditions the same. They characterized the difference in the jets using h, the distance of the top edge of the nozzle above the surface of the flat plate. The decay of the local maximum streamwise velocity and the development of the vertical and lateral half-widths of the jet are shown in figures 2.4 and 2.5, while the vertical and lateral growth rates reported by Davis and Winarto [13] are summarized in table 2.1. They found that the decay of local maximum streamwise velocity and the growth rates were approximately the same for the cases of h/D=1 and h/D=1.5. The position of the orifice did have a significant effect on the decay of the local maximum velocity and the development of the jet half-widths when $h/D > 1.5$. In particular, they found that the vertical half-width and vertical growth rate increased significantly when $h/D > 1.5$, while the lateral half-width and lateral growth rate decreased significantly.

There have also been a number of investigations that have examined the development of wall jets exiting round nozzles with different velocity profiles at the jet exit. For example, Davis and Winarto [13], Abrahamsson et al. [1], and Maslov et al. [42] measured the flow fields in the three-dimensional wall jet exiting a contoured nozzle with the top-hat velocity profile at the jet exit, while Newman et al. [45] and Eriksson et al.[15] performed measurements in the wall jet exiting a long pipe with the fully developed velocity profile. These studies make it possible to examine whether the change in velocity profiles at the jet exit affects the development of the wall jet. It should be noted that Newman et al.'s [45] experiments were performed with the bottom of the nozzle a half diameter above the surface of the horizontal plate, while the nozzles were flush with the horizontal plate in other cases. The decay of the local maximum streamwise velocity and the development of vertical and lateral half-widths reported in the different investigations are shown in figures 2.6 and 2.7. The decay of local maximum streamwise velocity and the lateral half-width measured in the wall jets exiting the contoured nozzles seem to be in reasonably good agreement though

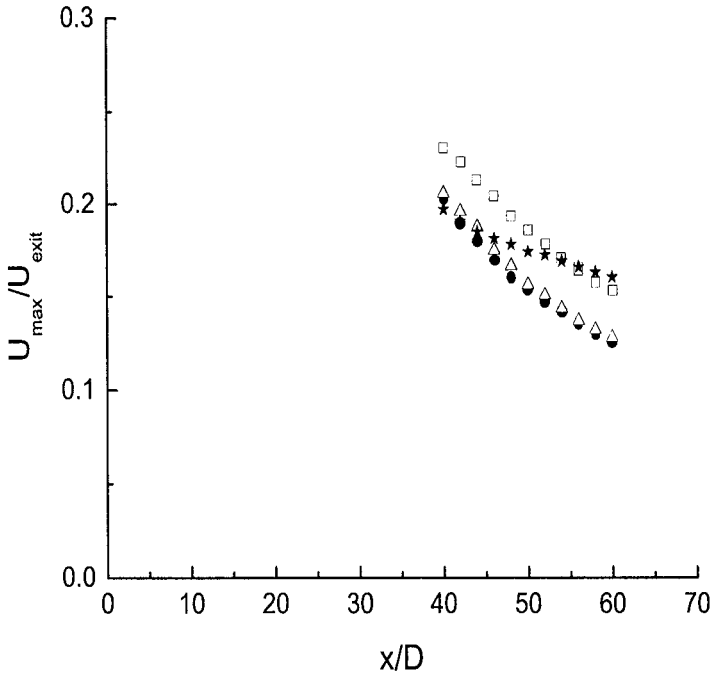

Figure 2.4: Decay of local maximum streamwise velocity in the wall jet exiting a contoured nozzle measured by Davis and Winarto[13] at • h/D=1, △ h/D=1.5, □ h/D=2.5 and ⋆ h/D=4.5.

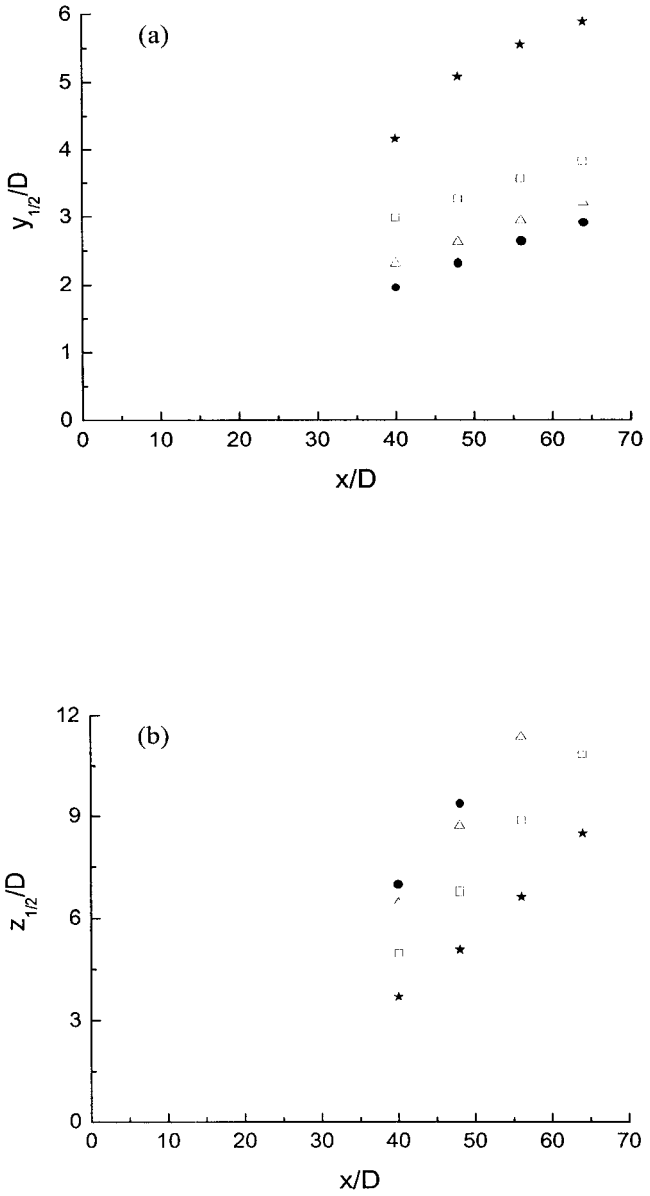

Figure 2.5: The development of (a) the vertical half-width and (b) the lateral half-width of the wall jet exiting a contoured nozzle measured by Davis and Winarto [13] at • h/D=1, △ h/D=1.5, □ h/D=2.5 and ⋆ h/D=4.5.

Davis and Winarto [13] only reported limited data in the far field. The decay of the local maximum streamwise velocity seems slower in the wall jets exiting the contoured nozzles than the wall jet exiting a long pipe reported by Eriksson et al. [15]. The lateral growth rate in the wall jets exiting the contoured nozzles with the top-hat velocity profile at the jet exit is $10 \sim 15\%$ larger than the wall jets exiting the long pipes with the fully developed velocity profile (cf. table 2.1). The Reynolds numbers in the investigations performed by Newman et al. [45] and Eriksson et al. [15] were 16,400 and 10,000 respectively, while the Reynolds numbers in the experiments performed by Abrahamsson et al. [1], Davis and Winarto [13], and Maslov et al. [42] were 79,000, 170,000 and 100,000 respectively. Thus, it is not clear whether the difference in the observed lateral growth rate is due to the differences in the velocity profiles or Reynolds numbers.

The measurements of the vertical half-width shown in figure 2.7 and the vertical growth rate (cf. table 2.1) reported by different investigations differed significantly even for the same exit velocity profile. In particular, the vertical half-width and vertical growth rate reported by Davis and Winarto[13] were significantly smaller than the results reported by Abrahamsson et al. [1] or Maslov et al. [42]. It should be noted that the boundary conditions in these facilities differed. There was a wall behind the jet nozzle in Abrahamsson et al.'s [1] and Maslov et al.'s [42] facilities to block the entrainment from behind the nozzle, while a back wall was not used in Davis and Winarto's [13] investigation.

Eriksson et al. [15] examined the effect that the presence of a wall behind the nozzle had on the development of wall jet exiting a long pipe using flow visualization for an exit Reynolds number of 10,000. The spread angle Eriksson et al. [15] measured from the images of the flow are summarized in table 2.2. They found that the largest vertical spread angle occurred when there was not a wall behind the nozzle. Somewhat surprisingly the smallest lateral growth occurred when there was a small wall behind

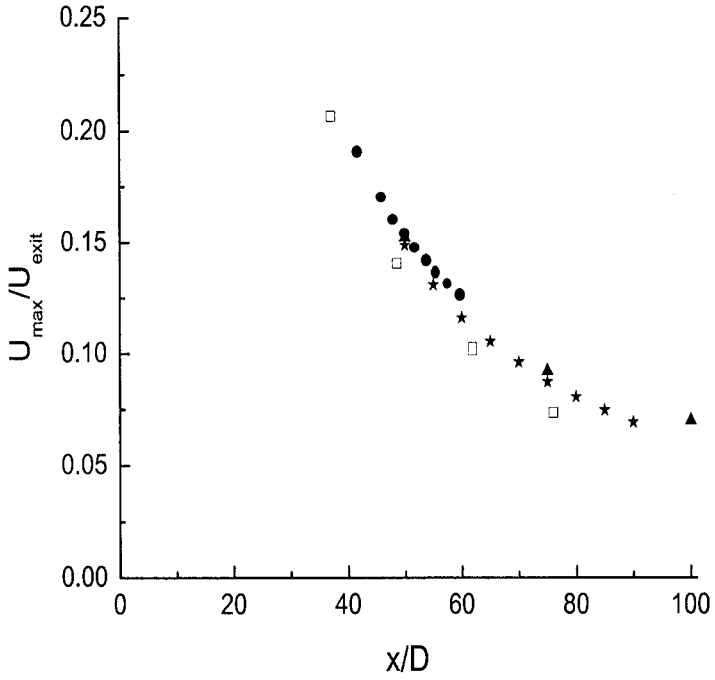

Figure 2.6: Decay of the local maximum streamwise velocity in the wall jet exiting a contoured nozzle measured by ★ Abrahamsson et al. [1], • Davis and Winarto [13], and ▲ Maslov et al. [42] and in the wall jet exiting a long pipe measured by □ Eriksson et al. [15].

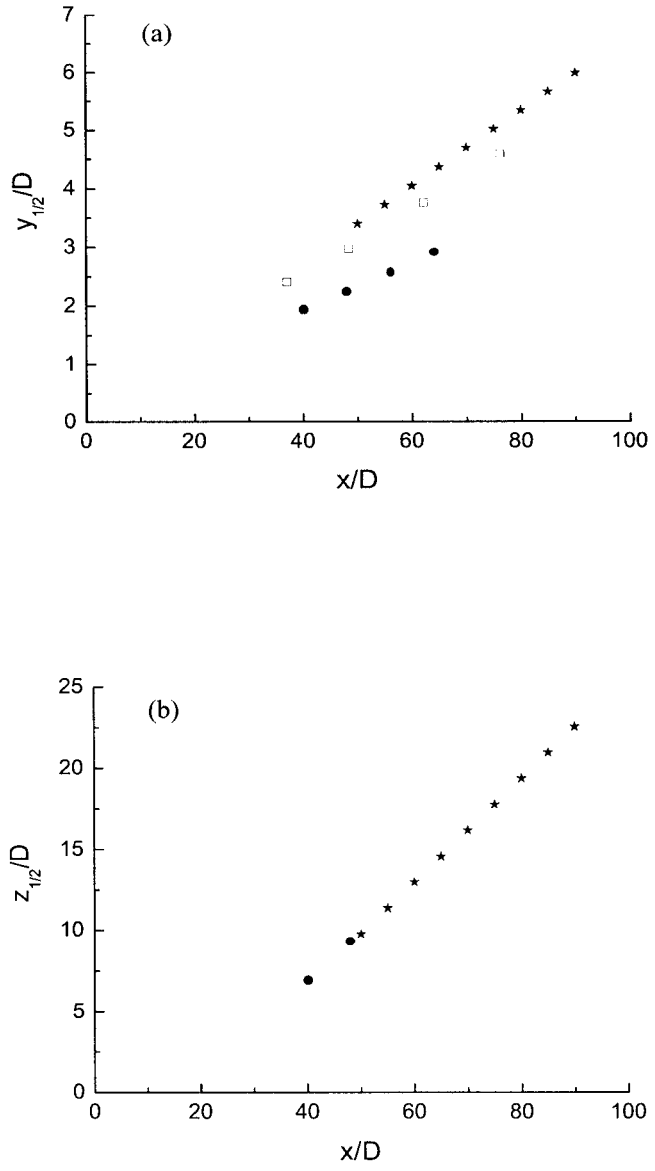

Figure 2.7: Development of (a) the vertical half-width and (b) the lateral half-width in the wall jet exiting a contoured nozzle measured by ⋆ Abrahamsson et al. [1], • Davis and Winarto [13] and in the wall jet exiting a long pipe measured by □ Eriksson et al. [15].

	Back wall height(/D)	Back wall width (/D)	Vertical spreading angle	Lateral spreading angle
High wall	92	240	4.89°	52°
Low wall	46	240	5.16°	47°
No wall	\	\	5.85°	51°

Table 2.2: The effect of the wall behind the nozzle on the spread of the jet in vertical and lateral directions reported by Ericksson et al. [15]

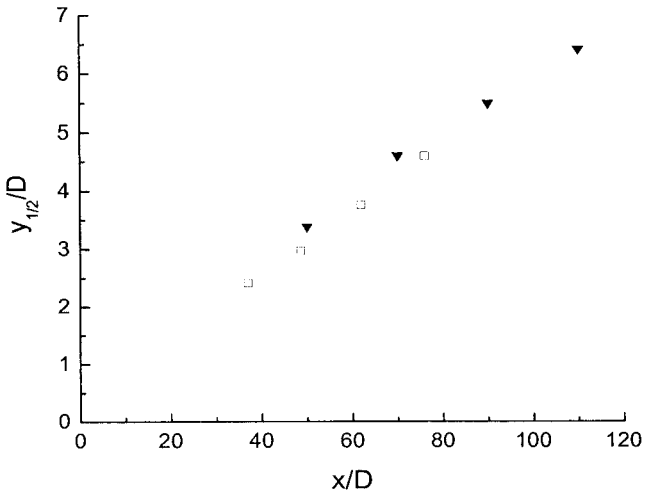

Figure 2.8: The effect of the wall behind the nozzle on the development of the vertical half-width measured □ with a back wall by Eriksson et al.[15], and ▼ without a back wall by Newman et al. [45].

the nozzle, whereas the lateral spread angle in the wall jet with the high wall was almost the same as without the wall behind the jet. Eriksson et al. [15] later measured the growth of the jet half-width in the wall jet exiting a long pipe with a wall behind the nozzle using hot-wire anemometry. They found the vertical and lateral growth rates in the far field were 0.055 and 0.27 respectively, similar to those reported by Newman et al. [45] for a long pipe without a back wall, 0.052 and 0.28 respectively. A comparison of the vertical half-width measured in two cases is shown in figure 2.8. There is a difference between the reported half-width measurements but there does not appear to be a large difference in the vertical growth rate of the jet. It is not clear why this differs from the flow visualization results reported by Eriksson et al. [15] but this will be investigated further here.

The effect of the entrainment on the jet growth was examined by Rajaratnam et al. [52]. They examined the growth of the wall jet exiting a 9.525 mm diameter nozzle and flowing into a 311.15 mm wide and 457.2 mm deep flume and a 1092.2 mm wide and 660.4 mm deep tank. A comparison of the vertical half-width and the lateral length scale, $z'_{1/2}$, at y/D=0.5 between two cases are shown in figure 2.9. It is clear that the narrow flume confined the entrainment in the lateral direction causing the lateral growth rate in the wall jet flowing into the narrow flume to be much less than the wall jet flowing into the wide tank in the region beyond x/D=30. There was not a significant difference in the vertical growth rate between the two cases though the tank was deeper than the flume.

There have been fewer investigations that examined the development of the profiles of the lateral velocity and the profiles of the turbulent Reynolds stresses in the three-dimensional wall jet. Padmanabham and Gowda [48] examined the normal stress in the wall jet exiting a segment with h/D=0.8 (cf. figure 2.2) at different streamwise locations. They found the profiles of the root mean square of streamwise fluctuating velocity, u', measured along the jet centerline and laterally across the jet at the height

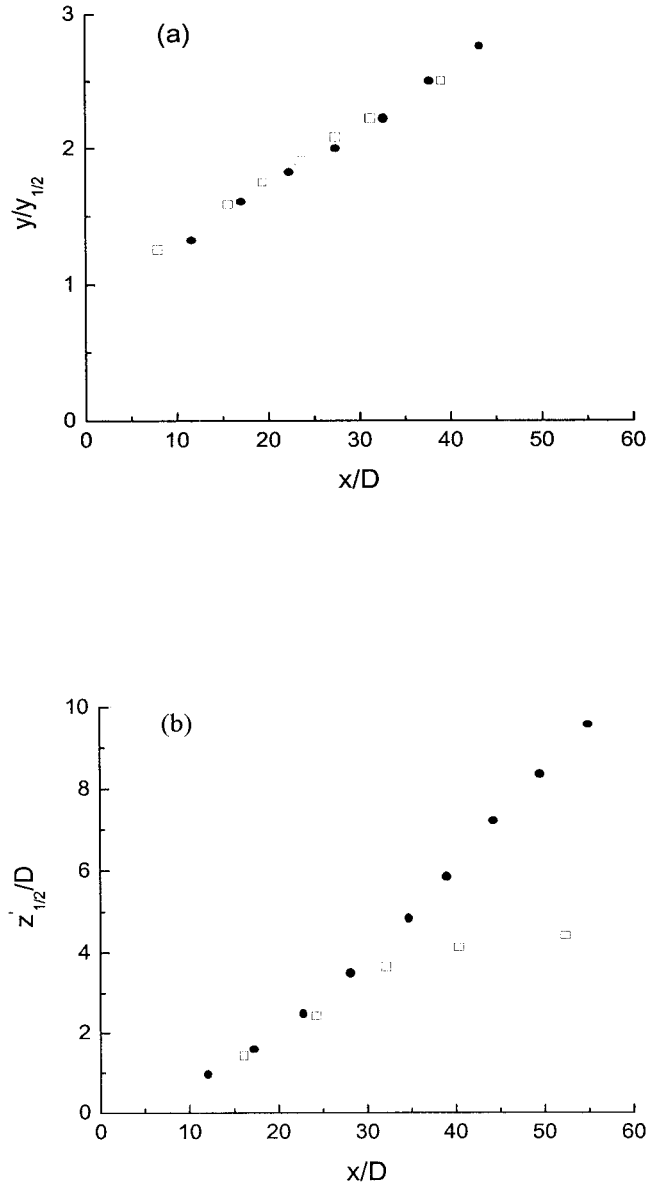

Figure 2.9: Development of length scales measured by Rajaratnam [52] in (a) vertical direction and (b) lateral direction in the three-dimensional wall jet flowing into □ a narrow flume and • a wide tank.

of the maximum velocity point approximately collapsed beyond x/h=50 (or x/D=40) when they were normalized by the local maximum mean streamwise velocity and the jet half-widths. Abrahamsson et al. [1] recently performed an extensive investigation of the far field of the three-dimensional wall jet formed by a round jet exiting a contoured nozzle. They measured the mean velocities, normal stresses and Reynolds shear stresses along the jet centerline and laterally across the jet at the height of the maximum velocity point from x/D=50 to x/D=90 for jets with exit Reynolds numbers ranging from 5.2×10^4 to 1.0×10^5. They reported that the development of the three-dimensional wall jet was independent of the jet exit Reynolds number in this range. The profiles of mean lateral velocity, W, were approximately self-similar when they were normalized by local maximum streamwise velocity and jet half-width though little scatter appeared in the profiles. The root mean square of fluctuating velocities, u' and w', were self-similar when they were normalized using the local maximum streamwise velocity and the jet half-widths. The profiles of Reynolds shear stress, $\overline{uw}$, normalized by the square of local maximum streamwise velocity, U_{max}^2, and the jet half-width also collapsed. They also reported that the mean vertical velocity of the wall jet was the second order compared to mean streamwise and lateral velocities. For example, $V_{max}/U_{max} = 1 - 2\%$ in the region from x/D=50 to 90.

2.2 Development of the Three-Dimensional Wall Jet in Near and Intermediate Fields

There have been fewer detailed investigations of near and intermediate fields in the three-dimensional wall jet. One of the initial extensive investigations of near and intermediate fields was performed by Viets and Sforza [67] in the wall jet exiting a rectangular orifice with a width to height ratio of 10. They found that the size of the

potential core decreased with the downstream distance and tended to disappear by x/H=10 causing the streamwise velocity profile to change significantly in this region. Thus, they stated that the near field ended at x/H=10. Beyond this point the local maximum streamwise velocity, U_{max}, began to decay as a function of the streamwise distance. They reported that the decay of local maximum streamwise velocity was given by $U_{max}/U_{exit} \sim (x/H)^{-0.162}$ in the region x/H=10 - 40. The profiles of mean streamwise velocity approximately became self-similar in the region $x/H \geq 40$ when they were normalized using the local maximum streamwise velocity and the jet half-width.

Padmanabham and Gowda [48] also performed detailed measurements in near and intermediate fields of the wall jets exiting a round orifice and segments of a round orifice (cf. figure 2.2). They found that the decay rates of local maximum streamwise velocity in the wall jets exiting the segments with different shapes were the power functions of the streamwise distance, x/h, in the region $x/h \geq 10$ indicating the intermediate field likely began at the streamwise position of x/h=10, where h was the distance of the top edge of the round orifice above the surface of the wall. However, their results showed that the local maximum mean streamwise velocity began to decay around x/h=6 for the segments of h/D=0.23 and h/D=0.8. Padmanabham and Gowda [48] also noted that the geometry of the exit orifice had significant effect on the decay of local maximum streamwise velocity as summarized in table 2.3. For example, the decay of the local maximum velocity in the wall jet exiting a segment with h/D=0.5 was given by $U_{max}/U_{exit} \sim (x/h)^{-0.63}$ that differed significantly from the results for segments of h/D=1 or h/D=0.23 given by $U_{max}/U_{exit} \sim (x/h)^{-0.75}$ and $U_{max}/U_{exit} \sim (x/h)^{-0.852}$ respectively. Padmanabham and Gowda [48] examined the profiles of mean streamwise velocity and root mean square of streamwise fluctuating velocity for the wall jet exiting a segment of h/D=0.8. They found that the profiles of mean streamwise velocity measured along the jet centerline and laterally across the

jet at the height of the maximum velocity point collapsed at $x/h \approx 22.5$, while the normalized profiles of root mean square of streamwise fluctuating velocity still changed until x/h=50 indicating that the intermediate field extend to $x/h \approx 50$ (or $x/D \approx 40$). Thus, the decay rates of the local maximum velocity reported by Padmanabham and Gowda[48] were calculated only for the initial portion of intermediate field.

Davis and Winarto [13] examined the development of the jet half-width in the wall jet exiting a contoured nozzle in the region $8 \leq x/D \leq 48$ as shown in figure 2.10. They found that the jet grew in the lateral direction much faster than in the vertical direction, and the anisotropy in the growth of the wall jet increased as the flow evolved downstream. The growth rate particularly the lateral growth rate was changing in the region $x/D < 40$. Davis and Winarto [13] reported that after x/D=40 the lateral growth rate became constant with a value of 0.32.

2.3 Evolution of the Large-Scale Structures

The large anisotropy in the growth rate observed in the three-dimensional wall jet is caused by the large-scale vortex structures that occur in the flow. Launder and Rodi [35] proposed that the development of this flow could be understood by examining the governing equation of streamwise vorticity in the three-dimensional wall jet. Launder and Rodi [35] argued that in the near and intermediate fields of the jet with high-Reynolds-number, the viscous diffusion term and the Reynolds stress terms were the higher order, so the first order governing vortex equation was given by

$$\frac{D\Omega_x}{Dt} = \Omega_x \frac{\partial U}{\partial x} + \Omega_y \frac{\partial U}{\partial y} + \Omega_z \frac{\partial U}{\partial z}, \tag{2.1}$$

or

$$\frac{D\Omega_x}{Dt} = \Omega_x \frac{\partial U}{\partial x} + \frac{\partial W}{\partial x}\frac{\partial U}{\partial y} - \frac{\partial V}{\partial x}\frac{\partial U}{\partial z}. \tag{2.2}$$

Segment (h/D)	Flow region	U_{max}/U_{exit}
0.23	$10 \leq x/h \leq 30$	$x^{-0.852}$
0.5	$10 \leq x/h \leq 20$	$x^{-0.63}$
0.8	$10 \leq x/h \leq 22.5$	$x^{-0.67}$
1	$10 \leq x/h \leq 18$	$x^{-0.75}$

Table 2.3: Decay of the maximum mean streamwise velocity in the intermediate field reported by Padmanabham and Gowda [48].

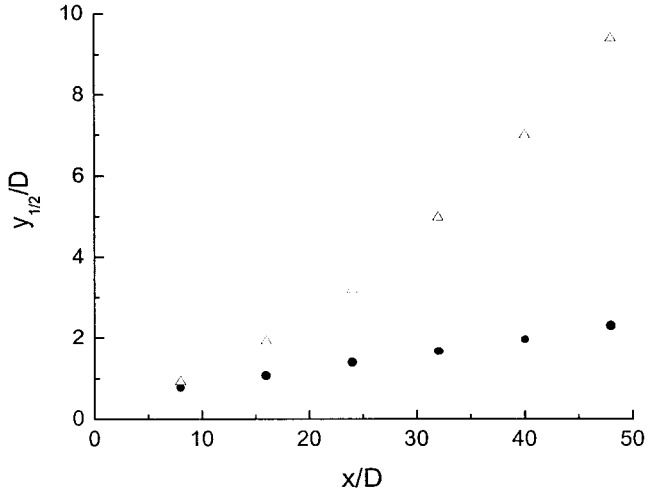

Figure 2.10: Jet half-widths of the wall jet measured by Davis and Winarto[13]. • the vertical half-width and △ the lateral half-width.

Launder and Rodi noted that for the axisymmetric free jet the last two terms on the right of equation 2.2 would balance so no mean streamwise vorticity was created in the flow field. They noted, however, that in the three-dimensional wall jet there must be regions of counter rotating mean streamwise vorticity on each side of the jet centerline in the y-z planes as shown in figure 2.11. These regions convect flow laterally away from the center of the jet causing the large lateral growth rate of the jet.

Iida and Matsuda [29] measured the mean streamwise vorticity of a wall jet exiting a round nozzle in the region $5 \leq x/D \leq 15$ by differentiating the mean velocity field. They found there were regions of mean streamwise vorticity on each side of the jet centerline as shown in figure 2.12. The broken and solid lines indicate counter clockwise and clockwise mean streamwise vorticity respectively, if they are viewed from the nozzle. The vorticity values have been normalized by the local maximum streamwise velocity, U_{max}, and the nozzle diameter, D. It is clear that they were regions of counter rotating vorticities, as proposed by Launder and Rodi [35], but these regions were situated laterally across the jet. The locations of the regions changed with the outer vortex inducing the inner vortex out and towards the wall as the flow evolved downstream. The measurements of Davis and Winarto[13] showed that the lateral growth rate of the jet continued to increase from $x/D = 15$ to $x/D = 40$ indicating the locations of the structures likely continue to change as the flow evolves downstream. This will be investigated further here.

Matsuda et al. [43] later performed conditional average measurements in the region $1.75 \leq x/D \leq 3.0$ to investigate the large-scale structures that contribute to the regions of mean streamwise vorticity measured by Iida and Matsuda [29]. In particular, they measured the velocity field conditioned on a positive peak of the streamwise fluctuating velocity on the centerline of the jet. The deformation of the vortex structure was determined by the time delay between trigger and the maximum

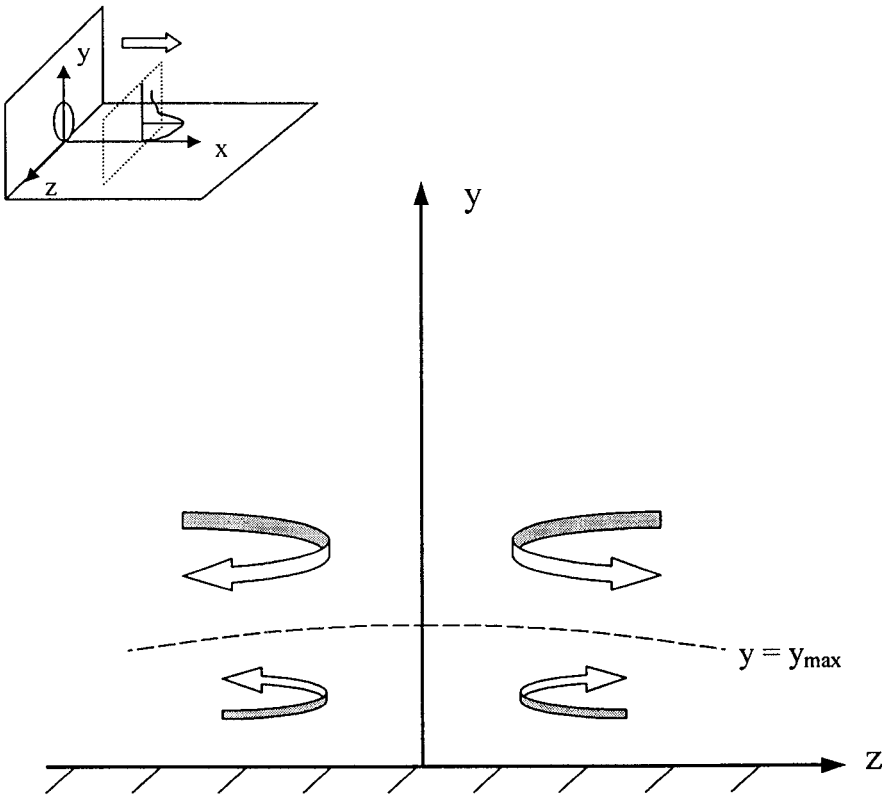

Figure 2.11: Schematic of streamwise vortices on y-z plane proposed by Launder and Rodi [35].

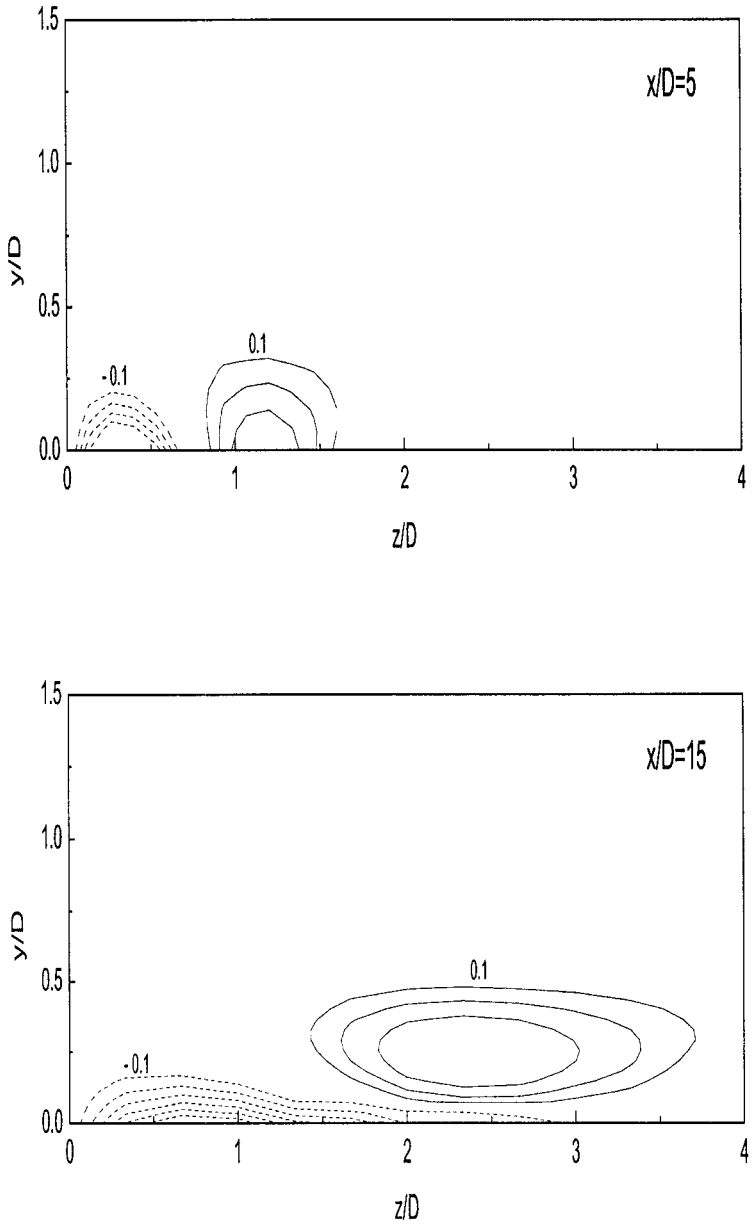

Figure 2.12: Schematic of streamwise vorticity contours reported by Iida and Matsuda [29].

instantaneous lateral velocity measured by cross-wire probes at each vertical location. They proposed that the outer region of mean streamwise vorticity was caused by a series of large-scale horseshoe structures with legs inclined relative to the streamwise direction in the region $y > y_m$ as shown in figure 2.13. These structures caused large regular deviations of positive vorticity to occur above $y = y_m$. However, Matsuda et al. didn't explain the cause of the inner region of streamwise vorticity.

Ewing and Pollard [16] and Ewing et al. [17] later used measurements of two-point, two-time correlations of the streamwise fluctuating velocity in the region $0.05 \leq y/D \leq 0.40$ of the wall jet to examine the evolution of the large-scale vortex structures in the region $3 \leq x/D \leq 14$. They proposed that both sets of region of mean streamwise vorticity were formed from the ring-like vortex structures shed from the round jet. Their measurements indicated that the bottom of the vortex structure interacted with the wall causing the bottom center of the vortex structures to move away from the wall and the outer bottom edges of structures to move close to the wall as shown in figure 2.14. The outer bottom edges were convected slower than the center of the vortex structure forming inner horseshoe vortices that contribute the inner regions of mean counter rotating streamwise vorticity. Ewing and Pollard [16] noted that the upper half of the vortex structure should be convected faster than the outer edges forming the outer horseshoe-like vortex structures in the outer region similar to that proposed by Matsuda et al. Thus, they suggested that the streamwise vortices both in the region near the centerline and the outer region were formed from the same structures. The structures on each side of the centerline would act to draw the flow down and eject it outward causing the large lateral velocity growth rate observed in the three-dimensional wall jet. Ewing et al. [17] also found that the outer streamwise vortices tended to induce the inner vortices towards the wall and outward as the flow evolved downstream causing the regions of the structures to become stacked as noted by Iida and Matsuda [43] in the mean vorticity measurements. Ewing and Pollard [16]

and Ewing et al. [17] primarily developed their model by examining the streamwise velocity correlations in the vertical direction of the jet. They only performed a limit amount of correlations in the lateral direction so it was not possible to examine the evolution of the large-scale vortex structures in the lateral direction.

Ewing and Pollard [16] and Ewing et al. [17] also performed flow visualization to examine the evolution of the large-scale structures. The images showed that the large lateral growth was caused by the lateral ejection of the flow near the wall. This was consistent with the model proposed Mastsuda et al. [43] and Ewing and Pollard [16] that the counter rotating vortices draw the flow down and eject it outward. They further noted that the flow ejections were not continuous. They noted there were peaks and valleys on the images taken on the x-y planes on the centerline of the jet. Ewing and Pollard [16] observed that the large lateral ejection occurred shortly after the passage of the peak regions on the x-y plane and then stopped before the next passage of the peak regions. Thus, they proposed that the evolution of the large-scale structures were highly intermittent. The images taken on the y-z planes also indicated that the flow ejection was not instantaneously symmetric to the centerline of the jet.

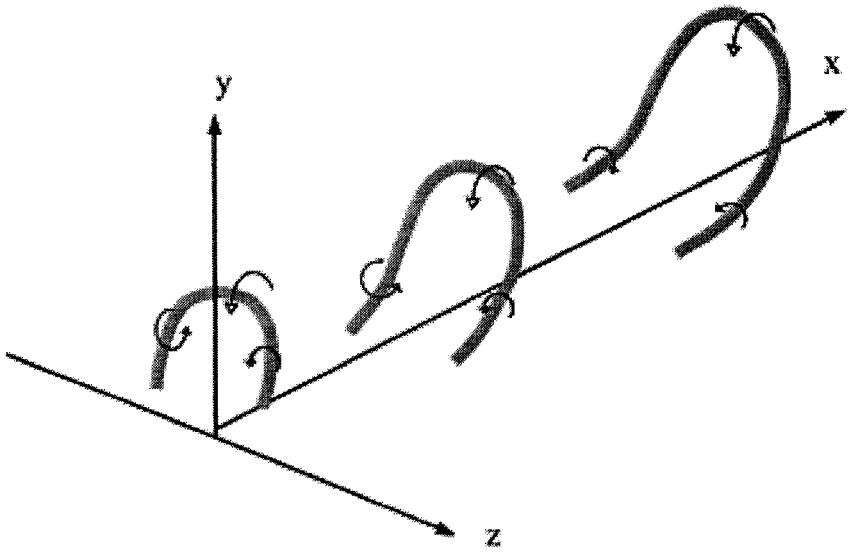

Figure 2.13: Schematic of the model for the large-scale structures in the near field of the three-dimensional wall jet proposed by Matsuda et al. [43].

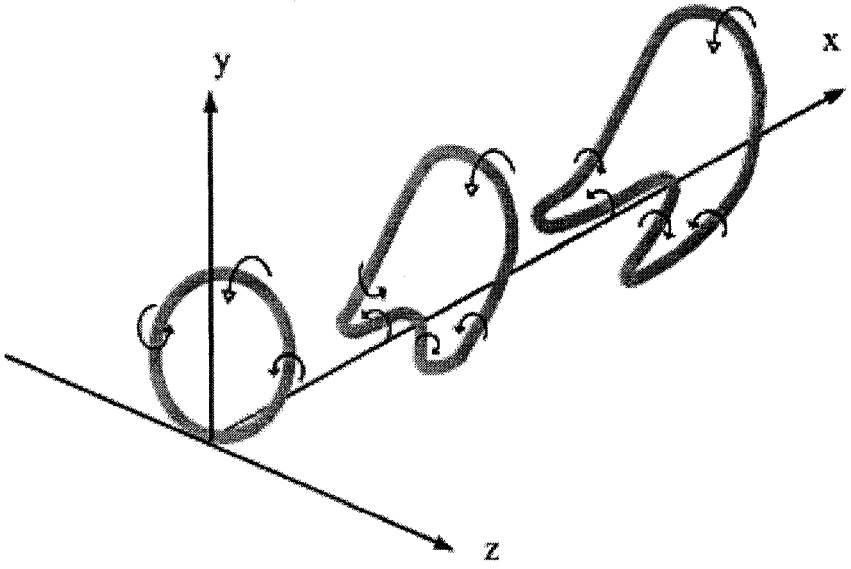

Figure 2.14: Schematic of the alternative model for the large-scale vortex structures in the three-dimensional wall jet proposed by Ewing and Pollard [16].

Chapter 3

Experimental Facilities and Techniques

The development of the three-dimensional wall jet was studied using three different jets as the source: a jet exiting a 38.1 mm (1.5in) diameter contoured nozzle, a jet exiting a long pipe with a diameter of 38.7 mm (1.525in)and a jet exiting a long pipe with a diameter of 12.7 mm (0.5in). These three nozzles were used to generate three-dimensional wall jets in a facility that included a large horizontal plate parallel to the jet centerline and a large vertical plate that could be mounted behind the nozzle. The profiles of the single-point moments of the turbulent field were measured using hot-wire anemometry with probes that were moved through the flow field using a computer controlled traverse. The evolution of the large-scale structures were examined by measuring the vertical and lateral correlations of the streamwise fluctuating velocities using one or two rakes of single hot-wire probes at different positions in the flow field.

The jet facilities and the three-dimensional wall jet facility are discussed first. The hot-wire anemometry system, calibration techniques and measurement techniques used in the measurements of the profiles and contours of the single-point moments

are then discussed. The preliminary measurements performed in the free jet to verify the jet and the measurement techniques are then presented. Finally, the hot-wire rakes, the hot-wire anemometry system and data analysis tools used to examine the development of the large-scale vortical structures in the three-dimensional wall jet are described.

3.1 Wall Jet Facilities

The first jet studied here exited a contoured nozzle with a diameter of 38.1 mm in the facility shown in figure 3.1. The air was supplied by a DAYTON 4C330 centrifugal blower driven by a 5HP, 3-phase AC motor. The flow from this blower entered a 1219 $\times$ 1016 $\times$ 1016 mm settling chamber that included three foam barriers at the entrance to make the flow uniform and a honeycomb consisting of approximately 100,000 127 mm long 3.175 mm diameter straws to reduce the large-scale structures in the flow. A screen was positioned downstream of this honeycomb in order to transition the wakes created by the honeycomb [37, 38]. The flow from the settling chamber then entered a 8in diameter pipe through a bellmouth designed to create an uniform flow in the pipe. A honeycomb and screens were included in the pipe to further reduce the turbulence in the flow. Finally the flow passed through a contoured nozzle with an area contraction ratio of 28:1. The profile of the nozzle was a fifth order polynomial to ensure the velocity profile was top-hat at the jet exit [28].

The second jet studied here exited a long pipe shown in figure 3.2. The flow from the same centrifugal blower entered a settling chamber through a diffuser. The flow in this settling chamber passed through a column of air filters that conditioned the flow. The flow then entered a long pipe with a diameter of 38.7 mm through a bellmouth. The length of pipe was 60 diameters.

The third jet exited a long pipe with a diameter of 12.7 mm and a length of 95

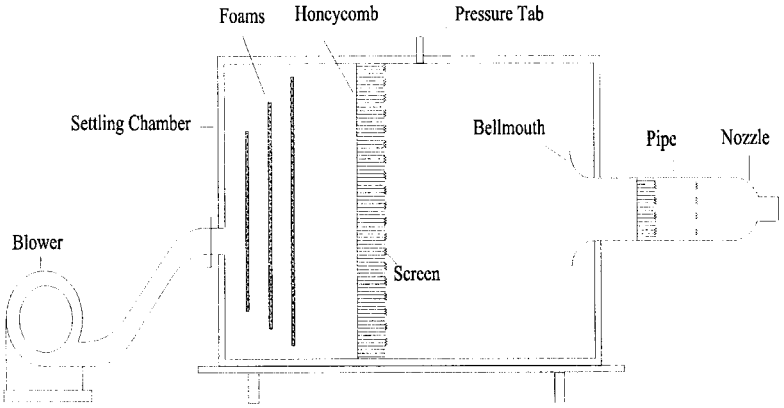

Figure 3.1: Schematic of the contoured nozzle jet facility.

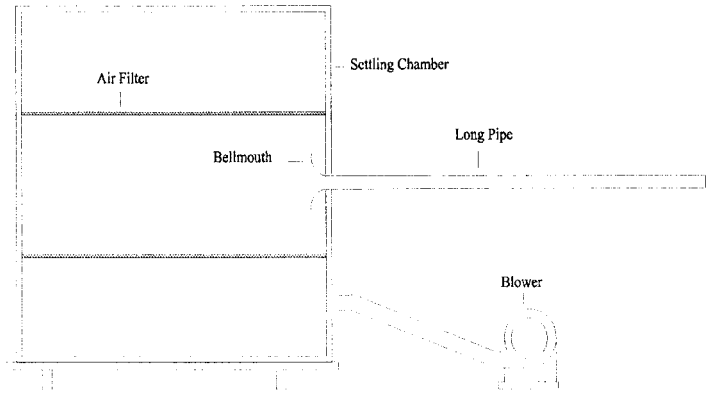

Figure 3.2: Schematic of the large diameter long pipe jet facility.

diameters. The air flow from this facility was supplied from a compressed air line with the maximum pressure of 0.62 Mpa (90 psi). The flow passed through a filter to remove the contaminants in the air and two pressure regulators that reduced the pressure fluctuation in the line before the air entered the pipe. The pressure regulator was connected to the long pipe using a flexible tube. A honeycomb containing straws with a diameter of 3.175 mm and a length of 63.5 mm were used at the entrance of the long pipe to remove any mean swirl from the flow.

The jets exiting these facilities flowed over a horizontal plate with a length of 1829 mm and a width of 2438 mm shown in figure 3.3. Previous studies [1, 16] have shown that this width was sufficient to ensure the development of the wall jet was not affected by the finite width of the plate. The length of the plate was 48 times the diameter of the contoured nozzle or large diameter long pipe. This was sufficient to examine the flow in the intermediate field. The length of the plate was 152 times the diameter of the small diameter long pipe so it could be used to investigate the development of the flow through the intermediate and far fields of the three-dimensional wall jet. The experimental apparatus was designed so that a vertical plate could be installed behind the nozzle to prevent the entrainment from behind the plate. The wall had a height of 1219 mm and a width of 2438 mm. The size of the room was approximately $6401 \times 5893 \times 3785$ mm that was found to be large enough to guarantee the entrainment into the three jets was not affected.

A three-dimensional traverse, shown in figure 3.4, was used to move the hot-wire probes through the flow field. The horizontal plane of the traverse was mounted 1200 mm above the horizontal plate. The traverse was moved in the vertical direction and lateral direction using two VEXTA step motors to ensure that the accuracy and repeatability of the profile measurements. The minimum step size of this traverse was 0.0254 mm. The traverse was moved manually in the streamwise direction. The measurement range of the traverse was approximately 500 mm in the vertical direction,

1200 mm in the lateral direction and 1750 mm in the streamwise direction.

The alignment of the wall jet facility was checked to ensure the traverse and the horizontal plate were parallel to the jet axis. Initially the centerline of the free jet was adjusted until it was parallel to the traverse. A dial indicator was used to ensure the horizontal plate was level with the traverse. The traverse, jet centerline and horizontal plate were in the range $0° - 0.15°$.

3.2 Measurements of the Single-Point Moments

The development of the three-dimensional wall jet was investigated for a range of different conditions. The effects of the initial and boundary conditions on the development of wall jet were investigated for the cases summarized in table 3.1. The development of wall jet was initially examined by measuring the profiles of the mean velocities and Reynolds stresses along the jet centerline and laterally across the jet at the height of the maximum streamwise velocity point for streamwise positions from x/D=3 to 40 in the large diameter wall jets and from x/D=10 to 90 in the small diameter wall jet. The profiles of streamwise mean velocity, U and turbulent stress, $\overline{u^2}$, were measured using single-wire probes, while the profiles of mean lateral velocity, W, and turbulent stresses, $\overline{v^2}$, $\overline{w^2}$, $\overline{uv}$ and $\overline{uw}$, were measured using cross-wire probes.

The contours of mean streamwise velocity and streamwise vorticity were also measured on y-z planes from x/D=3 to 40 and from x/D=6 to 40 respectively. The contours of mean streamwise velocity were measured at least 30×31 points on each y-z plane, while the contours of the mean streamwise vorticity were measured on a grid ranging from 15×21 to 20×21. Since the lateral growth rate is $3 - 5$ times larger than the growth rate in the vertical direction and the maximum lateral mean velocity is approximately $5 - 10$ times larger than the vertical mean velocity in the intermediate field of the three-dimensional wall jet, the mean streamwise vorticity

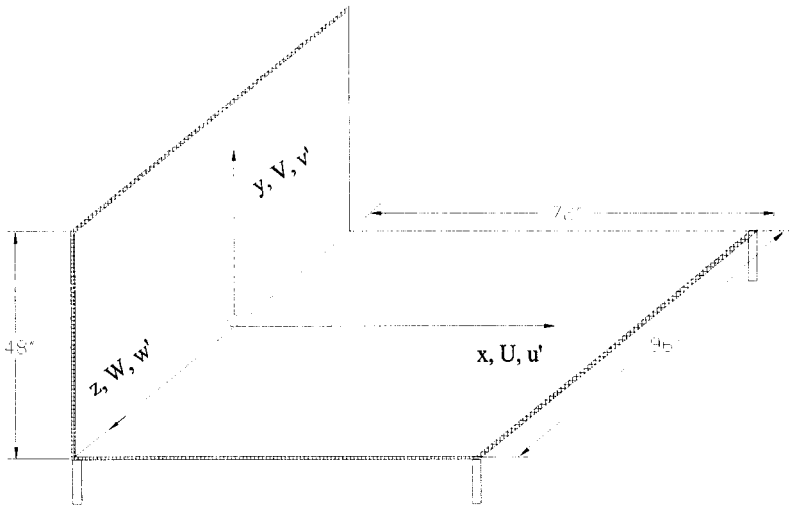

Figure 3.3: Schematic of the three-dimensional wall jet facility.

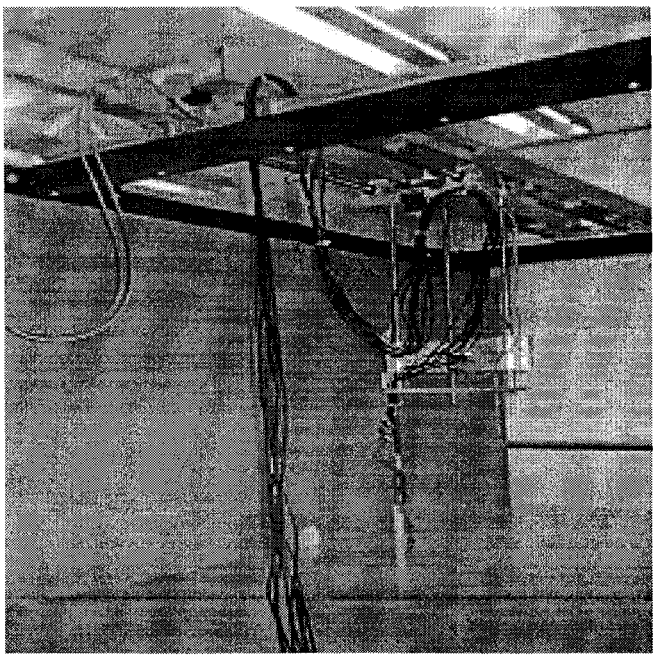

Figure 3.4: Photograph of the three-dimensional wall jet facility.

given by $\Omega_x = \partial W/\partial y - \partial V/\partial z$ was estimated here by $\Omega_x \approx \partial W/\partial y$ that was calculated by fitting fourth order polynomials to the lateral mean velocity measured along the vertical direction.

3.2.1 Hot-Wire Anemometry

The single-point moments of the turbulent flow field were measured using single hot-wire probes and cross-wire probes that were connected to a AN-2000 computerized anemometry system manufactured by A.A. Lab Systems. This anemometry system included a sample and hold board to ensure simultaneous sampling and a 14-bit A/D board to ensure a small quantization error. The single- and cross-wire probes used in this investigation were constructed by AUSPEX. The wires in these probes had a diameter of 0.005 mm and a length of 250 diameters for the single-wire probes and 300 diameters for the cross-wire probes.

3.2.2 Calibration of the Hot-Wire Probes

The hot-wires were calibrated at the exit of the contoured nozzle that was uniform to within 1.0%. The velocity of the jet was measured using a pressure tap installed on the top of the settling chamber. The pressure at this tap was measured using a VALIDYNE DP45 differential pressure transducer. The pressure at this point was initially calibrated by measuring the jet velocity using a Pitot tube and a water manometer with the resolution of 0.1mm.

The single wire probes were calibrated by measuring the output voltages of hot-wire anemometer for different velocities at jet exit. The voltages were recorded for 15 to 20 velocities in the range of the experiment. The results were then fitted using a fourth order polynomial to form a calibration curve. A typical result is shown in figure 3.5. The typical error in the fit was less than 0.2%.

Test	Jet exit	Back wall	Re_{exit}	$U_{exit}(m/s)$
Evolution of wall jet	38.1 mm contoured nozzle	Yes	108,000	45
Initial condition	38.1 mm contoured nozzle	Yes	108,000	45
	38.7 mm diameter pipe	Yes	108,000	44
	38.7 mm diameter pipe	Yes	68,000	28
Effect of the wall	38.7 mm diameter pipe	Yes	108,000	44
behind the nozzle	38.7 mm diameter pipe	No	108,000	44
Effect of the size	38.7 mm diameter pipe	Yes	108,000	44
of the wall/room	12.7 mm diameter pipe	Yes	68,000	80
Effect of the	12.7 mm diameter pipe	Yes	68,000	80
misalignment	12.7 mm diameter pipe	Yes	68,000	80

Table 3.1: Experimental conditions for single-point measurements.

The cross-wire probes, shown in figure 3.6, were calibrated using the Champagne-Sleicher law [9] given by

$$U_{eff1}^2 = U_0^2(sin^2\phi_1 + k_1^2 cos^2\phi_1), \tag{3.1}$$

and

$$U_{eff2}^2 = U_0^2[sin^2(\theta - \phi_1) + k_2^2 cos^2(\theta - \phi_1)], \tag{3.2}$$

where U_{eff1} and U_{eff2} are the effective velocities detected by wires 1 and 2 respectively, U_0 is the velocity vector in the plane of the cross-wire, $\phi 1$ is the angle between velocity vector and wire 1 and θ is the angle between wires 1 and 2. Here, k_1 and k_2 are angular sensitivities of wires 1 and 2 respectively. These, in general, are functions of the velocity, U_0, the angle of the flow and the ratio of the wire length to its diameter, l/d. The cross-wire probes were calibrated by initially positioning each wire perpendicular to the flow and calibrating it as a single wire to get a calibration between the effective velocity and output voltage. The angular sensitivities of the wires, k_1 and k_2, were determined by rotating the cross-wire probe through the angular region from 0 to 90°. Equations 3.1 and 3.2 were then used to determine the angular sensitivities of the wires, k_1 and k_2. The angular sensitivity of each wire with $l/d = 300$ was 0.15 ± 0.03 in the angular region $\phi = 5° \sim 60°$ in agreement with the results of Champagne [9]. It was found that the angular sensitivity of the wire were essentially independent of the velocity for a range U_0=8 to 45 m/s.

3.2.3 Errors in the Single-Point Measurements

One of the significant errors in the hot-wire measurements is the cross-flow error caused by the contribution from the other velocity component perpendicular to the hot-wire. Following the approach outlined by Shabbir et al. [55] for a two-dimensional flow, the cross-flow errors in the three-dimensional wall jet were estimated. The results

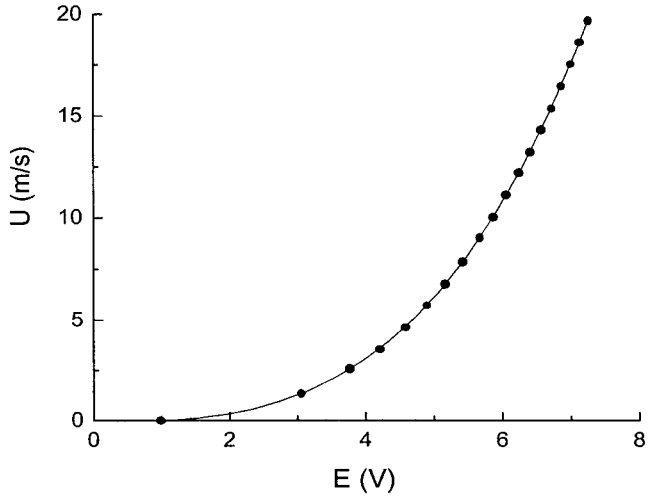

Figure 3.5: A typical calibration curve for a single hot-wire probe.

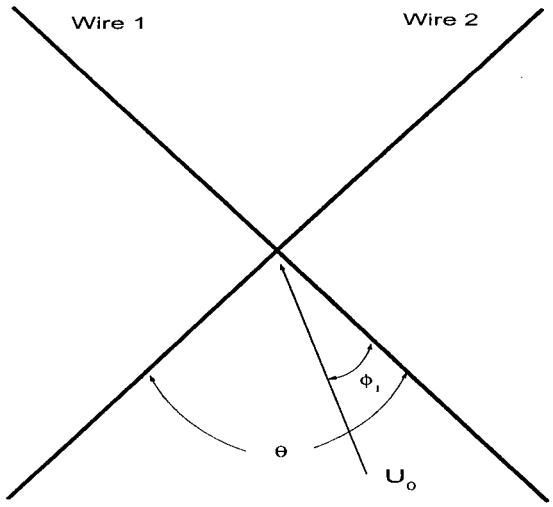

Figure 3.6: Schematic of a cross-wire probe.

for the cross-wire probe with an angle between two wires of 90° are listed in tables 3.2 - 3.4, where ΔU=$U_{measurement} - U$.

Rectification is also a major source of error in the hot-wire measurements, particularly in the measurements using the multi-wire probes. Since a hot-wire is only sensitive to the magnitude of the effective cooling velocity, rectification occurs when the flow reversal occurs in the single-wire measurements or when the resultant velocity changes to the other side of the wire in the measurements using cross-wire probes as shown in figure 3.7. In the measurements using the single wire probe the cross-flow becomes unacceptable large before the rectification is an issue. This is not always the case in the cross-wire measurements, particularly when there is a significant mean lateral velocity that biases the mean velocity towards one of the wires.

The effect of the rectification on the lateral velocity measurements can be approximately examined by looking at the phase diagram of the effective velocities [65]. If the resultant velocity is parallel to the wire 1 or wire 2, the effective velocities, shown in figure 3.8, for the two wires are given by

$$\widetilde{u}_{eff1} = k_1 \widetilde{u}_{eff2}, \tag{3.3}$$

or

$$\widetilde{u}_{eff2} = k_2 \widetilde{u}_{eff1}, \tag{3.4}$$

where $\widetilde{u}_{eff1}$ and $\widetilde{u}_{eff2}$ are the instantaneous effective velocities detected by wire 1 and 2 respectively. Thus, the cone of acceptance of the wires, which defines the velocities that can be uniquely resolved, falls between these two lines. If the density of the effective velocity points falling near either of the boundary lines is large, the measurements include a significant rectification error. The phase diagrams of the effective velocities were checked for a variety of lateral locations in the wall jets exiting the contoured nozzle and the long pipe. For example, the phase diagrams of the effective velocities measured across the jet at the height of the maximum

Single wire:

$$\Delta U = \frac{1}{2}\frac{V^2+\overline{v^2}}{U} - \frac{1}{2}\frac{\overline{uv^2}}{U^2} - \frac{V\overline{uv}}{U^2} + ...$$

$$\Delta\overline{u^2} = \frac{2V\overline{uv}+\overline{uv^2}}{U} + \frac{V^2\overline{v^2} - V^2\overline{u^2} + V\overline{v^3} - \overline{u^2v^2} - 2V\overline{u^2v}}{U^2} + \frac{1}{4}\frac{\overline{v^4}-\overline{v^2}^2}{U^2} + ...$$

Cross wire:

$$\Delta U = \frac{1}{1+k^2}(\frac{V^2+\overline{v^2}}{U} - \frac{\overline{uv^2}+2V\overline{uv}}{U^2}) + ...$$

$$\Delta V = -\frac{1}{1+k^2}(\frac{VW^2+V\overline{w^2}+2W\overline{vw}+\overline{vw^2}}{U^2}) + ...$$

$$\Delta W = -\frac{1}{1+k^2}(\frac{V^2W+W\overline{v^2}+2V\overline{vw}+\overline{v^2w}}{U^2}) + ...$$

$$\Delta\overline{u^2} = \frac{1}{1+k^2}(\frac{4V\overline{uv}+2\overline{uv^2}}{U} - \frac{2V^2\overline{u^2}+2\overline{u^2v^2}+4V\overline{u^2v}}{U^2}) + (\frac{1}{1+k^2})^2\frac{\overline{v^4}-\overline{v^2}^2}{U^2} + ...$$

$$\Delta\overline{v^2} = -\frac{1}{1+k^2}(\frac{V\overline{vw^2}+2W\overline{v^2w}+\overline{v^2w^2}}{U^2}) + ...$$

$$\Delta\overline{w^2} = -\frac{1}{1+k^2}(\frac{W\overline{v^2w}+2V\overline{vw^2}+\overline{v^2w^2}}{U^2}) + ...$$

$$\Delta\overline{uv} = \frac{1}{1+k^2}(\frac{\overline{vw^2}+2W\overline{vw}}{U} - \frac{W^2\overline{uv}+4W\overline{uvw}+V\overline{uw^2}+2\overline{uvw^2}}{U^2}) + ...$$

$$\Delta\overline{uw} = \frac{1}{1+k^2}(\frac{\overline{v^2w}+2V\overline{vw}}{U} - \frac{V^2\overline{uw}+4V\overline{uvw}+W\overline{uv^2}+2\overline{uv^2w}}{U^2}) + ...$$

Table 3.2: Estimates of the cross-flow error in the measurements using hot-wire techniques.

x/D	$y = y_{max}$	$y = y_{1/2}$	$z = z_{1/2}$
10	0.5%	2.7%	2.7%
20	1.2%	3.5%	2.6%
30	1.3%	3.9%	2.1%
40	1.4%	4.0%	1.7%

Table 3.3: Estimates of the cross-flow error for streamwise velocity, U, in the measurements using the single hot-wire probe.

x/D	$y = y_{max}$	$y = y_{1/2}$	$z = z_{1/2}$
10	1.0%	5.3%	5.3%
20	2.4%	6.8%	5.1%
30	2.5%	7.6%	4.1%
40	2.7%	7.8%	3.3%

Table 3.4: Estimates of the cross-flow error for streamwise velocity, U, the measurements using the cross-wire probe.

streamwise velocity point at x/D=30 are shown in figure 3.9. It is clear there aren't a significant number of points near the boundary lines at the jet centerline and a small number of points are near the boundary lines at $z/z_{1/2} \approx 1.0$ indicating that the effect of rectification on the measurements is not significant in the region $z/z_{1/2} \leq 1.0$. However, there are a significant number of points near the boundary line, $\widetilde{u}_{eff1} = k_1\widetilde{u}_{eff2}$, at $z/z_{1/2} \approx 1.5$ indicating that measurements in the lateral locations beyond $z/z_{1/2} = 1.5$ include significant errors. The phase diagrams of the effective velocities measured in the near and intermediate fields indicate the rectification error in the cross-wire measurements is not significant in the region $z/z_{1/2} \leq 1.5$ for $x/D \leq 20$ and in the region $z/z_{1/2} \leq 1.0$ for $x/D \leq 40$.

The effect of the rectification was also checked for the profiles measured along the jet centerline in the near and intermediate fields. It was also found that there was not a significant rectification error in the region $y/y_{1/2} \leq 1.0$.

The change of the fluid temperature is another source of error in hot-wire measurements. The jet and room temperature were monitored during the measurements performed here using two E-type thermocouples sampled using a 16-channel COMPUTER-BOARDS PCI-CIO-TC data acquisition board with a resolution of $0.04°C$. It was found that the jet and room temperature changed less than $1°C$ during every 8 hours period of measurements. The error caused by this change in the fluid temperature was examined by calibrating a single hot-wire probe at different fluid temperatures as shown in figure 3.10. It was found that the maximum relative error in the velocity was approximate $1.5\%/°C$. In order to reduce the effect of change in the fluid temperature, the temperature correlation technique proposed by Beuther[2] was used. In this case the calibration was written as a correlation between Reynolds number and Nusselt number given by

$$R_e = A_0 + A_1 N_u^{1/2} + A_2 N_u + A_3 N_u^{3/2} + A_4 N_u^2, \tag{3.5}$$

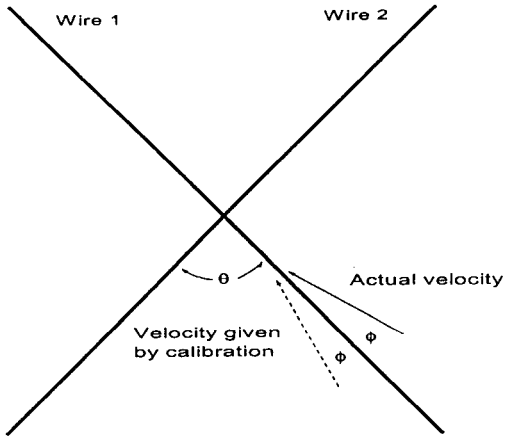

Figure 3.7: Rectification in measurements using cross-wire probe.

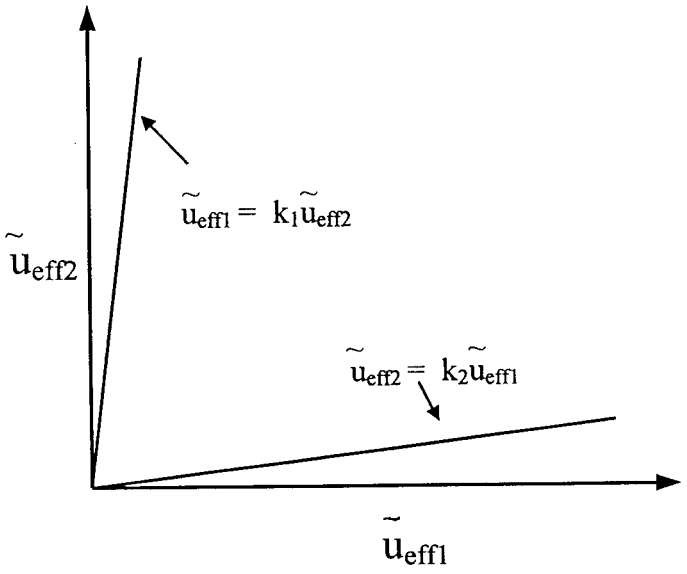

Figure 3.8: Phase diagram for the resultant velocity parallel to wire 1 or wire 2.

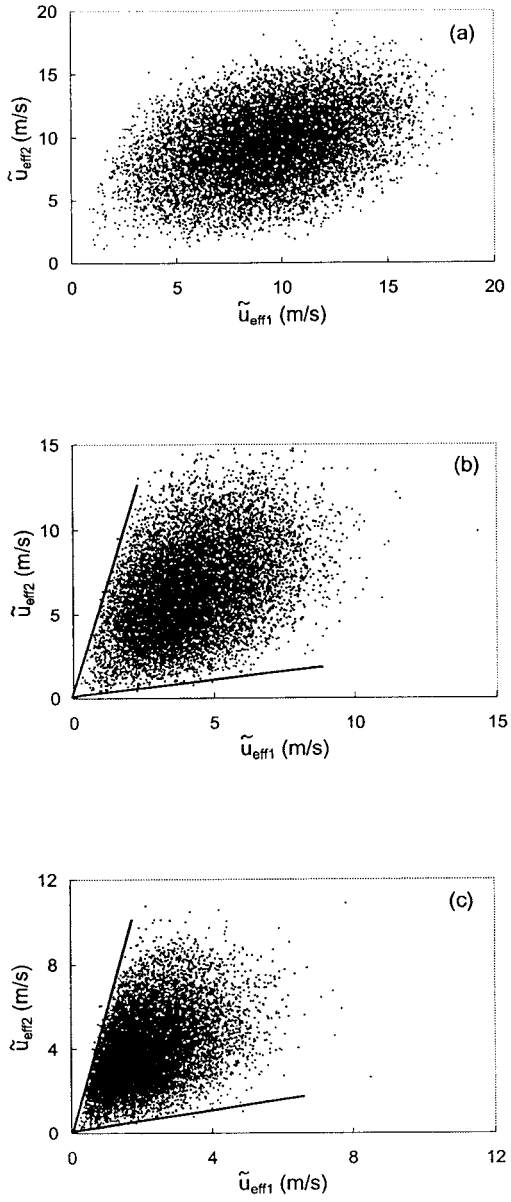

Figure 3.9: Phase diagrams in the measurements of lateral moments at (a) $z/z_{1/2} = 0$, (b) $z/z_{1/2} \approx 1.0$, and (c) $z/z_{1/2} \approx 1.5$ for x/D=30.

where A are calibration constants that are in principle independent of the ambient temperature. Using the energy balance for the wire this can then be written as a correlation between velocity of the flow and output voltage given by

$$U = C_0 + C_1 E(\frac{T_s - T_{f,c}}{T_s - T_{f,m}})^{1/2} + C_2 E^2(\frac{T_s - T_{f,c}}{T_s - T_{f,m}}) \\ + C_3 E^3(\frac{T_s - T_{f,c}}{T_s - T_{f,m}})^{3/2} + C_4 E^4(\frac{T_s - T_{f,c}}{T_s - T_{f,m}})^2, \tag{3.6}$$

where C are again independent of the ambient temperature. Here, R_e and N_u are Reynolds number and Nusselt number of the flow over the wire, $T_{f,c}$ and $T_{f,m}$ are the fluid temperature during the calibration and measurements, T_s is the hot-wire temperature in measurements and E is the voltage measured by the anemometer. The relative error in the velocity caused by the change in the fluid temperature was less than $0.4\%/°C$ after the temperature compensation. It should be noted that this was the error in mean velocity measurements. The error in the measurements of the fluctuating velocity was much smaller because the measurements depended primarily on the slope of the calibration and were fairly independent to the shifts in this curve.

The major random error in this investigation was the uncertainty in the estimator of the moment caused by the finite sampling time. The uncertainties of estimators for the mean velocities and Reynolds stresses are given by [62]

$$\xi_U = \frac{u'/U}{\sqrt{N}}, \tag{3.7}$$

$$\xi_W = \frac{w'/W}{\sqrt{N}}, \tag{3.8}$$

$$\xi_{u^2} = \frac{1}{\sqrt{N}} \sqrt{\frac{\overline{u^4}}{\overline{u^2}^2}}, \tag{3.9}$$

where N is the number of independent points. It is generally argued that only points sampled approximately every three characteristic time scales are independent [24] so that N can be estimated as

$$N = \frac{T}{3\tau_l}, \tag{3.10}$$

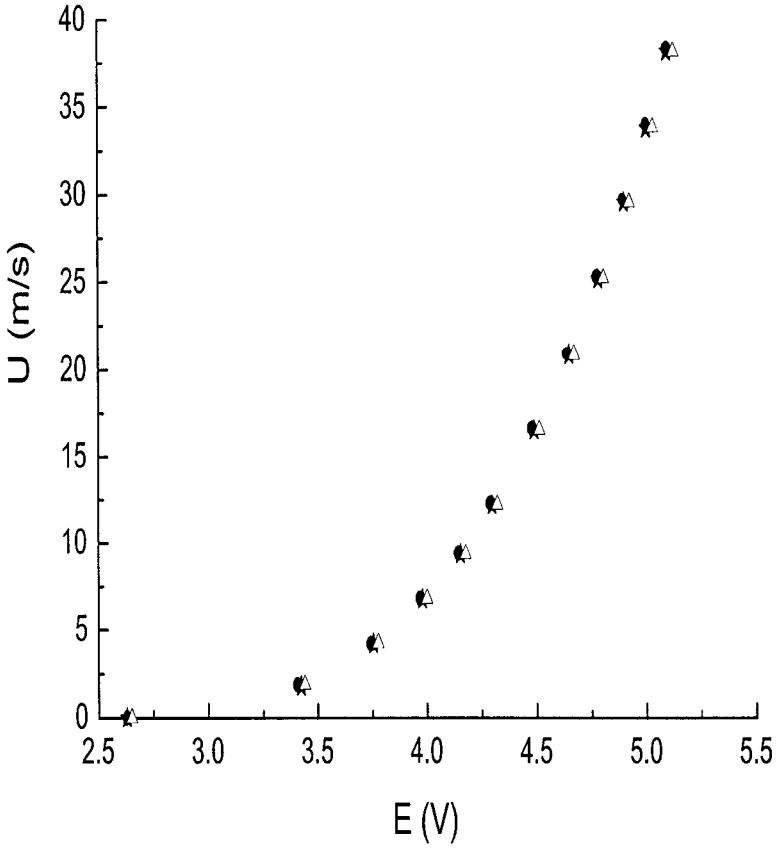

Figure 3.10: Comparison of the calibration curves at different fluid temperatures. • T=25.5°C, ⋆ T=24.3°C and △ T=22.8°C.

where T is the sampling time, τ_l is the integral time scale given by [36]

$$\tau_l = \frac{1}{\overline{u^2}} \int_0^\infty R_{uu}(\tau) d\tau. \tag{3.11}$$

Here, R_{uu} is the two-time correlation of the streamwise fluctuating velocity. It should be noted that the estimate of uncertainty in the measurement is the standard deviation. Thus, the uncertainty of estimator for conventionally used 95% confidence level is twice of this value. The sample time required for the measurements of the profiles in mean velocities and Reynolds stresses in the region from x/D=3 to 40 was determined using this approach. The uncertainties of estimators at 95% confidence level for the streamwise and lateral moments measured in the wall jet with an exit Reynolds number of 108,000 are shown in tables 3.5 and 3.6 respectively. The uncertainties of the estimators for the measurements used to compute the contours of the mean streamwise velocity and vorticity were approximately 4% and 8% in the intermediate field because a reduced sampling time was used in these measurements. In the single-point measurements for both profiles of the moments and the contours of the mean streamwise velocity and vorticity the filter cut-off frequency and sampling frequency were 4,000 Hz and 1,000 Hz, respectively.

3.2.4 Single-Point Measurements in the Free Jet

The jet facilities were constructed as part of this investigation and the measurement systems were being used for the first time so they were initially verified by performing single-point measurements in the jets exiting the contoured nozzle and the long pipe. In particular, the velocity profiles at the jet exit were examined and the symmetry of the jet were checked. The measurements of the moments were also compared with other investigations.

x/D	Sample time (s)	Uncertainty in estimator of U at $y = y_{max}$	Uncertainty in estimator of U at $y = y_{1/2}$	Uncertainty in estimator of U at $z = z_{1/2}$	Uncertainty in estimator of u'
3	8	0.2%	1.0%	1.0%	2.9%
6	10	0.2%	1.1%	1.1%	3.0%
10	15	0.5%	1.0%	1.0%	2.4%
15	20	0.7%	1.4%	1.2%	3.0%
20	30	0.8%	1.6%	1.2%	3.0%
25	30	1.0%	1.8%	1.4%	3.4%
30	40	1.1%	1.9%	1.5%	3.6%
35	50	1.0%	1.8%	1.3%	3.2%
40	60	1.1%	1.9%	1.5%	3.8%

Table 3.5: Sampling time and uncertainty in the estimators of the streamwise moments for a 95% confidence level.

x/D	Sample time (s)	Uncertainty in estimator of W at $z = z_{1/2}$	Uncertainty in estimator of w'
6	40	11.2%	1.0%
10	40	8.6%	1.5%
15	40	4.9%	2.1%
20	40	4.2%	2.6%
25	40	3.8%	3.0%
30	50	3.8%	3.2%
35	50	3.6%	3.2%
40	50	4.6%	4.4%

Table 3.6: Sampling time and uncertainty in the estimators of the lateral moments for a 95% confidence level.

Free Jet Exiting the Contoured Nozzle

Initially profiles of mean streamwise velocity and turbulence intensity were measured at the exit of the contoured nozzle with a Reynolds number of 96,000 shown in figure 3.11. It is evident that the profiles of the mean velocity were uniform to within 1.0% and the turbulence intensity was less than 0.25% that was lower than most other investigations.

The symmetry of profiles of the mean streamwise velocity and the root mean square of the fluctuating velocity were checked at a variety of locations. For example, the profiles of mean streamwise velocity and profiles of root mean square of streamwise fluctuating velocity measured at x/D=20 are shown in figures 3.12 and 3.13 respectively. The average deviations of mean velocity and root mean square of streamwise fluctuating velocity measured on the opposite sides of the jet centerline were less than 0.2% and 0.3% respectively indicating the jet was symmetric and the traverse was well aligned with the jet.

The development of the jet was characterized by examining the decay of the local maximum streamwise velocity shown in figure 3.14. It is clear that the maximum streamwise velocities at x/D=3 and x/D=5 were approximately the same as the mean velocity at the jet exit indicating the potential core still existed in this region. The local maximum velocity decreased rapidly after x/D=8. The decay of the velocity measured in this investigation was in good agreement with the data reported by Wygnanski and Fiedler [69].

The spectra of the streamwise fluctuating velocity were also checked from x/D=0 to x/D=4. For example, the spectra of the streamwise fluctuating velocity measured on the jet centerline at x/D=3 at different Reynolds numbers are shown in figure 3.15, where F is the power spectrum of the streamwise fluctuating velocity. It is clear that the spectra are smooth as expected and they collapse when they are appropriately non-dimensionalized. The non-dimensional spectra measured at r/D=0.13 for x/D=3

were also compared with data from Glauser [24] shown in figure 3.16. The two measurements are in reasonable agreement and both had a reasonable Strouhal number of approximately 0.46.

Free Jet Exiting a Long Pipe

Initially profiles of mean streamwise velocity and root mean square of fluctuating velocity were measured at the exit of the jet exiting a 38.7 mm diameter long pipe with the length of 60 diameters. The results, shown in figures 3.17 and 3.18, were compared with the profiles of the flow exiting a long pipe with the length of 95 diameters and 200 diameters [15] respectively. It is clear that the profiles of mean streamwise velocity and root mean square of streamwise fluctuating velocity for all cases and the 1/7 law were in good agreement indicating the shorter pipe is reasonably fully developed.

The symmetry of the jet exiting a 38.7 mm diameter long pipe was also checked at a variety of locations. For example, the profiles of mean streamwise velocity and profiles of root mean square of streamwise fluctuating velocity measured at x/D=20 are shown in figures 3.19 and 3.20 respectively. The average deviations of mean streamwise velocity and root mean square of streamwise fluctuating velocity measured on the opposite sides of the jet centerline were less than 0.5% and 1.0% respectively indicating the jet exiting a long pipe was also symmetric.

More extensive measurements of the near and intermediate fields of the free jet exiting the contoured nozzle and the long pipe were performed. These are currently being compiled and will be documented in an internal report.

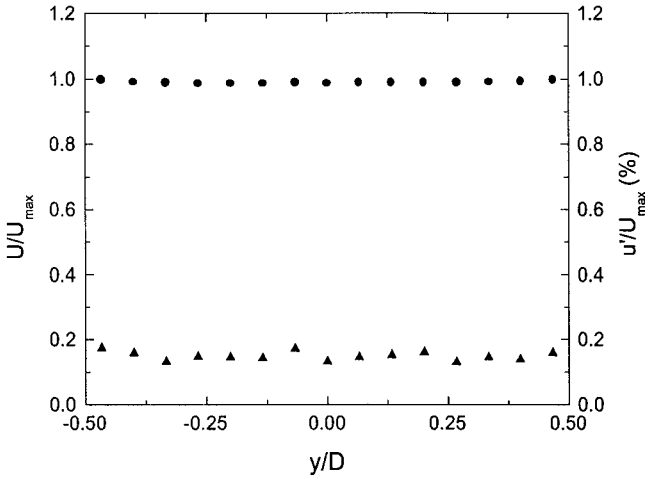

Figure 3.11: Profiles of the mean streamwise velocity and root mean square of fluctuating velocity measured at the exit of a contoured nozzle with $Re_{exit} = 96,000$. • U/U_{max} and ▲ u'/U_{max}.

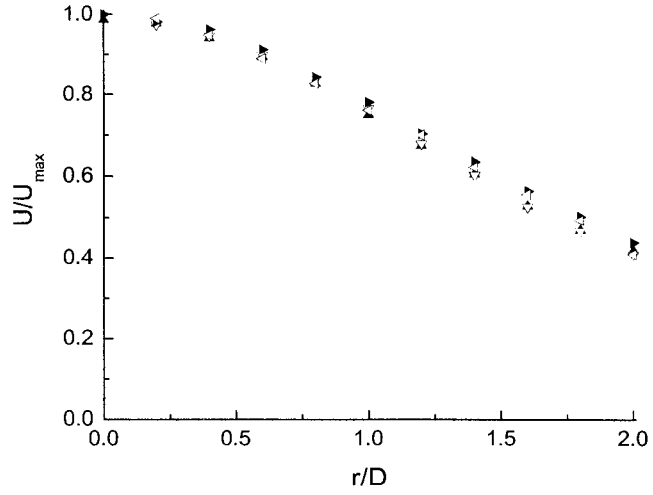

Figure 3.12: Profiles of the mean streamwise velocity in the free jet exiting a contoured nozzle at x/D=20 in ▲ +y direction, ▽ -y direction, ▶ +z direction and ◁ -z direction.

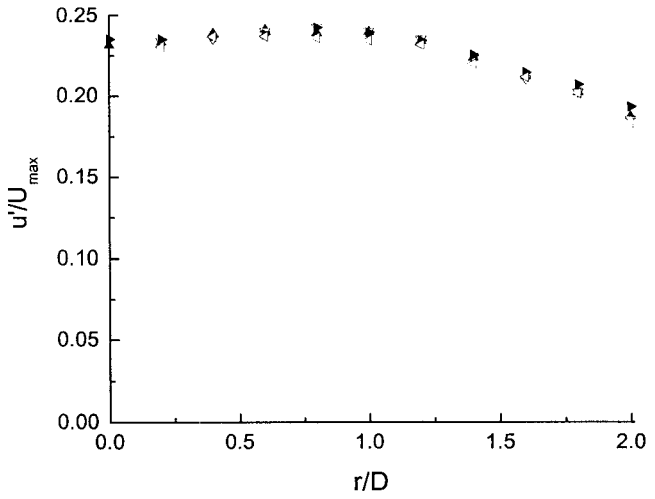

Figure 3.13: Profiles of the root mean square of the streamwise fluctuating velocity in the free jet exiting a contoured nozzle at x/D=20 in ▲ +y direction, ▽ -y direction, ▶ +z direction and ◁ -z direction.

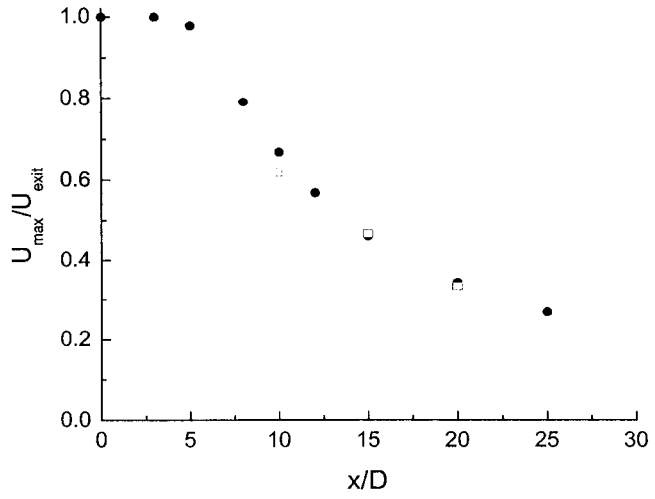

Figure 3.14: The decay of the local maximum mean streamwise velocity of the free jet exiting a contoured nozzle measured • in this investigation and □ by Wygnanski and Fiedler [69].

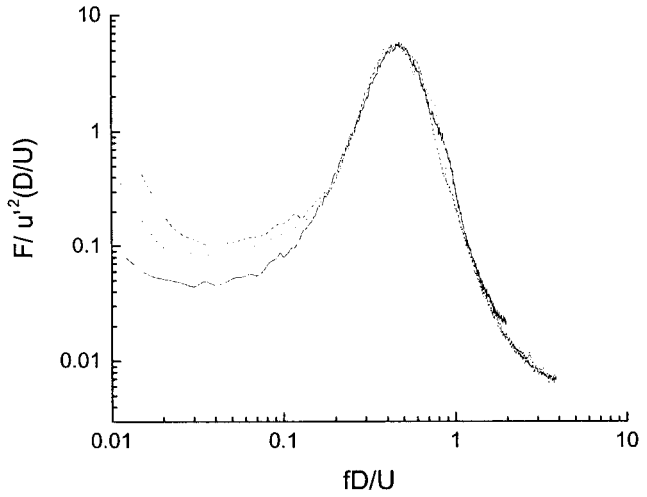

Figure 3.15: Non-dimensional power spectra of the streamwise fluctuating velocity measured at r/D=0 for x/D=3 at $-$ $Re_{exit} = 96,000$, $- - -$ $Re_{exit} = 67,000$ and ... $Re_{exit} = 48,000$.

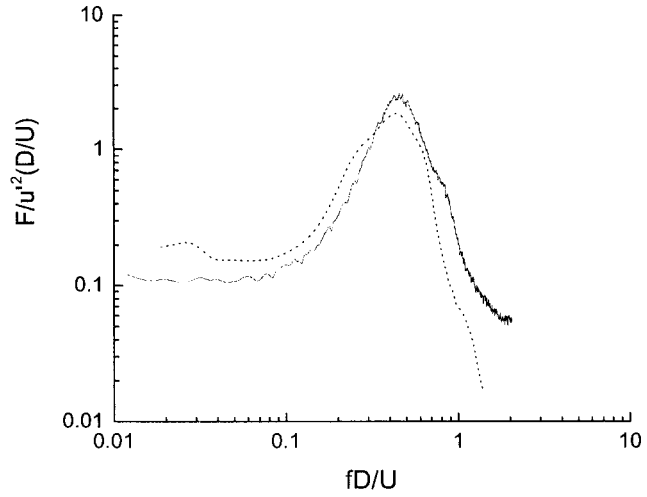

Figure 3.16: Non-dimensional power spectra of the streamwise fluctuating velocity measured at r/D=0.13 for x/D=3 $-$ in this investigation at $Re_{exit} = 96,000$ and ... reported by Glauser [24] at $Re_{exit} \approx 130,000$.

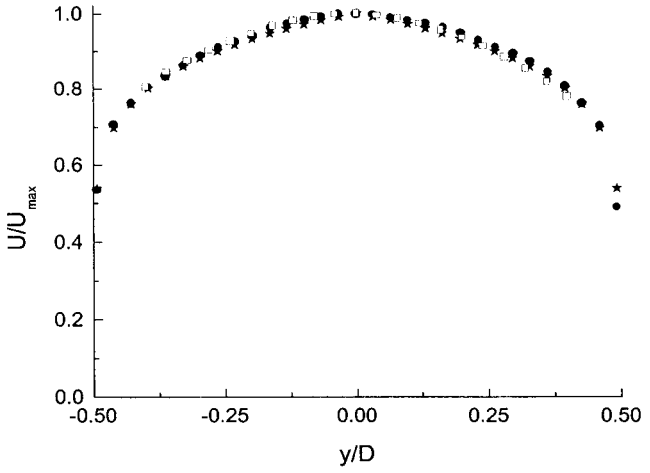

Figure 3.17: Profiles of the mean streamwise velocity at the exit of jet exiting • a pipe with a diameter of 38.7 mm and a length of 60 diameters at Re_{exit}=96,000, □ a pipe with a diameter of 12.7 mm and a length of 90 diameters at Re_{exit}=32,000 and ⋆ 1/7 law.

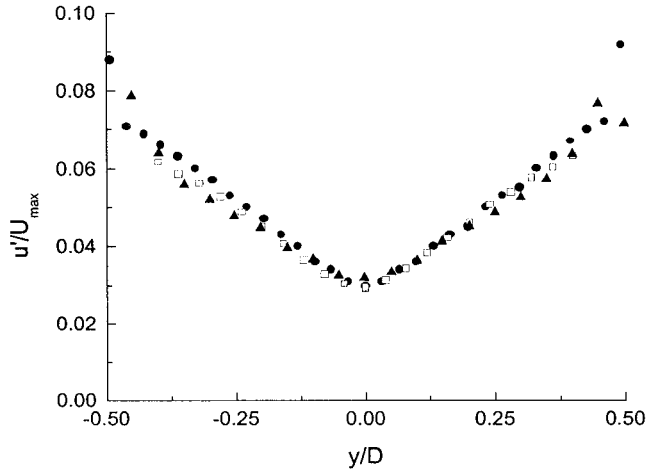

Figure 3.18: Profiles of the root mean square of the streamwise fluctuating velocity measured at the exit of jet exiting • a pipe with a diameter of 38.7 mm and a length of 60 diameters at Re_{exit}=96,000, □ a pipe with a diameter of 12.7 mm and a length of 90 diameters at Re_{exit}=32,000 and ▲ a pipe with a length of 200 diameter at Re_{exit}=10,000 reported by Eriksson et al. [15].

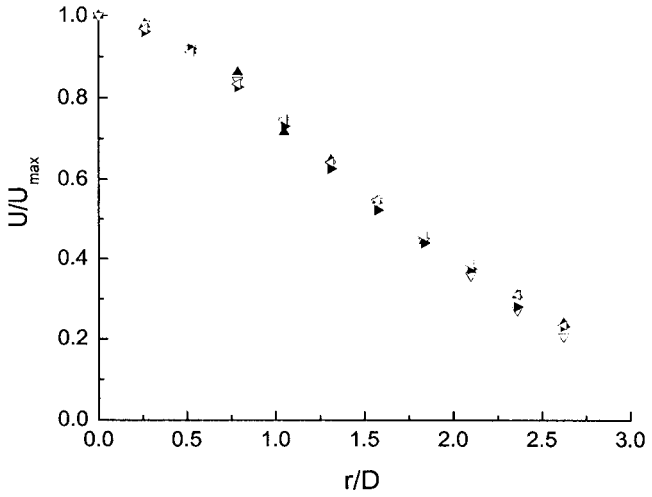

Figure 3.19: Profiles of the mean streamwise velocity in the free jet exiting a 38.7 mm diameter long pipe at x/D=20 in ▲ +y direction, ▽ -y direction, ► +z direction and ◁ -z direction.

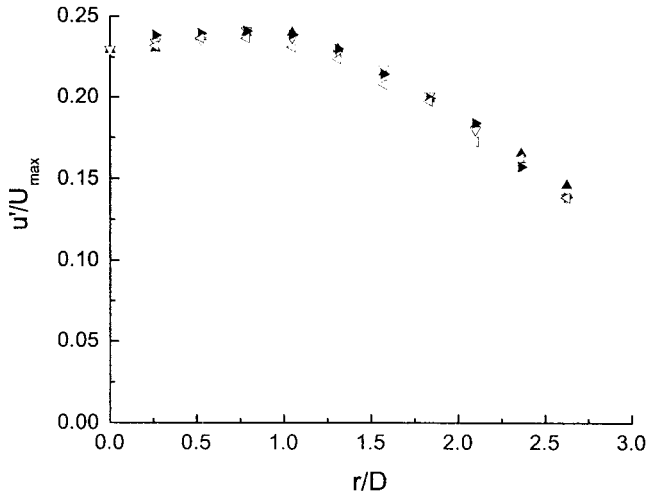

Figure 3.20: Profiles of the root mean square of streamwise fluctuating velocity in the free jet exiting a 38.7 mm diameter long pipe at x/D=20 in ▲ +y direction, ▽ -y direction, ► +z direction and ◁ -z direction.

3.3 Measurements of the Two-Point, Two-Time Correlation

Following the approach outlined by Ewing and Pollard [16] and Ewing et al. [17], the development of the large-scale structures were investigated using measurements of two-point, two-time correlations of streamwise fluctuating velocity. In this case, the measurements of both vertical and lateral correlations were performed using two rakes of single hot-wire probes operated using a 16-channel anemometry system that was built in house. The instruments used in these measurements are described first. The signal analysis techniques used in the measurements and the measurement conditions are then outlined.

3.3.1 Instrumentation

The measurements of two-point, two-time correlation were performed using two-rakes of single wire probes constructed in house. The probes, shown in figure 3.21, consisted of two 0.46 mm (0.018in) diameter stainless steel leads housed in a ceramic shell contained inside a 3.175 mm (0.125in) diameter brass tube. The tungsten hot-wire, with a diameter of 0.005 mm and a length of 200 diameters, was welded to stainless steel leads. The single-wire probes were held on a rake with a thickness of 6.35 mm, shown in figure 3.22. The rake was designed containing 30 3.175 mm diameter holes. The distance between two adjacent holes was 3.81 mm (0.15in) and the center of the bottom hole was 1.59 mm (0.0625in) above the bottom of the rake.

The hot-wire probes were operated using a 16-channel anemometry system. The design of the anemometers followed the anemometer used by Citriniti [12] outlined previously by Perry [50]. In the McMaster design each channel contained a single CTA with a signal conditioning unit that consisted of an offset, gain, a 5-order Bessel

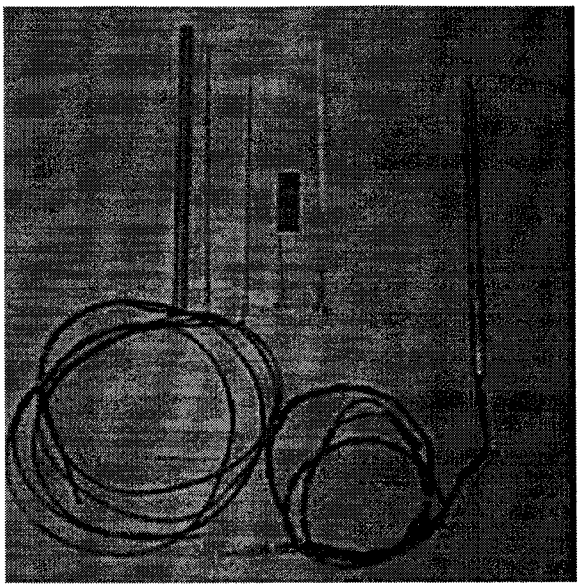

Figure 3.21: Photograph of a single hot-wire probe and its components.

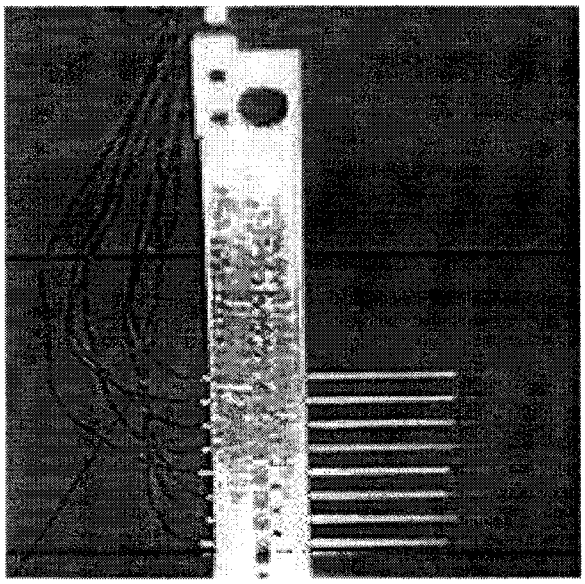

Figure 3.22: Photograph of the rake of single hot-wires.

filter and a sample and hold unit. The spectra of the streamwise fluctuating velocity at the centerline of wall jet at x/D=3 were measured using McMaster anemometer, DANTEC DISA55M and A.A. LAB AN-2000 anemometer respectively. The results are shown in figure 3.23. It is apparent that the McMaster anemometer exhibited almost the same performance as the commercial anemometers, particularly the same as DISA55M anemometer in the frequency range from f=0 Hz to 10,000 Hz. The consistency of the 16 channels of the McMaster anemometer was checked by measuring the spectra of the streamwise fluctuating velocity on the centerline of the wall jet at x/D=3 and the results are shown in figure 3.24. It is clear that the magnitudes of the spectra measured using 16 channels were in good agreement. The standard deviation of the calibration drift was also checked during 72 hours operation and it was found that there was no unacceptable drift.

The output signals from the anemometry system were sampled using a MICROSTAR DAP5200 A/D board with 14-bit A/D converter. In order to reduce the sample time delay amongst the anemometer channels, 32 channels were set to be active in the data acquisition software so that the sample time delay between two adjacent channels was reduced to 3×10^{-6} s if the sampling frequency was 10,240 Hz that was small compared to 0.001 - 0.01 s, the typical time delay found in the measurements.

3.3.2 Data Analysis

The two-point, two-time correlation and the correlation coefficient between different hot-wire probes in the rakes were determined by computing the cross-spectra between the streamwise fluctuating velocities measured at the two points given by

$$R(x, y, z, y', z', \tau) = \int_{-\infty}^{+\infty} F(x, y, z, y', z', f) e^{i2\pi f \tau} df, \tag{3.12}$$

and

$$\rho(x, y, z, y', z', \tau) = \frac{R(x, y, z, y', z', \tau)}{u'(x, y, z) u'(x, y', z')}. \tag{3.13}$$

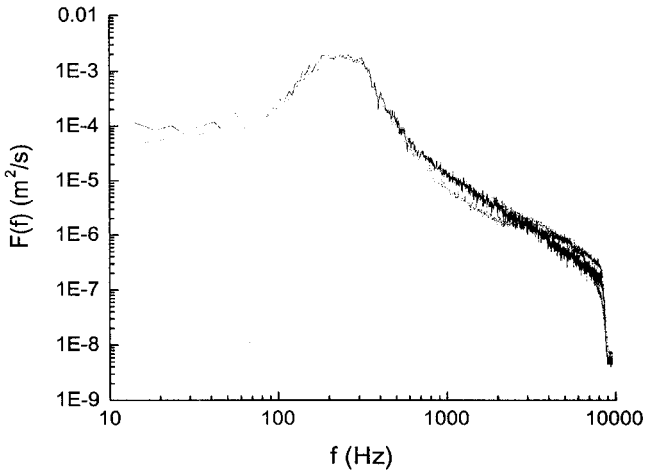

Figure 3.23: Power spectra of the streamwise fluctuating velocity measured on the centerline of the wall jet at x/D=3 using McMaster anemometer(solid line), DANTEC DISA55M anemometer (dot line) and A.A. LAB AN-2000 anemometer (dash line) at Re_{exit}=48,000.

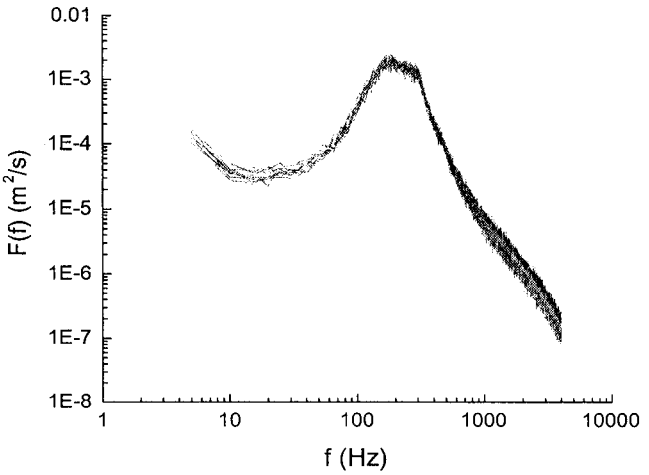

Figure 3.24: Power spectra of the streamwise fluctuating velocity on the centerline at x/D=3 measured using 16 channels of McMaster anemometry system at Re_{exit}=48,000.

Here, the cross-spectrum, $F(x, y, z, y', z', f)$, was calculated in terms of the Fourier coefficient of the streamwise fluctuating velocity, $\hat{u}(x, y, z, f)$, and its complex conjugate, $\hat{u}^*(x, y', z', f)$, that is given by [68]

$$F(x, y, z, y', z', f) = \frac{\hat{u}(x, y, z, f)\hat{u}^*(x, y', z', f)}{T}, \tag{3.14}$$

where T is the sampling time for each data block.

3.3.3 Measurement Conditions

The measurements were performed in the region from x/D=3 to x/D=40 using two rakes that each contained 8 single hot-wire probes placed 3.81mm or 7.62mm apart. In particular, measurements were carried out with one rake fixed at a given lateral location and the other rake was moved laterally across the jet so that the evolution of the large-scale structures were examined both in vertical and lateral directions. The Reynolds number was set to 108,000 at the jet exit that corresponded to the exit velocity of 45 m/s in the region x/D=20 to 40. In order to improve the ratio of the signal to noise, the gain for the anemometer was set so the measurements were performed in the region x/D=3 to 15 at $Re_{exit} = 72,000$ corresponding to the exit velocity of 30 m/s.

The filter cut-off frequency and sampling frequency were 4,000 Hz and 10,240 Hz, respectively. Tan-atichat et al. [62] showed that the standard deviation in the spectra computed by block averaging was proportional to $1/\sqrt{N}$, where N is the sampled blocks. The cross-spectra were computed here by block averaging 120 to 160 blocks of 2048 to 4096 points yielding an uncertainty of 8% - 9%.

Chapter 4

Similarity Analysis of Governing Equations

Previous investigations have shown that the velocity and Reynolds stress profiles measured in the far field of the three-dimensional wall jet were self-similar when they were scaled using the local maximum streamwise velocity and the jet half-widths. These investigations did not, however, show that these self-similar solutions were consistent with the governing equations for the three-dimensional wall jet. The first step in this investigation was to examine if the governing equations for the three-dimensional wall jet have self-similar solutions. These scales developed in this analysis will then be used to examine how the profiles of the mean velocities and Reynolds stresses in the intermediate region evolve to the self-similar state.

Following the approach outlined by George et al. [21] for the two dimensional wall jet, the three-dimensional wall jet was decomposed into inner and outer layers, characterized by $\overline{y} = y/y_{1/2}$ and $y^+ = y/\eta$ as shown in figure 4.1. Here, $y_{1/2}$ is the vertical jet half-width and η is the vertical length scale of inner layer given by $\eta = \nu/u_*$, where u_* is the streamwise friction velocity. The vertical length scale of

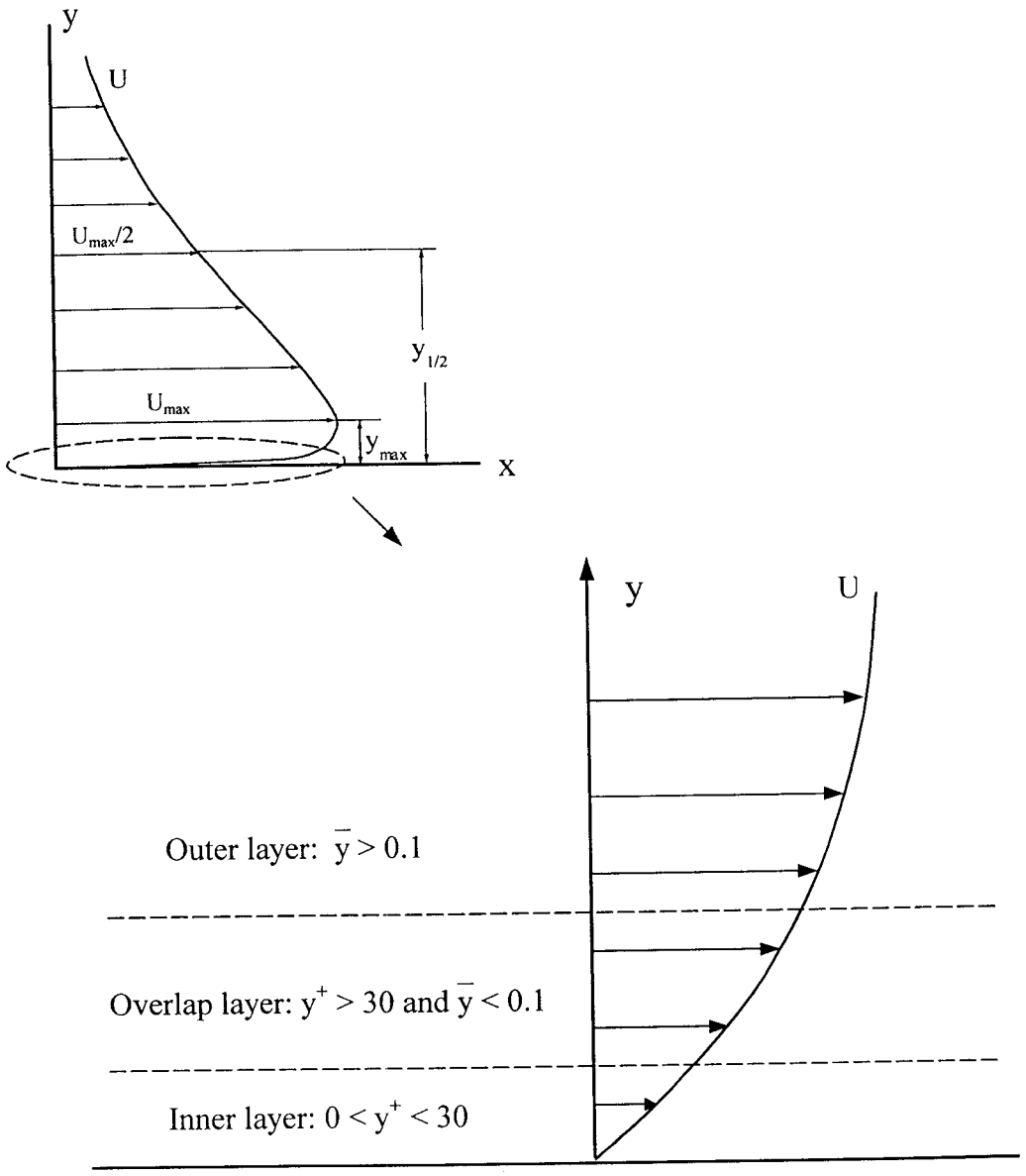

Figure 4.1: Schematic of inner and outer layers of wall jet.

inner layer, η, is much smaller than the vertical half-width, $y_{1/2}$, in a high-Reynolds-number wall jet. In this chapter, the similarity solutions for both inner layer and outer layer of the three-dimensional wall jet are developed. The predictions of this analysis for the outer layer are then compared with the measurements in the far field of the jet exiting the long pipe.

4.1 Similarity Analysis of the Outer Layer

Using the standard thin shear layer scaling arguments, i.e., $y_{1/2} \ll x$ and $y_{1/2} < z_{1/2}$, it can be shown that the first order continuity equation and mean momentum equations in the outer layer are given by

$$\frac{\partial U}{\partial x} + \frac{\partial V}{\partial y} + \frac{\partial W}{\partial z} = 0, \tag{4.1}$$

$$U\frac{\partial U}{\partial x} + V\frac{\partial U}{\partial y} + W\frac{\partial U}{\partial z} = -\frac{\partial \overline{uv}}{\partial y}, \tag{4.2}$$

$$U\frac{\partial W}{\partial x} + V\frac{\partial W}{\partial y} + W\frac{\partial W}{\partial z} = -\frac{\partial \overline{vw}}{\partial y}, \tag{4.3}$$

where U, V, W are the mean velocities in the streamwise, x, vertical, y, and lateral, z, directions and u, v, w are the fluctuating velocities in these three directions respectively. Following George et al.[21], it is proposed that the profiles of the mean velocities and turbulent stresses in the three-dimensional wall jet have self-similar solutions of the form given in table 4.1, where $\overline{z} = z/z_{1/2}$ and $z_{1/2}$ is the lateral half-width of the jet. These solutions are then substituted into the equations to determine if they are consistent with the equations. Integrating the continuity equation from the wall or more properly the top of the inner layer, it follows that

$$V = -\frac{dU_o}{dx}y_{1/2}I_1 - U_o\frac{dy_{1/2}}{dx}I_1 + U_o\frac{dy_{1/2}}{dx}\overline{y}f_{U,o} + \frac{U_o}{z_{1/2}}\frac{dz_{1/2}}{dx}y_{1/2}\frac{\partial I_1}{\partial \overline{z}} - \frac{W_o}{z_{1/2}}y_{1/2}\frac{\partial I_2}{\partial \overline{z}}, \tag{4.4}$$

where

$$I_1 = \int_0^{\overline{y}} f_{U,o}(\widetilde{y})d\widetilde{y} \tag{4.5}$$

and

$$I_2 = \int_0^{\overline{y}} f_{W,o}(\widetilde{y})d\widetilde{y}. \tag{4.6}$$

Substituting this result and proposed solutions for other moments into the first order mean momentum equations yields

$$\left[U_o\frac{dU_o}{dx}\right] f_{U,o}^2 - \left[\frac{U_o^2}{z_{1/2}}\frac{dz_{1/2}}{dx}\right] f_{U,o}\frac{\partial f_{U,o}}{\partial \overline{z}}\overline{z} - \left[U_o\frac{dU_o}{dx}\right] I_1\frac{\partial f_{U,o}}{\partial \overline{y}} - \left[\frac{U_o^2}{y_{1/2}}\frac{dy_{1/2}}{dx}\right] I_1\frac{\partial f_{U,o}}{\partial \overline{y}} + \left[\frac{U_o^2}{z_{1/2}}\frac{dz_{1/2}}{dx}\right]\frac{\partial f_{U,o}}{\partial \overline{y}}\overline{z}\frac{\partial I_1}{\partial \overline{z}} - \left[\frac{U_oW_o}{z_{1/2}}\right]\frac{\partial f_{U,o}}{\partial \overline{y}}\frac{\partial I_2}{\partial \overline{z}} + \left[\frac{U_oW_o}{z_{1/2}}\right]\frac{\partial f_{U,o}}{\partial \overline{z}} f_{W,o} = -\left[\frac{R_{uv,o}}{y_{1/2}}\right]\frac{\partial r_{uv}}{\partial \overline{y}}, \tag{4.7}$$

and

$$\left[U_o\frac{dW_o}{dx}\right] f_{U,o}f_{W,o} - \left[\frac{U_oW_o}{z_{1/2}}\frac{dz_{1/2}}{dx}\right] f_{U,o}\frac{\partial f_{W,o}}{\partial \overline{z}}\overline{z} - \left[W_o\frac{dU_o}{dx}\right] I_1\frac{\partial f_{W,o}}{\partial \overline{y}} - \left[\frac{U_oW_o}{y_{1/2}}\frac{dy_{1/2}}{dx}\right] I_1\frac{\partial f_{W,o}}{\partial \overline{y}} + \left[\frac{U_oW_o}{z_{1/2}}\frac{dz_{1/2}}{dx}\right]\frac{\partial f_{W,o}}{\partial \overline{y}}\overline{z}\frac{\partial I_1}{\partial \overline{z}} - \left[\frac{W_o^2}{z_{1/2}}\right]\frac{\partial f_{W,o}}{\partial \overline{y}}\frac{\partial I_2}{\partial \overline{z}} + \left[\frac{W_o^2}{z_{1/2}}\right]\frac{\partial f_{W,o}}{\partial \overline{z}} f_{W,o} = -\left[\frac{R_{vw,o}}{y_{1/2}}\right]\frac{\partial r_{vw}}{\partial \overline{y}}. \tag{4.8}$$

The proposed solutions are consistent with the first order momentum equations if the terms in square brackets have the same x-dependence, i.e.,

$$\left[U_o\frac{dU_o}{dx}\right] \propto \left[\frac{U_o^2}{y_{1/2}}\frac{dy_{1/2}}{dx}\right] \propto \left[\frac{U_o^2}{z_{1/2}}\frac{dz_{1/2}}{dx}\right] \propto \left[\frac{U_oW_o}{z_{1/2}}\right] \propto \left[\frac{R_{uv,o}}{y_{1/2}}\right], \tag{4.9}$$

and

$$\left[U_o\frac{dW_o}{dx}\right] \propto \left[\frac{U_oW_o}{y_{1/2}}\frac{dy_{1/2}}{dx}\right] \propto \left[\frac{U_oW_o}{z_{1/2}}\frac{dz_{1/2}}{dx}\right] \propto \left[\frac{W_o^2}{z_{1/2}}\right] \propto \left[\frac{R_{vw,o}}{y_{1/2}}\right]. \tag{4.10}$$

Thus, the momentum equations have self-similar solutions if

$$\left[\frac{1}{y_{1/2}}\frac{dy_{1/2}}{dx}\right] \propto \left[\frac{1}{z_{1/2}}\frac{dz_{1/2}}{dx}\right], \tag{4.11}$$

or

$$y_{1/2} \propto z_{1/2}^{n}, \tag{4.12}$$

and the constraints for the scales of mean velocities and Reynolds stresses given in table 4.1 are satisfied. It is clear that there would be two different velocity scales in the flow if the lateral growth rate is not constant, i.e.,

$$W_o \propto U_o \frac{dz_{1/2}}{dx}. \tag{4.13}$$

The ratio of these scales is a measure of the angles of the streamlines so there are two velocity scales in the region of streamline curvature as expected. This differs from the traditional approach where only one velocity scale, U_o, was used to normalize the profiles of velocities and Reynolds stresses [1, 20] that clearly can not account for the streamline curvature. It will be shown later that the profiles of the moments particularly the profiles of lateral mean velocity collapse better when they are normalized by the velocity scale, W_o, deduced from the similarity analysis in the region where the growth rate is not constant.

The mean streamwise vorticity given by

$$\Omega_x = \frac{\partial W}{\partial y} - \frac{\partial V}{\partial z}, \tag{4.14}$$

is often used to examine the development of the large-scale structures in the three-dimensional wall jet. Substituting the proposed similarity solutions in this definition yields

$$\begin{aligned}[\Omega_{x,o}] f_{\Omega,o} = &\left[\frac{U_o}{y_{1/2}}\frac{dz_{1/2}}{dx}\right]\frac{\partial f_{W,o}}{\partial \overline{y}} + \left\{\left[\frac{dU_o}{dx}\frac{y_{1/2}}{z_{1/2}}\right] + \left[\frac{U_o}{z_{1/2}}\frac{dy_{1/2}}{dx}\right]\right\}\frac{\partial I_1}{\partial \overline{z}} \\ &- \left[\frac{U_o}{z_{1/2}}\frac{dy_{1/2}}{dx}\right]\overline{y}\frac{\partial f_{U,o}}{\partial \overline{z}} - \left[U_o\frac{y_{1/2}}{z_{1/2}^2}\frac{dz_{1/2}}{dx}\right]\frac{\partial^2 I_1}{\partial \overline{z}^2} + \left[W_o\frac{y_{1/2}}{z_{1/2}^2}\right]\frac{\partial^2 I_1}{\partial \overline{z}^2}.\end{aligned} \tag{4.15}$$

The relative size of these terms can be compared by taking the ratio yielding

$$\frac{\frac{\partial V}{\partial z}}{\frac{\partial W}{\partial y}} \propto \frac{\left[U_0 \frac{y_{1/2}}{z_{1/2}^2}\frac{dz_{1/2}}{dx}\right]}{\left[\frac{U_0}{y_{1/2}}\frac{dz_{1/2}}{dx}\right]} \propto \left(\frac{y_{1/2}}{z_{1/2}}\right)^2. \tag{4.16}$$

The term $\partial V/\partial z$ is generally neglected based on the scaling argument that the lateral half-width, $z_{1/2}$, is much larger than the vertical half-width, $y_{1/2}$. As long as this holds in the far field, the scale for the streamwise vorticity, Ω_x, will have the same x-dependence scale as the term, $\partial W/\partial y$, i.e., $U_o(dz_{1/2}/dx)/y_{1/2}$.

The similarity analysis can also be extended to equations for turbulent Reynolds stresses. The first order equations for $\overline{u^2}$, $\overline{v^2}$ and $\overline{w^2}$, are given by

$$U\frac{\partial \overline{u^2}}{\partial x} + V\frac{\partial \overline{u^2}}{\partial y} + W\frac{\partial \overline{u^2}}{\partial z} = 2\overline{\frac{p}{\rho}\frac{\partial u}{\partial x}} - \frac{\partial \overline{u^2 v}}{\partial y} - \frac{\partial \overline{u^2 w}}{\partial z} - 2\overline{uv}\frac{\partial U}{\partial y} - 2\overline{uw}\frac{\partial U}{\partial z} - 2\varepsilon_u, \tag{4.17}$$

$$U\frac{\partial \overline{v^2}}{\partial x} + V\frac{\partial \overline{v^2}}{\partial y} + W\frac{\partial \overline{v^2}}{\partial z} = 2\overline{\frac{p}{\rho}\frac{\partial v}{\partial y}} - \frac{2}{\rho}\frac{\partial \overline{pv}}{\partial y} - \frac{\partial \overline{v^3}}{\partial y} - \frac{\partial \overline{v^2 w}}{\partial z} - 2\varepsilon_v, \tag{4.18}$$

and

$$U\frac{\partial \overline{w^2}}{\partial x} + V\frac{\partial \overline{w^2}}{\partial y} + W\frac{\partial \overline{w^2}}{\partial z} = 2\overline{\frac{p}{\rho}\frac{\partial w}{\partial z}} - \frac{\partial \overline{vw^2}}{\partial y} - \frac{\partial \overline{w^3}}{\partial z} - 2\overline{w^2}\frac{\partial W}{\partial z} - 2\varepsilon_w, \tag{4.19}$$

where ε is the dissipation term. Since the flow is incompressible, the pressure-strain terms in these equations must satisfy

$$\overline{\frac{p}{\rho}\frac{\partial u}{\partial x}} + \overline{\frac{p}{\rho}\frac{\partial v}{\partial y}} + \overline{\frac{p}{\rho}\frac{\partial w}{\partial z}} = 0. \tag{4.20}$$

George et al. [21] showed that the convection terms were equal or smaller than the first order production terms in the Reynolds shear stress equations for the two-dimensional wall jet if the vertical growth rate was constant or less than linear as $x \to \infty$. The

same is also true here in the equations for the Reynolds shear stresses, $\overline{uv}$, $\overline{uw}$, and $\overline{vw}$ given by

$$\underline{U\frac{\partial \overline{uv}}{\partial x}} + \underline{V\frac{\partial \overline{uv}}{\partial y}} + \underline{W\frac{\partial \overline{uv}}{\partial z}} = \overline{\frac{p}{\rho}\left(\frac{\partial u}{\partial y} + \frac{\partial v}{\partial x}\right)} - \frac{1}{\rho}\frac{\partial \overline{pu}}{\partial y} - \frac{\partial \overline{uv^2}}{\partial y} - \overline{v^2}\frac{\partial U}{\partial y}, \tag{4.21}$$

$$\underline{U\frac{\partial \overline{uw}}{\partial x}} + \underline{V\frac{\partial \overline{uw}}{\partial y}} + \underline{W\frac{\partial \overline{uw}}{\partial z}} = \overline{\frac{p}{\rho}\left(\frac{\partial u}{\partial z} + \frac{\partial w}{\partial x}\right)} - \frac{\partial \overline{uvw}}{\partial y} - \frac{\partial \overline{uw^2}}{\partial z} - \overline{w^2}\frac{\partial U}{\partial z}, \tag{4.22}$$

and

$$\underline{U\frac{\partial \overline{vw}}{\partial x}} + \underline{V\frac{\partial \overline{vw}}{\partial y}} + \underline{W\frac{\partial \overline{vw}}{\partial z}} = \overline{\frac{p}{\rho}\left(\frac{\partial v}{\partial z} + \frac{\partial w}{\partial y}\right)} - \frac{1}{\rho}\frac{\partial \overline{pw}}{\partial y} - \frac{\partial \overline{v^2 w}}{\partial y} - \overline{v^2}\frac{\partial W}{\partial y}. \tag{4.23}$$

It is hypothesized that the equations of normal stresses have self-similar solutions of the form given in tables 4.1 and 4.2. Substituting the proposed solutions into equations for normal stresses and the pressure-strain terms yields

$$\begin{aligned}
&[U_o\frac{dR_{uu,o}}{dx}]f_{U,o}r_{uu,o} - [\frac{U_oR_{uu,o}}{z_{1/2}}\frac{dz_{1/2}}{dx}]f_{U,o}\frac{\partial r_{uu,o}}{\partial \overline{z}}\overline{z} - \left[R_{uu,o}\frac{dU_o}{dx}\right]I_1\frac{\partial r_{uu,o}}{\partial \overline{y}} - \\
&\left[\frac{U_oR_{uu,o}}{y_{1/2}}\frac{dy_{1/2}}{dx}\right]I_1\frac{\partial r_{uu,o}}{\partial \overline{y}} + \left[\frac{U_oR_{uu,o}}{z_{1/2}}\frac{dz_{1/2}}{dx}\right]\frac{\partial I_1}{\partial \overline{z}}\overline{z}\frac{\partial r_{uu,o}}{\partial \overline{y}} - \\
&\left[\frac{U_oR_{uu,o}}{z_{1/2}}\frac{dz_{1/2}}{dx}\right]\frac{\partial I_2}{\partial \overline{z}}\frac{\partial r_{uu,o}}{\partial \overline{y}} + \left[\frac{U_oR_{uu,o}}{z_{1/2}}\frac{dz_{1/2}}{dx}\right]f_{W,o}\frac{\partial r_{uu,o}}{\partial \overline{z}} = [P_u]\,p_u - \\
&\left[\frac{T_{uuv,o}}{y_{1/2}}\right]\frac{\partial t_{uuv,o}}{\partial \overline{y}} - \left[\frac{T_{uuw,o}}{z_{1/2}}\right]\frac{\partial t_{uuw,o}}{\partial \overline{z}} - 2\left[\frac{U_o^3}{y_{1/2}}\frac{dy_{1/2}}{dx}\right]r_{uv,o}\frac{\partial f_{U,o}}{\partial \overline{y}} - \\
&2\left[\frac{U_oR_{uw,o}}{z_{1/2}}\right]r_{uw,o}\frac{\partial f_{U,o}}{\partial \overline{z}} - 2\,[D_u]\,d_u,
\end{aligned} \tag{4.24}$$

$$\begin{aligned}
&[U_o\frac{dR_{vv,o}}{dx}]f_{U,o}r_{vv,o} - [\frac{U_oR_{vv,o}}{z_{1/2}}\frac{dz_{1/2}}{dx}]f_{U,o}\frac{\partial r_{vv,o}}{\partial \overline{z}}\overline{z} - \left[R_{vv,o}\frac{dU_o}{dx}\right]I_1\frac{\partial r_{vv,o}}{\partial \overline{y}} - \\
&\left[\frac{U_oR_{vv,o}}{y_{1/2}}\frac{dy_{1/2}}{dx}\right]I_1\frac{\partial r_{vv,o}}{\partial \overline{y}} + \left[\frac{U_oR_{vv,o}}{z_{1/2}}\frac{dz_{1/2}}{dx}\right]\frac{\partial I_1}{\partial \overline{z}}\overline{z}\frac{\partial r_{vv,o}}{\partial \overline{y}} - \\
&\left[\frac{U_oR_{vv,o}}{z_{1/2}}\frac{dz_{1/2}}{dx}\right]\frac{\partial I_2}{\partial \overline{z}}\frac{\partial r_{vv,o}}{\partial \overline{y}} + \left[\frac{U_oR_{vv,o}}{z_{1/2}}\frac{dz_{1/2}}{dx}\right]f_{W,o}\frac{\partial r_{vv,o}}{\partial \overline{z}} = [P_v]\,p_v - \\
&[P_{pv}]\,p_{pv} - \left[\frac{T_{vvv,o}}{y_{1/2}}\right]\frac{\partial t_{vvv,o}}{\partial \overline{y}} - \left[\frac{T_{vvw,o}}{z_{1/2}}\right]\frac{\partial t_{vvw,o}}{\partial \overline{z}} - 2\,[D_v]\,d_v,
\end{aligned} \tag{4.25}$$

$$[U_o\frac{dR_{ww,o}}{dx}]f_{U,o}r_{ww,o} - [\frac{U_oR_{ww,o}}{z_{1/2}}\frac{dz_{1/2}}{dx}]f_{U,o}\frac{\partial r_{ww,o}}{\partial\overline{z}}\overline{z} - \left[R_{ww,o}\frac{dU_o}{dx}\right]I_1\frac{\partial r_{ww,o}}{\partial\overline{y}} - \left[\frac{U_oR_{ww,o}}{y_{1/2}}\frac{dy_{1/2}}{dx}\right]I_1\frac{\partial r_{ww,o}}{\partial\overline{y}} + \left[\frac{U_oR_{ww,o}}{z_{1/2}}\frac{dz_{1/2}}{dx}\right]\frac{\partial I_1}{\partial\overline{z}}\overline{z}\frac{\partial r_{ww,o}}{\partial\overline{y}} - \left[\frac{U_oR_{ww,o}}{z_{1/2}}\frac{dz_{1/2}}{dx}\right]\frac{\partial I_2}{\partial\overline{z}}\frac{\partial r_{ww,o}}{\partial\overline{y}} + \left[\frac{U_oR_{ww,o}}{z_{1/2}}\frac{dz_{1/2}}{dx}\right]f_{W,o}\frac{\partial r_{ww,o}}{\partial\overline{z}} = [P_w]\,p_w - \left[\frac{T_{vww,o}}{y_{1/2}}\right]\frac{\partial t_{vww,o}}{\partial\overline{y}} - \left[\frac{T_{www,o}}{z_{1/2}}\right]\frac{\partial t_{www,o}}{\partial\overline{z}} - 2\left[\frac{U_oR_{ww,o}}{z_{1/2}}\frac{dz_{1/2}}{dx}\right]r_{ww,o}\frac{\partial f_{W,o}}{\partial\overline{z}} - 2\,[D_w]\,d_w, \quad (4.26)$$

and

$$[P_u]p_u + [P_v]\,p_v + [P_w]\,p_w = 0. \quad (4.27)$$

These equations have self-similar solutions if the terms in the square brackets have the same x-dependence, i.e.,

$$\left[U_o\frac{dR_{uu,o}}{dx}\right] \propto \left[\frac{U_oR_{uu,o}}{z_{1/2}}\frac{dz_{1/2}}{dx}\right] \propto \left[R_{uu,o}\frac{dU_o}{dx}\right] \propto \left[\frac{U_oR_{uu,o}}{y_{1/2}}\frac{dy_{1/2}}{dx}\right] \propto [P_u] \propto \left[\frac{T_{uuv}}{y_{1/2}}\right] \propto \left[\frac{T_{uuw}}{z_{1/2}}\right] \propto \left[\frac{U_o^3}{y_{1/2}}\frac{dy_{1/2}}{dx}\right] \propto \left[\frac{U_oR_{uw,o}}{z_{1/2}}\right] \propto [D_u]\,, \quad (4.28)$$

$$[U_o\frac{dR_{vv,o}}{dx}] \propto [\frac{U_oR_{vv,o}}{z_{1/2}}\frac{dz_{1/2}}{dx}] \propto [R_{vv,o}\frac{dU_o}{dx}] \propto [\frac{U_oR_{vv,o}}{y_{1/2}}\frac{dy_{1/2}}{dx}] \propto [P_v] \propto [P_{pv}] \propto \left[\frac{T_{vvv,o}}{y_{1/2}}\right] \propto \left[\frac{T_{vvw,o}}{z_{1/2}}\right] \propto [D_v], \quad (4.29)$$

$$[U_o\frac{dR_{ww,o}}{dx}] \propto [\frac{U_oR_{ww,o}}{z_{1/2}}\frac{dz_{1/2}}{dx}] \propto [R_{ww,o}\frac{dU_o}{dx}] \propto [\frac{U_oR_{ww,o}}{y_{1/2}}\frac{dy_{1/2}}{dx}] \propto [P_w] \propto \left[\frac{T_{vww,o}}{y_{1/2}}\right] \propto \left[\frac{T_{www,o}}{z_{1/2}}\right] \propto [D_w], \quad (4.30)$$

and

$$P_u \propto P_v \propto P_w. \quad (4.31)$$

It follows the constraints for the scales of the moments, $\overline{u^2}$, $\overline{v^2}$, $\overline{w^2}$, $\overline{uw}$, $\overline{u^2v}$, $\overline{u^2w}$, $\overline{v^3}$, $\overline{v^2w}$, $\overline{vw^2}$, and $\overline{w^3}$ in table 4.1 and the results of the pressure-strain terms, $\overline{\frac{p}{\rho}\frac{\partial u}{\partial x}}$, $\overline{\frac{p}{\rho}\frac{\partial v}{\partial y}}$,

and $\overline{\frac{p}{\rho}\frac{\partial w}{\partial z}}$, the pressure-transport term, $\frac{1}{\rho}\overline{\frac{\partial pv}{\partial y}}$, and the dissipation terms, ε_u, ε_v, and ε_w, in table 4.2 are satisfied.

Substituting the above solutions for Reynolds stresses and the proposed solutions given in tables 4.1 and 4.2 into the Reynolds shear stress equations 4.21 - 4.23 yields

$$\underline{\left\{\left[2U_o^2\frac{dU_o}{dx}\frac{dy_{1/2}}{dx}\right]+\left[U_o^3\frac{d^2y_{1/2}}{dx^2}\right]\right\}f_{U,o}r_{uv,o}}-\underline{\left[\frac{U_o^3}{z_{1/2}}\frac{dy_{1/2}}{dx}\frac{dz_{1/2}}{dx}\right]f_{U,o}\overline{z}\frac{\partial r_{uv,o}}{\partial\overline{z}}}$$
$$-\underline{\left[U_o^2\frac{dU_o}{dx}\frac{dy_{1/2}}{dx}\right]I_1\frac{\partial r_{uv,o}}{\partial\overline{y}}}-\underline{\left[\frac{U_o^3}{y_{1/2}}(\frac{dy_{1/2}}{dx})^2\right]I_1\frac{\partial r_{uv,o}}{\partial\overline{y}}}+\underline{\left[\frac{U_o^3}{z_{1/2}}\frac{dy_{1/2}}{dx}\frac{dz_{1/2}}{dx}\right]}\times$$
$$\frac{\partial I_1}{\partial\overline{z}}\frac{\partial r_{uv,o}}{\partial\overline{y}}-\underline{\left[\frac{U_o^3}{z_{1/2}}\frac{dy_{1/2}}{dx}\frac{dz_{1/2}}{dx}\right]}\frac{\partial I_2}{\partial\overline{z}}\frac{\partial r_{uv,o}}{\partial\overline{y}}+\underline{\left[\frac{U_o^3}{z_{1/2}}\frac{dy_{1/2}}{dx}\frac{dz_{1/2}}{dx}\right]}f_{W,o}\frac{\partial r_{uv,o}}{\partial\overline{z}}$$
$$=[P_{uv}]p_{uv}-[P_{pu}]p_{pu}-\left[\frac{T_{uvv,o}}{y_{1/2}}\right]\frac{\partial t_{uvv,o}}{\partial\overline{y}}-\left[\frac{U_0^3}{y_{1/2}}\right]r_{vv,o}\frac{\partial f_{U,o}}{\partial\overline{y}},\quad(4.32)$$

$$\underline{\left\{\left[2U_o^2\frac{dU_o}{dx}\frac{dz_{1/2}}{dx}\right]+\left[U_o^3\frac{d^2z_{1/2}}{dx^2}\right]\right\}f_{U,o}r_{uw,o}}-\underline{\left[\frac{U_o^3}{z_{1/2}}(\frac{dz_{1/2}}{dx})^2\right]f_{U,o}\overline{z}\frac{\partial r_{uw,o}}{\partial\overline{z}}}$$
$$-\underline{\left[U_o^2\frac{dU_o}{dx}\frac{dz_{1/2}}{dx}\right]I_1\frac{\partial r_{uw,o}}{\partial\overline{y}}}-\underline{\left[\frac{U_o^3}{y_{1/2}}\frac{dy_{1/2}}{dx}\frac{dz_{1/2}}{dx}\right]I_1\frac{\partial r_{uw,o}}{\partial\overline{y}}}+\underline{\left[\frac{U_o^3}{z_{1/2}}(\frac{dz_{1/2}}{dx})^2\right]}\times$$
$$\frac{\partial I_1}{\partial\overline{z}}\frac{\partial r_{uw,o}}{\partial\overline{y}}-\underline{\left[\frac{U_o^3}{z_{1/2}}(\frac{dz_{1/2}}{dx})^2\right]}\frac{\partial I_2}{\partial\overline{z}}\frac{\partial r_{uw,o}}{\partial\overline{y}}+\underline{\left[\frac{U_o^3}{z_{1/2}}(\frac{dz_{1/2}}{dx})^2\right]}f_{W,o}\frac{\partial r_{uw,o}}{\partial\overline{z}}$$
$$=[P_{uw}]p_{uw}-\left[\frac{T_{uvw,o}}{y_{1/2}}\right]\frac{\partial t_{uvw,o}}{\partial\overline{y}}-\left[\frac{T_{uww,o}}{z_{1/2}}\right]\frac{\partial t_{uww,o}}{\partial\overline{z}}-\left[\frac{U_0^3}{z_{1/2}}\right]r_{ww,o}\frac{\partial f_{U,o}}{\partial\overline{z}},\quad(4.33)$$

and

$$\underline{\left\{\left[2U_o^2\frac{dU_o}{dx}\frac{dy_{1/2}}{dx}\frac{dz_{1/2}}{dx}\right]+\left[U_o^3\frac{d^2y_{1/2}}{dx^2}\frac{dz_{1/2}}{dx}\right]+\left[U_o^3\frac{dy_{1/2}}{dx}\frac{d^2z_{1/2}}{dx^2}\right]\right\}f_{U,o}r_{vw,o}}$$
$$-\underline{\left[\frac{U_o^3}{z_{1/2}}\frac{dy_{1/2}}{dx}(\frac{dz_{1/2}}{dx})^2\right]f_{U,o}\overline{z}\frac{\partial r_{vw,o}}{\partial\overline{z}}}-\underline{\left[U_o^2\frac{dU_o}{dx}\frac{dy_{1/2}}{dx}\frac{dz_{1/2}}{dx}\right]I_1\frac{\partial r_{vw,o}}{\partial\overline{y}}}$$
$$-\underline{\left[\frac{U_o^3}{y_{1/2}}(\frac{dy_{1/2}}{dx})^2\frac{dz_{1/2}}{dx}\right]I_1\frac{\partial r_{vw,o}}{\partial\overline{y}}}+\underline{\left[\frac{U_o^3}{z_{1/2}}\frac{dy_{1/2}}{dx}(\frac{dz_{1/2}}{dx})^2\right]}\frac{\partial I_1}{\partial\overline{z}}\frac{\partial r_{vw,o}}{\partial\overline{y}}$$
$$-\underline{\left[\frac{U_o^3}{z_{1/2}}\frac{dy_{1/2}}{dx}(\frac{dz_{1/2}}{dx})^2\right]}\frac{\partial I_2}{\partial\overline{z}}\frac{\partial r_{vw,o}}{\partial\overline{y}}+\underline{\left[\frac{U_o^3}{z_{1/2}}\frac{dy_{1/2}}{dx}(\frac{dz_{1/2}}{dx})^2\right]}f_{W,o}\frac{\partial r_{vw,o}}{\partial\overline{z}}$$
$$=[P_{vw}]p_{vw}-[P_{pw}]p_{pw}-\left[\frac{U_0^3}{y_{1/2}}\frac{dz_{1/2}}{dx}\right]\frac{\partial t_{vvw,o}}{\partial\overline{y}}-\left[\frac{U_0^3}{y_{1/2}}\frac{dz_{1/2}}{dx}\right]r_{vv,o}\frac{\partial f_{W,o}}{\partial\overline{y}}.\quad(4.34)$$

The Reynolds shear stress equations have the self-similar solutions if the first order terms in the square brackets have the same x-dependence, i.e.,

$$[P_{uv}] \propto [P_{pu}] \propto \left[\frac{T_{uvv}}{y_{1/2}}\right] \propto \left[\frac{U_o^3}{y_{1/2}}\right], \tag{4.35}$$

$$[P_{uw}] \propto \left[\frac{T_{uvw}}{y_{1/2}}\right] \propto \left[\frac{T_{uww}}{z_{1/2}}\right] \propto \left[\frac{U_o^3}{z_{1/2}}\right], \tag{4.36}$$

and

$$[P_{vw}] \propto [P_{pw}] \propto \left[\frac{U_o^3}{y_{1/2}}\frac{dz_{1/2}}{dx}\right]. \tag{4.37}$$

It follows that the constraints for the scales of the moments, $\overline{uv^2}$, $\overline{uvw}$, and $\overline{uw^2}$, given in table 4.1, and the results for the pressure-strain terms and pressure-transport terms given in table 4.2 are satisfied. Comparing the convection terms to the first order production terms in the equations of Reynolds shear stresses, $\overline{uv}$, $\overline{uw}$ and $\overline{vw}$, it follows

$$\underline{\left[U_o^2\frac{dU_o}{dx}\frac{dy_{1/2}}{dx}\right]} \propto \underline{\left[U_o^3\frac{d^2y_{1/2}}{dx^2}\right]} \propto \underline{\left[\frac{U_o^3}{z_{1/2}}\frac{dy_{1/2}}{dx}\frac{dz_{1/2}}{dx}\right]} \propto \underline{\left[\frac{U_o^3}{y_{1/2}}(\frac{dy_{1/2}}{dx})^2\right]} \leq \left[\frac{U_0^3}{y_{1/2}}\right], \tag{4.38}$$

$$\underline{\left[U_o^2\frac{dU_o}{dx}\frac{dz_{1/2}}{dx}\right]} \propto \underline{\left[U_o^3\frac{d^2z_{1/2}}{d^2x})\right]} \propto \underline{\left[\frac{U_o^3}{z_{1/2}}(\frac{dz_{1/2}}{dx})^2\right]} \propto \underline{\left[\frac{U_o^3}{y_{1/2}}\frac{dy_{1/2}}{dx}\frac{dz_{1/2}}{dx}\right]} \leq \left[\frac{U_0^3}{z_{1/2}}\right], \tag{4.39}$$

and

$$\underline{\left[U_o^2\frac{dU_o}{dx}\frac{dy_{1/2}}{dx}\frac{dz_{1/2}}{dx}\right]} \propto \underline{\left[U_o^3\frac{d^2y_{1/2}}{dx^2}\frac{dz_{1/2}}{dx}\right]} \propto \underline{\left[U_o^3\frac{dy_{1/2}}{dx}\frac{d^2z_{1/2}}{dx^2}\right]} \propto$$
$$\propto \underline{\left[\frac{U_o^3}{z_{1/2}}\frac{dy_{1/2}}{dx}(\frac{dz_{1/2}}{dx})^2\right]} \propto \underline{\left[\frac{U_o^3}{y_{1/2}}(\frac{dy_{1/2}}{dx})^2\frac{dz_{1/2}}{dx}\right]} \leq \left[\frac{U_0^3}{y_{1/2}}\frac{dz_{1/2}}{dx}\right]. \tag{4.40}$$

Thus, the convection terms are equal or less than the first order product terms if both the vertical and lateral growth rates are constant or less than linear as x approaches infinity. It should be noted here that in the similarity analysis for the equations of Reynolds stresses the product term $\overline{uv}\partial U/\partial y$ is assumed to be the dominant term. If this is the case, the lateral growth rate is constant or less than linear as x approaches infinity.

Self-similar solution	Constraint
$U(x,y,z) = U_o(x) f_{U,o}(\overline{y},\overline{z})$	$U_o = U_{max}$
$W(x,y,z) = W_o(x) f_{W,o}(\overline{y},\overline{z})$	$W_o \propto U_o(dz_{1/2}/dx)$
$\Omega_x(x,y,z) = \Omega_{x,o}(x) f_{\Omega_x,o}(\overline{y},\overline{z})$	$\Omega_{x,o} \propto U_o(dz_{1/2}/dx)/y_{1/2}$
$\overline{u^2}(x,y,z) = R_{uu,o}(x) r_{uu,o}(\overline{y},\overline{z})$	$R_{uu,o} \propto U_o^2$
$\overline{v^2}(x,y,z) = R_{vv,o}(x) r_{vv,o}(\overline{y},\overline{z})$	$R_{vv,o} \propto U_o^2$
$\overline{w^2}(x,y,z) = R_{ww,o}(x) r_{ww,o}(\overline{y},\overline{z})$	$R_{ww,o} \propto U_o^2$
$\overline{uv}(x,y,z) = R_{uv,o}(x) r_{uv,o}(\overline{y},\overline{z})$	$R_{uv,o} \propto U_o^2(dy_{1/2}/dx)$
$\overline{uw}(x,y,z) = R_{uw,o}(x) r_{uw,o}(\overline{y},\overline{z})$	$R_{uw,o} \propto U_o^2(dz_{1/2}/dx)$
$\overline{vw}(x,y,z) = R_{vw,o}(x) r_{vw,o}(\overline{y},\overline{z})$	$R_{vw,o} \propto U_o^2(dy_{1/2}/dx)(dz_{1/2}/dx)$
$\overline{u^2v}(x,y,z) = T_{uuv,o}(x) t_{uuv,o}(\overline{y},\overline{z})$	$T_{uuv,o} \propto U_o^3(dy_{1/2}/dx)$
$\overline{u^2w}(x,y,z) = T_{uuw,o}(x) t_{uuw,o}(\overline{y},\overline{z})$	$T_{uuw,o} \propto U_o^3(dz_{1/2}/dx)$
$\overline{uv^2}(x,y,z) = T_{uvv,o}(x) t_{uvv,o}(\overline{y},\overline{z})$	$T_{uvv,o} \propto U_o^3$
$\overline{uvw}(x,y,z) = T_{uvw,o}(x) t_{uvw,o}(\overline{y},\overline{z})$	$T_{uvw,o} \propto U_o^3 y_{1/2}/z_{1/2}$
$\overline{uw^2}(x,y,z) = T_{uww,o}(x) t_{uww,o}(\overline{y},\overline{z})$	$T_{uww,o} \propto U_o^3$
$\overline{v^3}(x,y,z) = T_{vvv,o}(x) t_{vvv,o}(\overline{y},\overline{z})$	$T_{vvv,o} \propto U_o^3(dy_{1/2}/dx)$
$\overline{v^2w}(x,y,z) = T_{vvw,o}(x) t_{vvw,o}(\overline{y},\overline{z})$	$T_{vvw,o} \propto U_o^3(dz_{1/2}/dx)$
$\overline{vw^2}(x,y,z) = T_{vww,o}(x) t_{vww,o}(\overline{y},\overline{z})$	$T_{vww,o} \propto U_o^3(dy_{1/2}/dx)$
$\overline{w^3}(x,y,z) = T_{www,o}(x) t_{www,o}(\overline{y},\overline{z})$	$T_{www,o} \propto U_o^3(dz_{1/2}/dx)$

Table 4.1: Similarity solutions for the moments in the outer layer of the wall jet.

Self-similar solution	Constraint
$\overline{p/\rho\partial u/\partial x}(x,y,z) = P_u(x)p_u(\overline{y},\overline{z})$	$P_u \propto U_o^3/y_{1/2}(dy_{1/2}/dx)$
$\overline{p/\rho\partial v/\partial y}(x,y,z) = P_v(x)p_v(\overline{y},\overline{z})$	$P_v \propto U_o^3/y_{1/2}(dy_{1/2}/dx)$
$\overline{p/\rho\partial z/\partial z}(x,y,z) = P_w(x)p_w(\overline{y},\overline{z})$	$P_w \propto U_o^3/y_{1/2}(dy_{1/2}/dx)$
$\overline{p/\rho(\partial u/\partial y + \partial v/\partial x)}(x,y,z) = P_{uv}(x)p_{uv}(\overline{y},\overline{z})$	$P_{uv} \propto U_o^3/y_{1/2}$
$\overline{p/\rho(\partial u/\partial z + \partial w/\partial x)}(x,y,z) = P_{uw}(x)p_{uw}(\overline{y},\overline{z})$	$P_{uw} \propto U_o^3/z_{1/2}$
$\overline{p/\rho(\partial v/\partial z + \partial w/\partial y)}(x,y,z) = P_{vw}(x)p_{vw}(\overline{y},\overline{z})$	$P_{vw} \propto U_o^3/y_{1/2}(dz_{1/2}/dx)$
$1/\rho\partial\overline{pu}/\partial y(x,y,z) = P_{pu}(x)p_{pu}(\overline{y},\overline{z})$	$P_{pu} \propto U_o^3/y_{1/2}$
$1/\rho\partial\overline{pv}/\partial x(x,y,z) = P_{pv}(x)p_{pv}(\overline{y},\overline{z})$	$P_{pv} \propto U_o^3/y_{1/2}(dy_{1/2}/dx)$
$1/\rho\partial\overline{pw}/\partial y(x,y,z) = P_{pw}(x)p_{pw}(\overline{y},\overline{z})$	$P_{pw} \propto U_o^3/y_{1/2}(dz_{1/2}/dx)$
$\epsilon_u(x,y,z) = D_u(x)d_u(\overline{y},\overline{z})$	$D_u \propto U_o^3/y_{1/2}(dy_{1/2}/dx)$
$\epsilon_v(x,y,z) = D_u(x)d_v(\overline{y},\overline{z})$	$D_v \propto U_o^3/y_{1/2}(dy_{1/2}/dx)$
$\epsilon_w(x,y,z) = D_u(x)d_w(\overline{y},\overline{z})$	$D_w \propto U_o^3/y_{1/2}(dy_{1/2}/dx)$

Table 4.2: Similarity solutions for the pressure-strain terms, pressure-transport terms and dissipation terms in Reynolds stress equations of the outer layer.

4.2 Similarity Analysis of the Inner Layer

Following the approach outlined by George et al. [21] for the two-dimensional wall jet, it can be shown that the first order momentum equations in the inner layer of the three-dimensional wall jet are given by

$$0 = -\frac{\partial \overline{uv}}{\partial y} + \nu \frac{\partial^2 U}{\partial y^2}, \tag{4.41}$$

and

$$0 = -\frac{\partial \overline{vw}}{\partial y} + \nu \frac{\partial^2 W}{\partial y^2}. \tag{4.42}$$

These equations can be integrated to yield

$$\frac{\tau_{w,x}}{\rho} = u_*^2 = -\overline{uv} + \nu \frac{\partial U}{\partial y}, \tag{4.43}$$

and

$$\frac{\tau_{w,z}}{\rho} = w_*^2 = -\overline{vw} + \nu \frac{\partial W}{\partial y}, \tag{4.44}$$

where u_* and w_* are the streamwise and lateral friction velocities. It is proposed that the momentum equations in the inner layer have the self-similar solutions of the form given in table 4.3. Substituting the proposed solutions into the equations 4.43 and 4.44 yields

$$[R_{u_*^2}] f_{u_*^2} = -[R_{uv,i}] f_{uv,i} + [\nu \frac{U_i}{\eta}] \frac{\partial f_{U,i}}{\partial y^+}, \tag{4.45}$$

and

$$[R_{w_*^2}] f_{w_*^2} = -[R_{vw,i}] f_{vw,i} + [\nu \frac{W_i}{\eta}] \frac{\partial f_{W,i}}{\partial y^+}. \tag{4.46}$$

Thus, the equations have self-similar solutions if the constraints for the scales in table 4.3 are satisfied. As it will be shown here these solutions can be used to develop a friction laws for the three-dimensional wall jet. The measurements of the profiles here did not extend into inner layer so the similarity analysis is not extended to this layer.

Self-Similar Solution	Constraint
$u_*^2(x,z) = R_{u_*^2}(x) f_{u_*^2}(\overline{z})$	$R_{u_*^2} = u_{*,max}^2$
$w_*^2(x,z) = R_{w_*^2}(x) f_{w_*^2}(\overline{z})$	$R_{w_*^2} = w_{*,max}^2$
$U(x,y,z) = U_i(x) f_{U,i}(y^+,\overline{z})$	$U_i \propto u_{*,max}$
$W(x,y,z) = W_i(x) f_{W,i}(y^+,\overline{z})$	$W_i \propto w_{*,max}^2/u_{*,max}$
$\overline{uv}(x,y,z) = R_{uv,i}(x) f_{uv,i}(y^+,\overline{z})$	$R_{uv,i} \propto u_{*,max}^2$
$\overline{vw}(x,y,z) = R_{vw,i}(x) f_{vw,i}(y^+,\overline{z})$	$R_{vw,i} \propto w_{*,max}^2$

Table 4.3: Similarity solutions for the moments in the inner layer of the wall jet.

4.3 Friction Laws

The friction laws for the three-dimensional wall jet can be determined by matching the inner and outer equations in the overlap layer where the shear stresses, $\overline{uv}$ and $\overline{vw}$, are constant to first order. Thus, the first order scales for the Reynolds shear stresses, $\overline{uv}$ and $\overline{vw}$, in the inner and outer equations should be proportional so that

$$R_{uv,i} \propto R_{uv,o} \rightarrow u_{*,max}^2 \propto U_{max}^2 \frac{dy_{1/2}}{dx} \tag{4.47}$$

and

$$R_{vw,i} \propto R_{vw,o} \rightarrow w_{*,max}^2 \propto U_{max}^2 \frac{dy_{1/2}}{dx} \frac{dz_{1/2}}{dx}. \tag{4.48}$$

Therefore, the streamwise coefficient of friction at the centerline of the jet is given by

$$c_{f,z=0} = \frac{u_{*,max}^2}{U_{max}^2} \propto \frac{dy_{1/2}}{dx}, \tag{4.49}$$

and the ratio of two friction velocity scales can be written as

$$\frac{w_{*,max}}{u_{*,max}} \propto \sqrt{\frac{dz_{1/2}}{dx}}. \tag{4.50}$$

4.4 Comparison With Experiment Data

There have been a number of investigations that have shown that the development of the three-dimensional wall jet in the far field is self-similar by scaling the results using the local maximum velocity and the jet half-widths. The most notable exception to the similarity analysis is the scale for the mean lateral velocity, W. The development of the three-dimensional wall jet exiting a long pipe was examined here for an exit Reynolds number of 65,000 to determine if the results were consistent with the proposed similarity solutions. The development of the vertical and lateral half-widths of the jet are shown in figure 4.2. Here, $y_{1/2}$, the vertical half-width, is the distance along the centerline from the wall to the outer point where the velocity is half of the maximum velocity. Similarly, $z_{1/2}$, the lateral half-width, is the distance between the centerline and the point where the velocity is half of the maximum velocity at the height of the maximum velocity point. It is evident that the growth rates in the vertical and lateral directions are changing in the region $x/D \leq 40$. These two growth rates appear to become approximately constant at $x/D > 40$. The vertical and lateral growth rates are 0.060 and 0.28 respectively in the region $50 \leq x/D \leq 90$ that are in agreement with the results reported by Newman et al. [45] and Eriksson et al. [15].

The profiles of the mean streamwise velocity in the vertical direction along the centerline and laterally across the jet at the height of the local maximum streamwise velocity point measured at x/D=50, 60, 70, 80 and 90 are shown in figure 4.3. Here, the mean streamwise velocity has been normalized by the local maximum streamwise velocity and the coordinates have been normalized by the jet half-widths. It is evident that the profiles of normalized mean streamwise velocity collapse in the region from x/D=50 to 90.

The profiles of the mean lateral velocity normalized by the scale predicted in the

similarity analysis, i.e., $U_{max}dz_{1/2}/dx$, are shown in figure 4.4. It appears that the lateral velocity profiles approximately collapse in the region $x/D \geq 50$. It should be noted that the lateral growth rate used here to scale the mean lateral velocity profiles is constant in this region, i.e., 0.28. There is no difference to the collapse if the traditional scale, U_{max}, was used. However, it would make a significant difference in the intermediate field where there is significant streamline curvature. For example, the profiles of the mean lateral velocity normalized using the scale predicted here and the traditional scale at x/D=25, 30, 35 and 40 in the wall jet exiting a 38.7 mm diameter long pipe are shown in figures 4.5 and 4.6 respectively. Here, the lateral growth rate used to scale the mean lateral velocity profiles was changing in the region $x/D \leq 40$. It is apparent that the lateral velocity profiles normalized by the scale predicted in the similarity analysis approximately collapses in the region $x/D \geq 25$, whereas the profiles normalized by U_{max} do not collapse in this region indicating there are two velocity scales in the intermediate region of the three-dimensional wall jet.

The predicted similarity solutions for the Reynolds stresses were also examined in the wall jet exiting a 12.7 mm diameter long pipe. The profiles of the root mean square of fluctuating velocities, u', v' and w', measured at x/D=50, 60, 70, 80 and 90 are shown in figures 4.7 - 4.9 and the profiles of Reynolds shear stresses, $\overline{uv}$, and $\overline{uw}$, measured at the same positions are shown in figures 4.10 and 4.11. Here, the root mean square of fluctuating velocities, u', v' and w', have been normalized by the local maximum streamwise velocity, U_{max}, and the Reynolds shear stresses, $\overline{uv}$ and $\overline{uw}$, have been normalized by $U_{max}^2 dy_{1/2}/dx$ and $U_{max}^2 dz_{1/2}/dx$ respectively. It is clear that all the profiles of the Reynolds stresses normalized by the similarity scales approximately collapse in the region $x/D \geq 50$. This again confirms the scales predicted in the similarity analysis.

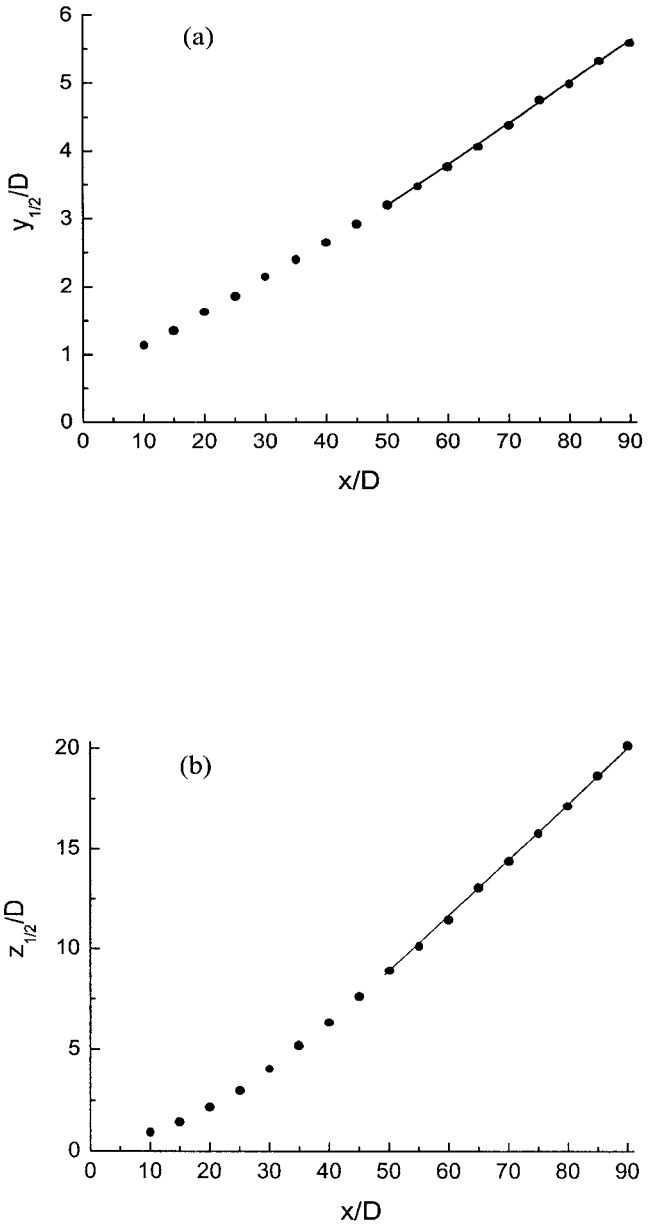

Figure 4.2: The development of (a) the vertical half-width and (b) the lateral half-width measured in the wall jet exiting a 12.7 mm diameter long pipe.

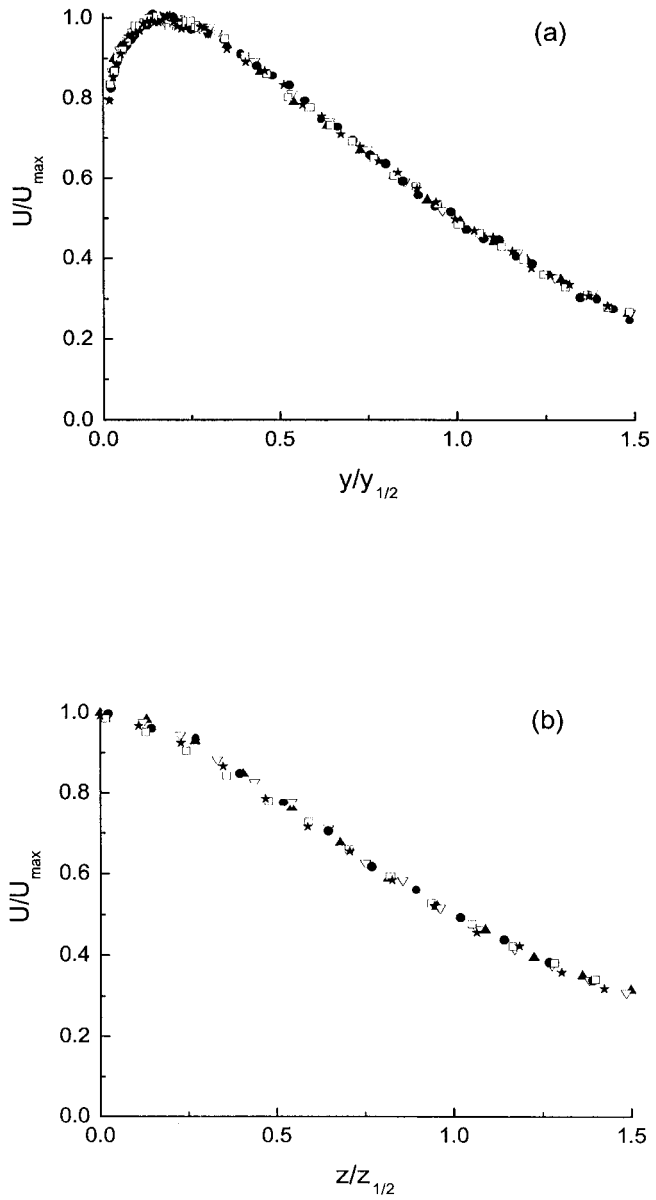

Figure 4.3: Profiles of the mean streamwise velocity measured (a) along the jet centerline and (b) laterally across the jet exiting a 12.7 mm diameter long pipe at ▲ x/D=50, ▽ x/D=60, • x/D=70, □ x/D=80 and ⋆ x/D=90.

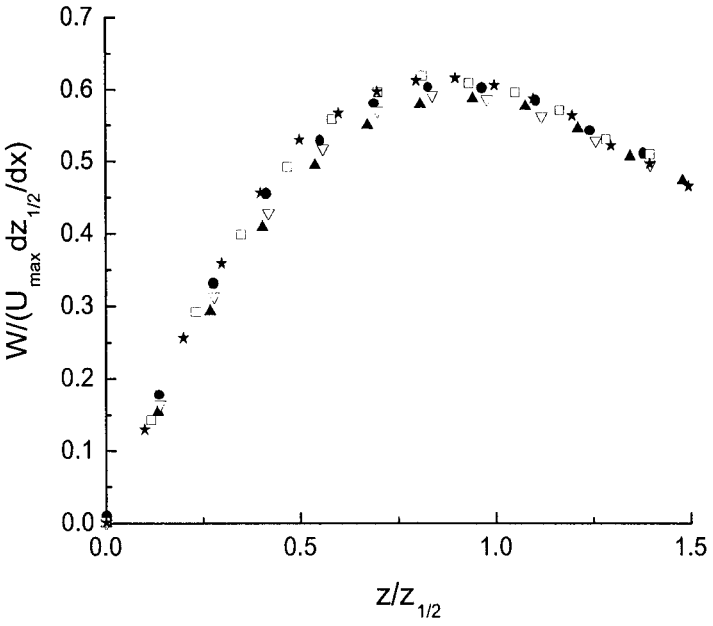

Figure 4.4: Profiles of the mean lateral velocity normalized by the similarity scale at ▲ x/D=50, ▽ x/D=60, • x/D=70, □ x/D=80 and ⋆ x/D=90 in the wall jet exiting a 12.7 mm diameter long pipe.

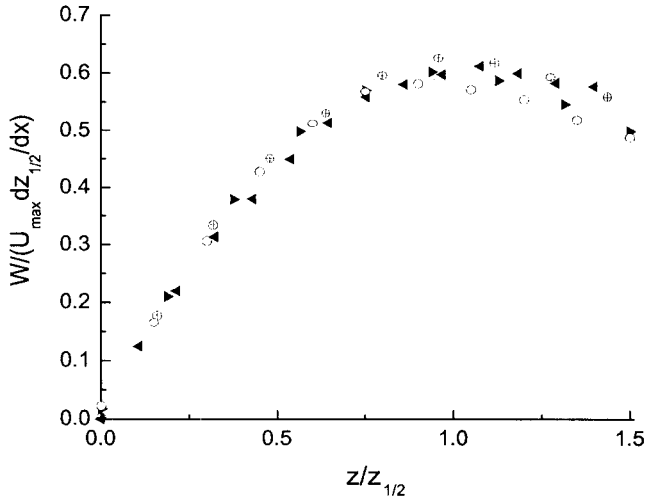

Figure 4.5: Profiles of the mean lateral velocity normalized by the similarity scale at ◀ x/D=25, ⊕ x/D=30, ▶ x/D=35 and ◯ x/D=40 in the wall jet exiting a 38.7 mm diameter long pipe.

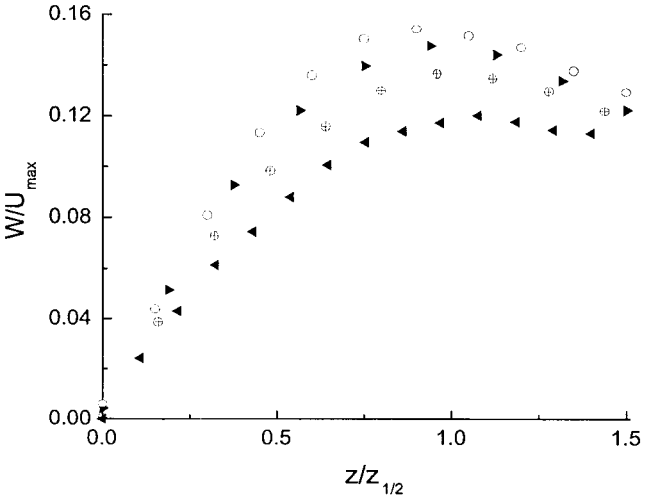

Figure 4.6: Profiles of the mean lateral velocity normalized by the traditional scale, U_{max}, at ◀ x/D=25, ⊕ x/D=30, ▶ x/D=35 and ◯ x/D=40 in the wall jet exiting a 38.7 mm diameter long pipe.

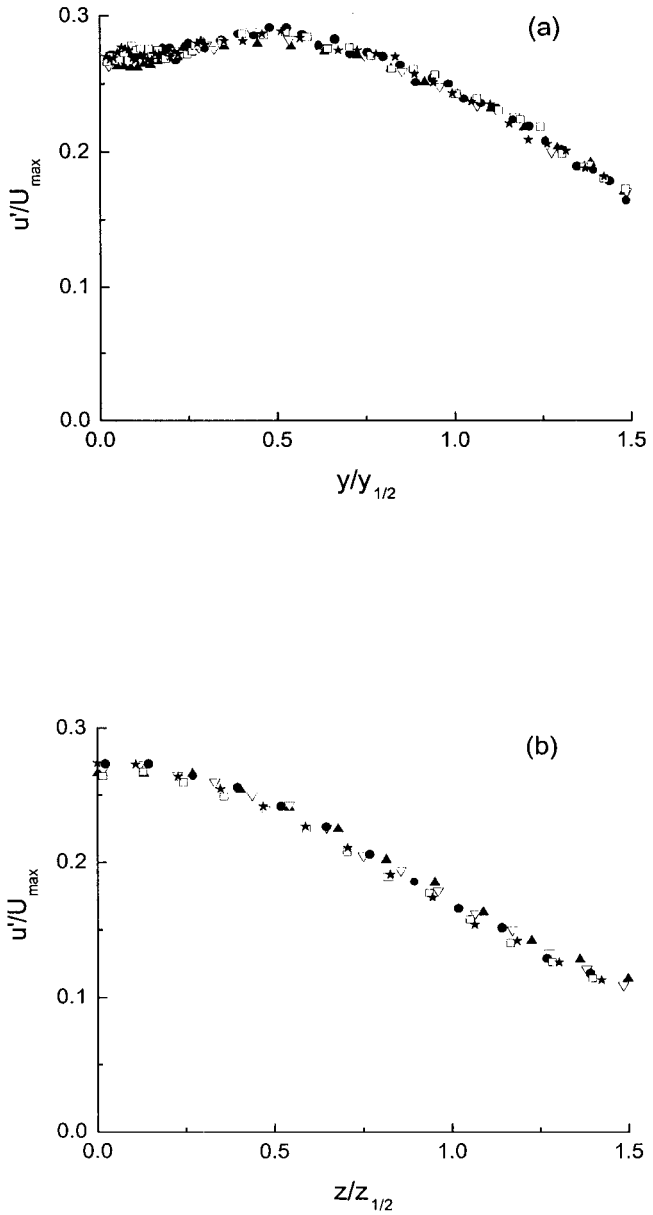

Figure 4.7: Profiles of the root mean square of the streamwise fluctuating velocity measured (a) along the jet centerline and (b) laterally across the jet exiting a 12.7 mm diameter long pipe at ▲ x/D=50, ▽ x/D=60, • x/D=70, □ x/D=80 and ⋆ x/D=90.

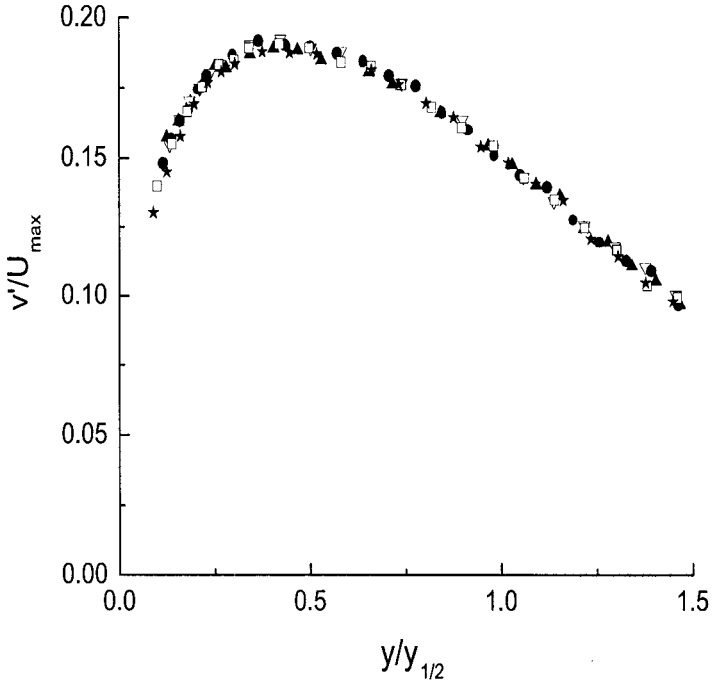

Figure 4.8: Profiles of the root mean square of the vertical fluctuating velocity measured along the centerline of jet exiting a 12.7 mm diameter pipe at ▲ x/D=50, ▽ x/D=60, • x/D=70, □ x/D=80 and ⋆ x/D=90.

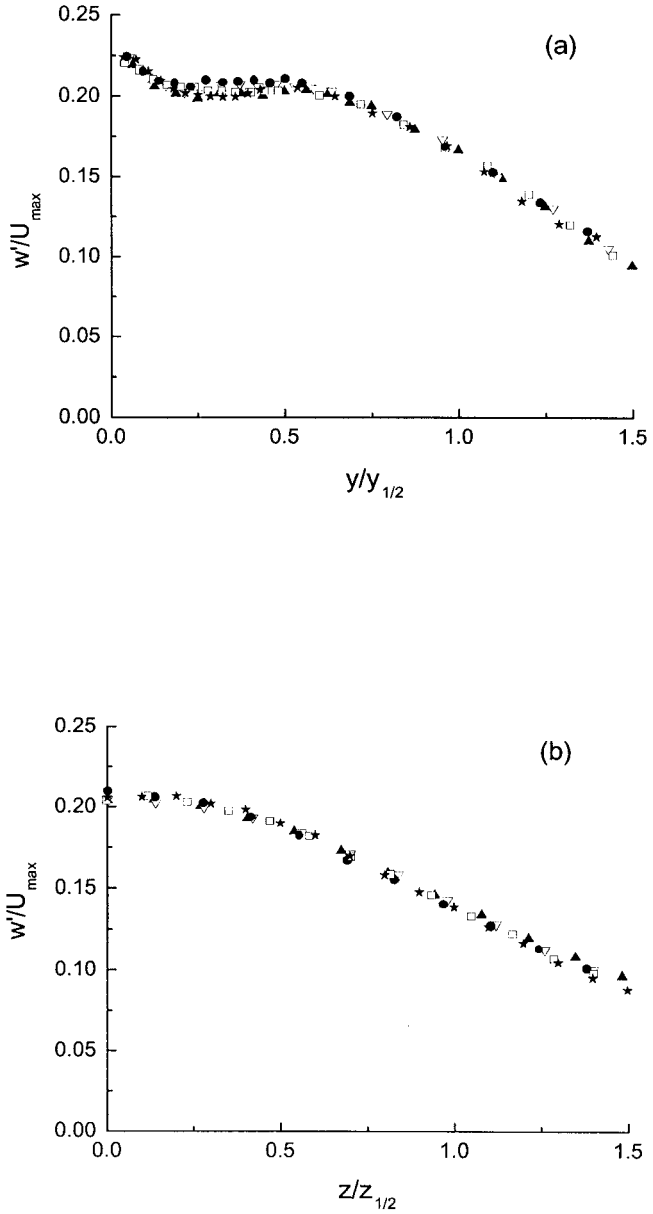

Figure 4.9: Profiles of the root mean square of the lateral fluctuating velocity measured (a) along the jet centerline and (b) laterally across the jet exiting a 12.7 mm diameter long pipe at ▲ x/D=50, ▽ x/D=60, • x/D=70, □x/D=80 and ⋆ x/D=90.

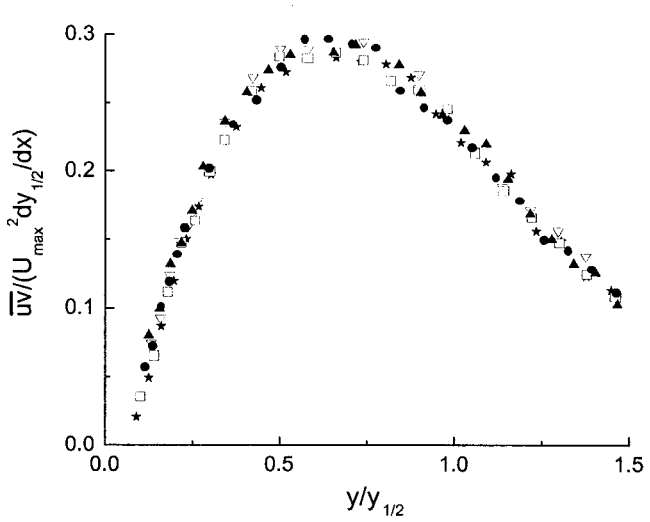

Figure 4.10: Profiles of shear stress, $\overline{uv}$, measured along the centerline of jet exiting a 12.7 mm diameter pipe at ▲ x/D=50, ▽ x/D=60, • x/D=70, □ x/D=80 and ⋆ x/D=90.

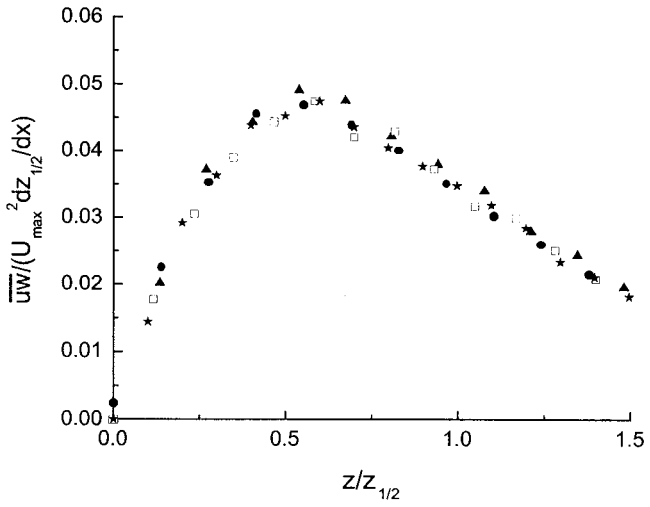

Figure 4.11: Profiles of shear stress, $\overline{uw}$, measured laterally across the jet exiting a 12.7 mm diameter pipe at ▲ x/D=50, ▽ x/D=60, • x/D=70, □ x/D=80 and ⋆ x/D=90.

Chapter 5

Single-Point Measurements

5.1 Development of the Three-Dimensional Wall Jet in Near and Intermediate Fields

The development of the wall jet in near and intermediate fields was initially examined for the jet exiting a contoured nozzle with a Reynolds number of 108,00 at the jet exit. Initially, the development of the jet was characterized by examining the decay of the local maximum streamwise velocity shown in figure 5.1. It is clear that the local maximum streamwise velocity, U_{max}, normalized by the mean velocity at the jet exit, U_{exit}, is in good agreement with the data reported by Davis and Winarto [13]. The local maximum velocity at x/D=6 is approximately the same as the mean velocity at jet exit indicating the existence of the potential core. It is traditionally argued that the decay of the mean streamwise velocity can be expressed as power law forms in the intermediate field. The decay of the maximum mean streamwise velocity on a log plot is shown in figure 5.2. It is clear that there are two regions in the intermediate field. The decay of the local maximum streamwise velocity in the region $10 \leq x/D \leq 20$ and in the region $20 \leq x/D \leq 40$ can be fitted by $U_{max}/U_{exit} = 5.325(x/D)^{-0.845}$ and

$U_{max}/U_{exit} = 13.156(x/D)^{-1.146}$ respectively.

The change in the ratio of the maximum lateral velocity, measured laterally across the jet at the height of the local maximum streamwise velocity point, to the local maximum streamwise velocity is shown in figure 5.3. It is clear that the lateral velocity develops very slowly in the region $x/D \leq 10$. The maximum lateral velocity normalized by the local maximum streamwise velocity increases significantly in the region $10 \leq x/D \leq 20$ and continues to increase through the region $20 \leq x/D \leq 40$ indicating there are two different velocity scales throughout the intermediate field. This is not unexpected since the similarity analysis predicts there should be two velocities scales in the flow when the lateral growth rate is not constant.

The development of the vertical position of the local maximum streamwise velocity, y_{max}, on the centerline of jet is shown in figure 5.4. It appears that the vertical position of the local maximum streamwise velocity begins to move towards the wall in the region from x/D=3 to 6 and then stays at approximately the same height until $x/D \approx 10$. It is interesting to note that the maximum velocity point again moves towards the wall in the region $10 \leq x/D \leq 20$. After x/D=20 the maximum velocity point begins, however, to move away from the wall. This again suggests that the near field should extend to x/D=10 and the intermediate field should be broken up into two regions: the region $10 \leq x/D \leq 20$ and the region $20 \leq x/D \leq 40$.

The development of the vertical and lateral jet half-widths are shown in figures 5.5 and 5.6. It is clear that the measurements of lateral half-width are in good agreement with the data reported by Davis and Winarto [13]. There also appears to be three regions for the evolution of the growth rate of the jet. The vertical growth rate initially increases in the near field from x/D=3 to 10. There is then a slight decrease in the region $10 \leq x/D \leq 20$. The vertical growth rate finally increases again in the region $20 \leq x/D \leq 40$. The lateral growth rate increases continuously in the region $10 \leq x/D \leq 20$, but the rate of this increase slows down in the region $20 \leq x/D \leq 40$.

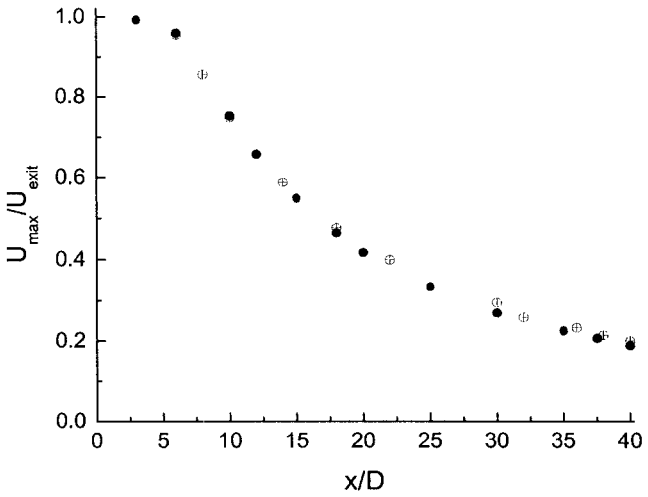

Figure 5.1: Decay of the local maximum streamwise velocity measured • in this investigation and ⊕ by Davis and Winarto [13].

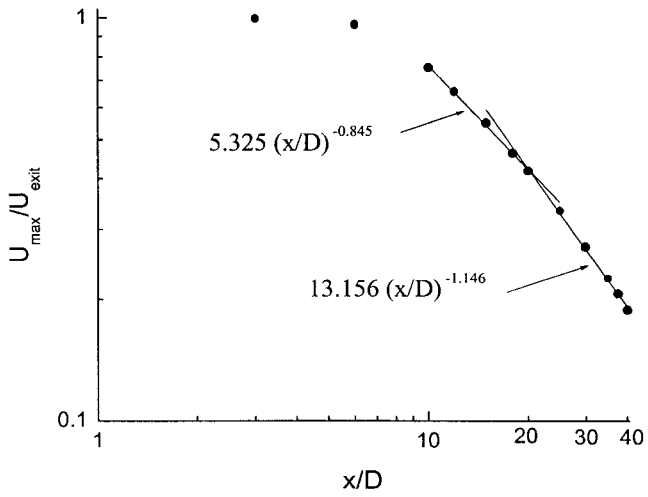

Figure 5.2: Decay of the local maximum streamwise velocity of the wall jet fitted by the power law.

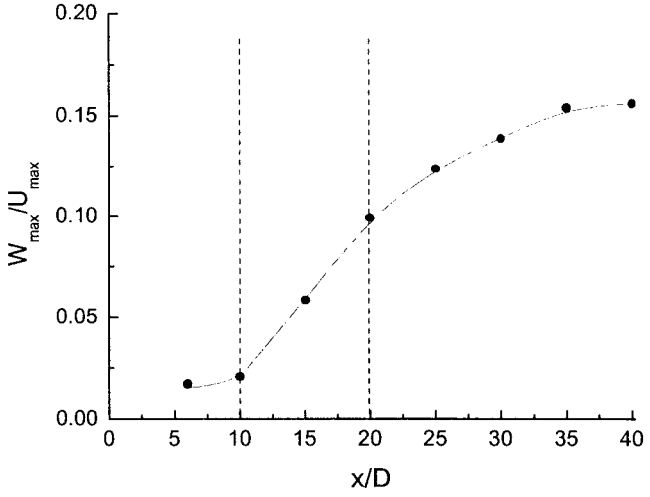

Figure 5.3: Development of the maximum lateral velocity at the height of the maximum streamwise velocity point.

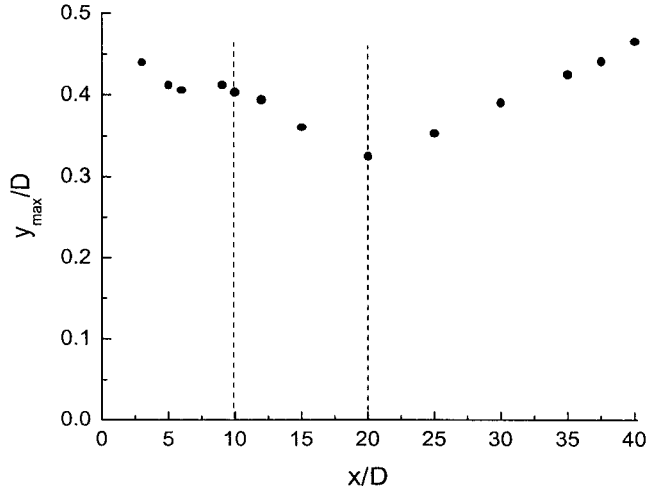

Figure 5.4: The height of the local maximum streamwise velocity point.

The vertical growth rate in this investigation is 0.052 at x/D=40, approximately the end of intermediate field, that falls between the values reported by Abrahamsson et al. [1], 0.065, and Davis and Winarto [13], 0.037, for wall jets exiting contoured nozzles in the far field. The lateral growth rate is 0.27 at x/D=40, that is smaller than the values reported by Abrahamsson et al. [1] and Davis and Winarto [13], 0.32, and Maslov et al. [42], 0.30, for the far field.

The profiles of the mean streamwise velocity and lateral velocity in the near field $0 \leq x/D \leq 10$ normalized by the jet exit velocity, U_{exit}, and the nozzle diameter, D, are shown in figures 5.7 and 5.8. The profiles of the mean streamwise velocity were measured along the centerline of the jet and laterally across the jet at the height of the maximum velocity point, while the profiles of the lateral velocity were measured across the jet at the height of the maximum velocity point. The potential core of the jet can be clearly seen at x/D=3 but decreases in size as the flow evolves downstream and disappears after x/D=6. The profiles of mean lateral velocity also change significantly in the near field. At x/D=6 the largest lateral velocity occurs at $z/D \approx 0.3$. Outside this point the lateral velocity decreases rapidly. As the flow evolves downstream to x/D=10 the peak in the lateral velocity shifts to $z/D \approx 0.55$ and the profile of the lateral velocity outside this point decays much slower. The profiles of the mean streamwise velocity and lateral velocity measured in the intermediate field are shown in figures 5.9 - 5.12. Here, the profiles of mean streamwise velocity in the intermediate field have been normalized by the local maximum streamwise velocity, U_{max}, and the jet half-widths, while the profiles of mean lateral velocity have been normalized by the similarity variables, $U_{max}dz_{1/2}/dx$, and the jet half-widths. Although the profiles of mean streamwise velocity measured laterally across the jet at the height of the maximum velocity point approximately collapse in the intermediate field, the vertical profiles of the streamwise velocity are still changing from x/D=10 to 20. As the flow evolves downstream the maximum velocity point moves towards the wall until it is

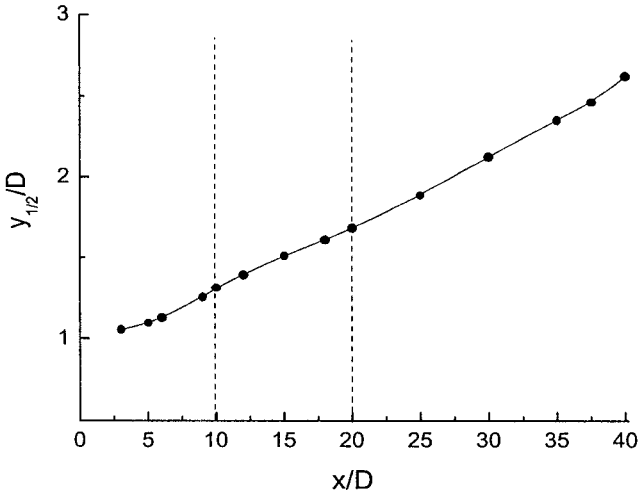

Figure 5.5: Development of the vertical jet half-width.

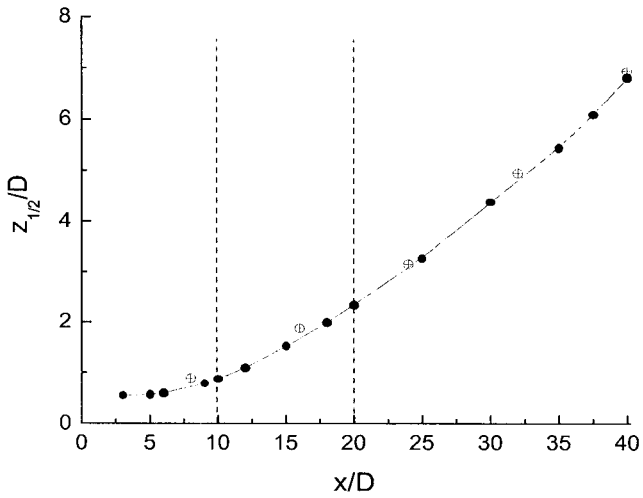

Figure 5.6: Development of the lateral jet half-width measured • in this investigation and ⊕ by Davis and Winarto [13].

located at $y/y_{1/2} \approx 0.2$. The profiles of the streamwise velocity are approximately the same after x/D=20. It is noted that the difference in the streamwise velocity profiles along the jet centerline from x/D=10 to 20 occurs mainly in the region $y/y_{1/2} \leq 0.5$ indicating the development of the flow is caused by its adjustment to the wall. The profiles of the lateral velocity evolve significantly in the region $10 \leq x/D \leq 20$. In particular, the lateral velocity profile spreads laterally outside and the value of the normalized lateral velocity increases significantly in this region. These profiles also approximately collapse beyond x/D=20.

The three-dimensional development of the velocity field was examined by measuring the distribution of the mean streamwise velocity over the entire cross-stream plane downstream of the jet. The contours of the mean streamwise velocity in the near field normalized by the jet exit velocity and nozzle diameter are shown in figure 5.13. The dotted line on these contour plots indicates the height of the maximum velocity point, while the solid arrow indicates the maximum jet width. It is evident that the height of the maximum velocity point and the maximum jet width do not coincide in the near field. Initially the jet begins to spread laterally near the wall at x/D=3 and the large lateral growth of the jet near the wall becomes apparent at x/D=6. Here, the height of the maximum jet width is well below the height of the maximum velocity point. The contours of the mean streamwise velocity in the intermediate field normalized using the local maximum velocity and nozzle diameter are shown in figures 5.14 and 5.15. The nozzle diameter has been used to normalize the contour plots in order to emphasize the change in the size of the jet. It appears that the maximum velocity point moves towards the wall, while the height of the maximum jet width moves away from the wall in the region $10 \leq x/D \leq 20$. The maximum velocity point and the height of the maximum jet width roughly coincide at x/D=20 - 25 and both move away from the wall after this point. The movement of the maximum velocity point towards the wall in the region $10 \leq x/D \leq 20$ likely

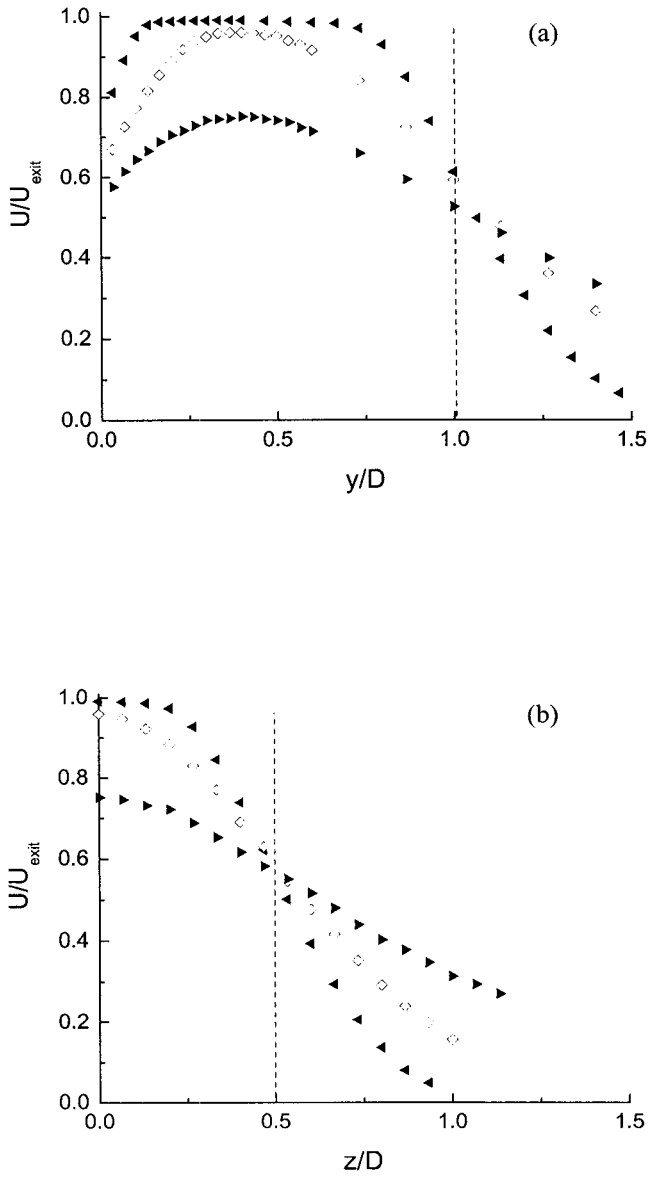

Figure 5.7: Profiles of the mean streamwise velocity measured (a) along the jet centerline and (b) laterally across the jet in the near field at ◀ x/D=3, ◊ x/D=6 and ▶ x/D=10.

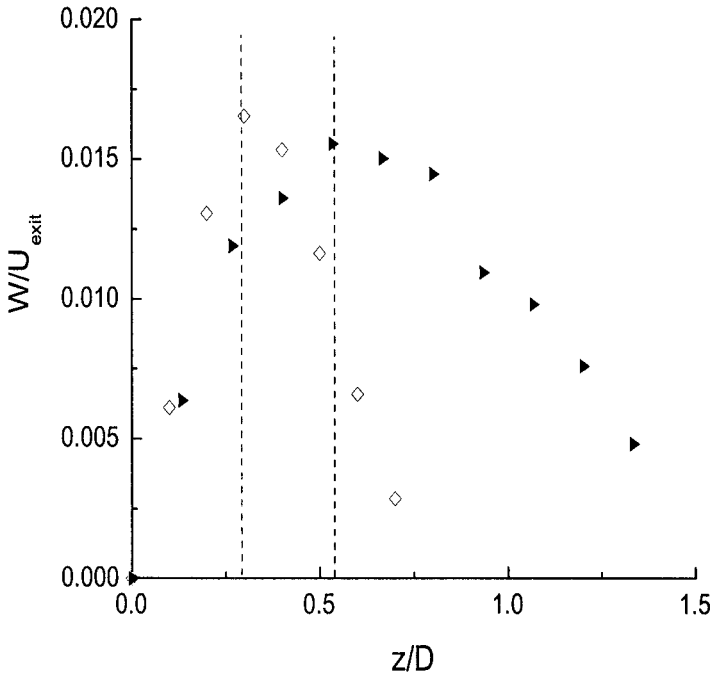

Figure 5.8: Profiles of the mean lateral velocity measured in the near field at ◊ x/D=6 and ▶ x/D=10.

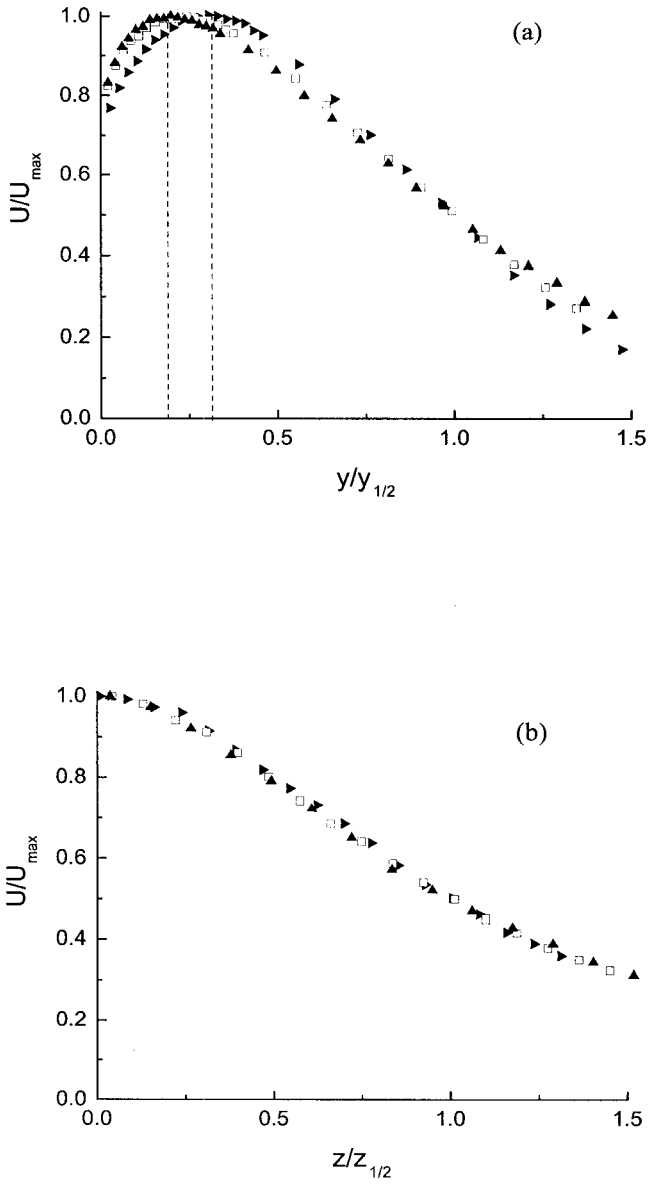

Figure 5.9: Profiles of the mean streamwise velocity measured (a) along the jet centerline and (b) laterally across the jet at the height of the local maximum velocity point in the intermediate field at ▶ x/D=10, □ x/D=15 and ▲ x/D=20.

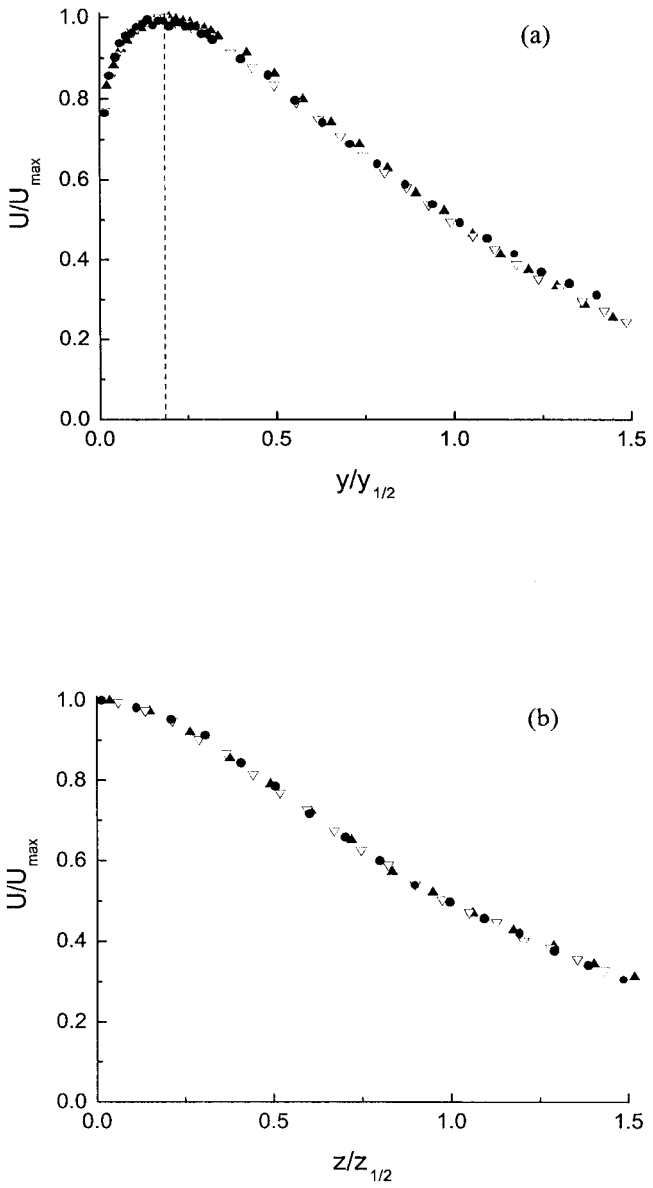

Figure 5.10: Profiles of the mean streamwise velocity measured (a) along the jet centerline and (b) laterally across the jet at the height of the local maximum velocity point in the intermediate field at ▲ x/D=20, ▽ x/D=30 and • x/D=40.

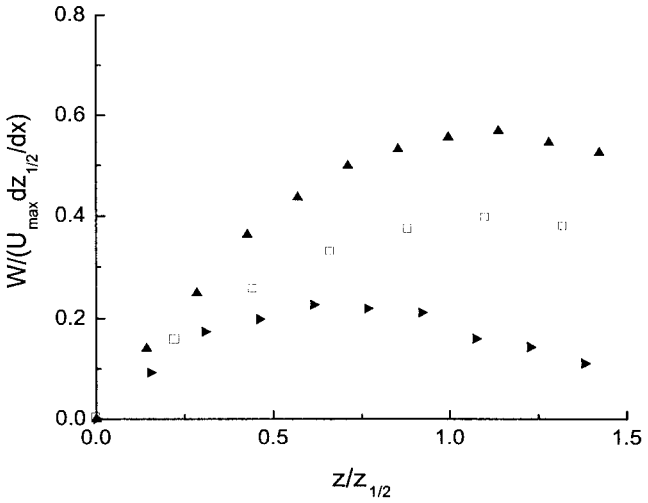

Figure 5.11: Profiles of mean lateral velocity measured in the intermediate field at ▶ x/D=10, □ x/D=15 and ▲ x/D=20.

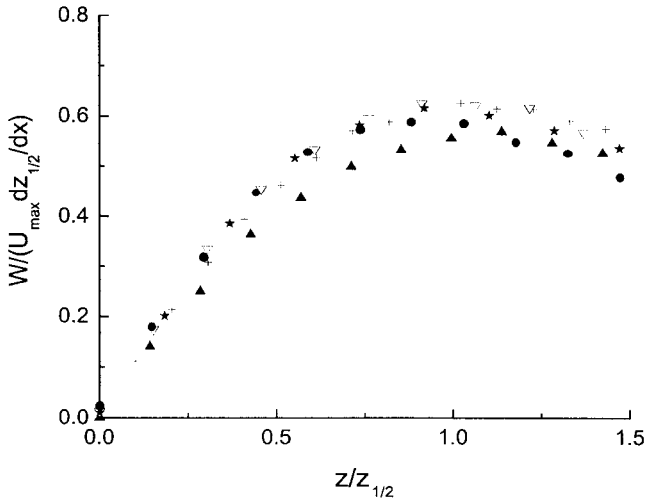

Figure 5.12: Profiles of mean lateral velocity measured in the intermediate field at ▲ x/D=20, + x/D=25, ▽ x/D=30, ⋆ x/D=35 and • x/D=40.

explains the inflection in the vertical half-width of the jet observed in this region. It is clear that the contours of the streamwise velocity are roughly similar for $x/D \geq 20$. The contours of the streamwise velocity normalized by the local maximum velocity and jet half-widths in this region are shown in figure 5.16. The results are similar but a close inspection shows that the region of the large lateral growth at the bottom of the jet is spreading slightly in the vertical direction as the flow evolves downstream indicating the mean velocity field is not yet fully self-similar.

The evolution of the jet can also be examined by measuring the contours of the mean streamwise vorticity at different downstream positions. The contours of the mean streamwise vorticity in the near field at x/D=6 and 10 normalized by the jet exit parameters, U_{exit}/D, and nozzle diameter, D, are shown in figure 5.17. The broken and solid lines here indicate clockwise and counter clockwise motions viewed from the nozzle. It is clear there are a pair of regions of counter rotating streamwise vorticity on each side of the jet centerline. The pair of regions of counter rotating vorticity are laterally across the jet at x/D=6. The reorientation of the mean streamwise vorticity responsible for increasing the lateral growth rate of the jet has been initiated by x/D=10, the end of the near field. This is consistent with the measurements reported by Iida and Matsuda [29]. The contours of the mean streamwise vorticity in the intermediate field normalized using the similarity variables, $(U_{max}dz_{1/2}/dx)/y_{1/2}$, and jet half-widths are shown in figures 5.18 and 5.19. It is clear that the reorientation of the vorticity initiated at the end of near field continues throughout the intermediate field. In particular, the outer region of streamwise vorticity induces the inner region towards the wall and outward until two regions are positioned roughly one above the other. The magnitude of the vorticity scaled using similarity variables also changes in the intermediate field. Particularly the magnitude of the scaled vorticity decreases as the flow evolves downstream. The reorientation and the change of the scaled vorticity appear to slow down after x/D=20. This reorientation and change of vorticity

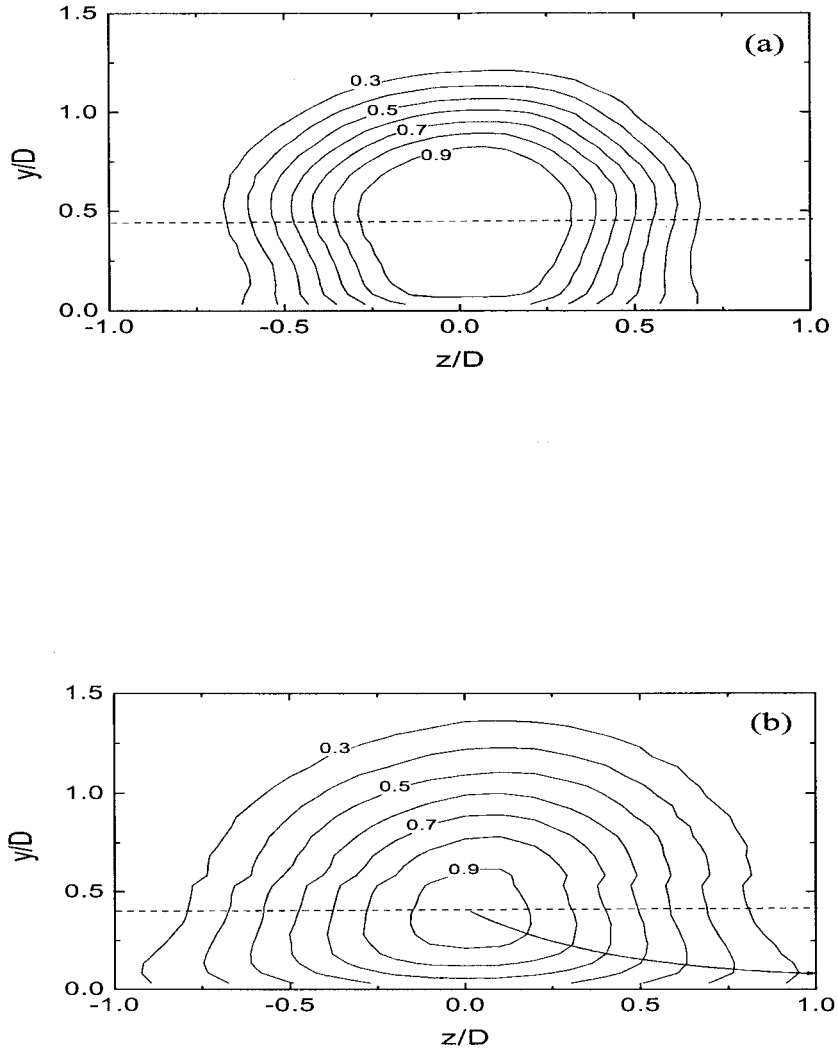

Figure 5.13: Contours of the mean streamwise velocity normalized by the jet exit velocity and the nozzle diameter in the near field at (a) x/D=3 and (b) x/D=6.

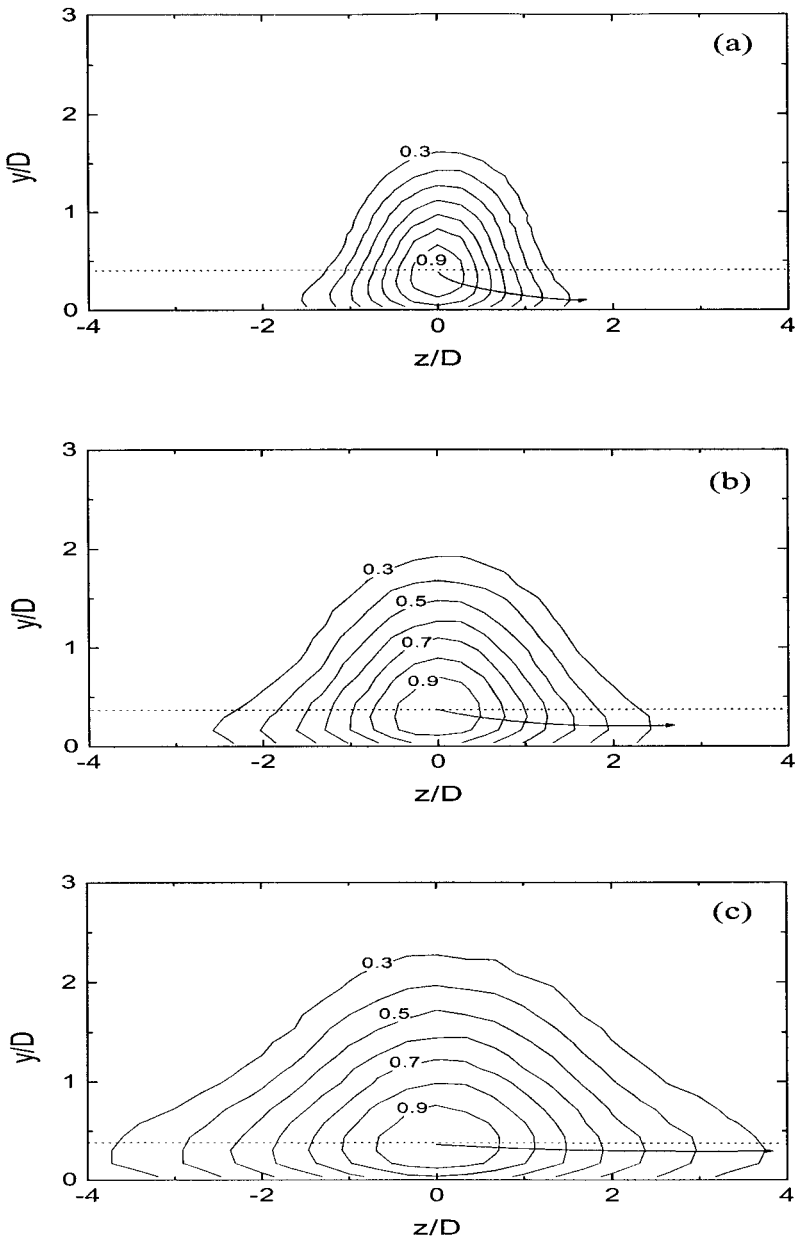

Figure 5.14: Contours of the mean streamwise velocity normalized by the local maximum streamwise velocity and nozzle diameter in the intermediate field at (a) x/D=10, (b) x/D=15 and (c) x/D=20.

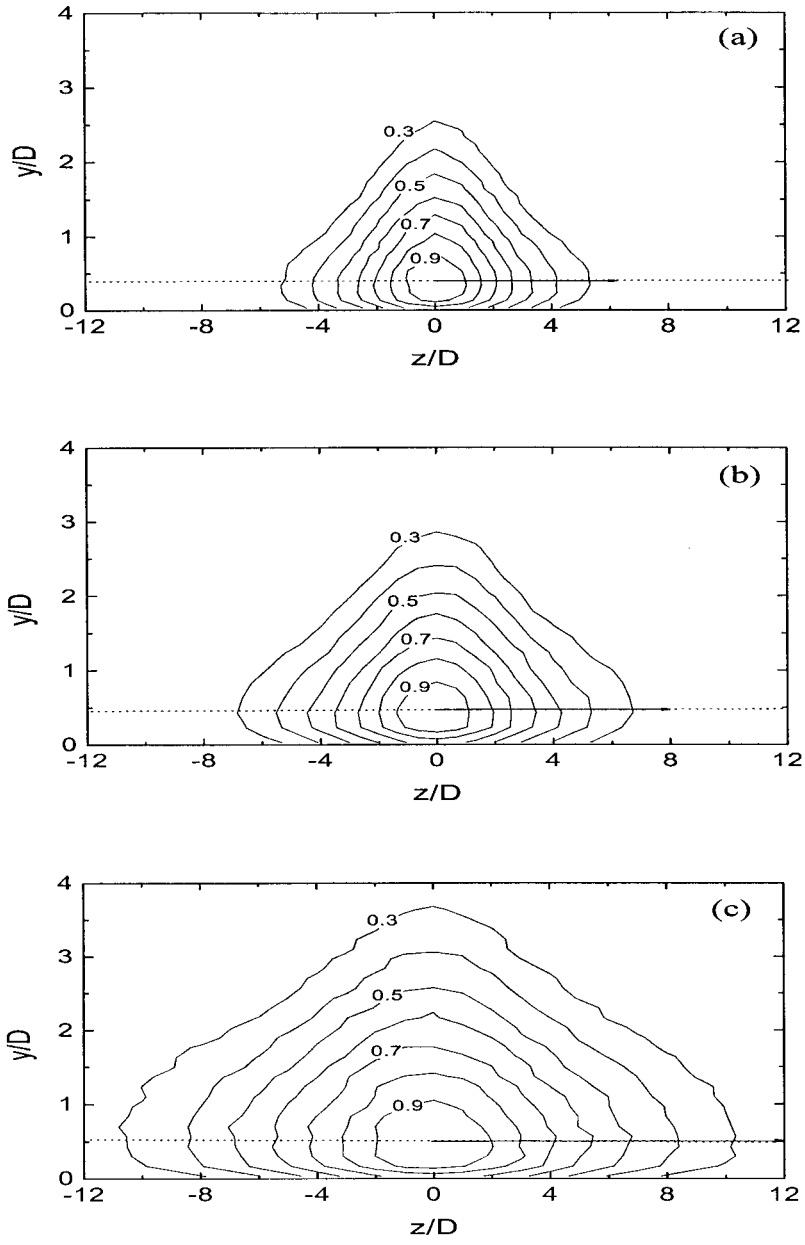

Figure 5.15: Contours of the mean streamwise velocity normalized by the local maximum streamwise velocity and nozzle diameter in the intermediate field at (a) x/D=25, (b) x/D=30 and (c) x/D=40.

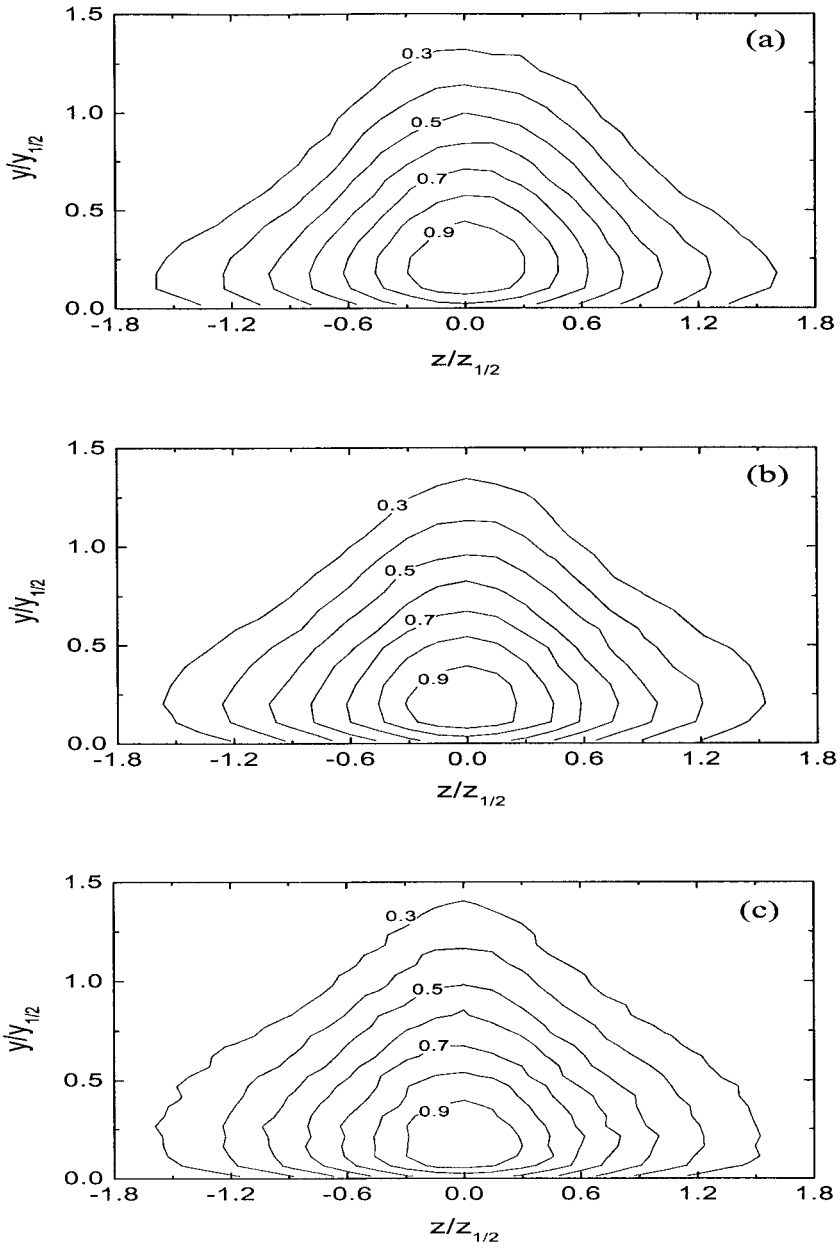

Figure 5.16: Contours of the mean streamwise velocity normalized by the local maximum streamwise velocity and jet half-widths in the intermediate field at (a) x/D=20, (b) x/D=30 and (c) x/D=40.

magnitude in the intermediate field likely explain why the lateral growth rate of the wall jet continues to increase throughout this region.

It is useful to examine the development of the turbulent Reynolds stresses in order to determine how the turbulent processes in the wall jet are changing in the near and intermediate fields. The profiles of the root mean square of fluctuating velocities, u', v' and w', and the Reynolds shear stresses, $\overline{uv}$, and $\overline{uw}$, in the near field normalized by jet exit parameters, U_{exit} or U_{exit}^2, and the nozzle diameter, D, are shown in figures 5.20 - 5.24. The profiles of u' and w' were measured both along the jet centerline and laterally across the jet at the height of the maximum streamwise velocity point. The profiles of v' or $\overline{uv}$ were not measured laterally across the jet because of the large cross flow error that would be caused by the mean lateral velocity. The measurements of normal stresses in the near field clearly show the strong development of the potential core in the wall jet. In particular, the size of the potential core, indicated by the dot line in the profiles along the jet centerline, decreases rapidly as the flow evolves downstream. The potential core eventually disappears after x/D=6. The turbulence level in the potential core region is still much less than the shear layer region, but increases significantly from x/D=6 to 10. The low turbulence level region is not apparent at x/D=10 indicating the shear layers on the opposite sides of the jet have merged at $x/D \approx 10$ and resulted in a fully turbulent jet. The profiles of $\overline{uv}$ and $\overline{uw}$ also change significantly in the near field. It is interesting to note that the zero point in the vertical profile of $\overline{uv}$ has shifted from the centerline by x/D=6 indicating the interaction with the wall is already moving the center of the jet towards the wall. The peak values of the Reynolds shear stresses, $\overline{uv}$ and $\overline{uw}$, are approximately at positions of y/D=1.0 and z/D=0.5, the edge of the jet nozzle. Away from these points the Reynolds shear stresses spread as the shear layers grow. The profiles of root mean square of fluctuating velocities, u', v' and w', and Reynolds shear stresses, $\overline{uv}$ and $\overline{uw}$, in the intermediate field normalized using similarity variables and the

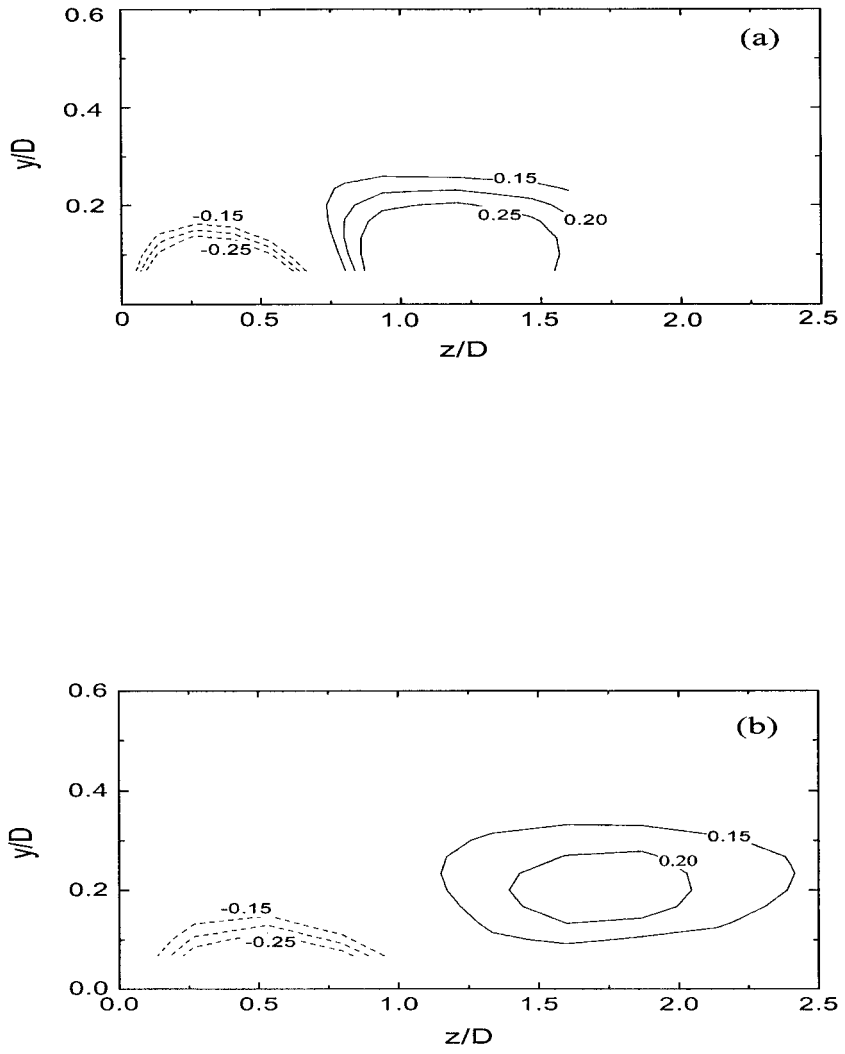

Figure 5.17: Contours of the mean streamwise vorticity normalized by U_{exit}/D and D in the near field at (a) x/D=6 and (b) x/D=10.

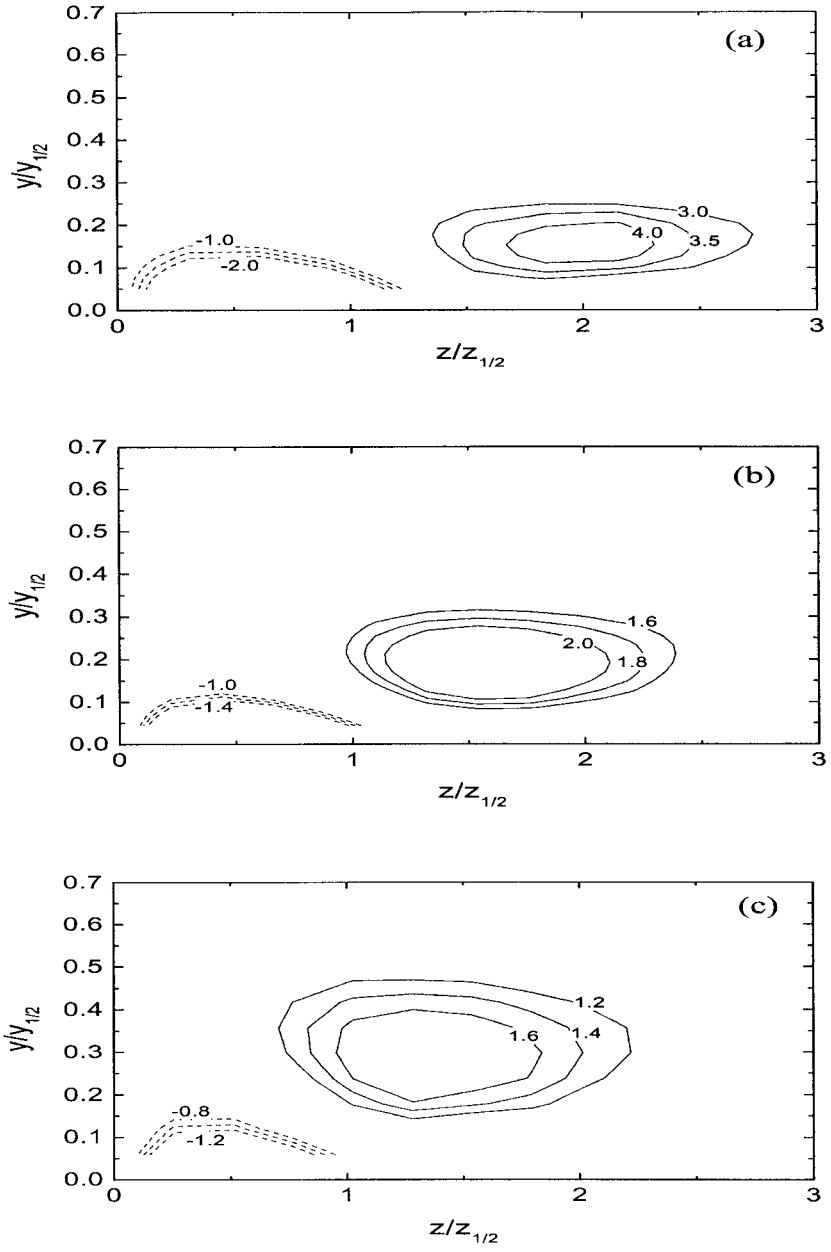

Figure 5.18: Contours of the mean streamwise vorticity normalized by the similarity variables, $(U_{max}dz_{1/2}/dx)/y_{1/2}$, and jet half-widths in the intermediate field at (a) x/D=10, (b) x/D=15 and (c) x/D=20.

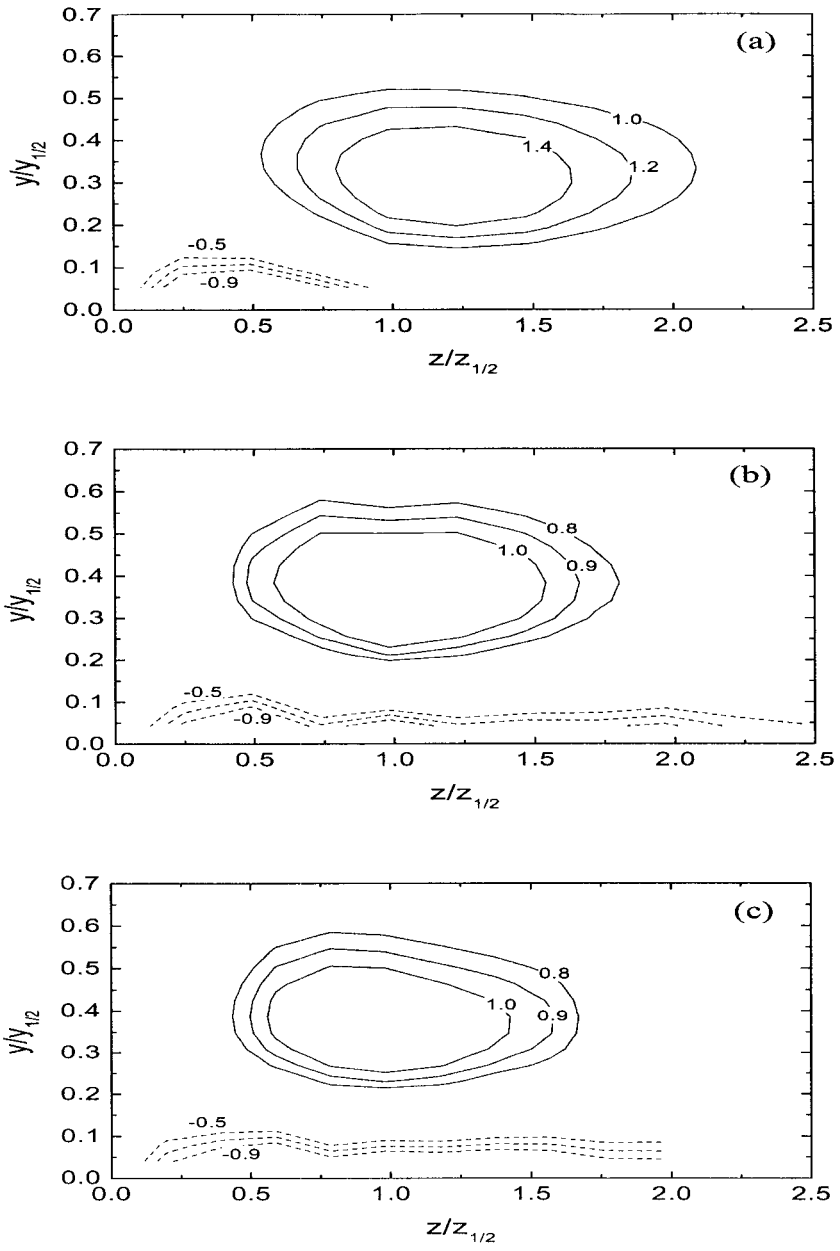

Figure 5.19: Contours of the mean streamwise vorticity normalized by the similarity variables, $(U_{max} dz_{1/2}/dx)/y_{1/2}$, and jet half-widths in the intermediate field at (a) x/D=25, (b) x/D=35 and (c) x/D=40.

jet half-widths are shown in figures 5.25 - 5.31. It is clear that the evolution of the Reynolds stresses continues throughout the intermediate field. As the flow evolves downstream the normalized fluctuating velocities continue to increase though this process slows down after x/D=20. The peaks in the root mean square of fluctuating velocities, u', v' and w', measured in the vertical profiles along the jet centerline move towards the wall until they are located at $y/y_{1/2} \approx 0.5$ for u' and w' and at $y/y_{1/2} \approx 0.4$ for v' at $x/D \approx 30$. The value of root mean square of fluctuating velocity, v', near the wall is, however, less than half of the values of u' and w' due to the damping effect of the wall [20]. The peaks in root mean square of fluctuating velocities in the lateral profiles move towards the jet centerline as the flow evolves downstream until they are at the centerline at $x/D \approx 30$. The Reynolds shear stress, $\overline{uv}$, changes the sign at $y/y_{1/2} \approx 0.3$, x/D=10. The point of zero shear stress, $\overline{uv}$, moves towards the wall as the flow evolves downstream until it is located at $y/y_{1/2} \approx 0.05$ in the region $x/D \geq 20$. It should be noted that the maximum mean streamwise velocity locates at $y/y_{1/2} \approx 0.2$. So there is a region $0.05 \leq y/y_{1/2} \leq 0.2$ where the standard gradient diffusion model for the Reynolds shear stress [31], i.e, $\overline{uv} = -\mu_t \partial U/\partial y$, does not apply. Here, μ_t is the eddy diffusivity of momentum. The peaks in Reynolds shear stress, $\overline{uv}$, in the vertical profiles along the jet centerline move towards the wall until they are located at $y/y_{1/2} \approx 0.65$ by x/D=30. The maximum shear of mean streamwise velocity, $\partial U/\partial y$, along the jet centerline also occurs at $y/y_{1/2} \approx 0.65$ indicating the production term, $-\overline{uv}\partial U/\partial y$, on the symmetry plane is largest at $y/y_{1/2} \approx 0.65$. This position is higher than the maximum in the normal stresses suggesting the turbulent diffusion may play an important role in this flow as it is the case for the round jet [28]. It also appears that the differences in the profiles of u', v', w' and $\overline{uv}$ at x/D=35 and 40 are not apparent suggesting the flow is approximately approaching far field.

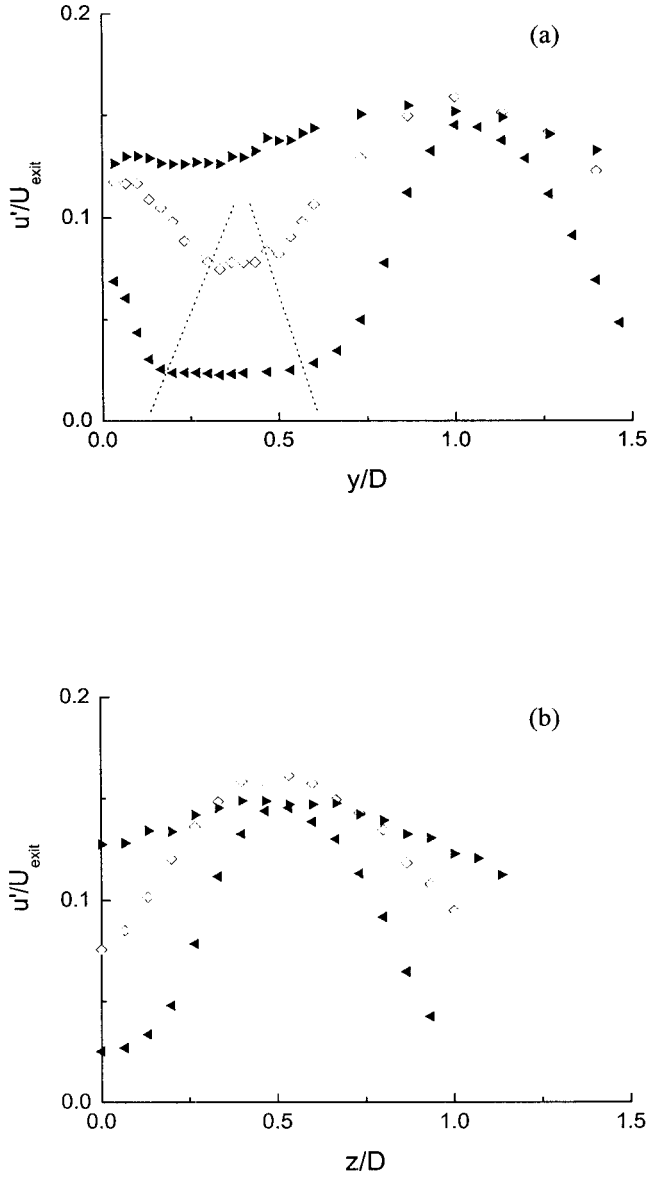

Figure 5.20: Profiles of the root mean square of the fluctuating velocity, u', measured (a) along the jet centerline and (b) laterally across the jet at the height of the local maximum velocity point in the near field at ◀ x/D=3, ◊ x/D=6 and ▶ x/D=10.

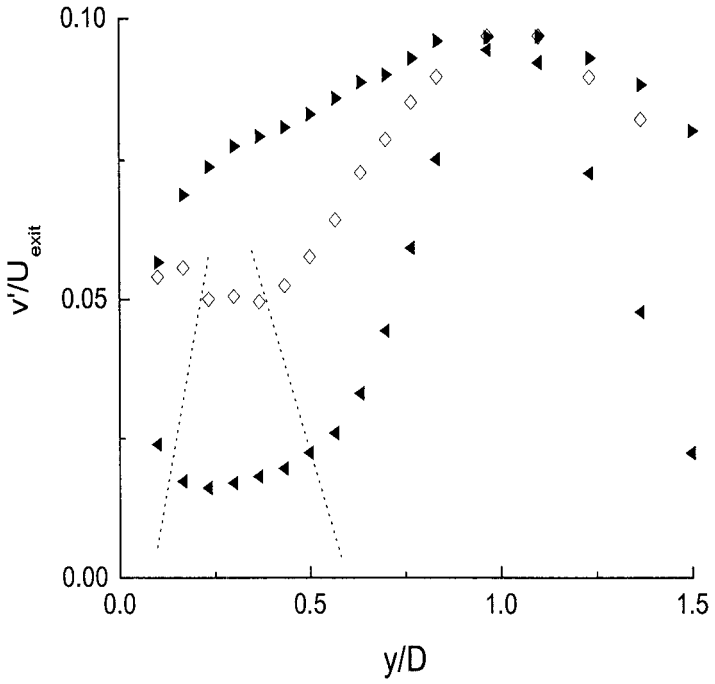

Figure 5.21: Profiles of the root mean square of the fluctuating velocity, v', measured in the near field at ◀ x/D=3, ◊ x/D=6 and ▶ x/D=10.

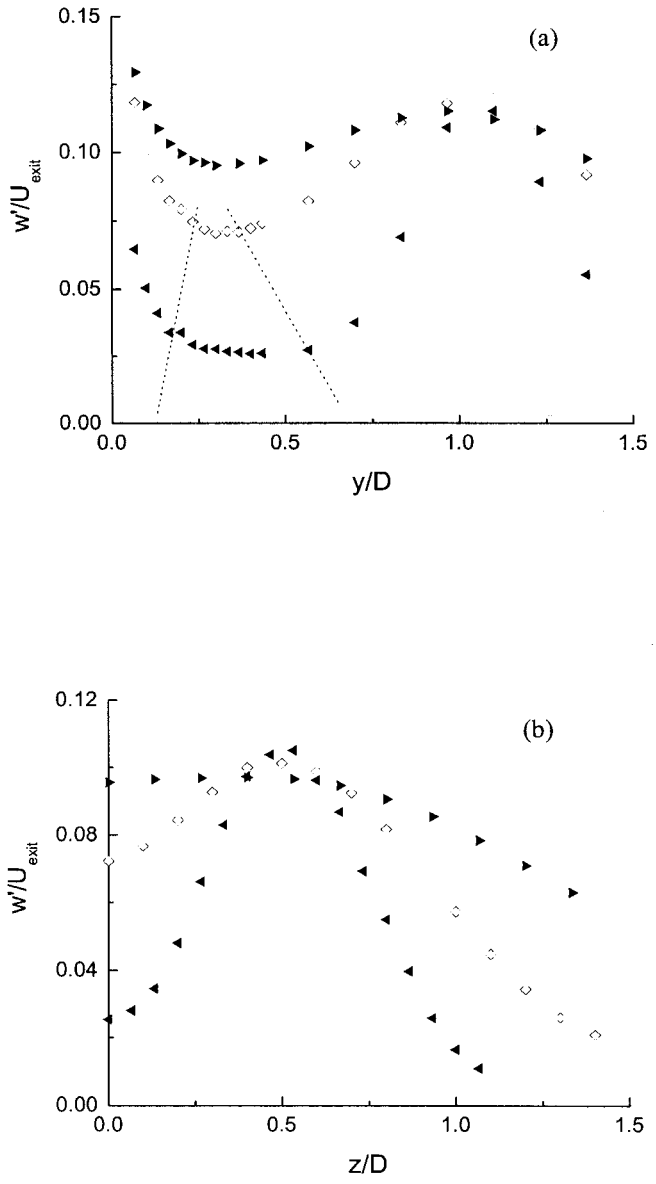

Figure 5.22: Profiles of the root mean square of the fluctuating velocity, w', measured (a) along the jet centerline and (b) laterally across the jet at the height of the local maximum velocity point in the near field at ◀ x/D=3, ◊ x/D=6 and ▶ x/D=10.

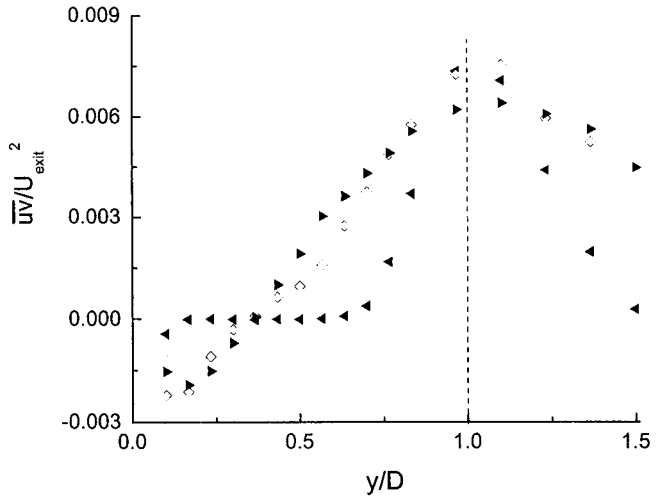

Figure 5.23: Profiles of shear stress, $\overline{uv}$, measured in the near field at ◀ x/D=3, ◊ x/D=6 and ▶ x/D=10.

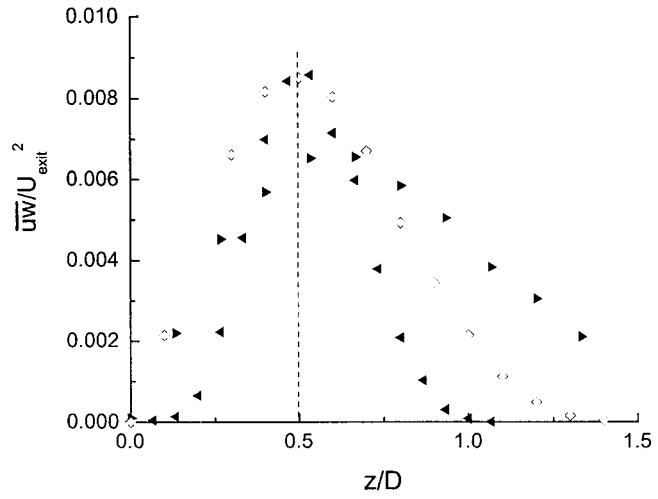

Figure 5.24: Profiles of shear stress, $\overline{uw}$, measured in the near field at ◀ x/D=3, ◊ x/D=6 and ▶ x/D=10.

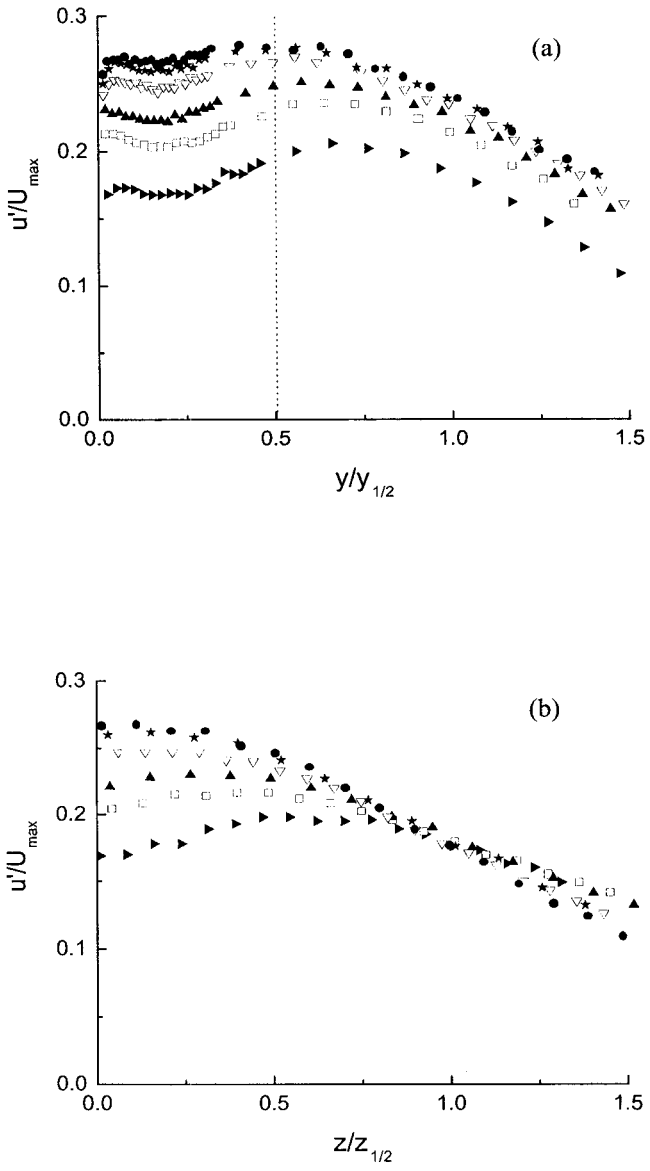

Figure 5.25: Profiles of the root mean square of the fluctuating velocity, u', measured (a) along the jet centerline and (b) laterally across the jet at the height of the local maximum velocity point in the intermediate field at ▶ x/D=10, □ x/D=15, ▲ x/D=20, ▽ x/D=30, ⋆ x/D=35 and • x/D=40.

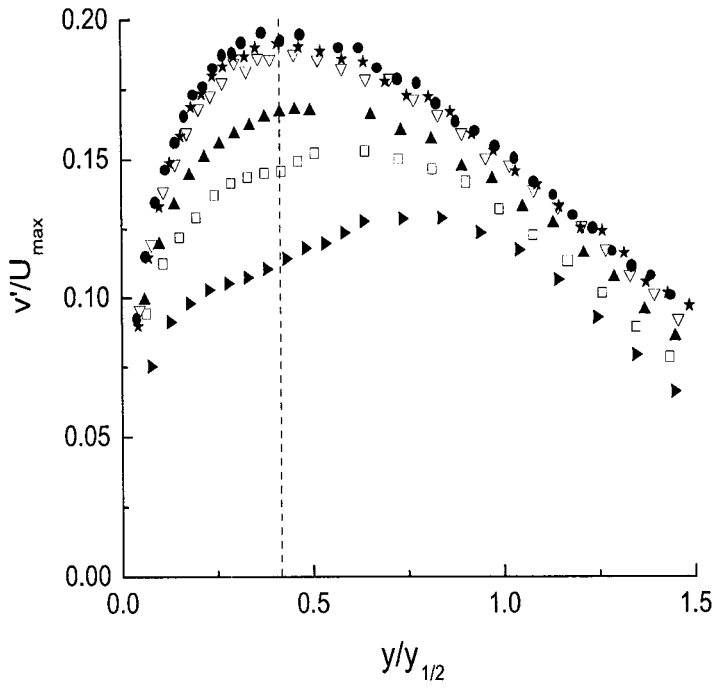

Figure 5.26: Profiles of the root mean square of the fluctuating velocity, v', measured in the intermediate field at ▶ x/D=10, □ x/D=15, ▲ x/D=20, ▽ x/D=30, ⋆ x/D=35 and • x/D=40.

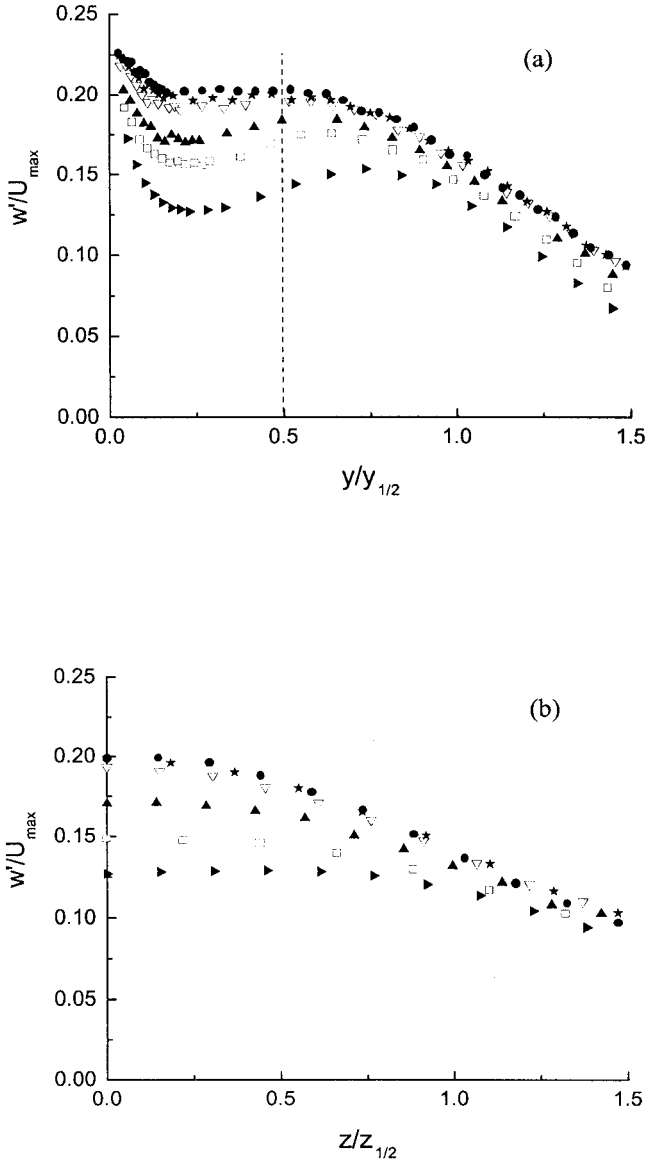

Figure 5.27: Profiles of the root mean square of the fluctuating velocity, w', measured (a) along the jet centerline and (b) laterally across the jet at the height of the local maximum velocity point in the intermediate field at ▶x/D=10, □x/D=15, ▲ x/D=20, ▽ x/D=30, ⋆ x/D=35 and • x/D=40.

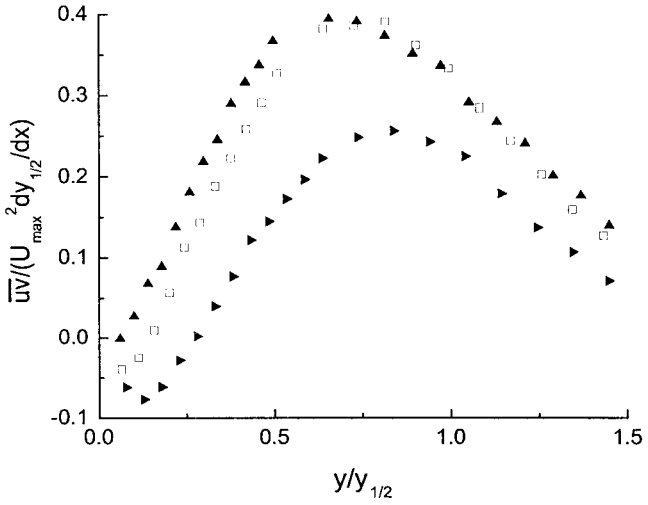

Figure 5.28: Profiles of shear stress, $\overline{uv}$, measured in the intermediate field at ▶ x/D=10, □ x/D=15 and ▲ x/D=20.

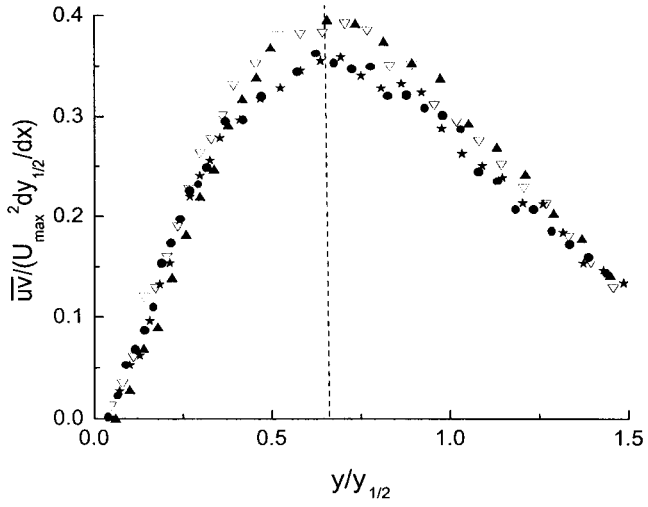

Figure 5.29: Profiles of shear stress, $\overline{uv}$, measured in the intermediate field at ▲ x/D=20, ▽ x/D=30, ⋆ x/D=35 and • x/D=40.

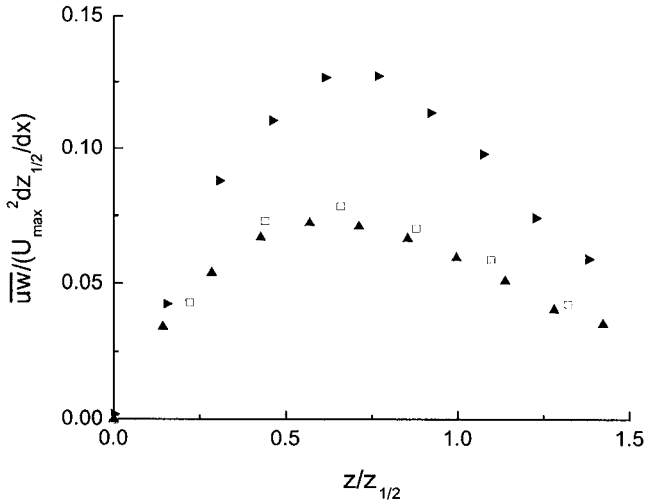

Figure 5.30: Profiles of shear stress, $\overline{uw}$, measured in the intermediate field at ▶ x/D=10, □ x/D=15 and ▲ x/D=20.

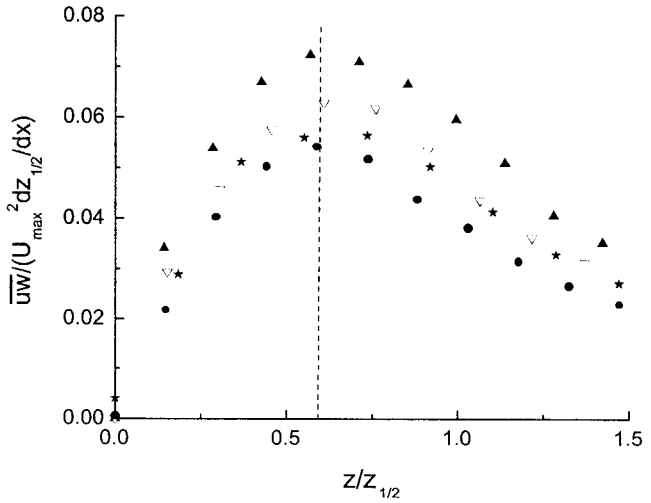

Figure 5.31: Profiles of shear stress, $\overline{uw}$, measured in the intermediate field at ▲ x/D=20, ▽ x/D=30, ⋆ x/D=35 and • x/D=40.

5.2 Effect of Initial Conditions

The effect of changing initial conditions on the development of wall jets exiting a round jet was examined by comparing the development of wall jets exiting the long pipe and the contoured nozzle with a Reynolds number of 108,000 at the jet exit. Measurements were also performed in the wall jet exiting the long pipe with a Reynolds number of 68,000 to examine if the development of the flow was affected by the jet exit Reynolds number. The experiments were performed in the same facility so boundary conditions were the same.

The development of the three jets were compared using the decay of the local maximum streamwise velocity and the growth of jet half-widths shown in figures 5.32 - 5.35. It is clear that the development of the flow is independent of the jet exit Reynolds number for the range of Reynolds number considered here, but the development of two jets exiting the contoured nozzle and the long pipe differ significantly. The local maximum mean streamwise velocity exiting the long pipe is initially larger than the contoured nozzle because the effect of mean velocity profile at the pipe exit persists throughout the near field. The maximum velocity then decays more rapidly in the intermediate field of the wall jet exiting the long pipe. The power law forms of the decay in the local maximum velocity of the jet exiting the long pipe in the two regions of the intermediate field $10 \leq x/D \leq 20$ and $20 \leq x/D \leq 40$ are $U_{max}/U_{exit} = 6.141(x/D)^{-0.851}$ and $U_{max}/U_{exit} = 17.067(x/D)^{-1.190}$ respectively. These differ from those in the contoured nozzle jet that are $U_{max}/U_{exit} = 5.325(x/D)^{-0.845}$ and $U_{max}/U_{exit} = 13.156(x/D)^{-1.146}$ in the corresponding regions. It is should be noted that the maximum streamwise velocity in the wall jet exiting the long pipe is still 10% larger than the jet exiting the contoured nozzle at x/D=40.

The vertical and lateral half-widths of the flow exiting the long pipe are approximately 0.05D and 0.24D smaller than the flow exiting the contoured nozzle in the

region $20 \leq x/D \leq 40$ indicating that the development of the jet exiting the long pipe is delayed. These differences exceed the experimental uncertainty in these measurements. The measurements were repeated in a number of experiments and in all cases it was found that half-widths of the flow exiting the long pipe were smaller. It appears, however, that growth rates of the two jets are similar in the region $20 \leq x/D \leq 40$. The growth rates of the jets were compared by shifting the origin of the jet exiting the long pipe by 0.8D. This offset is not the virtual origin of the jet because it is not defined using data from the far field. Rather, it is intended to offset the delayed development of the jet exiting the long pipe. The development of jet half-widths including this offset are shown in figure 5.35. It is clear that the data collapse in the region beyond x/D=20 indicating that the growth rates of the two jets in this region are approximately the same. The local maximum mean streamwise velocities of the two jets do not collapse after the shift of the jet origin as shown in figure 5.33 indicating that the decay of mean velocities do differ.

Thus, the results indicate that the growth rates of the three-dimensional wall jet exiting a round nozzle in the region $x/D \geq 20$ are not affected by the initial conditions of the jet, at least for jets exiting the contoured nozzle and long pipe. The growth rates in vertical and lateral directions at x/D=40, approximately the end of intermediate field, are 0.053 - 0.055 and 0.27 respectively. The lateral growth rate agrees well with the results for the far field of the wall jet exiting the long pipe found in this investigation and reported by Newman et al. [45] and Eriksson et al. [15]. It differs significantly from the value of 0.32 reported by Abrahamsson et al. [1] for the region $50 \leq x/D \leq 90$ in the wall jet exiting the contoured nozzle. It is not clear why there would be a difference in the growth rate between the measurement at x/D=40 and x/D=50 - 90 in the wall jet exiting the contoured nozzle and not for the long pipe. This requires further investigation.

The development of the jet half-widths, particularly the vertical jet half-width,

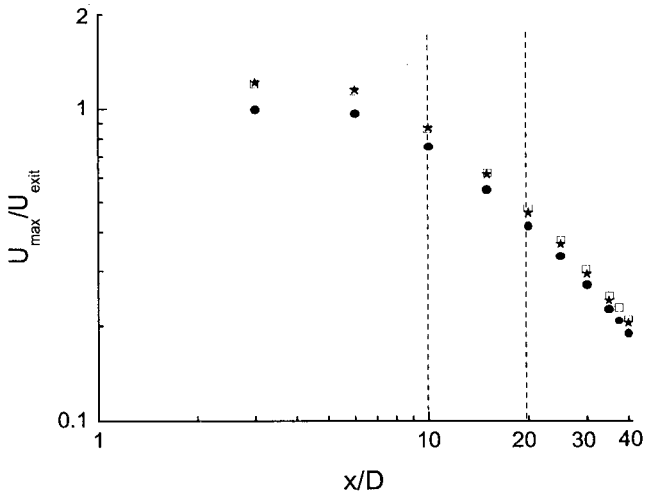

Figure 5.32: Decay of the local maximum streamwise velocity of wall jets exiting the contoured nozzle with • Re=108,000 and exiting the long pipe with □ Re=108,00 and ⋆ Re=65,000.

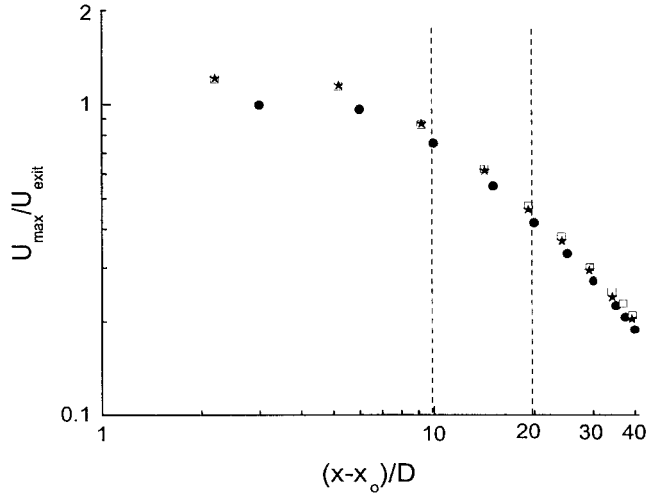

Figure 5.33: Decay of the local maximum streamwise velocity of wall jets exiting the contoured nozzle with x_o=0 for • Re=108,000 and exiting the long pipe with x_o=0.8D for □ Re=108,00 and ⋆ Re=65,000.

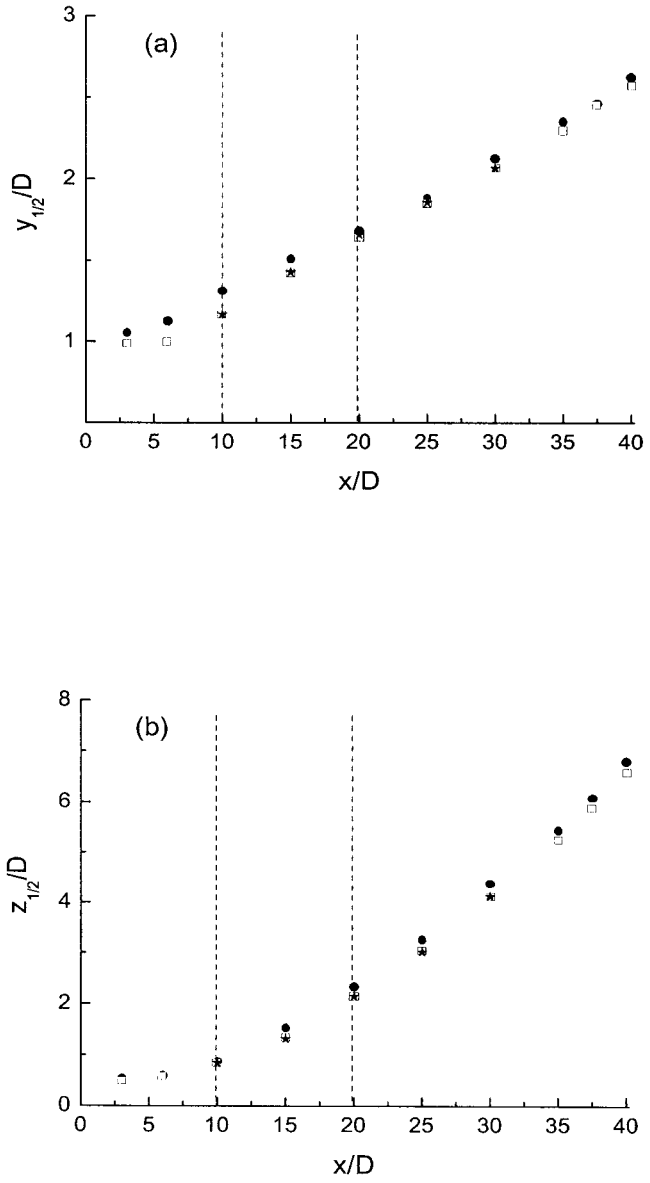

Figure 5.34: The development of (a) the vertical half-width and (b) the lateral half-width of wall jets exiting the contoured nozzle at • Re=108,000 and exiting the long pipe at □ Re=108,00 and ⋆ Re=65,000.

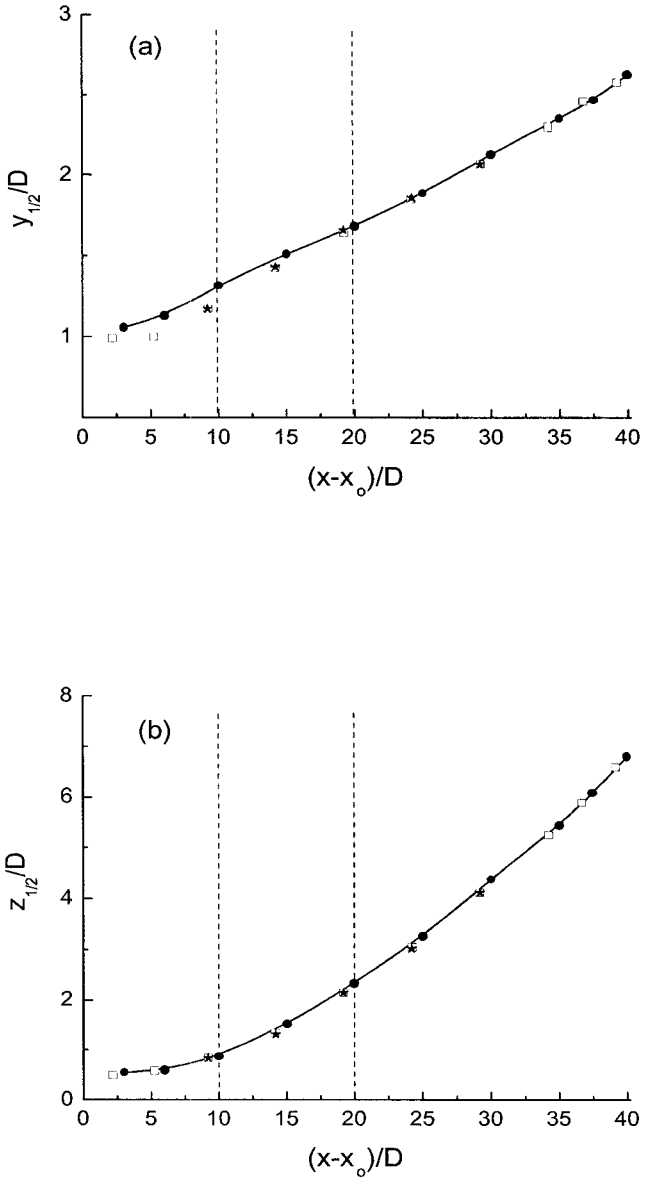

Figure 5.35: The development of (a) the vertical half-width and (b) the lateral half-width of wall jets exiting the contoured nozzle with x_o=0 for • Re=108,000 and exiting the long pipe with x_o=0.8D for □ Re=108,00 and ⋆ Re=65,000.

in the near field of the two jets differ significantly. The vertical spreading of the jet exiting the long pipe is delayed relative to the wall jet exiting the contoured nozzle throughout the near field and the intermediate field. The difference in the development of the jets exiting the two round nozzles can be understood further by examining the profiles of the velocity field. The profiles of the mean streamwise velocity and the mean lateral velocity normalized using the average exit velocity, U_{exit}, and the nozzle diameter, D, in the near field are shown in figures 5.36 and 5.37. The profiles of the streamwise velocity in the central region of the two jets differ significantly in the near field. In particular, the mean streamwise velocity exiting the long pipe is larger than the contoured nozzle in the central region of the jet from x/D=3 to 10. Outside this central region the difference in the profiles of the streamwise velocity in the two jets tends to disappear. Thus, close to the nozzle the definition of the jet half-width being the distance to half of the maximum velocity is not an equivalent measure in the two jets and likely should not be used to characterize the development of the jet in the near field. The profiles of the lateral velocity in the long pipe jet is initially broader than the contoured nozzle jet but after x/D=6 the profiles from the contoured nozzle are broader indicating more rapidly development of the wall jet exiting the contoured nozzle. A comparison of the profiles of mean streamwise and lateral velocity measured in the intermediate field from x/D=10 to 40 are shown in figures 5.38 - 5.41. Here, the profiles of mean streamwise and lateral velocities in the intermediate field have been normalized using the similarity variables and jet half-widths. It is clear that there is a difference between profiles of the mean streamwise velocity along the jet centerline at x/D=15. Beyond this point the differences in both vertical and lateral profiles of the mean streamwise velocity in the two jets tend to disappear. The difference in the lateral velocity profiles in the two jets also tends to disappear beyond x/D=20 indicating that the changing of initial conditions does not significantly affect the profiles of mean velocity in the region

$20 \leq x/D \leq 40$.

The three-dimensional development of the two jets can be compared by examining the contours of the mean streamwise velocity and the mean streamwise vorticity. The contours of the mean streamwise velocity in the near field at x/D=3 and 6 normalized by the average exit velocity and the nozzle diameter are shown in figure 5.42. It is clear that the development of the two jets differ in the near field. In particular, the large lateral growth of the jet apparent near the wall at x/D=6 in the wall jet exiting the contoured nozzle is not apparent for the wall jet exiting the long pipe. The contours of the mean streamwise velocity in the intermediate field normalized by the local maximum mean streamwise velocity and jet half-width are shown in figures 5.43 and 5.44. It appears that the difference in the contours of the mean streamwise velocity in the two jets persists until x/D=15. Thus, the development of the large lateral growth in the jet exiting the long pipe is delayed.

The contours of the mean streamwise vorticity in the near field at x/D=6 normalized by the jet exit parameters, U_{exit}/D, and the nozzle diameter, D, are shown in figure 5.45, while the contours of the mean streamwise vorticity in the intermediate field normalized using the similarity variables and jet half-widths are shown in figures 5.46 and 5.47. It is clear that the regions of mean streamwise vorticity occur in both jets by x/D=6 indicating that the deformation of the vortex rings responsible for the large lateral growth rate occurs in both jets. The reorientation of the regions of mean streamwise vorticity is delayed in the jet exiting the long pipe. For example, the reorientation of the vorticity responsible for increasing the lateral growth rate of the jet has been initiated in the jet exiting the contoured nozzle by x/D=10, while in the wall jet exiting the long pipe a pair of regions of counter rotating vorticity on each side of the jet centerline are still side by side at this position. There does not appear to be a large difference in the orientation of the mean streamwise vorticity at x/D=15 but a close inspection of the figures indicate the contours of the mean

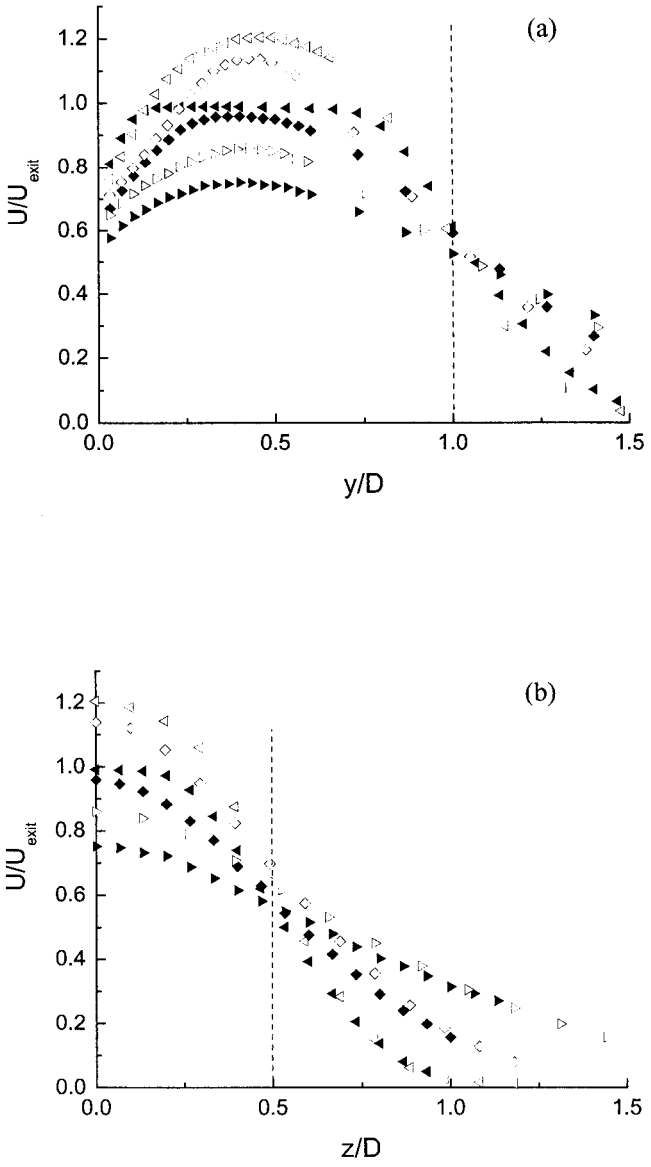

Figure 5.36: Profiles of the mean streamwise velocity measured (a) along the jet centerline and (b) laterally across the jet exiting the long pipe in the near field at ◁ x/D=3, ◇ x/D=6 and ▷ x/D=10 and the wall jet exiting the contoured nozzle at corresponding locations represented by solid symbols.

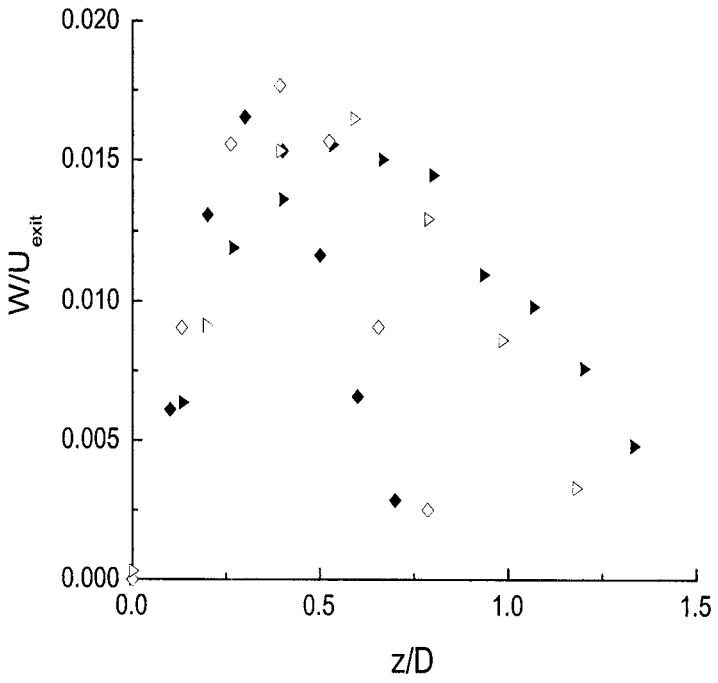

Figure 5.37: Profiles of the mean lateral velocity of the wall jet exiting the long pipe in the near field at ◊x/D=6 and ▷ x/D=10 and the wall jet exiting the contoured nozzle at corresponding locations represented by solid symbols.

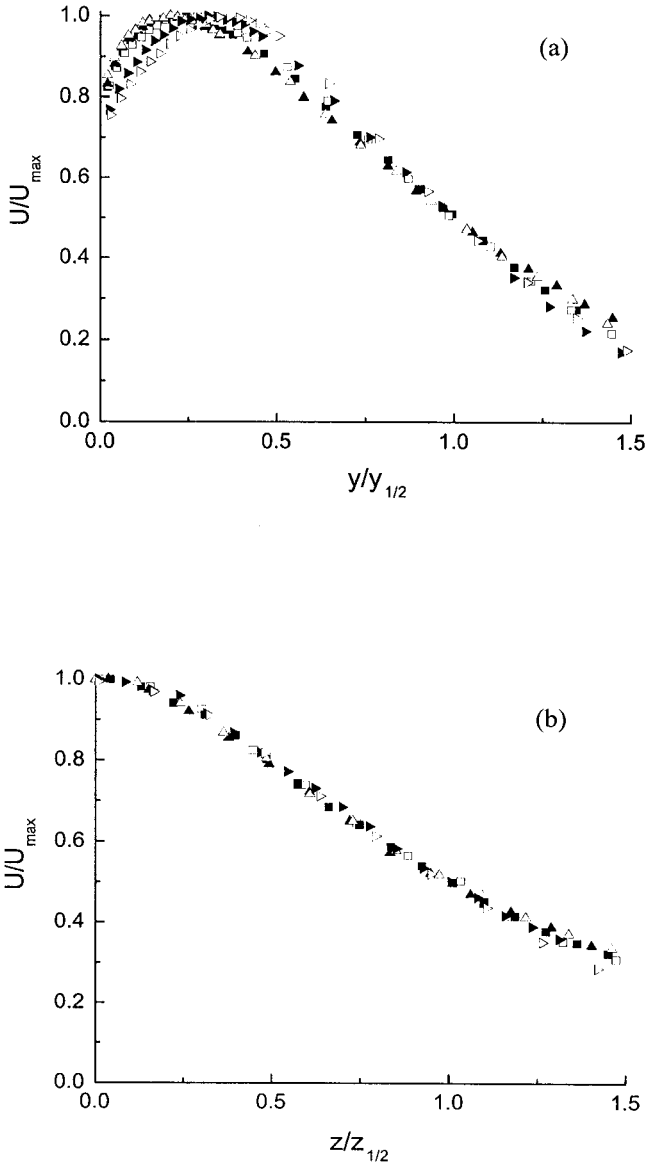

Figure 5.38: Profiles of the mean streamwise velocity measured (a) along the jet centerline and (b) laterally across the jet exiting the long pipe in the intermediate field at ▷ x/D=10, □ x/D=15 and △ x/D=20 and the wall jet exiting the contoured nozzle at corresponding locations represented by solid symbols.

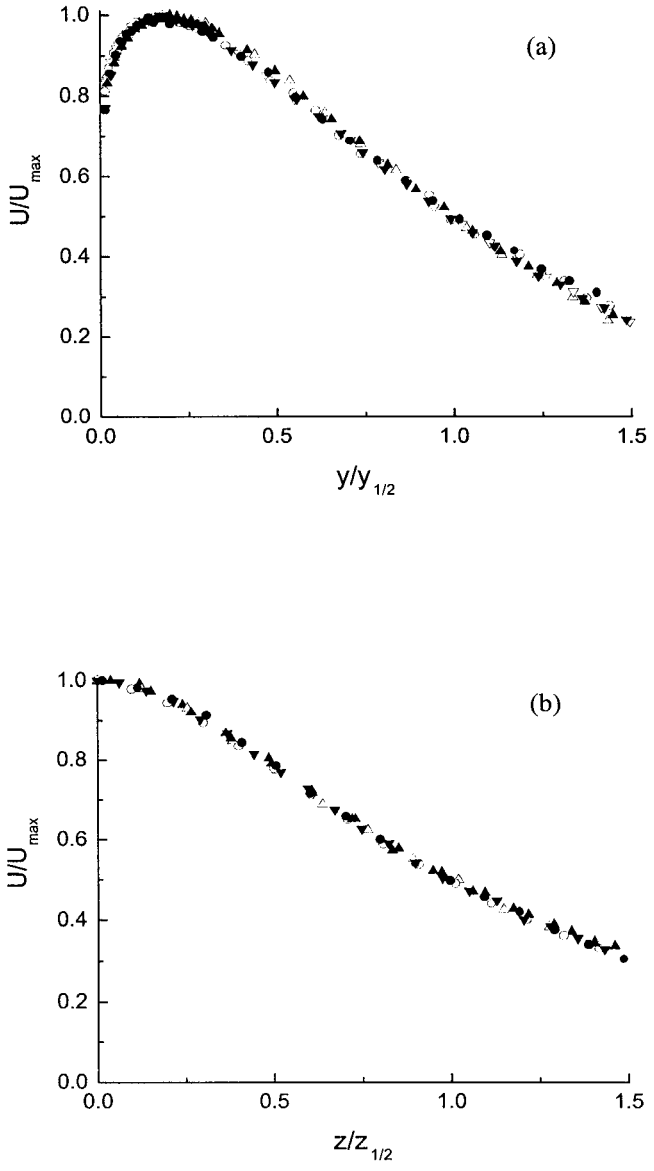

Figure 5.39: Profiles of the mean streamwise velocity measured (a) along the jet centerline and (b) laterally across the jet exiting the long pipe in the intermediate field at (a) Δ x/D=20, ∇ x/D=30 and $\bigcirc$ x/D=40 and the wall jet exiting the contoured nozzle at corresponding locations represented by solid symbols.

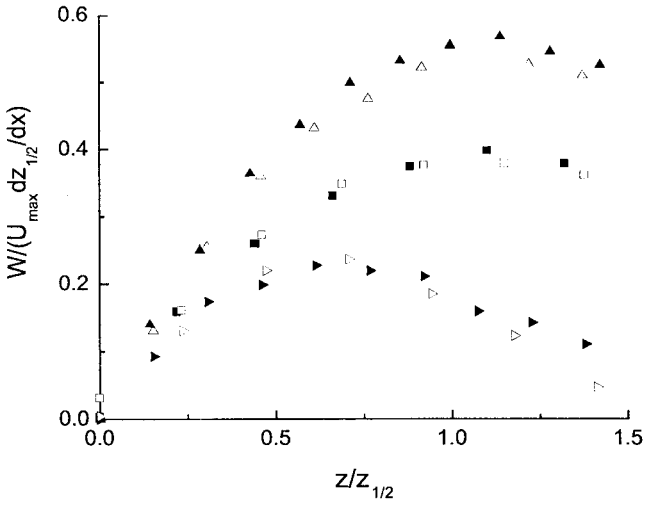

Figure 5.40: Profiles of the mean lateral velocity of the wall jet exiting the long pipe in the intermediate field at ▷ x/D=10, □ x/D=15 and △ x/D=20 and the wall jet exiting the contoured nozzle at corresponding locations represented by solid symbols.

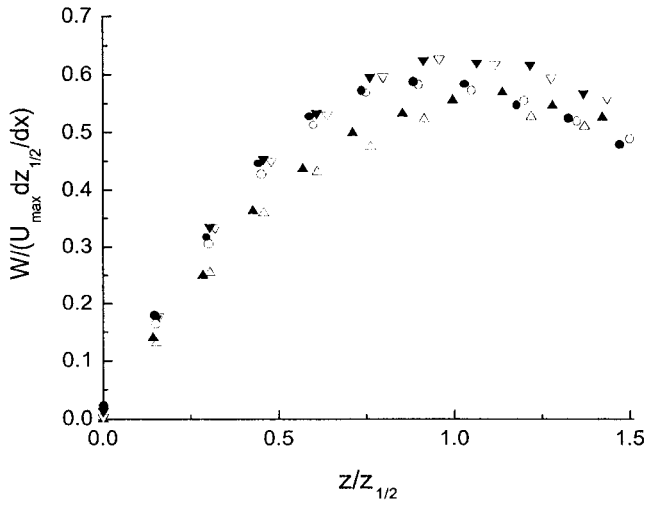

Figure 5.41: Profiles of the mean lateral velocity of the wall jet exiting the long pipe in the intermediate field at △ x/D=20, ▽ x/D=30 and ◯ x/D=40 and the wall jet exiting the contoured nozzle at corresponding locations represented by solid symbols.

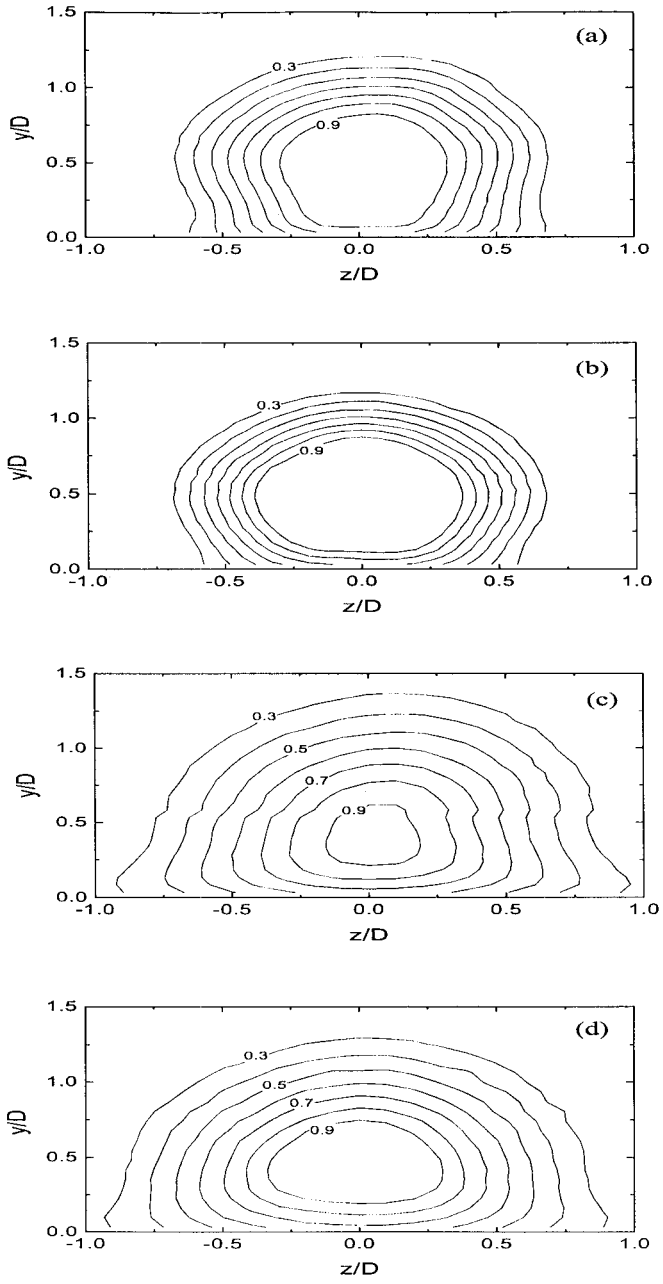

Figure 5.42: Contours of the mean streamwise velocity normalized by average exit velocity, U_{exit}, and nozzle diameter, D, in the wall jet exiting the contoured nozzle at (a) x/D=3, (c) x/D=6 and in the wall jet exiting the long pipe at (b) x/D=3, (d) x/D=6.

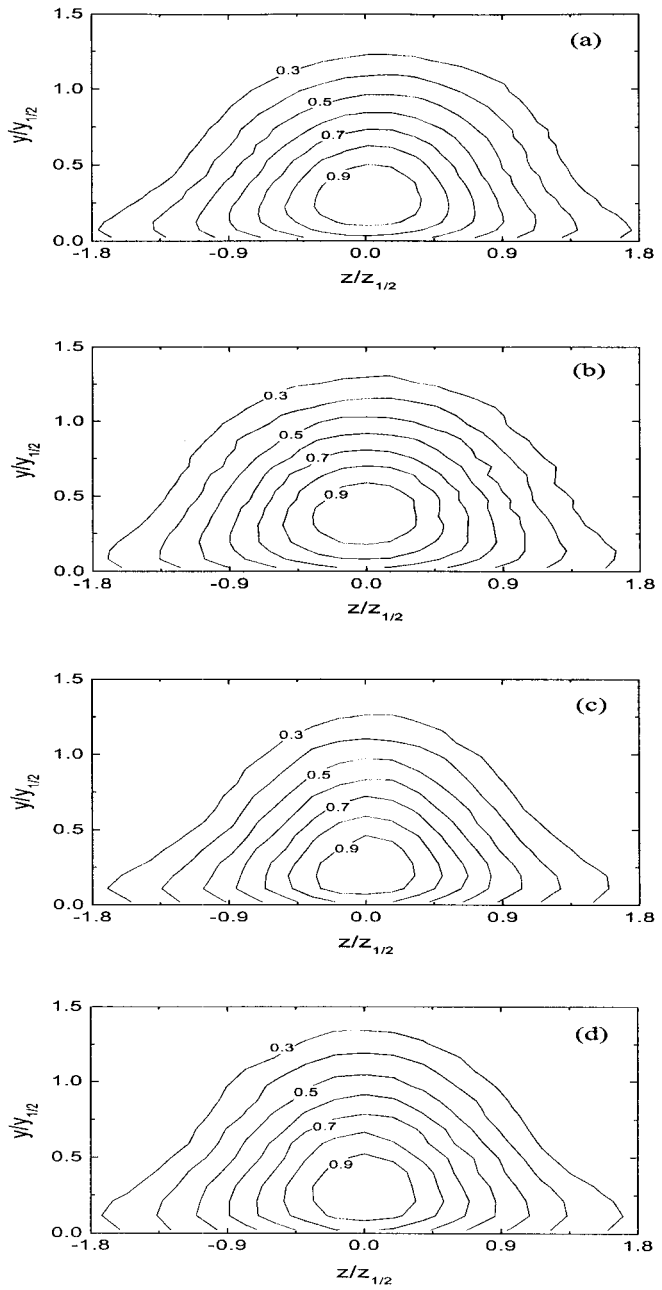

Figure 5.43: Contours of the mean streamwise velocity normalized by local maximum velocity, U_{max} and jet half-width in wall jet exiting the contoured nozzle at (a) x/D=10, (c) x/D=15 and in the wall jet exiting the long pipe at (b) x/D=10, (d) x/D=15.

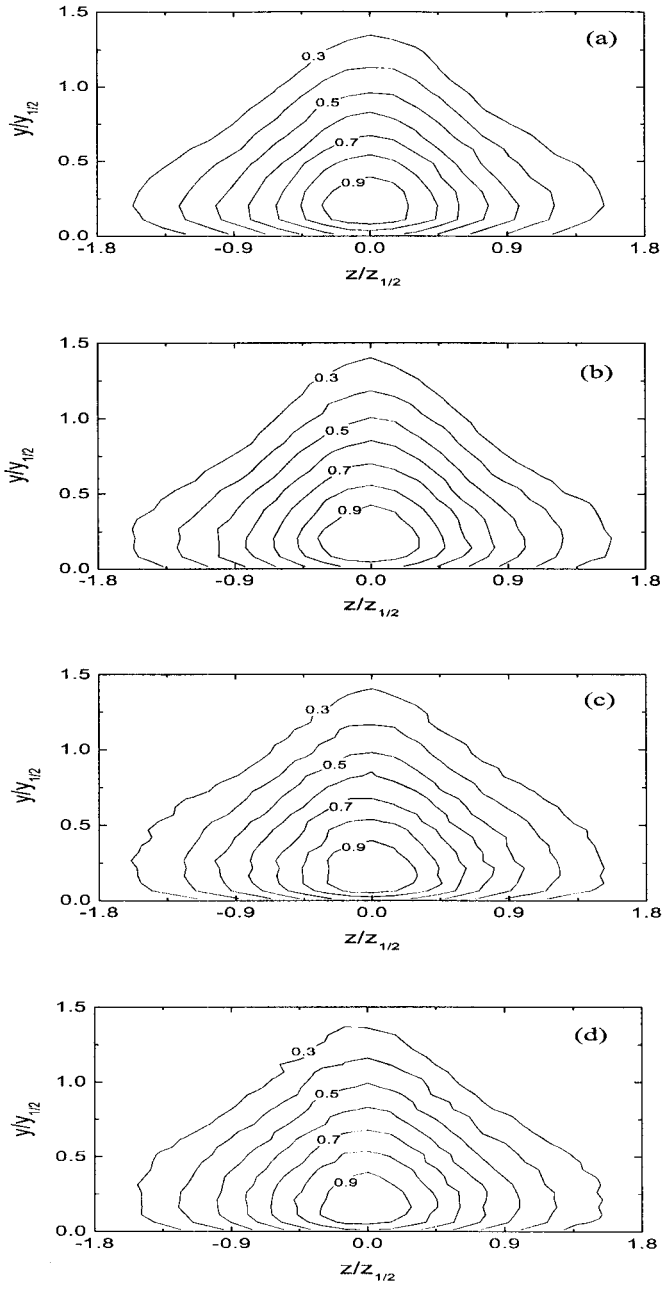

Figure 5.44: Contours of the mean streamwise velocity normalized by local maximum velocity, U_{max}, and jet half-width in the wall jet exiting the contoured nozzle at (a) x/D=30, (c) x/D=40 and in wall jet exiting the long pipe at (b) x/D=30, (d) x/D=40.

streamwise vorticity are slightly more rotated in the jet exiting the contoured nozzle. The differences in the normalized contours of the mean streamwise vorticity of the two jets are not apparent by x/D=30.

The profiles of the root mean square of fluctuating velocities, u', v' and w', and Reynolds shear stresses, $\overline{uv}$ and $\overline{uw}$, in the near field are shown in figures 5.48 - 5.52. It is clear that the profiles of both normal stresses and shear stresses differ significantly in the near field of the two jets. The level of u', v' and w' are larger in the potential core region of the wall jet exiting the long pipe because the turbulence intensity at the exit of the long pipe is much higher than the contoured nozzle jet. Reynolds shear stresses, $\overline{uv}$ and $\overline{uw}$, are approximately zero in the potential core region in the wall jet exiting the contoured nozzle causing the values of $\overline{uv}$ and $\overline{uw}$ in the near field of this wall jet are smaller. The profiles of root mean square of fluctuating velocities and Reynolds shear stresses measured in the intermediate field are shown in figures 5.53 - 5.59. Here, the profiles are again normalized using similarity variables. It is clear that the difference in the profiles of u' in the two jets is not apparent beyond x/D=10, but the differences in the profiles of v', w', $\overline{uv}$ or $\overline{uw}$ extend to the intermediate field. In particular, the differences in profiles of v', w', $\overline{uv}$ or $\overline{uw}$ in the two jets mainly occurs in the central region $0 < y/y_{1/2} \leq 1$ along the jet centerline and $0 < z/z_{1/2} \leq 1$ across the jet from x/D=10 to 20. After x/D=20 the differences are significantly reduced and are not apparent by x/D=30. It should be noted that the value of w' is larger for the wall jet exiting the long pipe jet at x/D=10 if normalized by the average jet exit velocity as shown in figure 5.50, but is smaller when it is normalized using the local maximum velocity as shown in figure 5.55. The level of $\overline{uv}$ shown in figure 5.56 also become smaller at x/D=10 and 15 for the wall jet exiting the long pipe if normalized by the similarity variables, $U_{max}^2 dy_{1/2}/dx$. Thus, part of the difficulty in interpreting differences in profiles of turbulent stresses in the region $x/D \leq 20$ is determining the correct velocity scale to use.

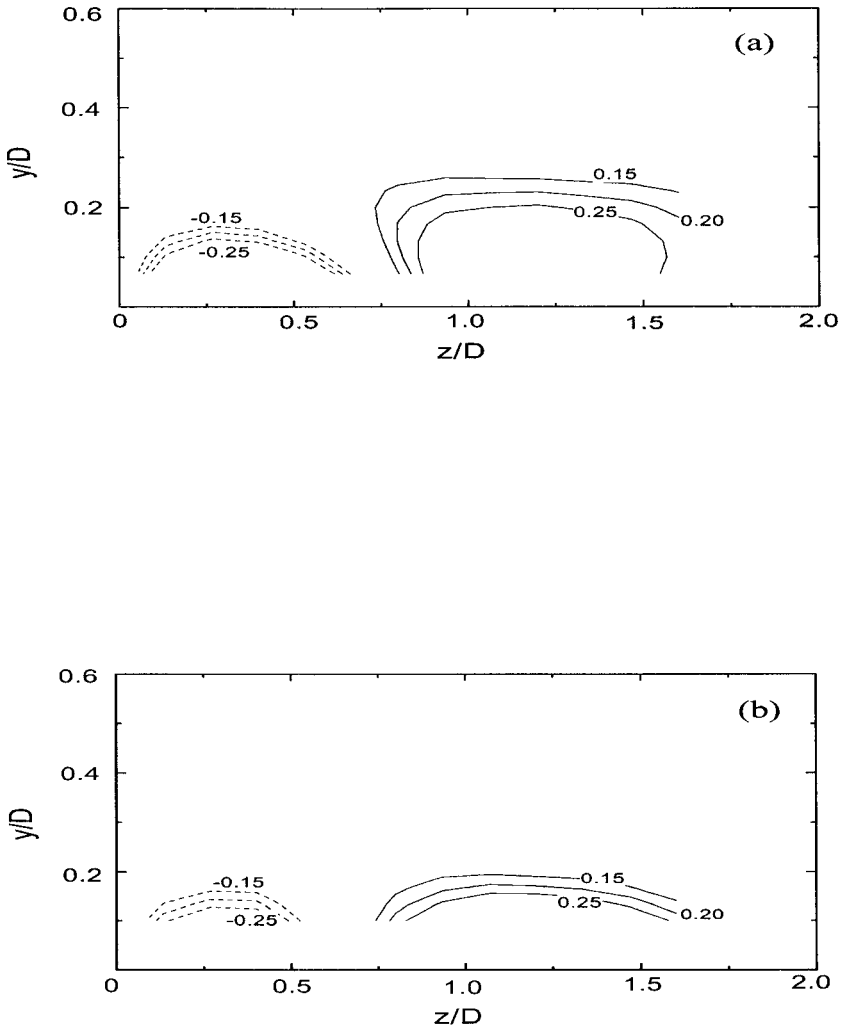

Figure 5.45: Contours of the mean streamwise vorticity normalized by the average exit velocity, U_{exit}, and nozzle diameter, D, at x/D=6 (a) in the wall jet exiting the contoured nozzle and (b) in the wall jet exiting the long pipe.

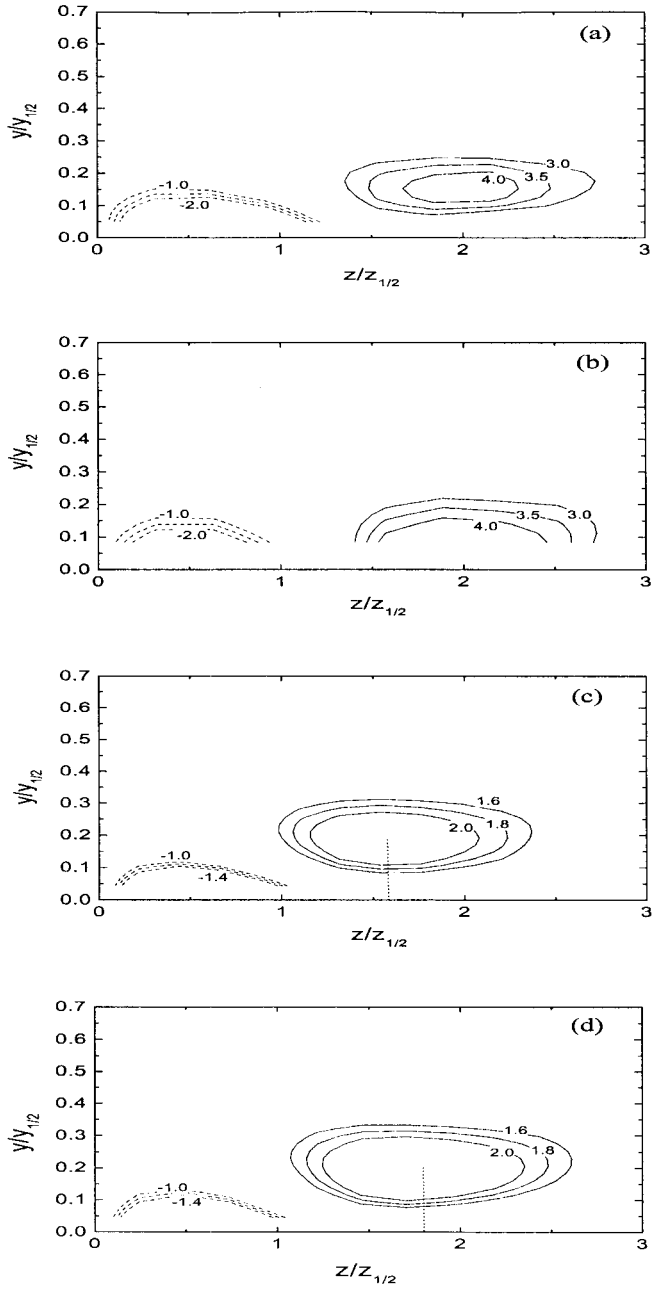

Figure 5.46: Contours of the mean streamwise vorticity normalized using similarity variables, $(U_{max} dz_{1/2}/dx)/y_{1/2}$, and the jet half-width in the intermediate field of the wall jet exiting the contoured nozzle at (a) x/D=10, (c) x/D=15 and the wall jet exiting the long pipe at (b) x/D=10, (d) x/D=15.

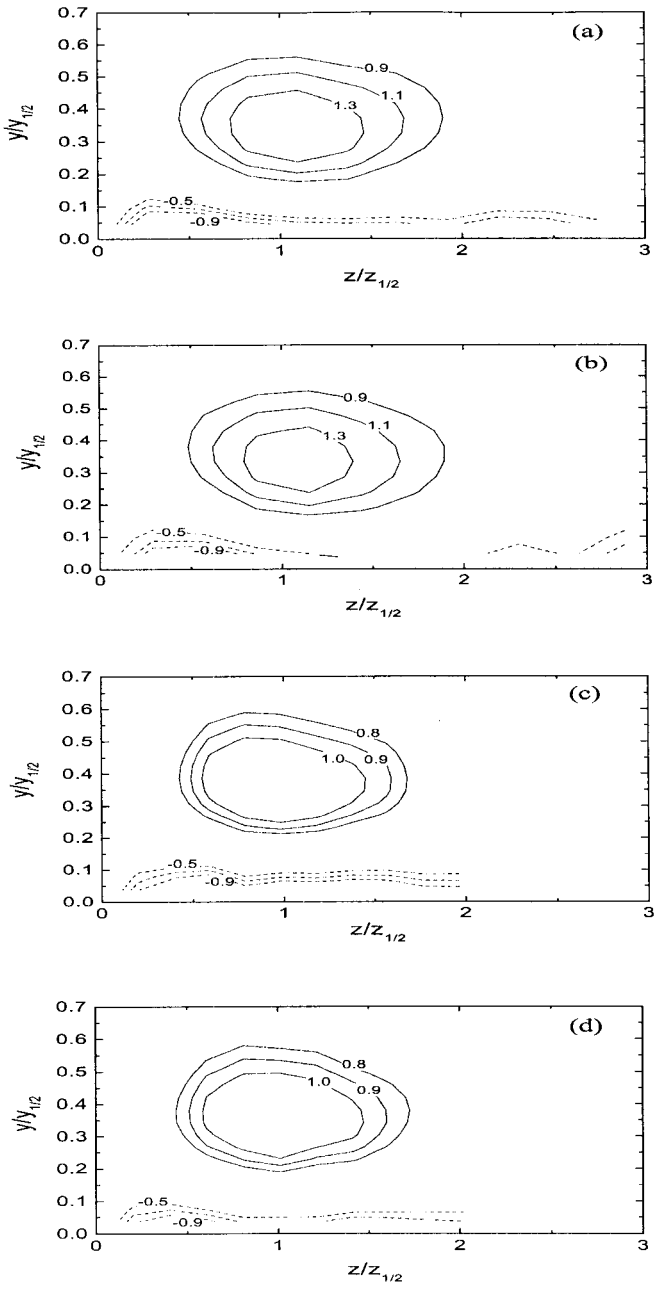

Figure 5.47: Contours of the mean streamwise vorticity normalized using similarity variables, $(U_{max} dz_{1/2}/dx)/y_{1/2}$, and the jet half-width in the intermediate field of the wall jet exiting the contoured nozzle at (a) x/D=30, (c) x/D=40 and the wall jet exiting the long pipe at (b) x/D=30, (d) x/D=40.

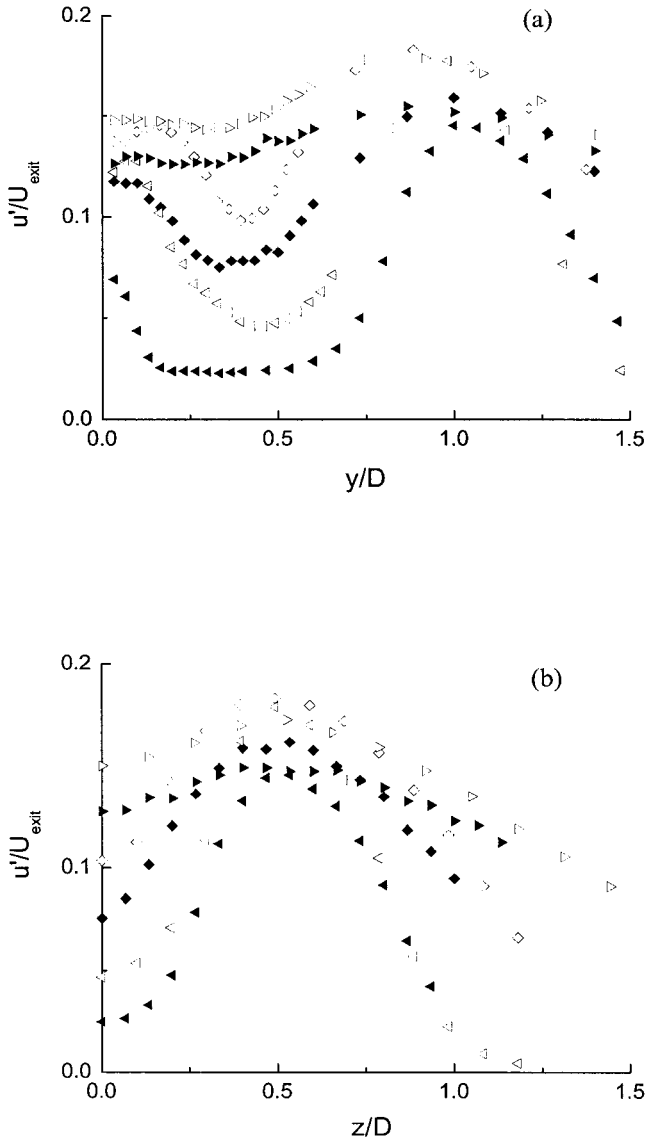

Figure 5.48: Profiles of the root mean square of the streamwise fluctuating velocity, u', measured (a) along the jet centerline and (b) laterally across the jet exiting the long pipe in the near field at ◁ x/D=3, ◇ x/D=6 and ▷ x/D=10 and the wall jet exiting the contoured nozzle at corresponding locations represented by solid symbols.

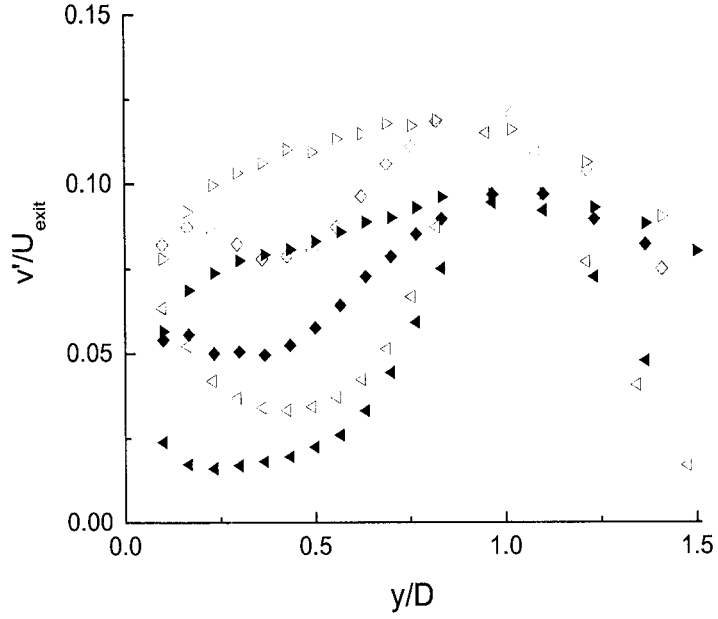

Figure 5.49: Profiles of the root mean square of the vertical fluctuating velocity, v', measured in the near field of the wall jet exiting the long pipe at ◁ x/D=3, ◇ x/D=6 and ▷ x/D=10 and the wall jet exiting the contoured nozzle at corresponding locations represented by solid symbols.

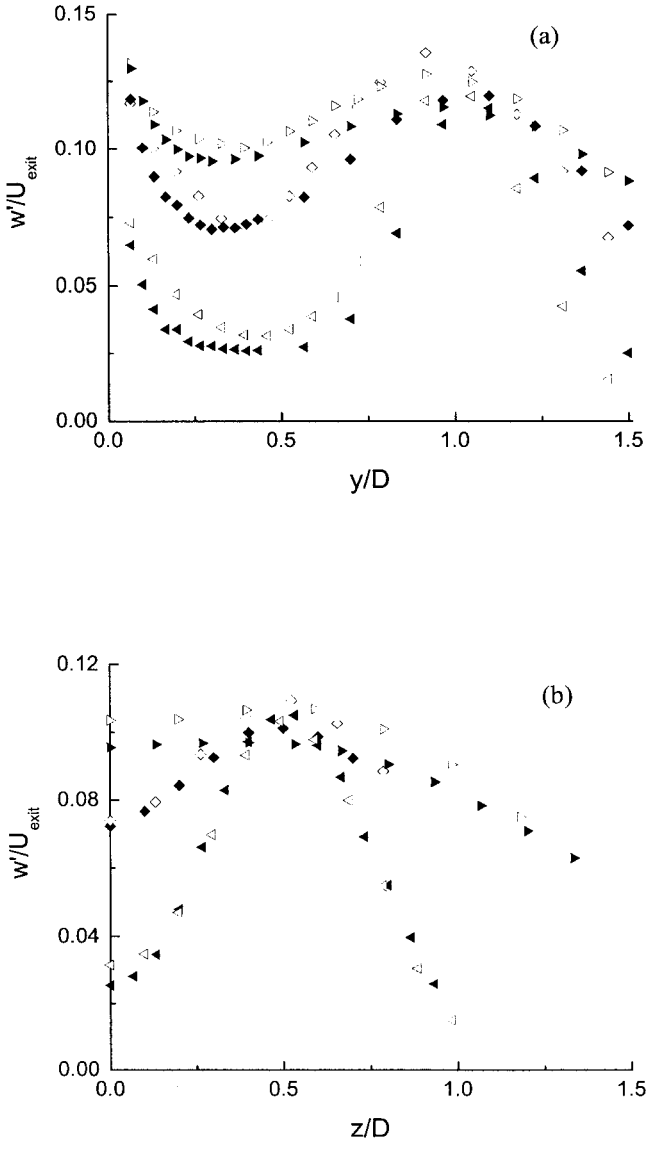

Figure 5.50: Profiles of the root mean square of the lateral fluctuating velocity, w', measured (a) along the jet centerline and (b) laterally across the jet exiting the long pipe in the near field at ◁ x/D=3, ◇ x/D=6 and ▷ x/D=10 and the wall jet exiting the contoured nozzle at corresponding locations represented by solid symbols.

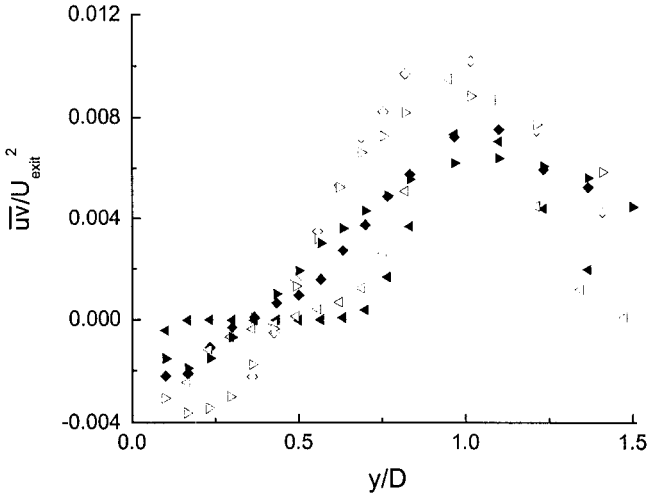

Figure 5.51: Profiles of Reynolds stress, $\overline{uv}$, measured in the near field of the wall jet exiting the long pipe at ◁ x/D=3, ◇x/D=6 and ▷ x/D=10 and the wall jet exiting the contoured nozzle at corresponding locations represented by solid symbols.

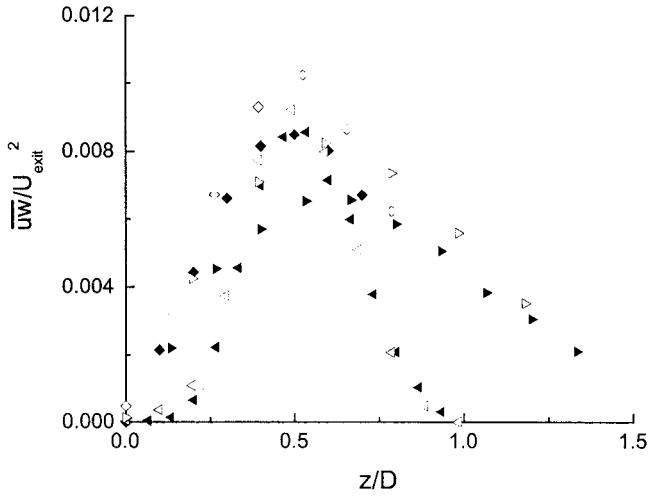

Figure 5.52: Profiles of Reynolds stress, $\overline{uw}$, measured in the near field of the wall jet exiting the long pipe at ◁ x/D=3, ◇x/D=6 and ▷ x/D=10 and the wall jet exiting the contoured nozzle at corresponding locations represented by solid symbols.

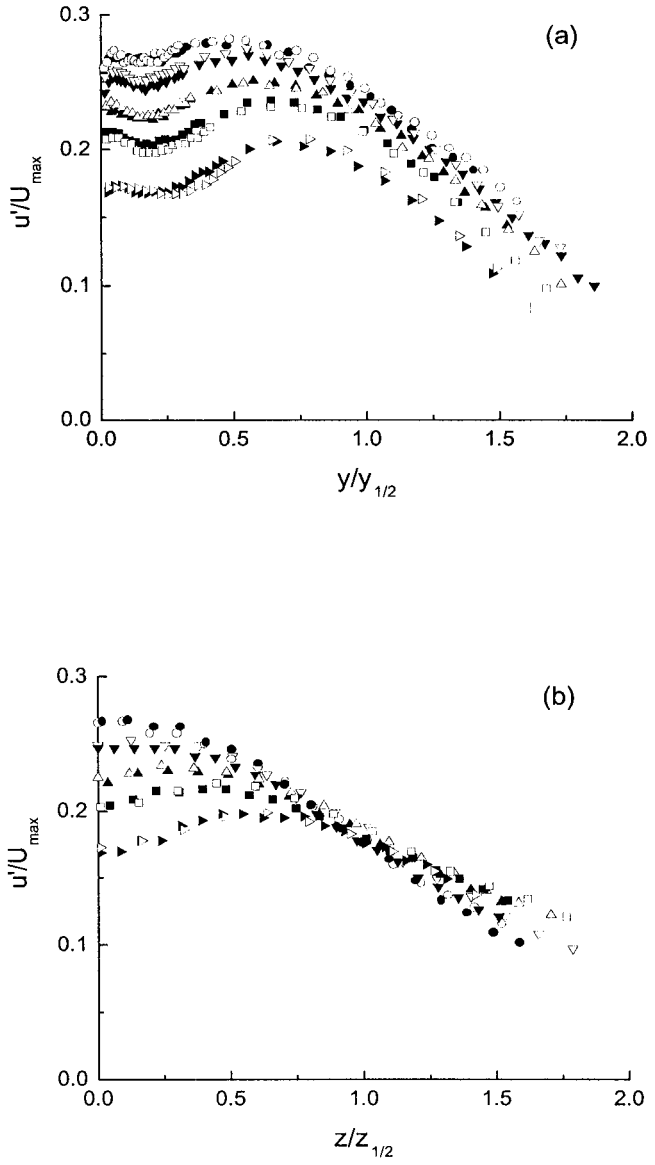

Figure 5.53: Profiles of the root mean square of the streamwise fluctuating velocity, u', measured (a) along the jet centerline and (b) laterally across the jet exiting the long pipe in the intermediate field at ▷ x/D=10, □ x/D=15, △ x/D=20, ▽ x/D=30 and ◯ x/D=40 and the wall jet exiting the contoured nozzle at corresponding locations represented by solid symbols.

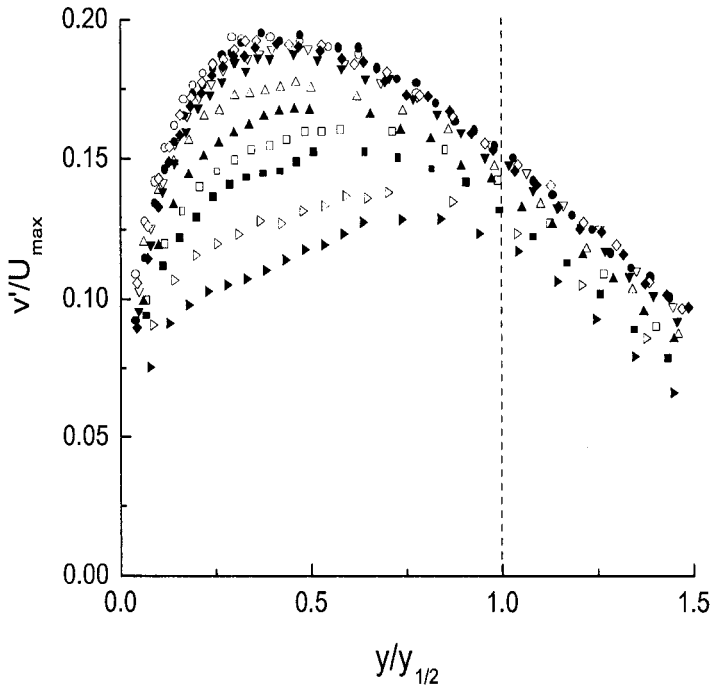

Figure 5.54: Profiles of the root mean square of the vertical fluctuating velocity, v', measured in the intermediate field of wall jet exiting the long pipe at ▷ x/D=10, □ x/D=15, △ x/D=20, ▽ x/D=30, ◇ x/D=35 and ○ x/D=40 and the wall jet exiting the contoured nozzle at corresponding locations represented by solid symbols.

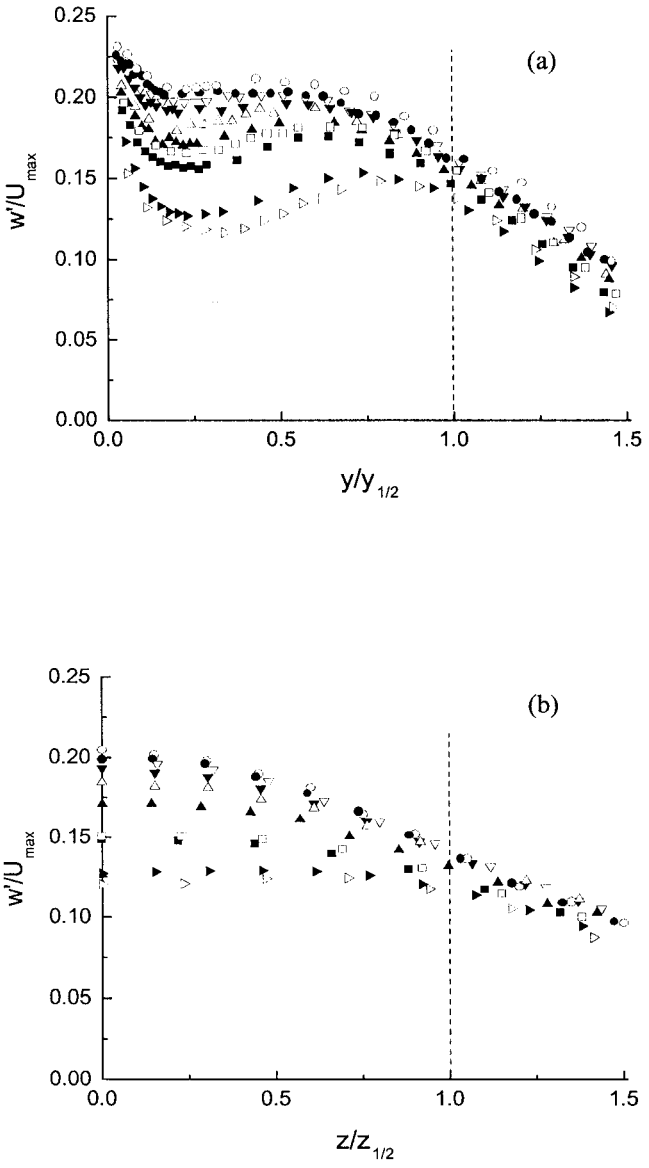

Figure 5.55: Profiles of the root mean square of the lateral fluctuating velocity, w', measured (a) along the jet centerline and (b) laterally across the jet exiting the long pipe in the intermediate field at ▷ x/D=10, □ x/D=15, △ x/D=20, ▽ x/D=30 and ◯ x/D=40 and the wall jet exiting the contoured nozzle at corresponding locations represented by solid symbols.

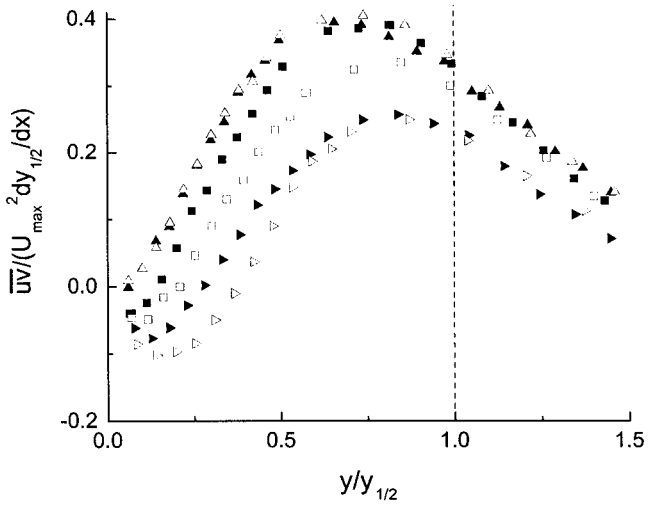

Figure 5.56: Profiles of Reynolds shear stresses, $\overline{uv}$, measured in the intermediate field of the wall jet exiting the long pipe at ▷ x/D=10, □ x/D=15, △ x/D=20 and the wall jet exiting the contoured nozzle at corresponding locations represented by solid symbols.

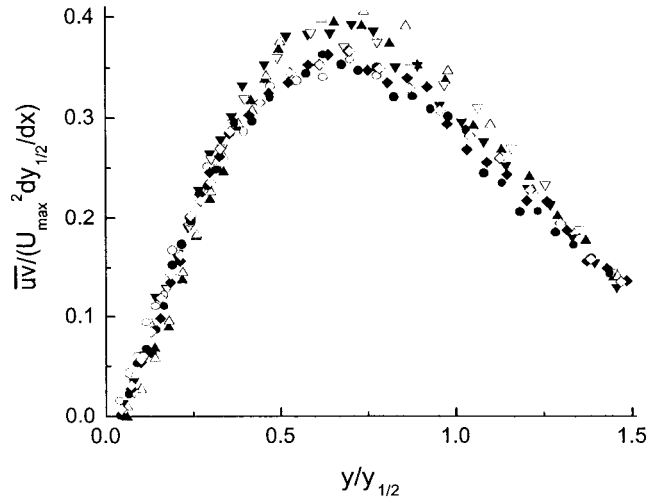

Figure 5.57: Profiles of Reynolds shear stresses, $\overline{uv}$, measured in the intermediate field of the wall jet exiting the long pipe at △ x/D=20, ▽ x/D=30, ◇ x/D=35 and ○ x/D=40 and the wall jet exiting the contoured nozzle at corresponding locations represented by solid symbols.

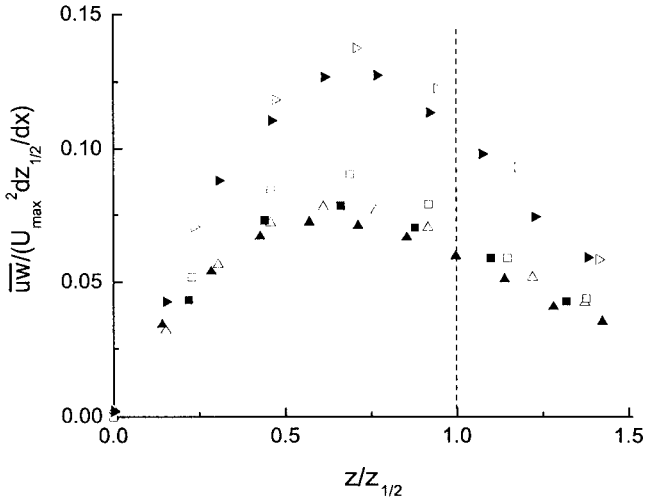

Figure 5.58: Profiles of Reynolds shear stresses, $\overline{uw}$, measured in the intermediate field of the wall jet exiting the long pipe at ▷ x/D=10, □ x/D=15, △ x/D=20 and the wall jet exiting the contoured nozzle at corresponding locations represented by solid symbols.

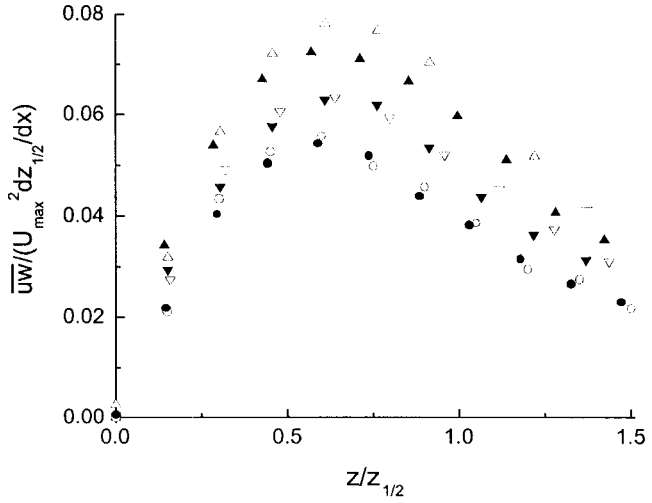

Figure 5.59: Profiles of Reynolds shear stresses, $\overline{uw}$, measured in the intermediate field of the wall jet exiting the long pipe at △ x/D=20, ▽ x/D=30 and ◯ x/D=40 and the wall jet exiting the contoured nozzle at corresponding locations represented by solid symbols.

5.3 Effect of Boundary Conditions

The measurements in this investigation indicate that the growth rates of the three-dimensional wall jets in the intermediate field are the similar for the contoured nozzle and the long pipe. This differs significantly from the results reported by Abrahamsson et al. [1]. The results of Eriksson et al. [15] suggested that one possible explanation for the difference could be differences in the boundary conditions. Their results, however, were essentially qualitative since they were based on flow visualization. Thus, a further investigation of the effect of the boundary conditions was initiated to determine if this could explain the difference in the grow rates observed in the previous investigations. This has been accomplished by performing the measurements for 3 cases summarized in table 3.1 to examine the effect of the presence of a wall behind the nozzle, change in size of this wall or the room and the misalignment of the horizontal plate on the development of the three-dimensional wall jet.

5.3.1 Effect of the Presence of a Wall Behind the Nozzle

The effect of a wall behind the nozzle was examined by measuring the wall jet exiting the 38.7 mm diameter long pipe with and without a wall behind the nozzle. The Reynolds number at the jet exit for both cases was 108,000. A comparison of the decay of the maximum streamwise velocity and the vertical and lateral half-widths of the jet are shown in figures 5.60 and 5.61. It is clear that the presence of a wall behind the nozzle does not have a significant effect on the lateral half-width of the jet. There is a small difference in the decay of the maximum velocity and the vertical half-width, i.e., the local maximum velocity and the vertical half-width in the wall jet without a wall behind the nozzle are 1-2% smaller and 1-2% larger than those of the wall jet with this wall respectively, but these differences fall in the range of the experimental uncertainty.

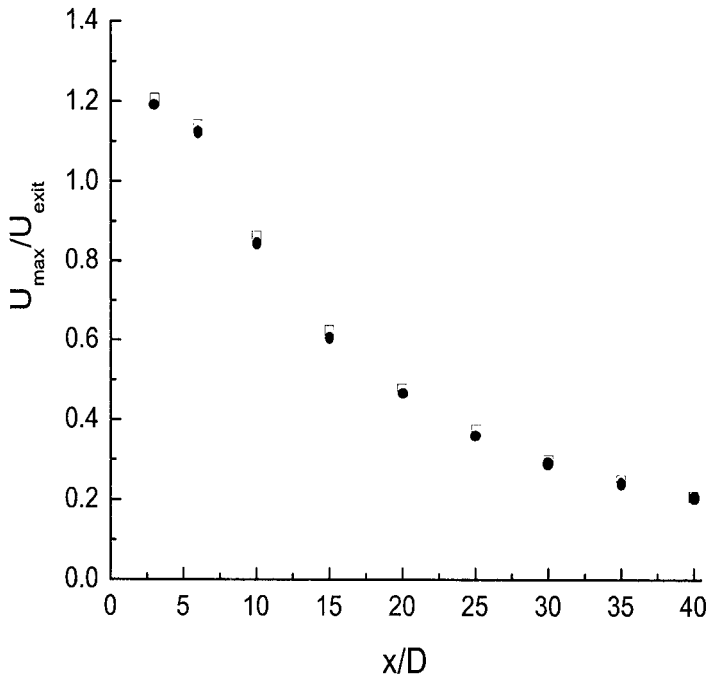

Figure 5.60: The decay of the local maximum streamwise velocity of the wall jets exiting the 38.7 mm diameter pipe □ with a wall behind the nozzle and • without this wall.

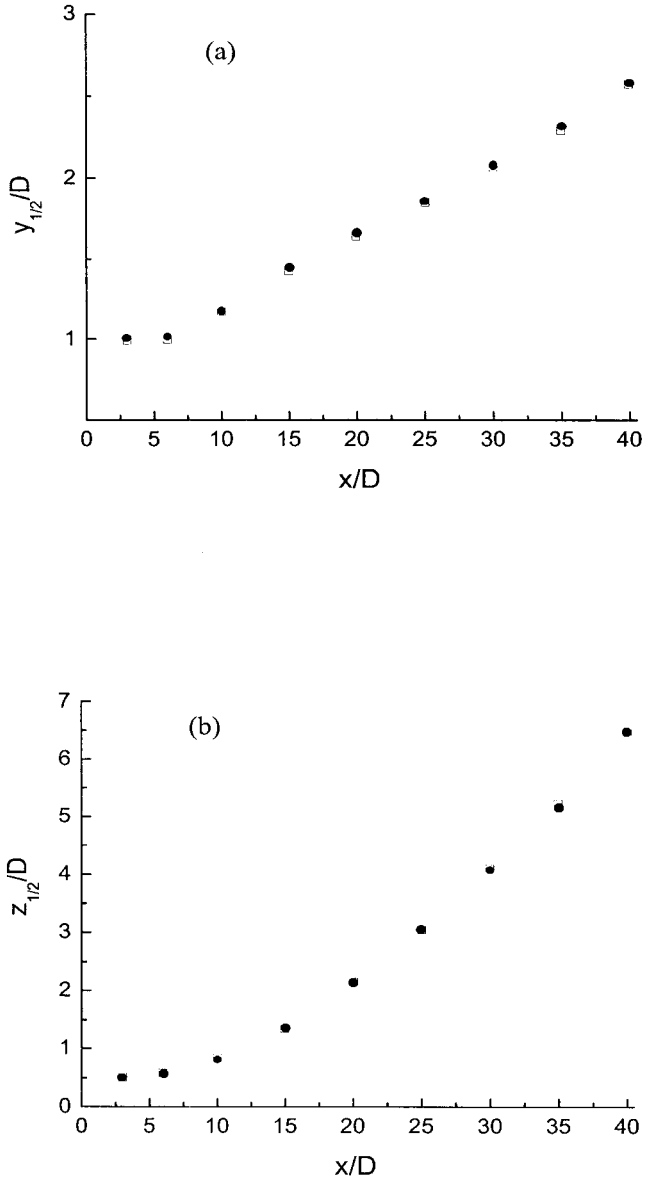

Figure 5.61: The development of (a) the vertical half-width and (b) the lateral half-width of the wall jets exiting the 38.7 mm diameter pipe □ with a wall behind the nozzle and • without this wall.

The profiles of mean streamwise velocity, U, and the profiles of root mean square of streamwise fluctuating velocity, u', are shown in figures 5.62 - 5.65. Here, the profiles of the mean streamwise velocity and root mean square of fluctuating velocity in near field have been normalized by the average jet exit velocity, U_{exit}, and the nozzle diameter, D, while these profiles in the intermediate field have been normalized by the local maximum velocity and jet half-widths. It appears that the presence of a wall behind the nozzle does not have a significant effect on the profiles of mean streamwise velocity and root mean square of fluctuating velocity both in near and intermediate fields.

5.3.2 Effect of Changing Size of the Wall or the Room

The measurements were also repeated for a wall jet exiting the 12.7 mm diameter long pipe to examine the effect of changing the size of the wall behind the nozzle or the room. It was not possible to accurately measure the profiles of moments in the near field so the effect of change in size of the wall behind the nozzle or the room was examined in the intermediate field. Present measurements indicate that the development of the wall jet is independent of the Reynolds number in the range of 65,000 - 108,000 so the Reynolds number of this flow was set to 65,000 to ensure the flow was incompressible. The results were compared to the measurements from the large diameter jet. Although not formally correct the jet exit velocity of the small diameter pipe was set by the extrapolation from the measurements at x/D=20 using the large diameter pipe data. A comparison of the decay of the local maximum velocity in the two jets is shown in figure 5.66. It is clear that the local maximum streamwise velocities at other streamwise locations for the jet exiting the small pipe are approximately the same as the jet exiting the large pipe indicating that the change in the size of the wall behind the nozzle or the room does not significantly affect the decay of the local maximum velocity.

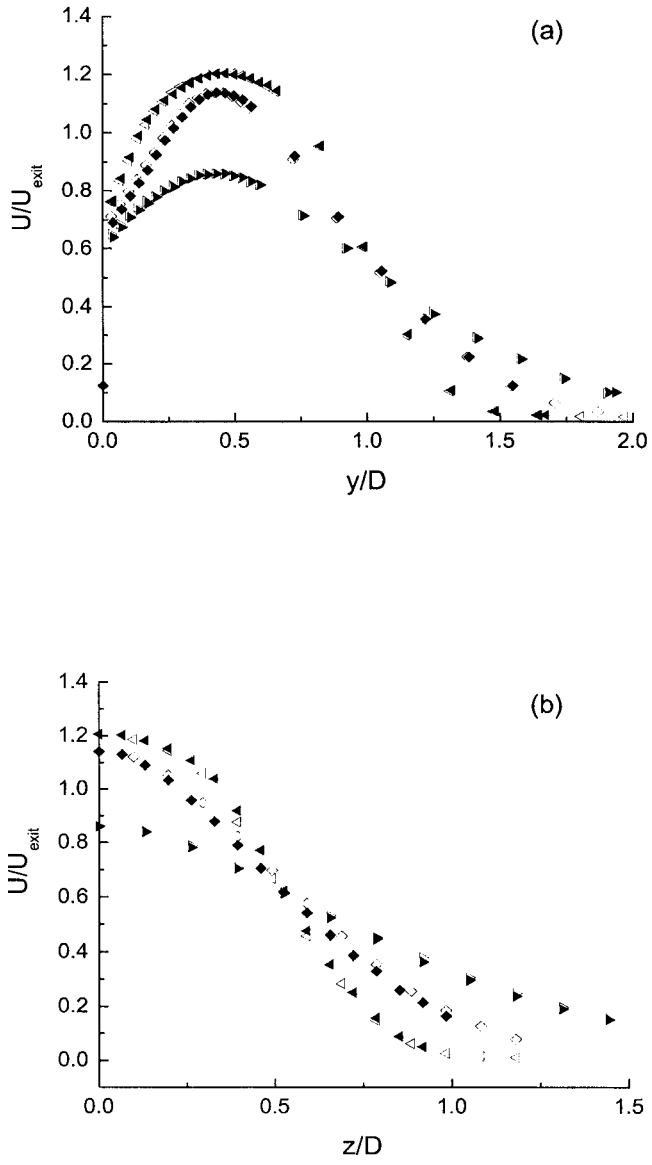

Figure 5.62: Profiles of the mean streamwise velocity measured (a) along the centerline of the jet and (b) laterally across the jet exiting the 38.7 mm diameter pipe with a wall behind the nozzle in the near field at ◁ x/D=3, ◇x/D=6, ▷x/D=10 and without this wall at corresponding locations represented by solid symbols.

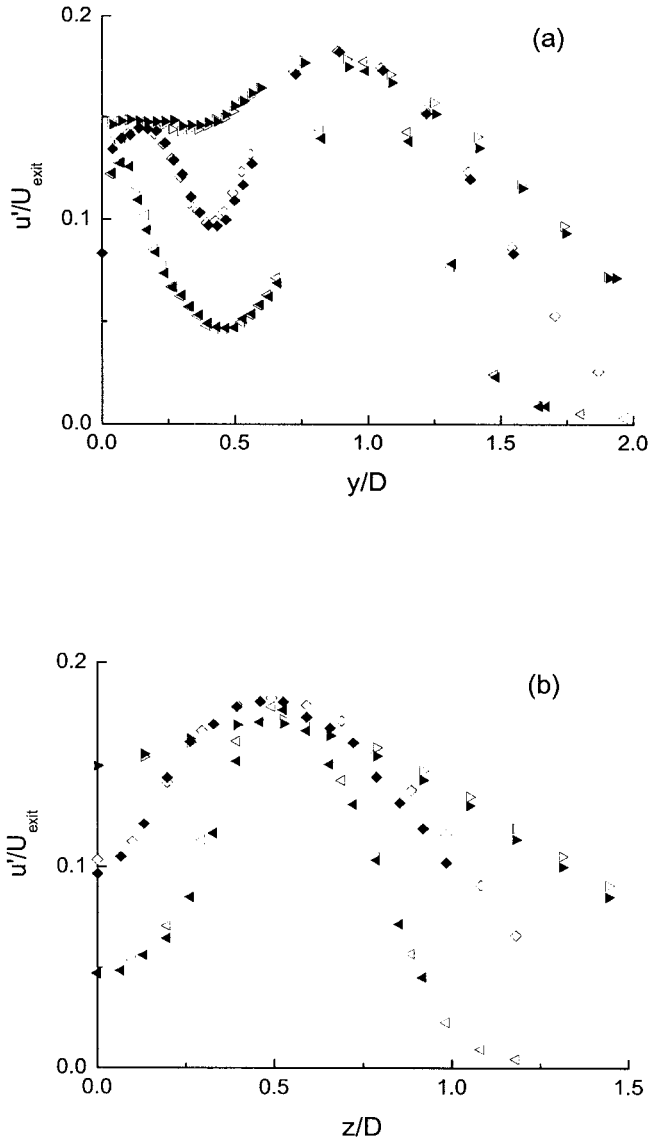

Figure 5.63: Profiles of the root mean square of the fluctuating velocity, u', measured (a) along the centerline of the jet and (b) laterally across the jet exiting the 38.7 mm diameter pipe with a wall behind the nozzle in the near field at ◁ x/D=3, ◇ x/D=6, ▷ x/D=10 and without this wall at corresponding locations represented by solid symbols.

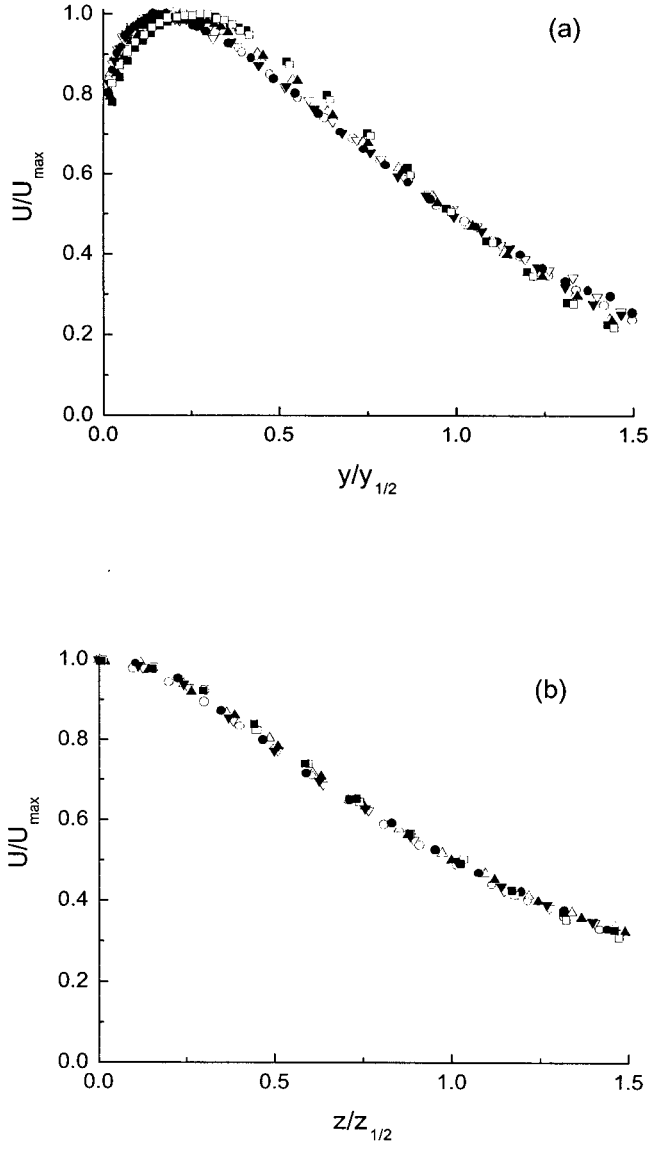

Figure 5.64: Profiles of the mean streamwise velocity measured (a) along the centerline of the jet and (b) laterally across the jet exiting the 38.7 mm diameter pipe with a wall behind the nozzle in the intermediate field at □ x/D=15, △ x/D=20, ▽ x/D=30, ◯ x/D=40 and without this wall at corresponding locations represented by solid symbols.

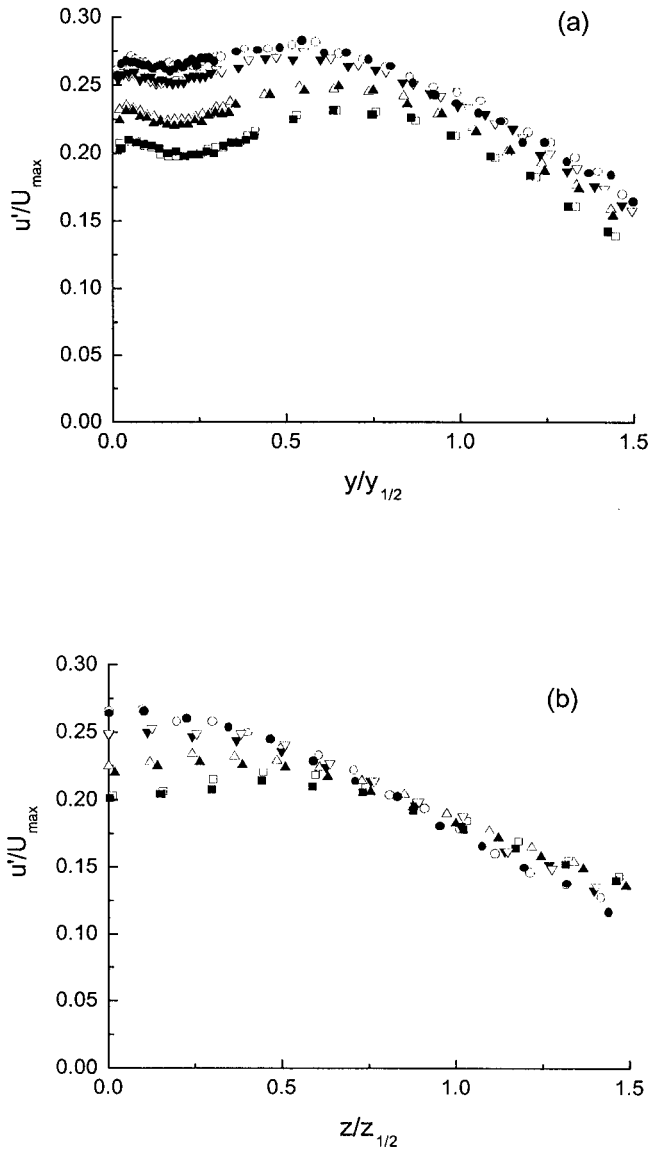

Figure 5.65: Profiles of the root mean square of the fluctuating velocity, u', measured (a) along the centerline of the jet and (b) laterally across the jet exiting the 38.7 mm diameter pipe with a wall behind the nozzle in the intermediate field at □ x/D=15, △ x/D=20, ▽ x/D=30, ◯ x/D=40 and without this wall at corresponding locations represented by solid symbols.

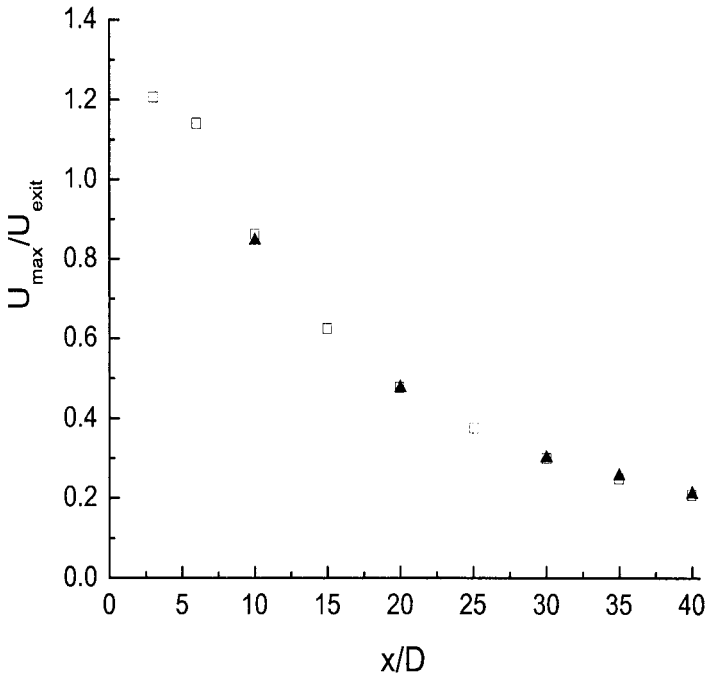

Figure 5.66: The decay of the maximum streamwise velocity of the wall jets exiting □ the 38.7 mm diameter pipe and ▲ the 12.7 mm diameter pipe.

The development of the vertical and lateral jet half-widths in the two jets are shown in figure 5.67. The lateral jet half-width of the two jets are approximately the same indicating the change in the size of the wall behind the nozzle or the room does not significantly affect the lateral growth of the jet. There appears, however, to be a difference in both the vertical half-width and vertical growth rate in the two jets. The vertical half-width in the jet exiting the small diameter pipe seems to increase faster as the flow evolves downstream. The vertical half-width and vertical growth rate in the jet exiting the small diameter pipe are approximately 3% and 7% larger than those of the wall jet exiting a large diameter pipe at x/D=40.

The profiles of the mean streamwise velocity, U, and root mean square of streamwise fluctuating velocity, u', in the intermediate field normalized by the local maximum velocity and jet half-widths are shown in figures 5.68 and 5.69. The differences in the profiles of U and u' in the two jets are not apparent indicating that the change in the size of the wall behind the nozzle or the room does not significantly affect the profiles of the streamwise moments, though the vertical half-width and vertical growth rate are different in the two jets.

5.3.3 Effect of the Misalignment of Horizontal Plate

The effect of the misalignment of the horizontal plate on the wall jet was examined by comparing the measurements in wall jets where the angle between the surface of the horizontal plate and the jet axis were approximately 0° and 1° in clockwise direction respectively. The measurements were performed in the wall jet exiting the 12.7 mm diameter pipe with the Reynolds number of 65,000 at the jet exit in the region $10 \leq x/D \leq 80$. A comparison of the development of the vertical and lateral jet half-widths in the two wall jets are shown in figure 5.70. It is clear that misalignment of the horizontal plate has the significant effect on jet half-widths in both vertical and lateral directions. A 1° misalignment, which is a large misalignment of the horizontal

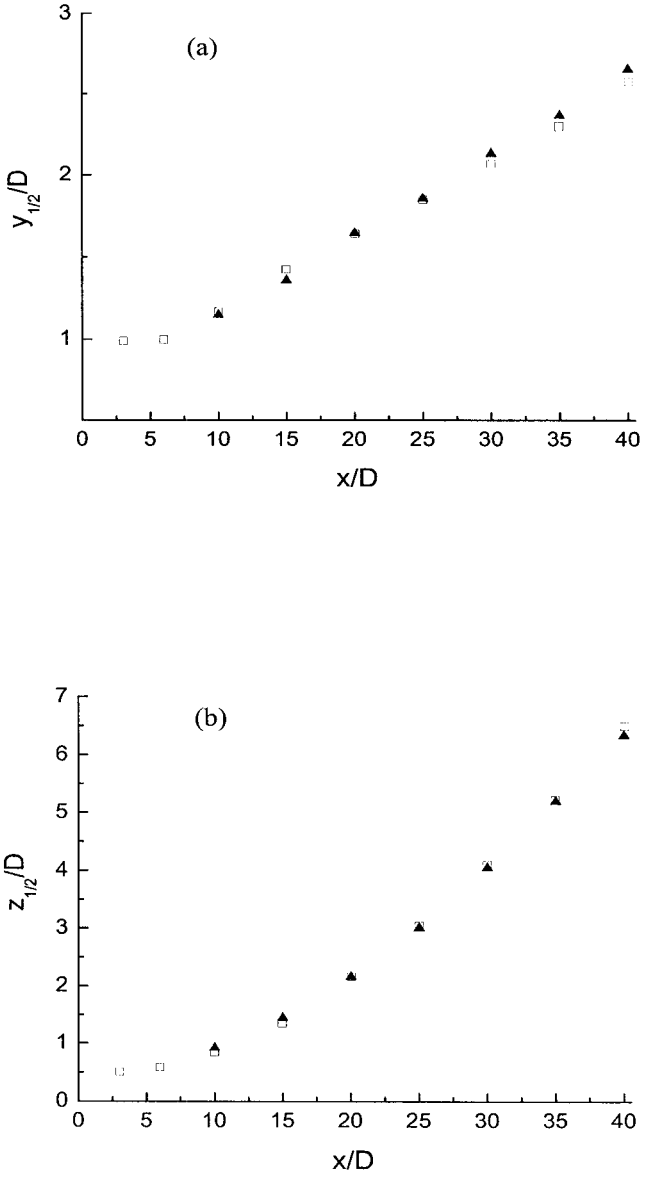

Figure 5.67: The development of (a) the vertical half-width and (b) the lateral half-width of the wall jets exiting □ the 38.7 mm diameter pipe and ▲ the 12.7 mm diameter pipe.

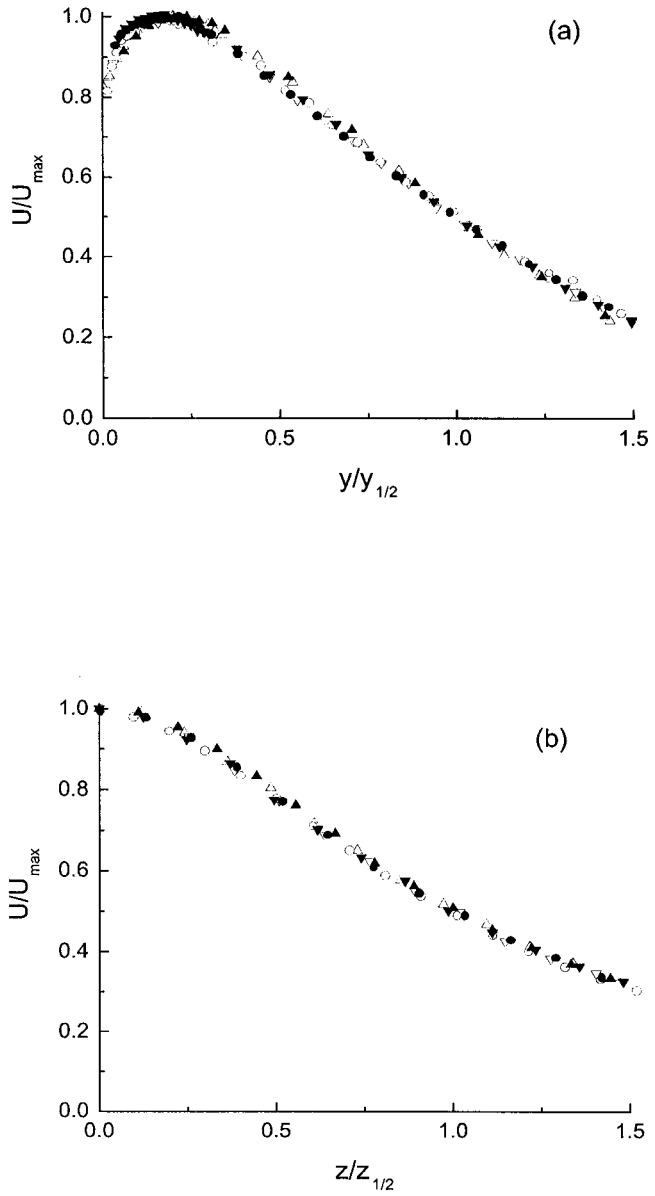

Figure 5.68: Profiles of the mean streamwise velocity measured (a) along the centerline of the jet and (b) across the jet exiting the 38.7 mm diameter pipe at △ x/D=20, ▽ x/D=30, ◯ x/D=40 and the 12.7 mm diameter pipe at corresponding locations represented by solid symbols.

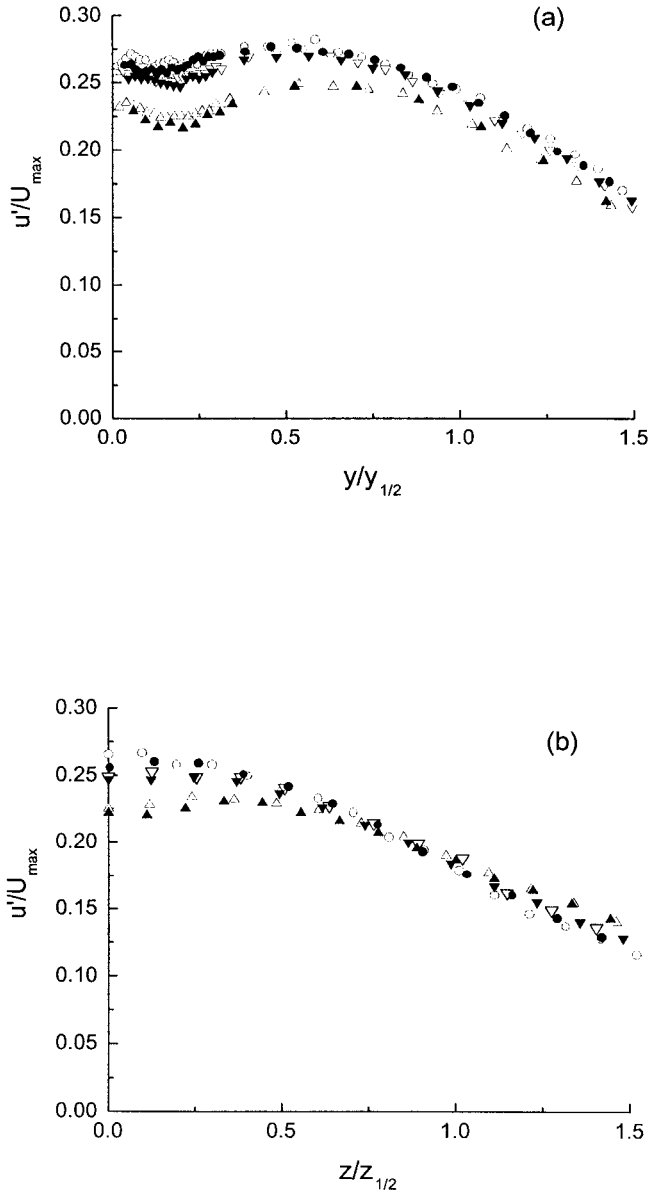

Figure 5.69: Profiles of the root mean square of the fluctuating velocity, u', measured (a) along the centerline of the jet and (b) across the jet exiting the 38.7 mm diameter pipe at $\triangle$ x/D=20, $\triangledown$ x/D=30, $\bigcirc$ x/D=40 and the 12.7 mm diameter pipe at corresponding locations represented by solid symbols.

plate, causes the vertical half-width to decrease approximately 0.3D and the lateral half-width to increase approximately 0.7D in the region $10 \leq x/D \leq 80$. However, it appears that the misalignment of the horizontal plate does not have a significant effect on the growth rates both in vertical and lateral directions.

The profiles of the mean streamwise velocity, U, and the root mean square of the streamwise fluctuating velocity, u', measured along the centerline of the jet and across the jet at the height of the maximum streamwise velocity point in the intermediate and far fields are shown in figures 5.71 and 5.72. There appears that a 1° misalignment of the horizontal plate does not have a significant effect on the profiles of the streamwise moments.

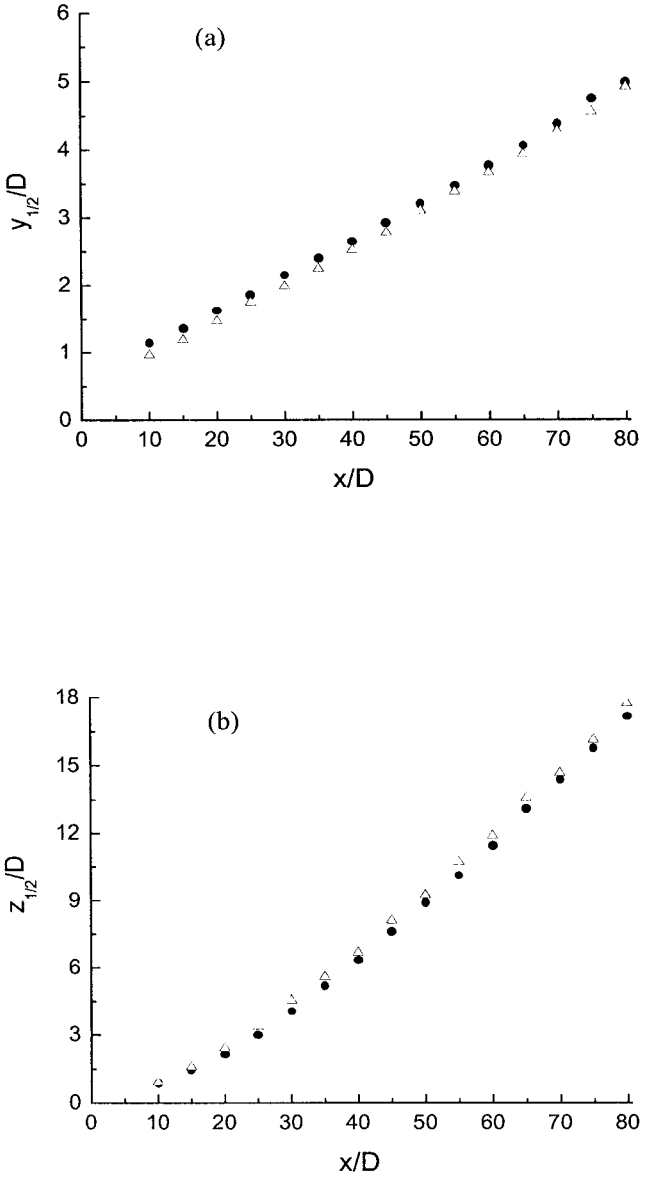

Figure 5.70: The development of (a) the vertical half-width and (b) the lateral half-width of the wall jets exiting the 12.7 mm diameter pipe • without the misalignment and △ with a 1° misalignment of the horizontal plate.

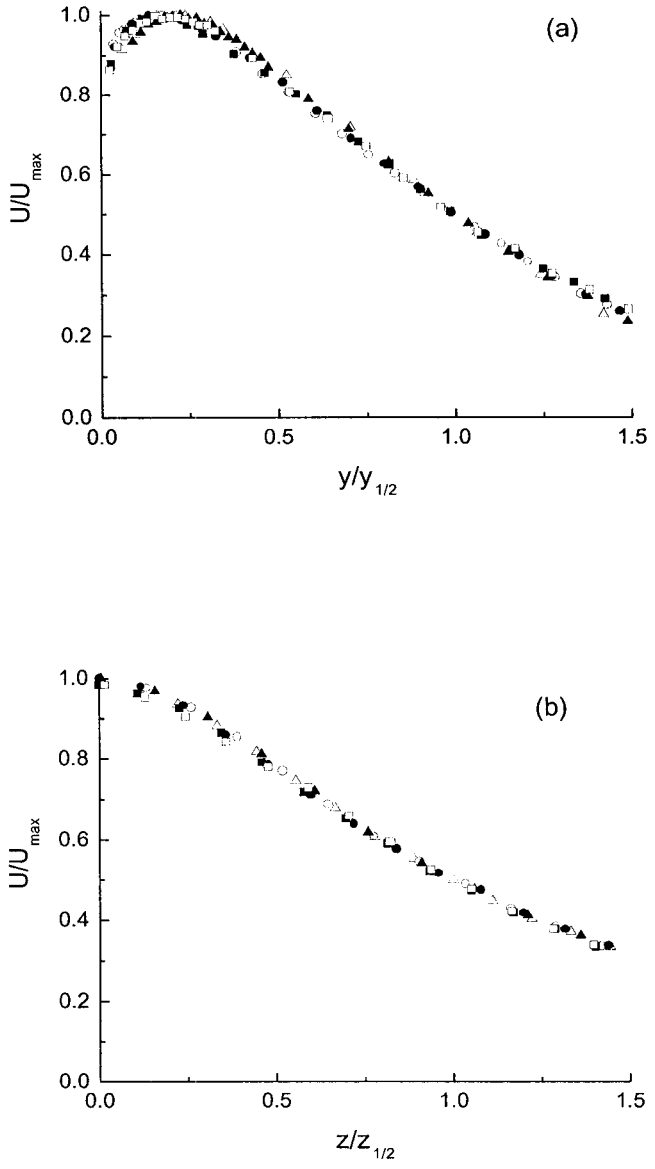

Figure 5.71: Profiles of the mean streamwise velocity measured (a) along the jet centerline and (b) across the jet exiting the 12.7 mm diameter pipe without the misalignment at Δx/D=20, $\bigcirc$x/D=40, $\square$x/D=60 and with a 1° misalignment of the horizontal plate at corresponding locations represented by solid symbols.

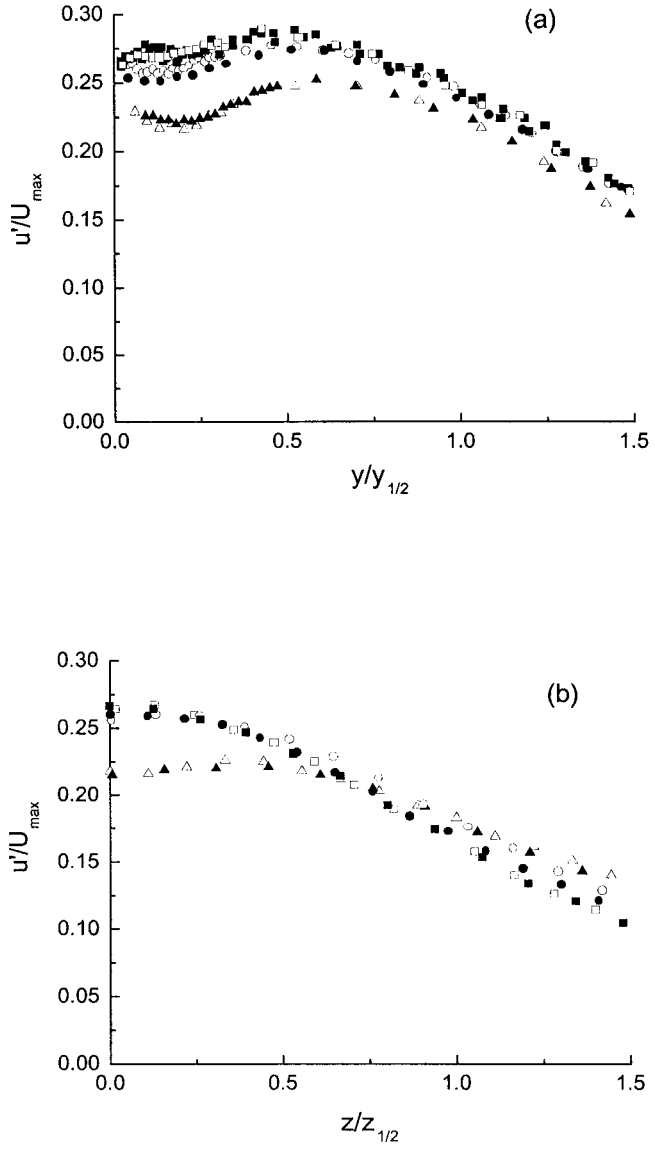

Figure 5.72: Profiles of the root mean square of the fluctuating velocity, u', measured (a) along the jet centerline and (b) across the jet exiting the 12.7 mm diameter pipe without the misalignment at Δx/D=20, $\bigcirc$x/D=40, $\square$x/D=60 and with a 1° misalignment of the horizontal plate at corresponding locations represented by solid symbols.

Chapter 6

Evolution of Large-Scale Structures

Matsuda et al. [43], Ewing and Pollard [16] and Ewing et al. [17] investigated the development of the three-dimensional wall jet in the near field and proposed a model to explain how the vortex rings developed in the near field of the jet to generate large-scale horseshoe vortex structures in the flow. The measurements of the contours of mean streamwise vorticity in the intermediate field presented here indicate that both the location and scale of the regions of streamwise vorticity are changing as the flow evolves from x/D=10 to 40. The objective here is to extend the measurements of the large-scale structures into the intermediate field to examine how the large-scale structures change in this region. This was accomplished by performing measurements of two-point, two-time correlation of the streamwise fluctuating velocity in vertical and lateral directions in the region $3 \leq x/D \leq 15$ with the Reynolds number at jet exit of 72,000 and in the region $20 \leq x/D \leq 40$ with the Reynolds number of 108,000. The measurements of correlations were performed in two rakes of single hot-wires with fixed spacing. Thus, the separation between the wires in the vertical direction relative to the vertical jet half-width, $y_{1/2}$, changed as the flow evolved downstream.

6.1 Inclination of Large-Scale Structures

Initially, the measurements of the two-point, two-time correlation in vertical direction were performed in the near field to confirm the model proposed by Ewing and Pollard [16]. The normalized correlation coefficients between the streamwise fluctuating velocity at y/D=0.45 and the velocities at y/D=0.35, y/D=0.25, y/D=0.15 and y/D=0.05 for $z/z_{1/2} = 0$ and $z/z_{1/2} = 1$ at x/D=3 and x/D=10 are shown in figures 6.1 and 6.2. It should be noted that the wire at y/D=0.45 is approximately at the center of the vortex ring. The measurements are in good agreement with the data reported by Ewing and Pollard [16]. It is clear that as the flow evolves downstream, the correlations between the velocity at y/D=0.45 and the velocities at y/D=0.05 and y/D=0.15 become negative on the centerline by x/D=10. Ewing and Pollard [16] noted that this negative correlation was consistent with the passage of a vortex structure aligned in the lateral direction between two wires. Thus, these measurements suggest the vortex structure on the centerline moves away from the wall as the flow evolves from x/D=3 to 10. Similarly, the vortex structure at the outer edge, e.g., $z/z_{1/2} = 1$, moves towards the wall as the flow travels downstream. Ewing and Pollard [16] proposed that the center of the vortex near the wall will now be convected faster than the outer edges near the wall so the vortex structure near the centerline deforms and inclines relative to the streamwise direction forming an inner horseshoe vortex. The upper part of the vortex structure near the outer edge also convects faster than its base causing the streamwise inclination at the outer edge forming a large outer horseshoe vortex as originally proposed by Matsuda et al. [43]. Ewing and Pollard [16] proposed that the legs of these two horseshoe vortices, shown in figure 2.14, were the cause of the regions of mean streamwise vorticity on each side of the centerline.

Measurements of two-point, two-time correlation of the streamwise fluctuating

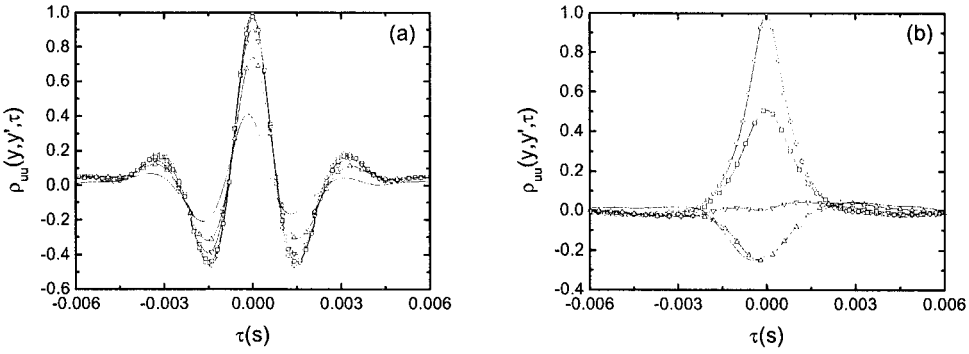

Figure 6.1: Correlation coefficient between the streamwise fluctuating velocity measured at y/D=0.45 and velocities at $-\circ$ $y'/D = 0.45$, $-\square$ $y'/D = 0.35$, $-\nabla$ $y'/D = 0.25$, $-\ \Delta$ $y'/D = 0.15$ and $-$ $y'/D = 0.05$ at (a)$z/z_{1/2} = 0$ and (b)$z/z_{1/2} = 1.0$ for x/D=3.

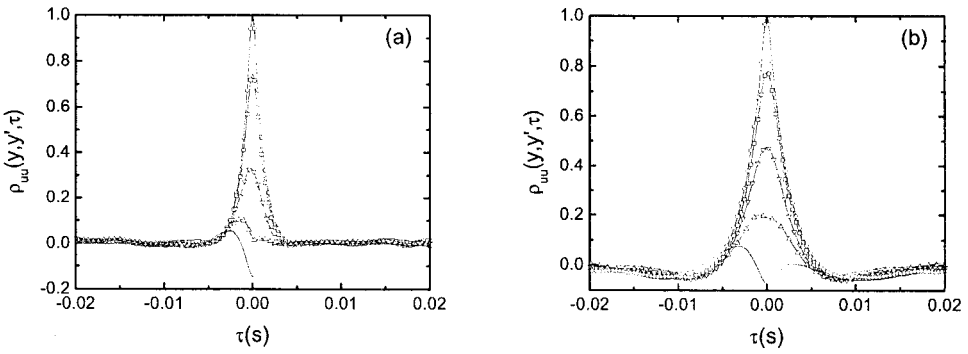

Figure 6.2: Correlation coefficient between the streamwise fluctuating velocity at y/D=0.45 and velocities at $-\circ$ $y'/D = 0.45$, $-\square$ $y'/D = 0.35$, $-\nabla$ $y'/D = 0.25$, $-\ \Delta$ $y'/D = 0.15$ and $-$ $y'/D = 0.05$ at (a)$z/z_{1/2} = 0$ and (b)$z/z_{1/2} = 1.0$ for x/D=10.

velocity in vertical direction were extended to the region $15 \leq x/D \leq 40$. The correlation coefficients between the streamwise fluctuating velocity at $y/y_{1/2} \approx 0.5$ and the other velocities at the lower positions at x/D=15 and 30 at $z/z_{1/2}$=0, 0.25, 0.5, 0.75, 1.0. 1.25 and 1.5 are shown in figures 6.3 and 6.4. It is clear that the evolution of large-scale vortex structures in the intermediate field differs significantly from the evolution of the structures in the near field. The strong negative correlations between the streamwise fluctuating velocity at $y/y_{1/2} = 0.49$ and the velocities at $y/y_{1/2} = 0.033$ and $y/y_{1/2} = 0.10$ on the jet centerline occur around τ=0 at x/D=15, while only the velocity at $y/y_{1/2} = 0.49$ and the velocity at $y/y_{1/2} = 0.023$ are negatively correlated around τ=0 at x/D=30. This suggests the inner horseshoe vortex structures are induced towards the wall as the flow evolves downstream in the intermediate field. The vertical correlation measurements at lateral positions off the centerline also suggest that the inner horseshoe vortex structures are moving towards the wall and outer vortex structures are moving relative towards the centerline of the jet that is consistent with the observation in the measurements of mean streamwise vorticity contours. For example, the negative correlation at x/D=30 disappears before $z/z_{1/2} = 0.5$. Beyond this lateral position the correlation between streamwise fluctuating velocity at $y/y_{1/2} = 0.49$ and the velocity at $y/y_{1/2} = 0.023$ becomes positive in the region around $z/z_{1/2} = 1.0$ that corresponds to the central region of outer vortex structures indicated by measurements of contours of mean streamwise vorticity. The negative correlations at x/D=15 disappear at $z/z_{1/2} \approx 1.25$ and the correlation between the velocity at $y/y_{1/2} = 0.49$ and the velocity at $y/y_{1/2} = 0.033$ becomes positive in the central region of the outer vortex structures that is around $z/z_{1/2} = 1.5$.

It is also clear there is a significant time delay between the correlations of the streamwise fluctuating velocity at $y/y_{1/2} \approx 0.5$ and the velocities at lower positions indicating the large-scale outer horseshoe vortex structure has inclined relative to the

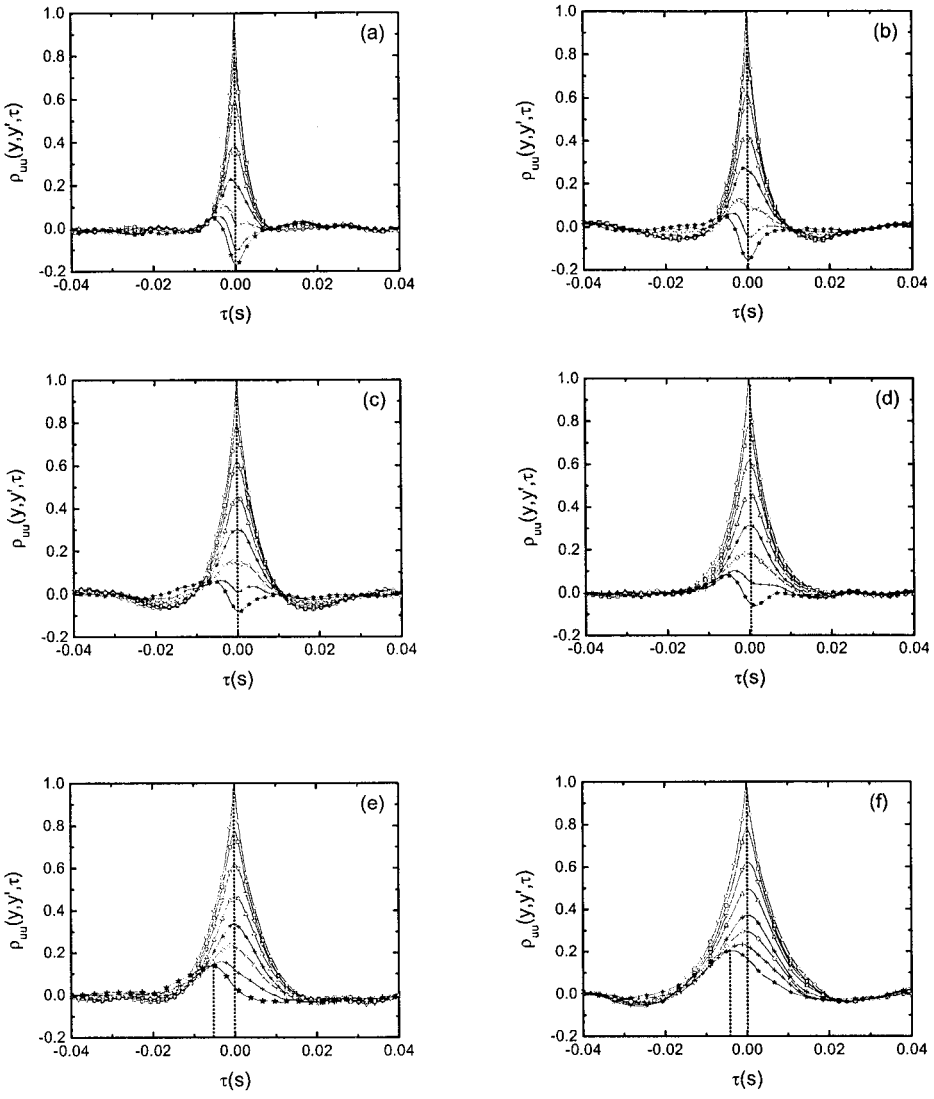

Figure 6.3: Correlation coefficient between the streamwise fluctuating velocity measured at $y/y_{1/2} = 0.49$ and velocities at $-\circ$ $y'/y_{1/2} = 0.49$, $-\square$ $y'/y_{1/2} = 0.43$, $-\triangledown$ $y'/y_{1/2} = 0.36$, $-\ \triangle$ $y'/y_{1/2} = 0.30$, $-*$ $y'/y_{1/2} = 0.23$, $-\diamond$ $y'/y_{1/2} = 0.16$, $-+$ $y/y_{1/2} = 0.10$ and $-\star$ $y'/y_{1/2} = 0.03$ at (a)$z/z_{1/2} = 0$, (b)$z/z_{1/2} = 0.5$, (c)$z/z_{1/2} = 0.75$, (d)$z/z_{1/2} = 1.0$, (e)$z/z_{1/2} = 1.25$ and (f)$z/z_{1/2} = 1.5$ for x/D=15.

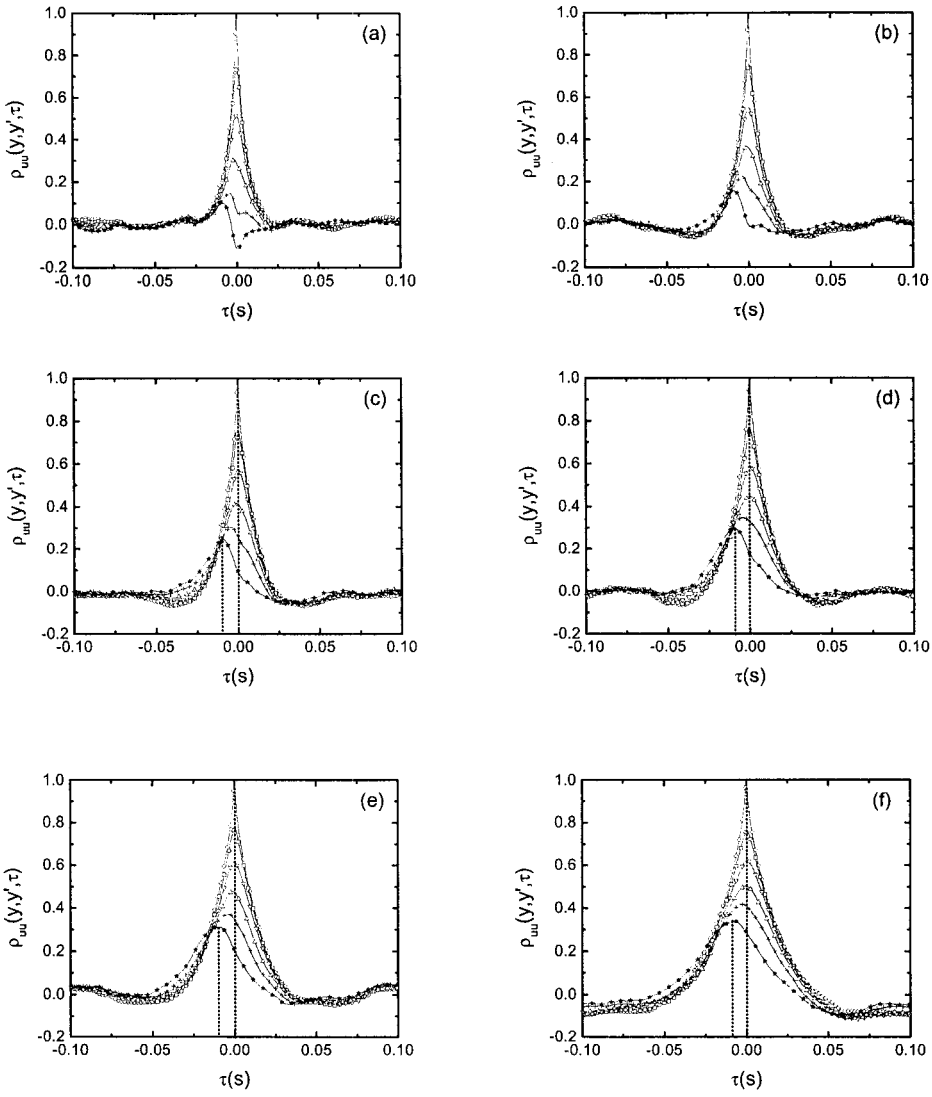

Figure 6.4: Correlation coefficient between the streamwise fluctuating velocity measured at $y/y_{1/2} = 0.49$ and velocities at $-\circ$ $y'/y_{1/2} = 0.49$, $-\square$ $y'/y_{1/2} = 0.40$, $-\nabla$ $y'/y_{1/2} = 0.31$, $-\ \triangle$ $y'/y_{1/2} = 0.21$, $-+$ $y/y_{1/2} = 0.12$ and $-\star$ $y'/y_{1/2} = 0.02$ at (a)$z/z_{1/2} = 0$, (b)$z/z_{1/2} = 0.5$, (c)$z/z_{1/2} = 0.75$, (d)$z/z_{1/2} = 1.0$, (e)$z/z_{1/2} = 1.25$ and (f)$z/z_{1/2} = 1.5$ for x/D=30 .

streamwise direction. This is also the case for the measurements at x/D=20, 25, 35 and 40 not shown here. The time delay of the peak correlation differs at the different downstream locations suggesting that the angle of inclination of the structures changes as the flow evolves downstream. The measurements of the mean streamwise vorticity suggest that the locations of the legs of the structures are changing relative to the jet half-width as the flow evolves downstream. Thus, in order to compare measurements at roughly the same location relative to the structure, the correlation measurements at $z/z_{1/2} = 1.25$ at x/D=20 and $z/z_{1/2} = 1.0$ at x/D=25 - 40, shown in figures 6.5 - 6.8, were compared. These measurements correspond roughly to the center of leg of the outer vortex structure. The results again suggest the large-scale structures are becoming more inclined relative to the streamwise direction as the flow evolves downstream. It should be noted that because the wires were in a fixed rake, the vertical distance between the adjacent wires in the measurements is constant for all streamwise locations so the normalized vertical distance differs.

In order to determine the spatial inclination of the large-scale structures in the streamwise direction, the convection velocity of the large-scale structures were estimated by measuring the time delay in two-point, two-time correlations between the velocities at each streamwise position x and the position x-0.2D and x-0.6D. For example, the correlations between the velocity at x/D=30, $z/z_{1/2} = 1.0$ and the velocities at x/D=29.8 and x/D=29.4 at $z/z_{1/2} = 1.0$ measured for different vertical positions are shown in figure 6.9. It was found that the time delay in the correlation between velocities at x and x-0.6D was almost three times of the time delay in the correlation between velocities at x and x-0.2D. The time delays were then used to compute the convection velocity of the large-scale structures at the different vertical locations. The convection velocities of the large-scale structures normalized by the local maximum streamwise velocity, U_{max}, in the region $15 \leq x/D \leq 40$ at different vertical positions are shown in figure 6.10. The convection velocities here were computed for the lateral

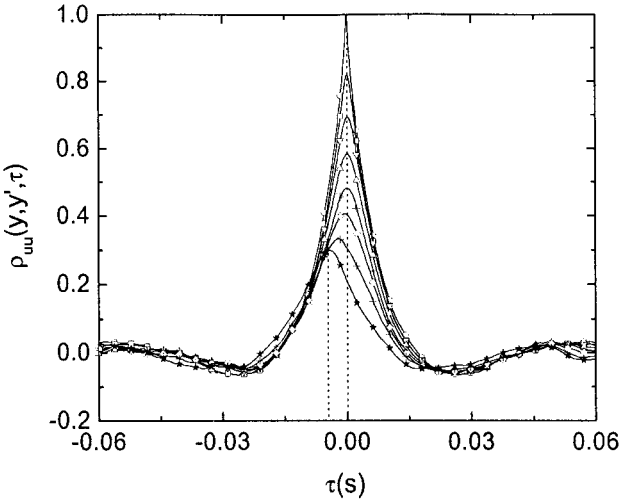

Figure 6.5: Correlation coefficient between the streamwise fluctuating velocity measured at $y/y_{1/2} = 0.45$ and velocities at $-\circ$ $y'/y_{1/2} = 0.45$, $-\square$ $y'/y_{1/2} = 0.39$, $-\nabla$ $y'/y_{1/2} = 0.33$, $-\ \triangle$ $y'/y_{1/2} = 0.27$, $-*$ $y'/y_{1/2} = 0.21$, $-\Diamond$ $y'/y_{1/2} = 0.15$, $-+$ $y/y_{1/2} = 0.09$ and $-\star$ $y'/y_{1/2} = 0.03$ at $z/z_{1/2} = 1.25$ and x/D=20 .

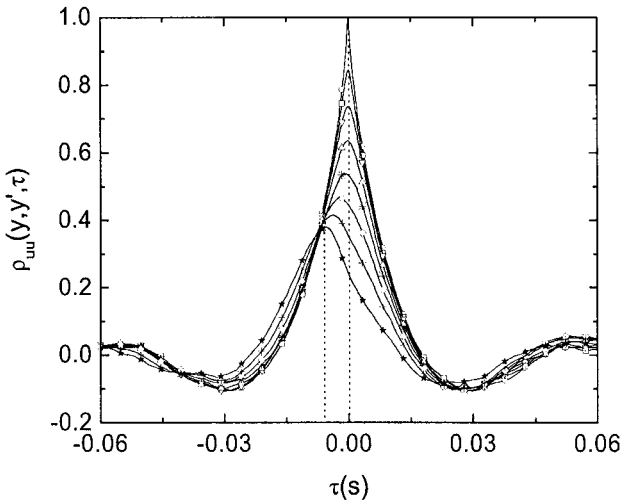

Figure 6.6: Correlation coefficient between the streamwise fluctuating velocity measured at $y/y_{1/2} = 0.40$ and velocities at $-\circ$ $y'/y_{1/2} = 0.40$, $-\square$ $y'/y_{1/2} = 0.34$, $-\nabla$ $y'/y_{1/2} = 0.29$, $-\ \triangle$ $y'/y_{1/2} = 0.24$, $-*$ $y'/y_{1/2} = 0.19$, $-\Diamond$ $y'/y_{1/2} = 0.13$, $-+$ $y/y_{1/2} = 0.08$ and $-\star$ $y'/y_{1/2} = 0.03$ at $z/z_{1/2} = 1.0$ and x/D=25.

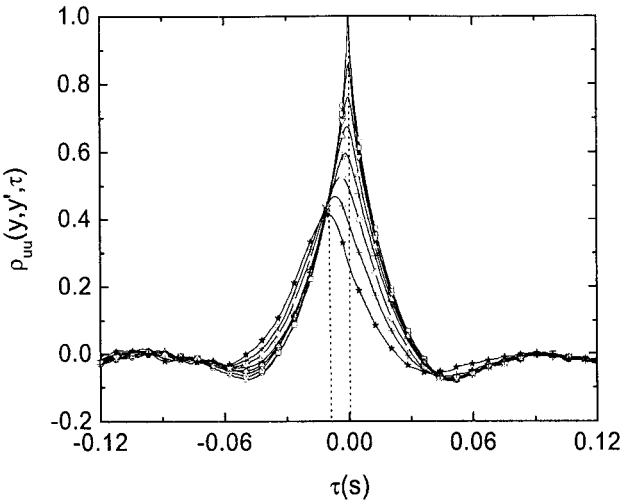

Figure 6.7: Correlation coefficient between the streamwise fluctuating velocity measured at $y/y_{1/2} = 0.32$ and velocities at $-\circ$ $y'/y_{1/2} = 0.32$, $-\square$ $y'/y_{1/2} = 0.28$, $-\nabla$ $y'/y_{1/2} = 0.23$, $-\ \triangle$ $y'/y_{1/2} = 0.19$, $-*$ $y'/y_{1/2} = 0.15$, $-\Diamond$ $y'/y_{1/2} = 0.11$, $-+$ $y/y_{1/2} = 0.06$ and $-\star$ $y'/y_{1/2} = 0.02$ at $z/z_{1/2} = 1.0$ and x/D=35.

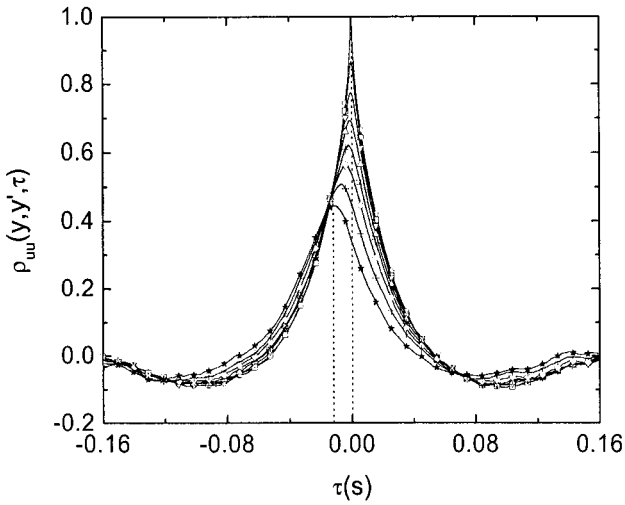

Figure 6.8: Correlation coefficient between the streamwise fluctuating velocity measured at $y/y_{1/2} = 0.29$ and velocities at $-\circ$ $y'/y_{1/2} = 0.29$, $-\square$ $y'/y_{1/2} = 0.25$, $-\nabla$ $y'/y_{1/2} = 0.21$, $-\ \triangle$ $y'/y_{1/2} = 0.17$, $-*$ $y'/y_{1/2} = 0.13$, $-\Diamond$ $y'/y_{1/2} = 0.10$, $-+$ $y/y_{1/2} = 0.06$ and $-\star$ $y'/y_{1/2} = 0.02$ at $z/z_{1/2} = 1.0$ and x/D=40.

locations at the center of the leg of the outer vortex structures given above. It is clear that the base of the large-scale structure convects more slowly than the upper part causing the large-scale structure to incline relative to the streamwise direction. This is consistent with the model proposed by Ewing and Pollard [16]. It is also interesting to note that the convection velocity relative to the maximum streamwise velocity increases as the flow evolves downstream.

The spatial inclination of the large-scale structures were then estimated using the time delay in the vertical correlations and the convection velocities of the large-scale structures given above. The streamwise inclination of the large-scale structures at x/D=15, 20, 25, 30, 35 and 40 are shown in figure 6.11. It is clear that the large-scale structure continues to grow as the flow evolves downstream. In particular, the length of the large-scale structure inclined relative to the streamwise direction grows as the flow travels downstream. The streamwise inclination was then normalized by the vertical and lateral half-widths of the jet and the results are shown in figures 6.12 and 6.13. It is clear that the results collapse much better when scaled by the vertical half-width indicating this is the characteristic scale. This is not unexpected since the inclination of the structures is caused by the mean shear normal to the plate. The increasing inclination of the structure should play some role in suppressing the spread rate of the jet normal to the plate and to enhance the lateral spread rate by directing the entrained flow towards the wall.

In order to confirm that the estimated inclination of the large-scale structures was correct, the two-point, two-time correlation measurements were performed using the single rake with the streamwise positions of the hot-wires adjusted to match the estimated streamwise inclination of the large-scale structures as shown in figure 6.14 and 6.15. The vertical distance between two adjacent single hot-wires was adjusted to 0.2D to reduce the effect of the wake and boundary layer caused by the forward hot-wires on the downstream wires further from the plate. There was also likely some

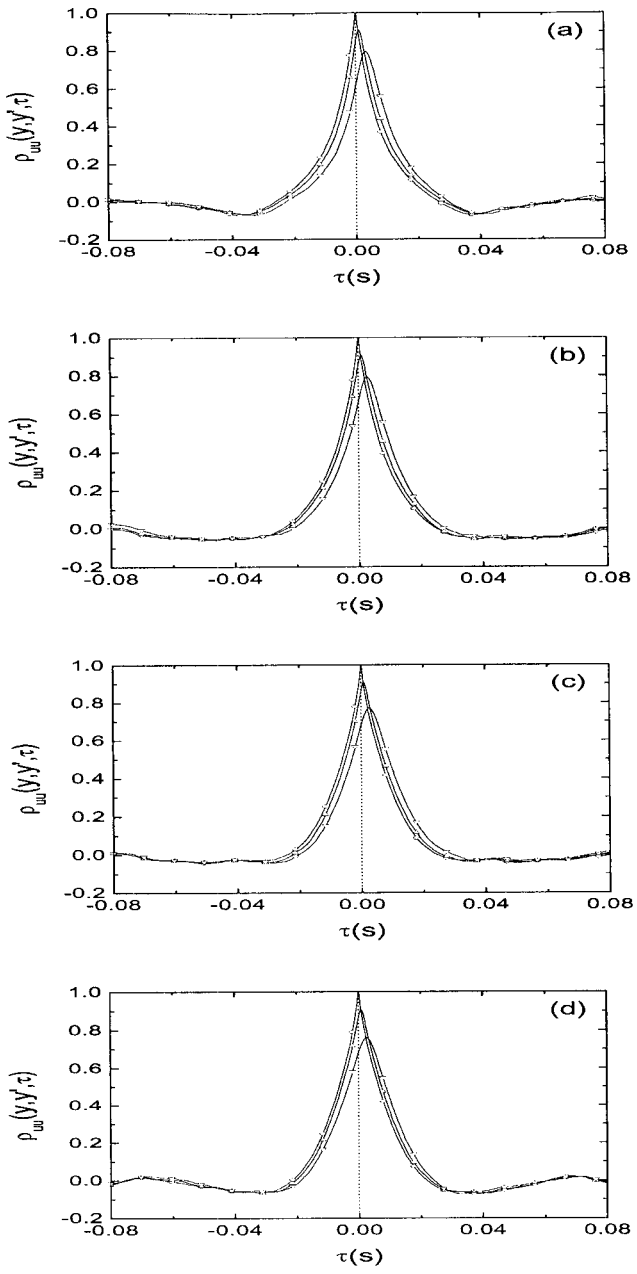

Figure 6.9: Correlation coefficient between streamwise fluctuating velocity measured at x/D=30 and velocities at $-\circ$ $x'/D = 30$, $-\triangle$ $x'/D = 29.8$ and $-\nabla$ $x'/D = 29.4$ for (a) $y/y_{1/2} = 0.023$, (b) $y/y_{1/2} = 0.07$, (c) $y/y_{1/2} = 0.16$ and (d)$y/y_{1/2} = 0.35$ and $z/z_{1/2} = 1.0$.

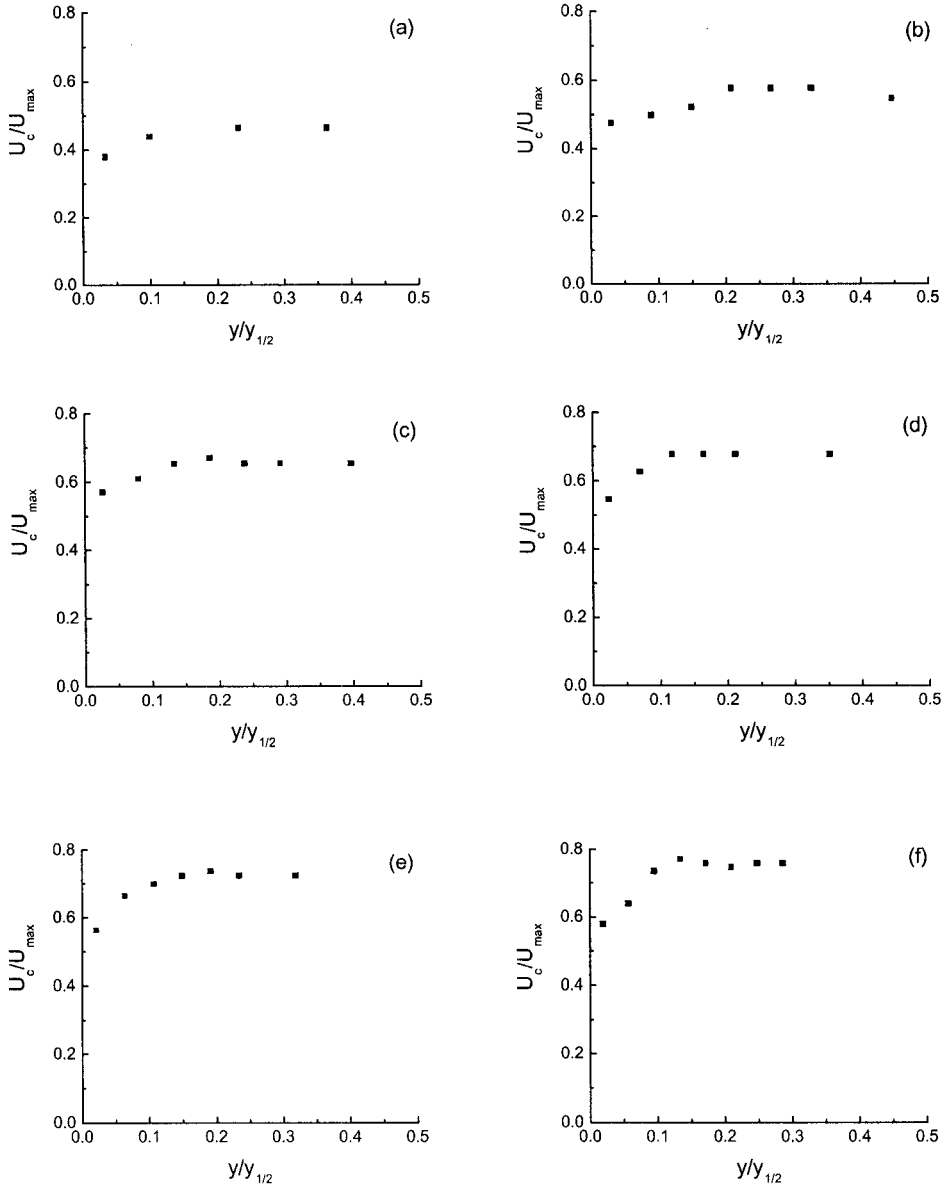

Figure 6.10: Convection velocity of the larger-scale structures computed at (a) $z/z_{1/2} = 1.5$ and x/D=15, (b) $z/z_{1/2} = 1.25$ and x/D=20, c) $z/z_{1/2} = 1.0$ and x/D=25, (d) $z/z_{1/2} = 1.0$ and x/D=30, e) $z/z_{1/2} = 1.0$ and x/D=35 and (f) $z/z_{1/2} = 1.0$ and x/D=40.

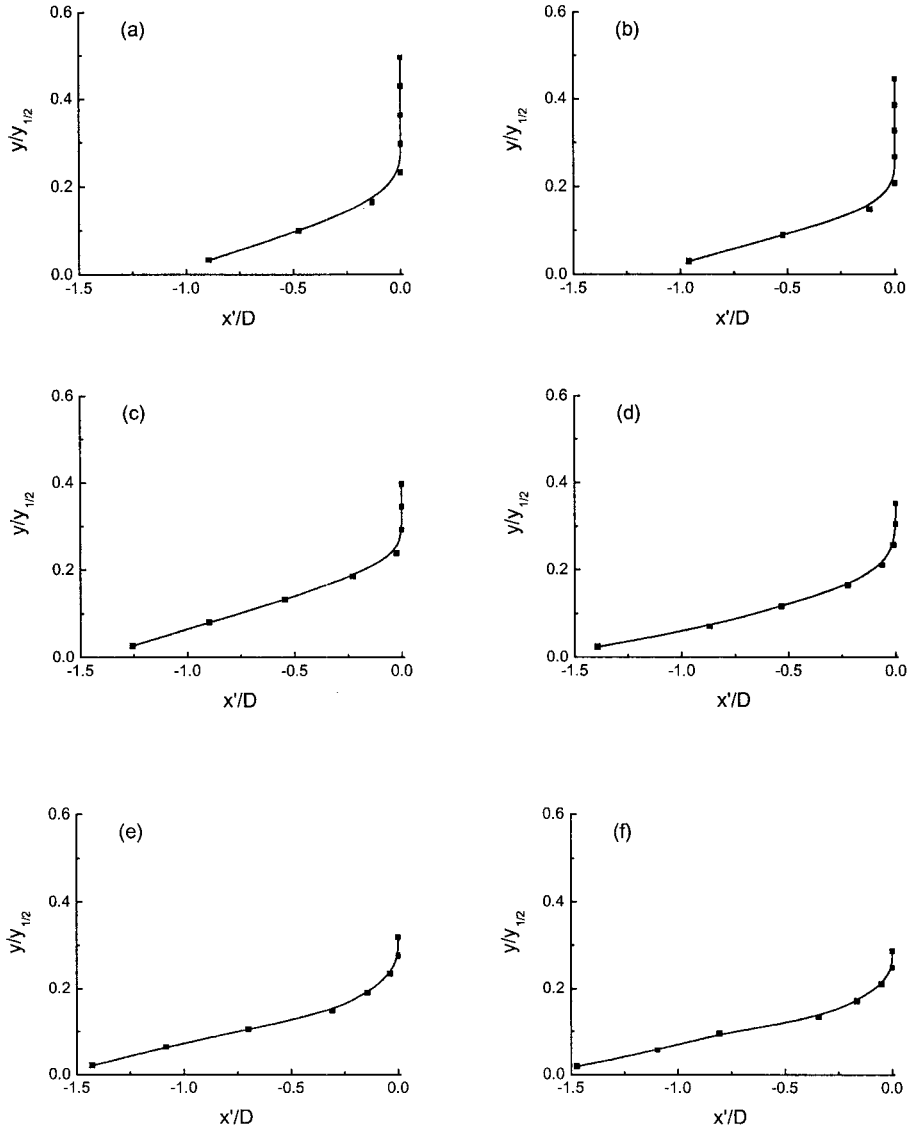

Figure 6.11: The streamwise inclination of the larger-scale structures estimated at (a) $z/z_{1/2} = 1.5$ and x/D=15, (b) $z/z_{1/2} = 1.25$ and x/D=20, c) $z/z_{1/2} = 1.0$ and x/D=25, (d) $z/z_{1/2} = 1.0$ and x/D=30, e) $z/z_{1/2} = 1.0$ and x/D=35 and (f) $z/z_{1/2} = 1.0$ and x/D=40.

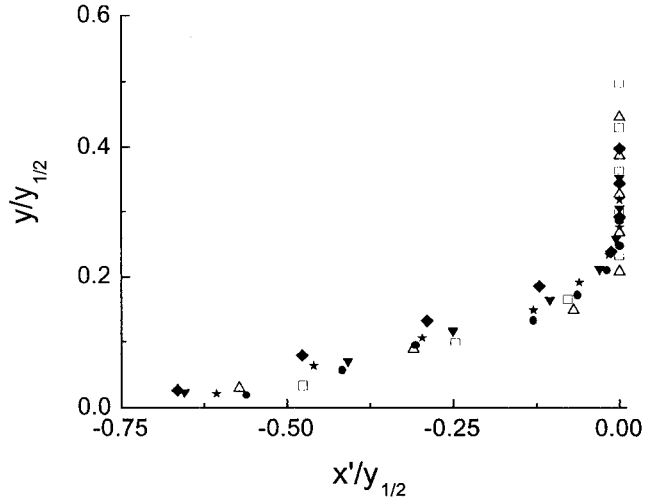

Figure 6.12: The streamwise inclination of the larger-scale structures normalized by the vertical half-width at □ $z/z_{1/2} = 1.5$ and x/D=15, △ $z/z_{1/2} = 1.25$ and x/D=20, ♦ $z/z_{1/2} = 1.0$ and x/D=25, ▼ $z/z_{1/2} = 1.0$ and x/D=30, ⋆ $z/z_{1/2} = 1.0$ and x/D=35 and • $z/z_{1/2} = 1.0$ and x/D=40.

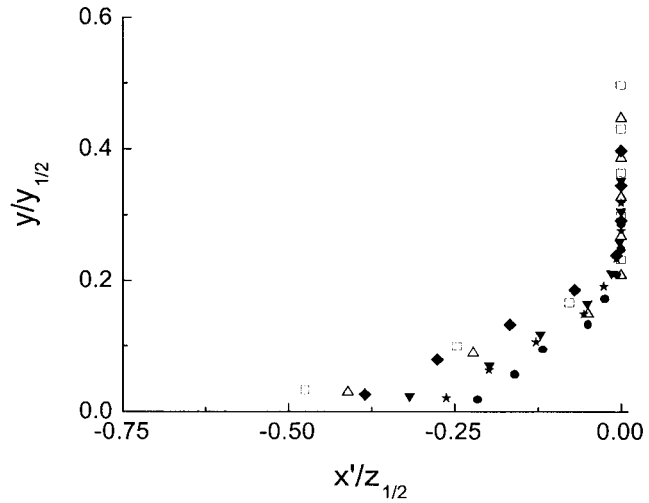

Figure 6.13: The streamwise inclination of the larger-scale structures normalized by the lateral half-width at □ $z/z_{1/2} = 1.5$ and x/D=15, △ $z/z_{1/2} = 1.25$ and x/D=20, ♦ $z/z_{1/2} = 1.0$ and x/D=25, ▼ $z/z_{1/2} = 1.0$ and x/D=30, ⋆ $z/z_{1/2} = 1.0$ and x/D=35 and • $z/z_{1/2} = 1.0$ and x/D=40.

blockage effect due to the probe holder. However, all of these effects would affect the correlation level rather than the time delay. The streamwise distances among the wires at different downstream locations are listed in table 6.1 and the vertical positions of the hot-wires normalized by the vertical half-width at different streamwise locations are listed in table 6.2. The correlation coefficients of the streamwise fluctuating velocity at y/D=0.65 and the other velocities measured at y/D=0.05, 0.25 and 0.45 at x/D=15, 20, 25, 30, 35 and 40 are shown in figure 6.16. It is clear that there is approximately no time delay in the correlation coefficients in the vertical direction at x/D=15, 20 and 25 confirming the estimate of the streamwise inclination of the structures at these locations. There is a slight time delay in the correlation coefficients between the streamwise velocity at y/D=0.65 and the velocity at y/D=0.05 at x/D=30, 35 and 40 because the finite length of the probe did not allow the lowest wire to be moved far enough forward. It was checked that the time delay at x/D=30, 35 and 40 was approximately consistent with the delay anticipated.

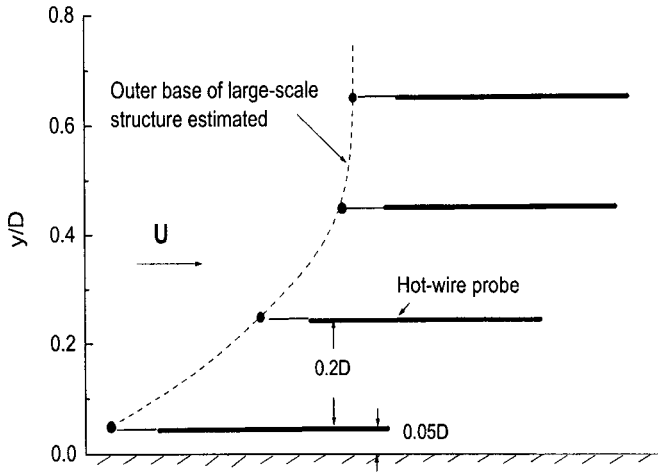

Figure 6.14: Schematic of the alignment of the hot-wire probes used in measurements for streamwise inclination of large-scale structures.

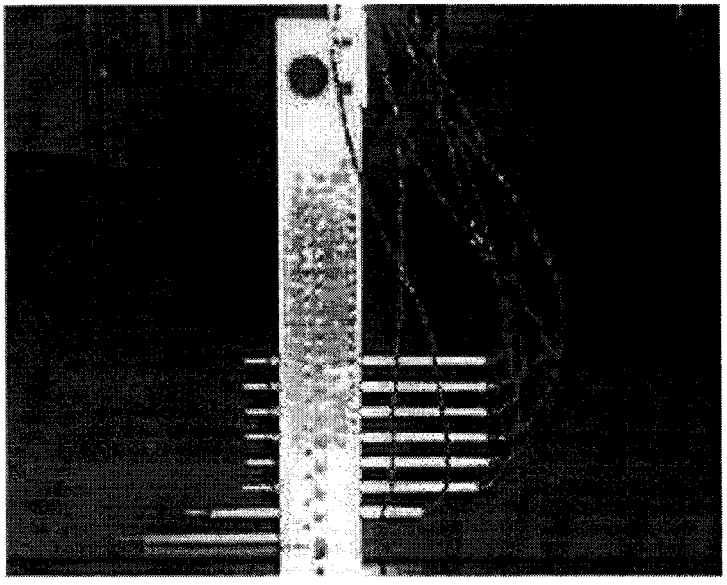

Figure 6.15: Photograph of the hot-wire rake used in measurements for streamwise inclination of large-scale structures at x/D=30.

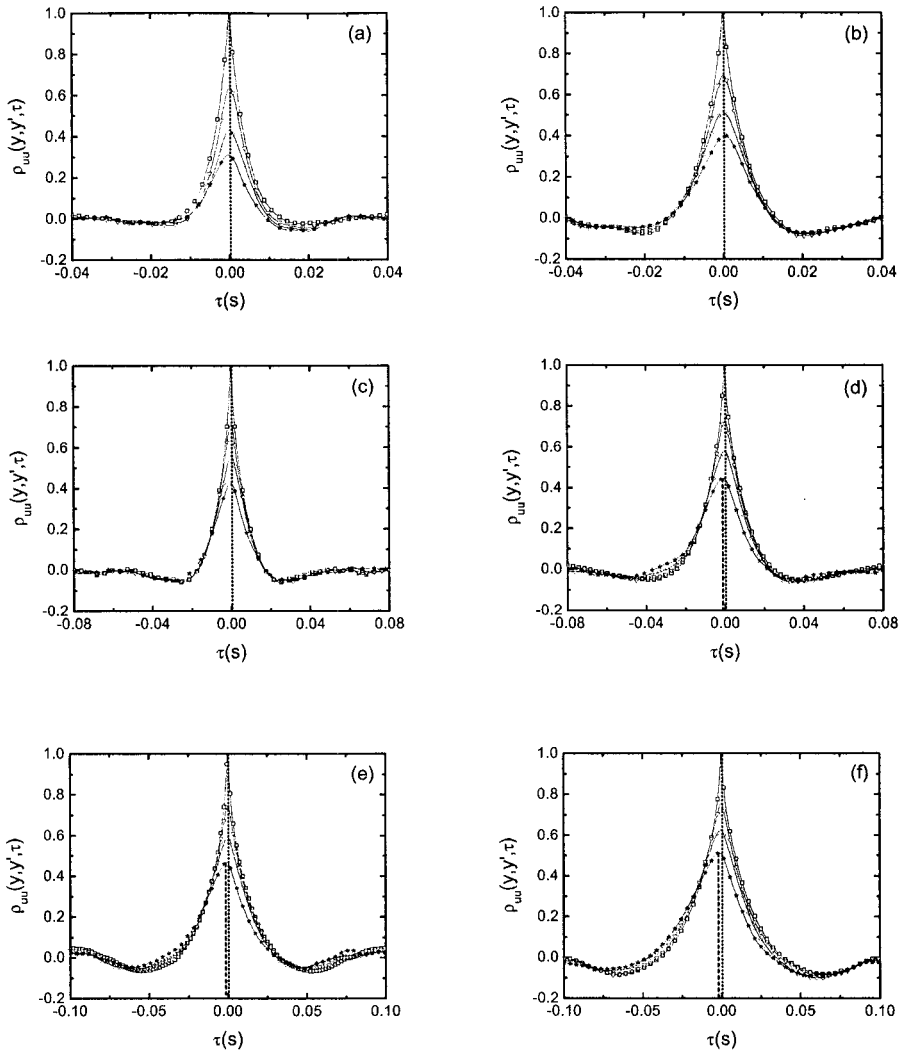

Figure 6.16: Correlation coefficient between streamwise fluctuating velocity measured at y/D= 0.65 and velocities at $-\square$ $y'/D = 0.65$, $-\triangledown$ $y'/D = 0.45$, $-\Diamond$ $y'/D = 0.25$ and $-\star$ $y'/D = 0.05$ for (a) x/D=15 and $z/z_{1/2} = 1.5$, (b) x/D=20 and $z/z_{1/2} = 1.25$, c) x/D=25 and $z/z_{1/2} = 1.0$, (d) x/D=30 and $z/z_{1/2} = 1.0$, e) x/D=35 and $z/z_{1/2} = 1.0$ and (f) x/D=40 and $z/z_{1/2} = 1.0$ using hot-wire rake with streamwise inclination.

x/D	Distance between wire at y/D=0.65 and wire at y/D=0.05	Distance between wire at y/D=0.65 and wire at y/D=0.25	Distance between wire at y/D=0.65 and wire at y/D=0.45
15	$0.70D \pm 0.10D$	$0.10D \pm 0.02D$	$0D \pm 0.02D$
20	$0.90D \pm 0.10D$	$0.10D \pm 0.02D$	$0D \pm 0.02D$
25	$1.20D \pm 0.10D$	$0.50D \pm 0.05D$	$0D \pm 0.02D$
30	$1.20D \pm 0.10D$	$0.50D \pm 0.05D$	$0.05D \pm 0.02D$
35	$1.20D \pm 0.10D$	$0.70D \pm 0.10D$	$0.10D \pm 0.02D$
40	$1.20D \pm 0.10D$	$0.80D \pm 0.10D$	$0.15D \pm 0.02D$

Table 6.1: The streamwise distances among the hot-wire probes used in the measurements of streamwise inclination of large-scale structures.

x/D	y/D=0.65 corresponding $y/y_{1/2} =$	y/D=0.45 corresponding $y/y_{1/2} =$	y/D=0.25 corresponding $y/y_{1/2} =$	y/D=0.05 corresponding $y/y_{1/2} =$
15	0.43	0.30	0.16	0.03
20	0.39	0.27	0.15	0.03
25	0.34	0.24	0.13	0.03
30	0.31	0.21	0.12	0.02
35	0.28	0.19	0.11	0.02
40	0.25	0.17	0.10	0.02

Table 6.2: The vertical positions of hot-wire probes normalized by the vertical half-width of jet for different streamwise locations.

6.2 Evolution of Large-Scale Structures in Lateral Direction

The evolution of the large-scale structures in the lateral direction was studied by examining the correlations of the streamwise fluctuating velocities at different lateral locations. Initially measurements were carried out with one rake fixed at $z/z_{1/2} = 0.75$ or $z/z_{1/2} = 1.0$ shown in figure 6.17 while the second rake was moved out towards the jet edge and across the centerline of jet. The correlation coefficients between the streamwise velocities measured at fixed positions and the velocities at the same height and different lateral positions at x/D=15, 20, 30 and 40 are shown in figures 6.18 - 6.21. It is clear there is a time delay in the peak correlation as the rake was moved out towards the jet edge. The time delay increases with the lateral position suggesting that the flow is convected laterally across the jet when the large-scale structures pass this plane. The time delay in the peak correlation also differs for different vertical heights. For example, measurements of the correlation between the streamwise fluctuating velocities at $z/z_{1/2} = 0.75$ and velocities at $z/z_{1/2} = 0.5$, 1.0 and 1.25 at x/D=40 shown in figure 6.21 indicate that the shortest time delay of the peak correlation occurs near the wall. The time delay gradually increases as the vertical distance increases until the vertical distance from the wall is greater than $0.40y_{1/2}$ that is corresponds approximately to the height of the center of outer region of mean streamwise vorticity at x/D=40. Above this point, the time delay of the peak correlations are approximately the same indicating the same lateral convection speed for the upper part of the large-scale vortex structures. Similar results were deduced for the measurements at other streamwise locations. The shortest time delay of the peak correlation near the wall suggests the most rapid lateral convection is occurring at this point, that is consistent with the notion that the flow below the outer region of the streamwise vorticity is laterally ejected along the wall by the passing of the

large-scale vortex structures.

The fast lateral convection velocity near the wall can be clearly seen from the lateral convection velocity distribution at different vertical locations. For example, the lateral convection velocities at $z/z_{1/2} \approx 1.0$ and x/D=40 that are calculated in terms of time delay of the peak correlation of streamwise fluctuating velocities between $z/z_{1/2} = 0.75$ and $z/z_{1/2} = 1.25$ are shown in figure 6.22. It is clear that the flow near the wall is laterally convected more than twice of the flow at $y/y_{1/2} \geq 0.40$ that likely represents the convection of the outer structures. It is interesting to note that the lateral convection velocity of the outer structures at $z/z_{1/2} \approx 1.0$ and x/D=40 is about $0.26U_{max}$, that is in agreement with the value of $0.22U_{max}$ that is calculated in terms of the measurements of mean streamwise vorticity contours. This likely confirms the correspondence between the large-scale structures and mean streamwise vorticity contours. It is also clear that the lateral convection velocities at $z/z_{1/2} \approx 1.0$ and x/D=40 are approximately three times of the mean lateral velocities at the corresponding vertical locations as shown in figure 6.22. This indicates that the mean lateral velocity of the flow is intensified by the quasi-periodical passage of the large-scale structures.

The other striking feature of lateral correlations of the streamwise fluctuating velocities is that the motions measured on the opposite sides of the jet centerline are negatively correlated at certain locations. For example, the correlation coefficients between the streamwise fluctuating velocities at $z/z_{1/2} = 1$ and the velocities at $z/z_{1/2} = -0.25$ and $z/z_{1/2} = -0.5$ are negative for the vertical positions $y/y_{1/2} > 0.17$ at x/D=15 as shown in figure 6.18. However, this is not true at x/D=40. Here, the streamwise fluctuating velocities at $z/z_{1/2} = 0.75$ and $z/z_{1/2} = -0.25$ or $z/z_{1/2} = -0.5$ seem uncorrelated. In order to gain more information about how the motions correlate on the opposite sides of the jet centerline, further measurements were performed by laterally traversing two hot-wire rakes away from the jet centerline. Initially,

the two rakes were positioned at $z/z_{1/2} = 0.25$ and $z/z_{1/2} = -0.25$ respectively and then they were traversed laterally towards the jet edges on both sides. The correlation coefficients of the streamwise fluctuating velocities measured for a range of lateral positions across the jet at x/D=15, 20, 30 and 40 are shown in figures 6.23 - 6.26. The streamwise fluctuating velocities measured at x/D=15 are negatively correlated from $z/z_{1/2} = \pm 0.25$ to $z/z_{1/2} = \pm 0.75$ for the vertical positions $y/y_{1/2} \geq 0.17$. There appears that normalized lateral positions, $z/z_{1/2}$, where the negative correlations occur, move towards the jet centerline as the flow evolves downstream. For example, the negative correlations only occur at $z/z_{1/2} = \pm 0.25$ at x/D=40 in the vertical positions $y/y_{1/2} > 0.17$. At all of these streamwise positions, the streamwise fluctuating velocities measured at the vertical locations close the wall, e.g., $y/y_{1/2} = 0.02 - 0.03$, are positively correlated at $z/z_{1/2} = \pm 0.25$. Measurements of the contours of mean streamwise vorticity indicate that the positively correlated motions are likely located in the region where the inner vortex structures pass, while the motions that are negatively correlated on the opposite sides of the jet centerline locate in the region where the flow is being both ejected out of the inner horseshoe vortex and swept between the outer and inner horseshoe vortices. The positive correlations in the region close to the wall suggest that the motions in the inner vortex structures on the opposite sides of the jet centerline are likely correlated. The negative correlations above the inner horseshoe vortex structures suggest that the two sets of horseshoe vortices are not necessarily symmetric to the jet centerline. Instead, the wires may intermittently be detecting the flow swept from the wall and the flow ejected between the legs of the horseshoe vortex structures. This is consistent with previous flow visualization measurements [16] that indicated that the large-scale structures bounded by the wall did tend to oscillate laterally around the jet centerline. This hypothesis needs to be investigated further.

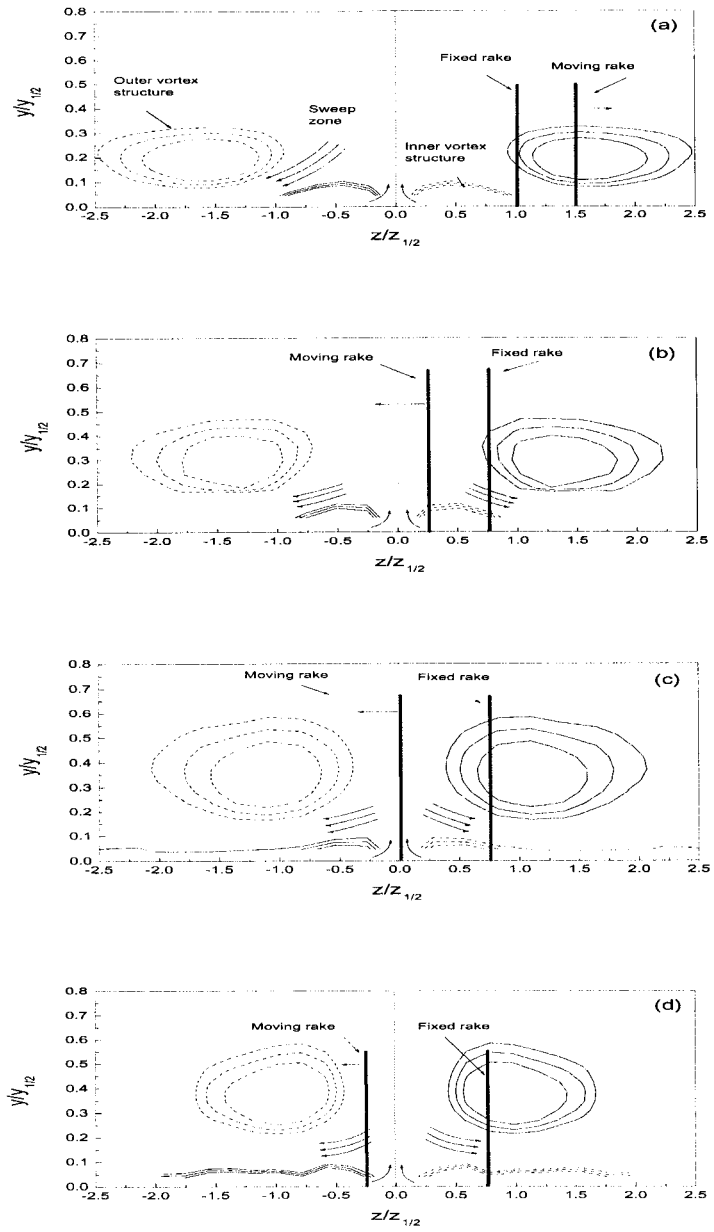

Figure 6.17: Lateral positions of the hot-wire rakes relative to large-scale vortex structures estimated by measurements of mean streamwise vorticity contours at (a) x/D=15, (b) x/D=20, (c) x/D=30 and (d) x/D=40.

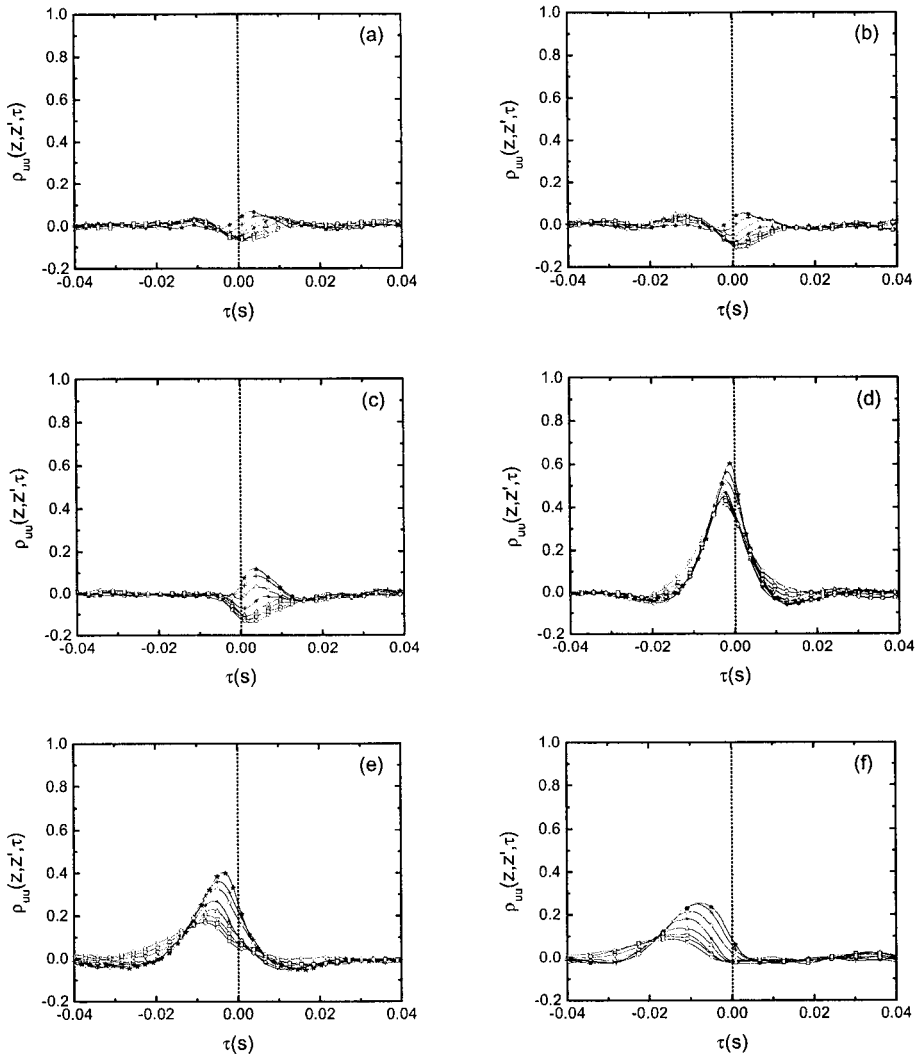

Figure 6.18: Correlation coefficient between streamwise fluctuating velocities measured at $z/z_{1/2} = 1$ and velocities at (a) $z'/z_{1/2} = -0.5$, (b)$z'/z_{1/2} = -0.25$, c)$z'/z_{1/2} = 0$, (d)$z'/z_{1/2} = 1.25$, (e) $z'/z_{1/2} = 1.5$ (f) $z'/z_{1/2} = 1.75$ at the same vertical positions $-\circ$ $y/y_{1/2} = 0.50$, $-\square$ $y'/y_{1/2} = 0.43$, $-\triangledown$ $y'/y_{1/2} = 0.36$, $-\ \triangle$ $y'/y_{1/2} = 0.30$, $-*$ $y'/y_{1/2} = 0.23$, $-\Diamond$ $y'/y_{1/2} = 0.17$, $-+$ $y/y_{1/2} = 0.10$ and $-\star$ $y'/y_{1/2} = 0.03$ for x/D=15.

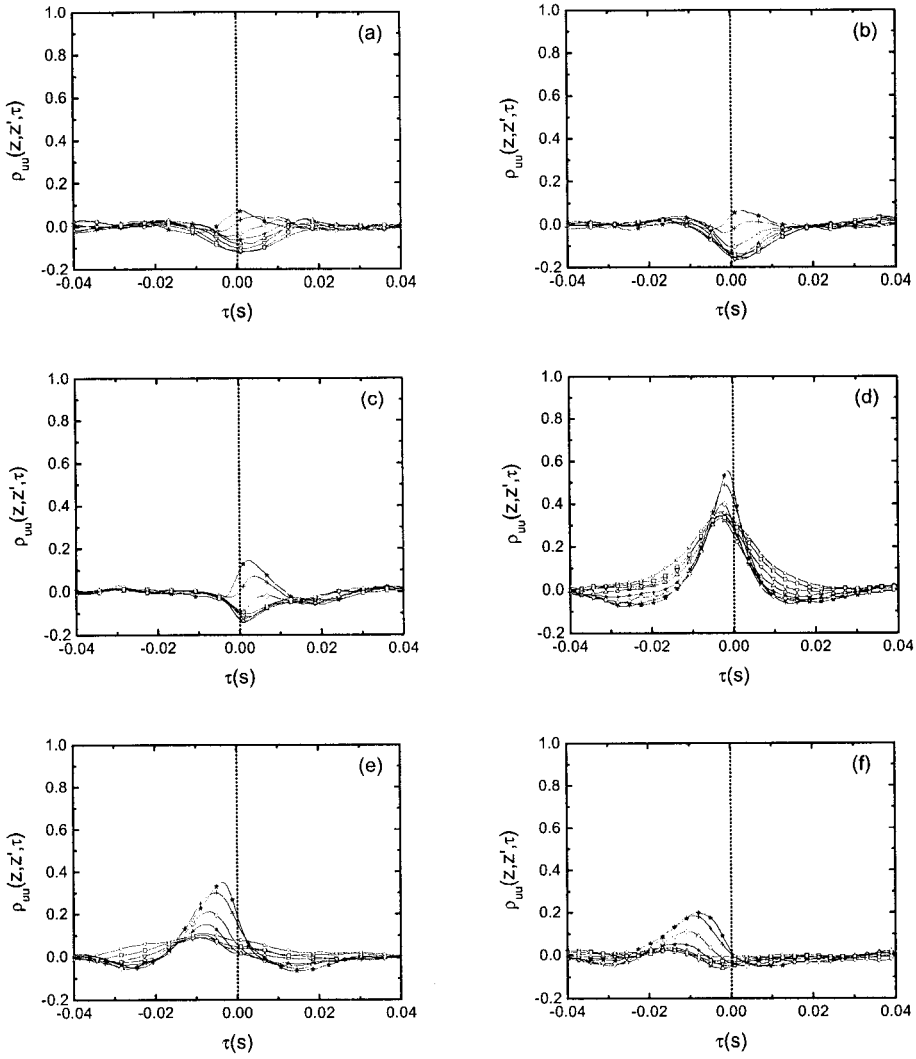

Figure 6.19: Correlation coefficient between streamwise fluctuating velocities measured at $z/z_{1/2} = 0.75$ and velocities at (a) $z'/z_{1/2} = -0.5$, (b)$z'/z_{1/2} = -0.25$, c)$z'/z_{1/2} = 0$, (d)$z'/z_{1/2} = 1.0$, (e) $z'/z_{1/2} = 1.25$ (f) $z'/z_{1/2} = 1.5$ at the same vertical positions $-\circ$ $y/y_{1/2} = 0.86$, $-\square$ $y'/y_{1/2} = 0.74$, $-\nabla$ $y'/y_{1/2} = 0.62$, $-\ \Delta$ $y'/y_{1/2} = 0.51$, $-*$ $y'/y_{1/2} = 0.39$, $-\Diamond$ $y'/y_{1/2} = 0.27$, $-+$ $y/y_{1/2} = 0.15$ and $-\star$ $y'/y_{1/2} = 0.03$ for x/D=20.

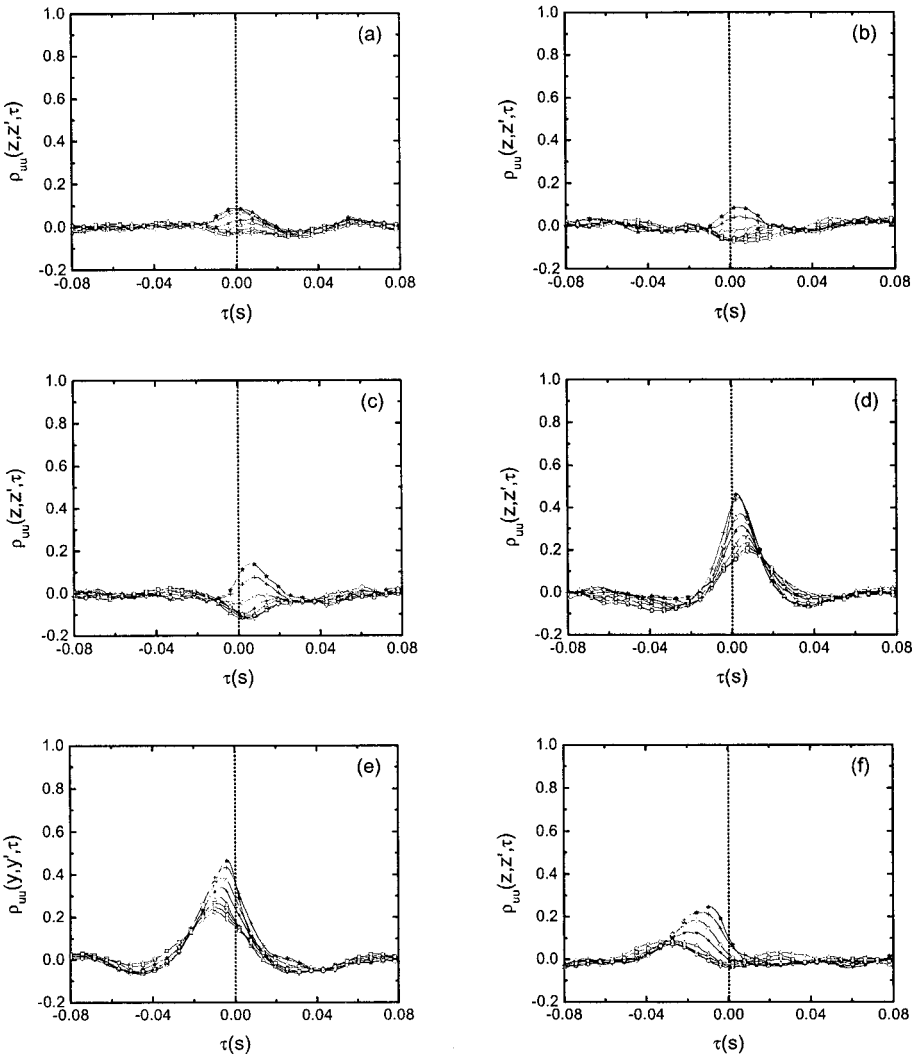

Figure 6.20: Correlation coefficient between streamwise fluctuating velocities measured at $z/z_{1/2} = 0.75$ and velocities at (a) $z'/z_{1/2} = -0.5$, (b)$z'/z_{1/2} = -0.25$, c)$z'/z_{1/2} = 0$, (d)$z'/z_{1/2} = 0.5$, (e) $z'/z_{1/2} = 1.0$ (f) $z'/z_{1/2} = 1.25$ at the same vertical positions $-\circ$ $y/y_{1/2} = 0.68$, $-\square$ $y'/y_{1/2} = 0.59$, $-\triangledown$ $y'/y_{1/2} = 0.49$, $-\ \triangle$ $y'/y_{1/2} = 0.40$, $-*$ $y'/y_{1/2} = 0.31$, $-\Diamond$ $y'/y_{1/2} = 0.21$, $-+$ $y/y_{1/2} = 0.12$ and $-\star$ $y'/y_{1/2} = 0.02$ for x/D=30.

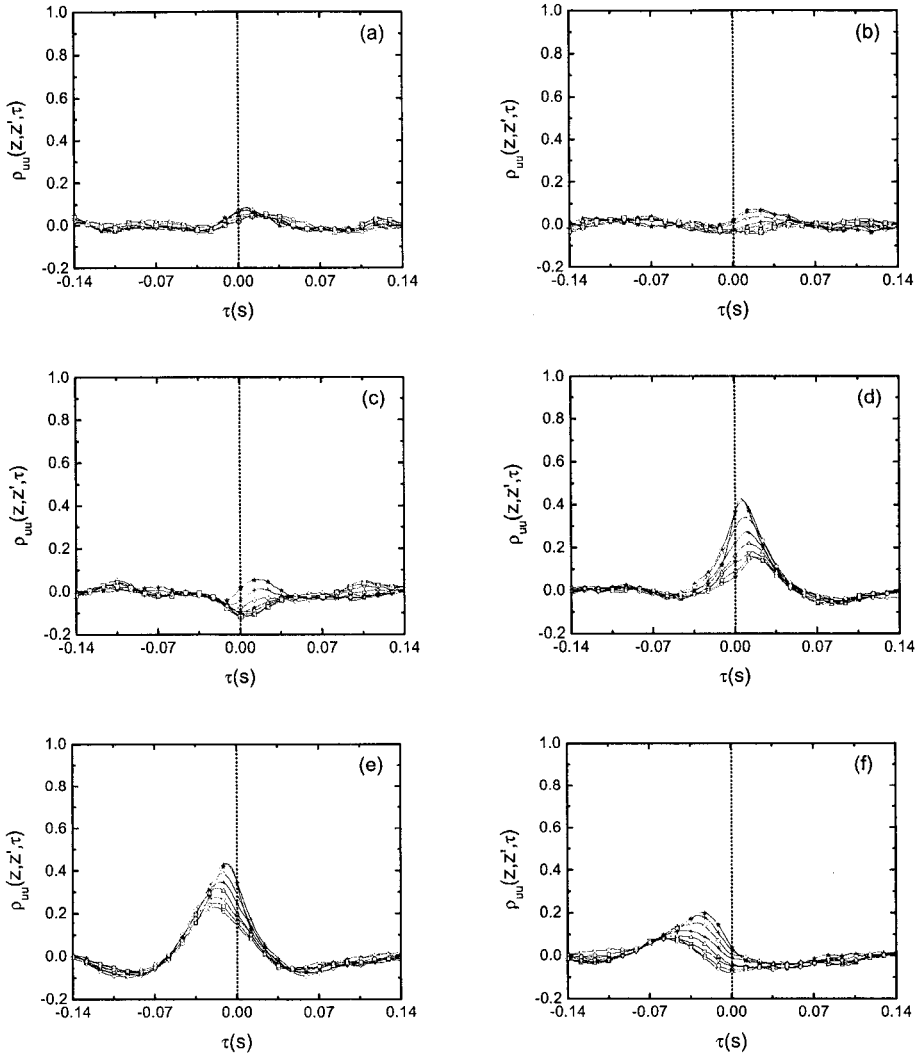

Figure 6.21: Correlation coefficient between streamwise fluctuating velocities measured at $z/z_{1/2} = 0.75$ and velocities at (a) $z'/z_{1/2} = -0.5$, (b)$z'/z_{1/2} = -0.25$, c)$z'/z_{1/2} = 0$, (d)$z'/z_{1/2} = 0.5$, (e) $z'/z_{1/2} = 1.0$ (f) $z'/z_{1/2} = 1.25$ at the same vertical positions $-\circ$ $y/y_{1/2} = 0.55$, $-\square$ $y'/y_{1/2} = 0.48$, $-\nabla$ $y'/y_{1/2} = 0.40$, $-\ \Delta$ $y'/y_{1/2} = 0.32$, $-*$ $y'/y_{1/2} = 0.25$, $-\Diamond$ $y'/y_{1/2} = 0.17$, $-+$ $y/y_{1/2} = 0.10$ and $-\star$ $y'/y_{1/2} = 0.02$ for x/D=40.

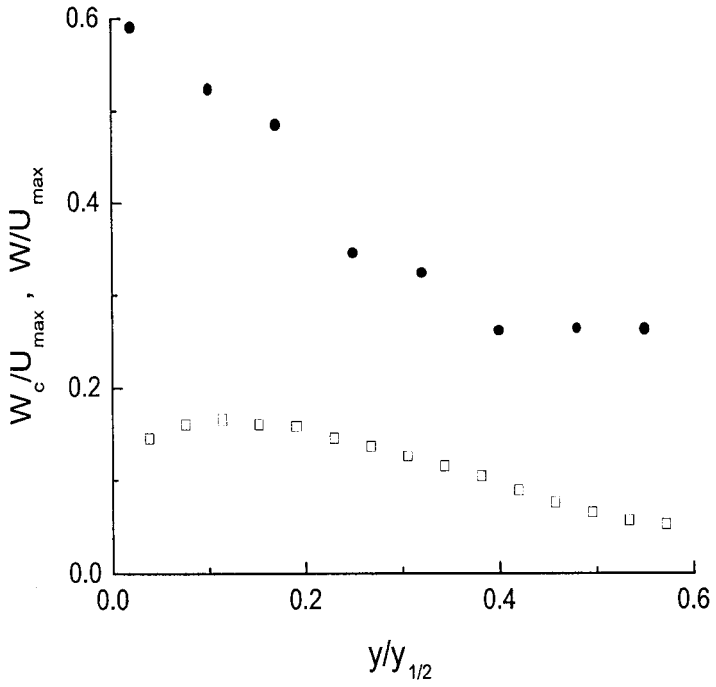

Figure 6.22: Comparison of the lateral convection velocity and mean lateral velocity at $z/z_{1/2} \approx 1.0$ and x/D=40. • Lateral convection velocity and □ mean lateral velocity.

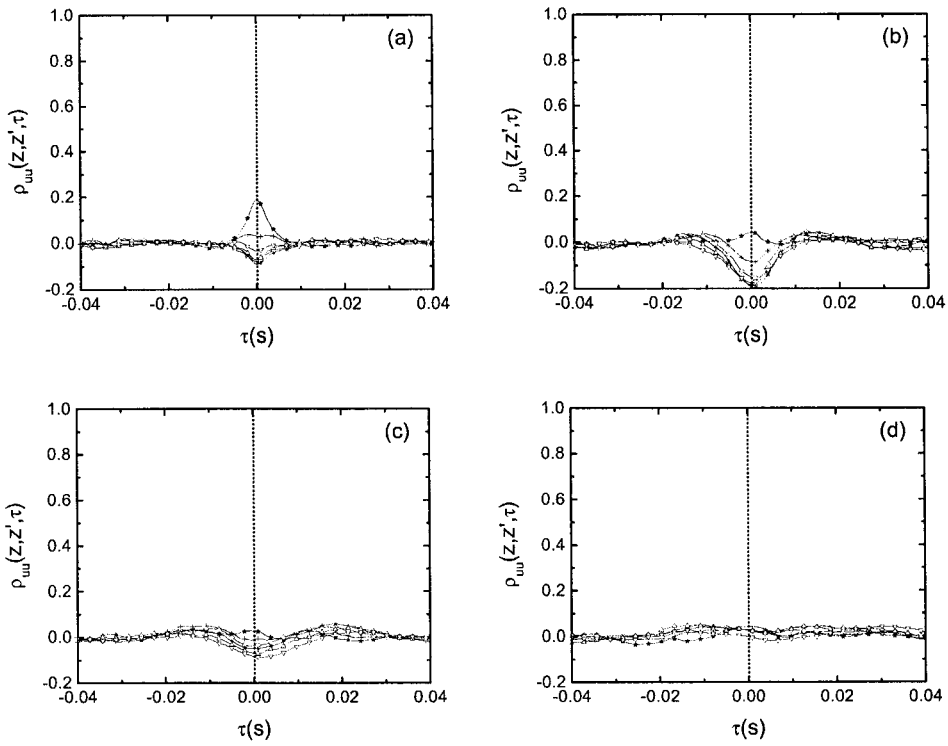

Figure 6.23: Correlation coefficient between streamwise fluctuating velocities measured at (a) $z/z_{1/2} = \pm 0.25$, (b) $z/z_{1/2} = \pm 0.5$, (c)$z/z_{1/2} = \pm 0.75$ and (d)$z/z_{1/2} = \pm 1.0$ at the same vertical positions $-\nabla$ $y'/y_{1/2} = 0.69$, $-$ Δ $y'/y_{1/2} = 0.56$, $-*$ $y'/y_{1/2} = 0.43$, $-\Diamond$ $y'/y_{1/2} = 0.30$, $-+$ $y/y_{1/2} = 0.17$ and $-\star$ $y'/y_{1/2} = 0.03$ for x/D=15.

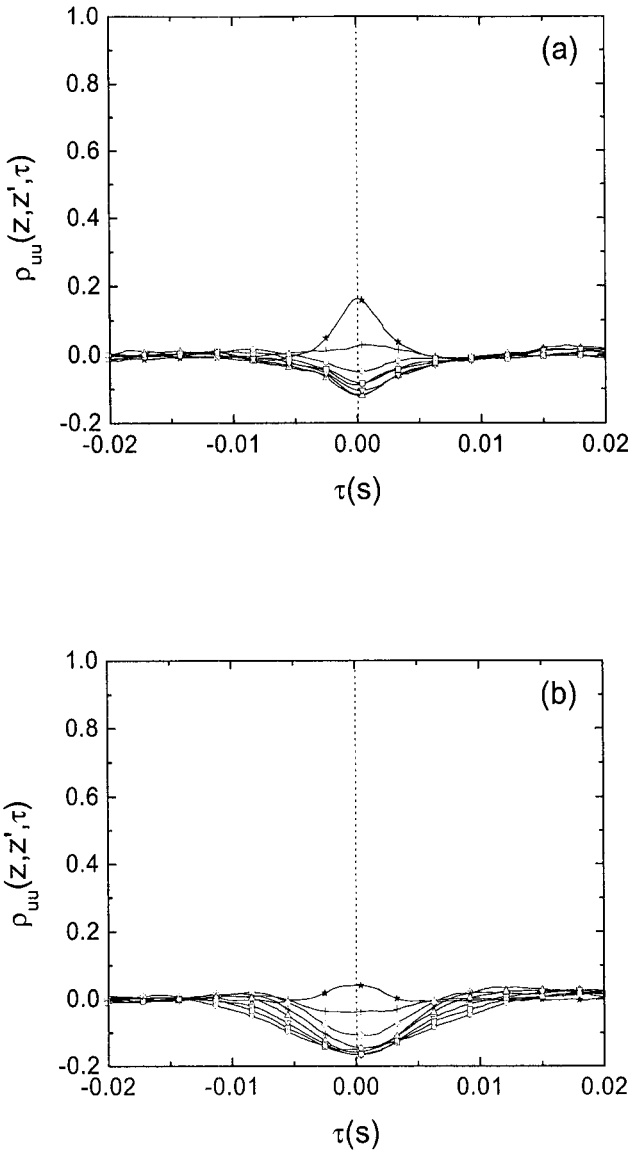

Figure 6.24: Correlation coefficient between streamwise fluctuating velocities measured at (a) $z/z_{1/2} = \pm 0.25$ and (b) $z/z_{1/2} = \pm 0.5$ at the same vertical positions $-\circ$ $y/y_{1/2} = 0.86$, $-\square$ $y'/y_{1/2} = 0.74$, $-\nabla$ $y'/y_{1/2} = 0.62$, $-\ \triangle$ $y'/y_{1/2} = 0.51$, $-*$ $y'/y_{1/2} = 0.39$, $-\Diamond$ $y'/y_{1/2} = 0.27$, $-+$ $y/y_{1/2} = 0.15$ and $-\star$ $y'/y_{1/2} = 0.03$ for x/D=20.

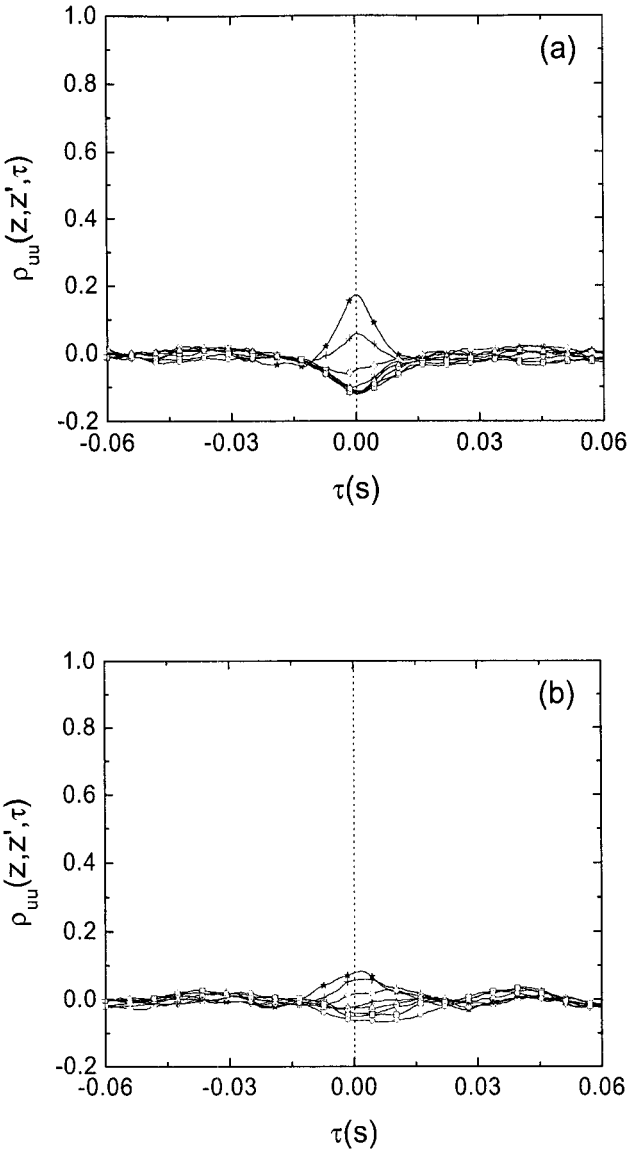

Figure 6.25: Correlation coefficient between streamwise fluctuating velocities measured at (a) $z/z_{1/2} = \pm 0.25$ and (b) $z/z_{1/2} = \pm 0.5$ at the same vertical positions $-\circ$ $y/y_{1/2} = 0.68$, $-\square$ $y'/y_{1/2} = 0.59$, $-\nabla$ $y'/y_{1/2} = 0.49$, $-\ \triangle$ $y'/y_{1/2} = 0.40$, $-*$ $y'/y_{1/2} = 0.30$, $-\Diamond$ $y'/y_{1/2} = 0.21$, $-+$ $y/y_{1/2} = 0.12$ and $-\star$ $y'/y_{1/2} = 0.02$ for x/D=30.

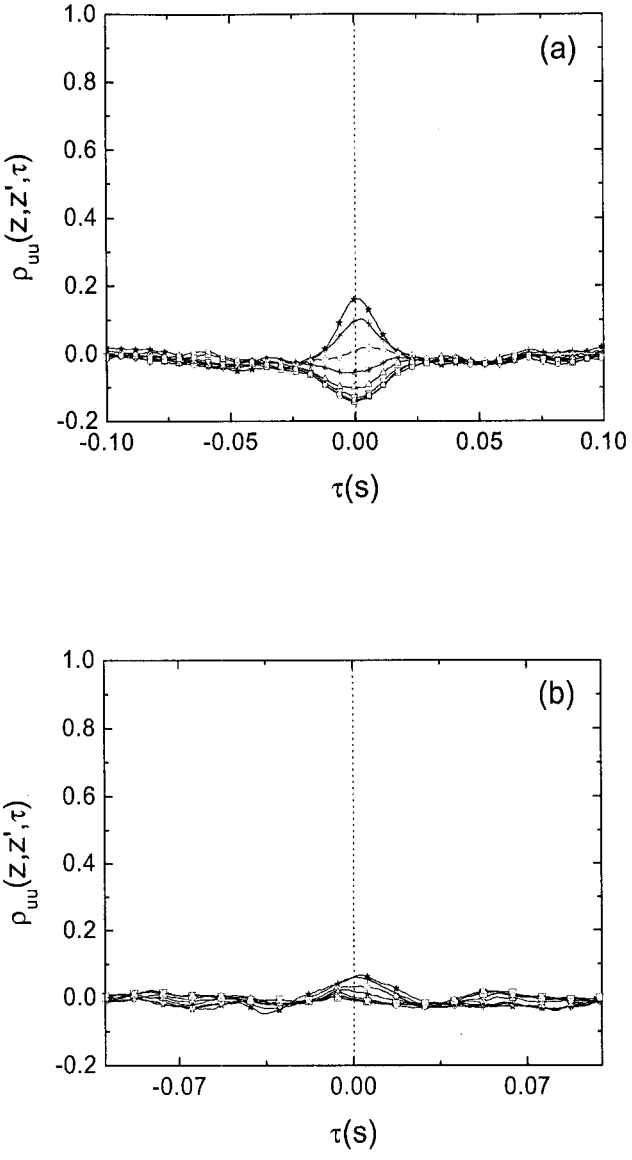

Figure 6.26: Correlation coefficient between streamwise fluctuating velocities measured at (a) $z/z_{1/2} = \pm 0.25$ and (b) $z/z_{1/2} = \pm 0.5$ at the same vertical positions $-\circ$ $y/y_{1/2} = 0.55$, $-\square$ $y'/y_{1/2} = 0.48$, $-\nabla$ $y'/y_{1/2} = 0.40$, $-\ \triangle$ $y'/y_{1/2} = 0.32$, $-*$ $y'/y_{1/2} = 0.25$, $-\Diamond$ $y'/y_{1/2} = 0.17$, $-+$ $y/y_{1/2} = 0.10$ and $-\star$ $y'/y_{1/2} = 0.02$ for x/D=40.

Chapter 7

Discussion and Concluding Remarks

A comprehensive investigation was performed to investigate a number of open questions about the development of the three-dimensional wall jet. In particular, the equations of moments were examined to determine if the wall jet has self-similar solutions as commonly thought. The effect of initial conditions on the development of the round jets was then examined in order to determine if these flows have significant different growth rates as reported in previous investigations. Finally, the development of the flow was examined to understand why the lateral growth rate of the flow increases significantly in the intermediate field and the role that the large-scale structures play in the process. Significant contributions were made in addressing these issues though in some cases the investigation identified issues that must be investigated further.

It was initially shown here that the first order Reynolds averaged governing equations for the three-dimensional wall jet do have self-similar solutions and the predictions from this analysis are in agreement with the measurements in the far field of a jet exiting a long pipe. The analysis predicted that the flow could have two different velocity scales for the mean streamwise and lateral velocities when the lateral growth

rate is not constant. It was shown that the profiles of the mean lateral velocity in the intermediate field where the growth rates were not constant collapsed with the scaling predicted in the similarity analysis suggesting the analysis properly predicts the feature of this flow.

Single-point measurements in the wall jet exiting a contoured nozzle have shown that there were two regions in the intermediate field. The position of the maximum velocity point moved towards the wall and the profiles of the moments and the reorientation of the regions of the mean streamwise vorticity underwent significant changes from x/D=10 to 20 indicating the flow was adjusting to the wall in this region. The position of the maximum velocity point moved away from the wall and changes in the profiles of the moments and the reorientation of the regions of the mean streamwise vorticity slowed down after $x/D = 20$ suggesting the flow was in the later stage of the intermediate field of the wall jet. Changes in profiles of turbulent stresses were not apparent by x/D=40 indicating the flow was approaching the far field.

The comparison of measurements in wall jets exiting the contoured nozzle and the fully developed long pipe have shown that the local maximum streamwise velocity in the jet exiting the long pipe was larger than the contoured nozzle through near and intermediate fields. The vertical and lateral half-widths of the flow exiting the long pipe were approximately 0.05D and 0.24D smaller than the flow exiting the contoured nozzle in the region beyond x/D=20, but the growth rates of two jets were approximately the same in this region. The differences in the profiles of moments in the two jets seemed to disappear by x/D=30.

The effect of the boundary conditions on the development of wall jets were examined for three cases: the presence of a wall behind the nozzle, the change in size of this wall or the room and the misalignment of the horizontal plate. It was found that changes in these boundary conditions did not have significant effects on the lateral

growth rate and profiles of the streamwise moments in the intermediate field. However, changes in the size of a wall behind the nozzle or the room appeared to affect the vertical half-width and the vertical growth rate.

Measurements of the vertical correlation of the streamwise fluctuating velocity in the wall jet exiting the contoured nozzle indicated there were large-scale vortex structures consisting two pair of horseshoe vortices in the flow. The inner vortex structures were induced towards the wall by the outer structures in the intermediate field and the legs of the outer structures inclined relative to the streamwise direction as the flow evolved downstream. It was found that this streamwise inclination of the outer vortex structures approximately collapsed when the vertical and streamwise distance were normalized using the vertical jet half-width. Measurements of the lateral correlations of the streamwise fluctuating velocity indicated that the flow below the outer region of the streamwise vorticity was laterally convected faster than the outer vortex structures.

Bibliography

[1] Abrahamsson, H., Johansson, B. and Lofdahl, L., 1997, "The turbulence field of a fully developed three-dimensional wall jet", Internal Report97/1, Chalmers University of Technology, Sweden.

[2] Beuther, P. D., 1980, "Experimental investigation of the axisymmetric turbulent buoyant plume", Ph.D. thesis, the state University of New York at Buffalo.

[3] Bradshaw, P., 1987, "Turbulent secondary flows", Annual Review of Fluid Mechanics, Vol. 19, pp. 53-74.

[4] Bradshaw, P., 1996, "Understanding and prediction of turbulent flow-1996", 1997, International Journal of Heat and Fluid Flow, Vol. 18, pp. 45-54.

[5] Bradshaw, P., 1996, "Turbulence modeling with application to turbomachinery", 1996, Proceedings of Aerospace Society, Vol. 32, pp. 575-624.

[6] Bruun, H. H., 1977, "A time-domain analysis of the large-scale flow structure in a circular jet. Part 1. Moderate Reynolds number", Journal of Fluid Mechanics, Vol. 83, pp. 641-671.

[7] Bruun, H. H., 1979, "A time-domain evalution of the large-scale flow structure in a turbulent jet.", Proceedings of Royal Society. A 367, pp. 193-218.

[8] Catalano, G. D., Morton, J. B. and Humphris, R. R., 1977, "An experimental investigation of a three-dimensional wall jet", AIAA Journal, Vol. 15, No.8, pp. 1146-1151.

[9] Champagne, H., Sleicher, C. A. and Wehrmann, O. H., 1967, "Turbulence measurements with inclined hot-wires. Part 1: Heat transfer experiments with inclined hot-wire", Journal of Fluid Mechanics, Vol. 28, pp. 153-176.

[10] Champagne, H. and Sleicher, C. A., 1967, "Turbulence measurements with inclined hot-wires. Part 2: Hot-wire response equation", Journal of Fluid Mechanics, Vol. 28, pp. 177-182.

[11] Chandrsuda, C., Mehta, R. D., Weir, A. D. and Bradshaw, P., 1978, "Effect of free-stream turbulence on large structure in turbulent mixing layers", Journal of Fluid Mechanics, Vol. 85, pp. 693-704.

[12] Citriniti, J. H., 1996, "Experimental investigation into the dynamics of the axisymmetric mixing layer utilizing the proper orthogonal decomposition", Ph.D. thesis, the state University of New York at Buffalo.

[13] Davis, M. R. and Winarto, H., 1980, " Jet diffusion from a circular nozzle above a solid plane", Journal of Fluid Mechanics, Vol. 101, pp. 201-221.

[14] Davies, P. O. A. L., 1966, " Turbulence structure in free jet", AIAA Journal, Vol. 4, No. 11, pp. 1971-1978.

[15] Eriksson J. G., Johansson B. and Lofdahl L., 1991, " Flow visualization and turbulence measurements in a three-dimensional plane turbulent wall jet", First European Fluid Mechanics Conference, England.

[16] Ewing, D. and Pollard, A., 1997, "Evolution of the large scale motions in a three-dimensional wall jet", AIAA Paper, No. 1997-1964.

[17] Ewing, D.,Benaissa, A., Pollard, A., Citriniti, J., Abrahamsson, H. and Lofdahl, L., 1997, "Contribution of large structures to the anisotropic spread rate in a wall jet issuing from a round nozzle", 10th International Sympoium on Transport Phenomena in Thermal Science and Process Engineering, Kyoto, Japan.

[18] Fisher, M. J. and Davies, A. L., 1964, "Correlation measurements in a non-frozen pattern of turbulence", Journal of Fluid Mechanics, Vol. 18, pp. 99-116.

[19] Fox, R. and McDonald, A., 1998, Introduction to Fluid Mechanics, 5th edition, John Wiley and Sons.

[20] Fujisawa, N. and Shirai, H., 1989, "Mean flow and turbulence characteristics of three-dimensional wall jet along plane surface", Transaction of Japanise Socitey in Aerospace Science, Vol. 32, No.95, pp.35-46.

[21] George, W. K., Abrahamsson, H., Eriksson, J., Karlsson, R. I., Lofdahl, L. and Wosnik, M., 2000, " A similarity theory for the turbulent plane wall jet without external stream", Journal of Fluid Mechanics, Vol. 425, pp. 367-411.

[22] George, W. K., Abrahamsson, H., Eriksson, J., Lofdahl, L. and Karlsson, R.I., 1997, " A similarity theory for the plane wall jet", Internal Report 97/7, Department of thermo and fluid dynamics, Chalmers University of Technology, Sweden.

[23] George, W. K., 1989, "Self-preservation of turbulent flows and its relation to initial conditions and coherent structures", Advances in Turbulence (ed. George and Arndt), NY.

[24] Glauser, M. N., 1987, "Coherent structures in the axisymmetric turbulent jet mixing layer", Ph.D. thesis, the state University of New York at Buffalo.

[25] Goldstein, I. and Richard, J., 1983, Fluid Mechanics Measurements, Hemisphere Publishing Corporation.

[26] Hinze, J. O.,1975, Turbulence, Second Edition, McGRAW-HILL.

[27] Hardin, J. C., 1990, Introduction to Time Series Analysis, Second printing, NASA Langley Research Center,Hampton, Virginia.

[28] Hussein, H. J., Capp, S. P. and George, W. K., 1994, " Velocity measurements in a high-Reynolds-number, momentum-conserving, axisymmetric, turbulent jet", Journal of Fluid Mechanics, Vol. 258, pp. 31-75.

[29] Iida, S. and Matsuda, H., 1988, "An experimental study of circular turbulent wall-jet along a convex wall", Transaction of Japanese Society of Mechanical Engineering, Series B, Vol. 54, No. 498, PP.354-360.

[30] Khritov, K. M., Lyubimov, D. A., Maslov, V. p., Mineec, B. I. and Secundov., 2002, "Three-dimensional wall jets: experiment, theory and application", AIAA paper, 2002-0732.

[31] Kays, W. M. M. and Crawford, M. E., 1993, Convective Heat and Mass Transfer, Third Edition, McGraw-Hill, Inc.

[32] Kim, K. C. and Adrian, R. J., 1999, "Very large-scale motion in the outer layer", Physics of Fluid, Vol. 11, pp. 417-422.

[33] Ko, N. W. M. and Davies, P. O. A. L., 1971, "The near field within the potential cone of subsonic cold jets", Journal of Fluid Mechanics, Vol. 50, pp. 49-78.

[34] Lau, J. C. and Fisher, M. J., 1975, "The vortex-street structure of turbulent jets. Part 1", Journal of Fluid Mechanics, Vol. 67, pp. 299-337.

[35] Launder, B. E. and Rodi, W., 1983, "The turbulent wall jet - measurements and modeling", Annual Review of Fluid Mechanics. Vol. 15, pp. 429-59.

[36] Libby, A. Paul, 1996, Introduction to Turbulence. Taylor & Francis.

[37] Loehrke, R. I. and Nagib, H. M., 1976, "Control of free-stream turbulence by means of honeycombs: A balance between suppression and generation", Journal of Fluids Engineering, pp. 342-353.

[38] Loehrke, R. I. and Nagib, H. M., 1972, "Experiments on management of free-stream turbulence", AGARD Report, No. 598.

[39] Lomas, C. G, 1985, Fundamentals of Hot Wire Anemometry. Cambridge University Press, Cambridge.

[40] Marusic, I., 2001, "On the role of large-scale structures in wall turbulence", Physics of Fluids, Vol. 13, pp. 735-743.

[41] Marusic, I., Kunkel, G. J. and Porte-Agel F., 2001, "Experimental study of wall boundary conditions for large-eddy simulation", Journal of Fluid Mechanics, Vol. 446, pp. 309-320.

[42] Maslov, V. P., Mineev, B. I., Secundov, A. N. and Vorobiev, A. N., 2001, "An experimental study of three-dimensional wall jets," AIAA Paper 2001-0449.

[43] Matsuda, H., Iida, s. and Hayakawa, M., 1990, "Coherent structures in three-dimensional wall jet", Journal of Fluids Engineering, Vol. 112, PP. 462-467.

[44] Morton, J. B., Catalano, G. D. and Humphris, R. R, 1978, "Some two-point statistical properties of a three-dimensional wall jet", AIAA Journal, Vol. 16, pp. 693-698.

[45] Newman, B.G.,Patel, R. P. and Tjio, H. K., 1972, "Three-dimensional wall jet originating from a circular orifice", Aeronautical Quartely, Vol. 23, pp. 188-200.

[46] Nickels, T. B. and Perry, A. E., 1996, "An experimental and theoretical study of the turbulent coflowing jet", Journal of Fluid Mechanics, Vol. 309, pp. 157-182.

[47] Nickels, T. B. and Marusic, I., 2001, "On the different contributions of coherent structures to the spectra of a turbulent round jet and turbulent boundary layer", Journal of Fluid Mechanics, Vol. 448, pp. 367-385.

[48] Padmanabham, G. and Gowda, B.H.L., 1991, "Mean and turbulence characteristics of a class of three-dimensional wall jets - Part1: Mean flow characteristics", Journal of Fluids Engineering, Vol. 113, pp. 620-628.

[49] Padmanabham, G. and Gowda, B.H.L., 1991, "Mean and turbulence characteristics of a class of three-dimensional wall jets - Part2: Turbulence characteristics", Journal of Fluids Engineering, Vol. 113, pp. 629-634.

[50] Perry, A.E., 1982, Hot-wire Anemometry. Clarendon Pree Oxford.

[51] Preston, J. H., 1954, "The determination of turbulent skin friction by means of Pitot tubes", Journal of the Royal Aeronautical Society, Vol. 58, pp. 109-121.

[52] Rajaratnam, N., ASCE, M. and Pani, B. S., January 1974, "Three-dimensional turbulent wall jets", Journal of Hydraulics Division, PP. 69-83.

[53] Robinson, S. k., 1991, "Coherent motions in the turbulent boundary layer", Annual Review of Fluid Mechnics, Vol. 23, pp. 601-639.

[54] Sforza, P. M. and Herbst, G., 1970, "A study of three-dimensional, incompressible, turbulent wall jets", AIAA Journal, Vol. 8, pp. 276-283.

[55] Shabbir, A., Beuther, P. D. and George, W. K., 1996, "X-wire response in turbulent flows of high-intensity turbulence and low mean velocities", Experimental Thermal and Fluid Science, Vol. 12, pp. 52-56.

[56] Sun, H. and Ewing, D., 2002, "Development of the large-scale structures in the intermediate field of the three-dimensional wall jet", FEDSM2002-31414, ASME Fluids Engineering Division Summer Meeting, Montreal.

[57] Sun, H. and Ewing, D., 2002,"Effect of initial and boundary conditions on development of Three-Dimensional turbulent wall jets", AIAA Paper, No. 2002-0777.

[58] Sun, H. and Ewing, D., 2001, "Effect of initial conditions on development of three-dimensional turbulent wall jets", Proceedings of 18th Canadian Congress of Applied Mechanics, Newfoundland.

[59] Sun, H. and Ewing, D., 2001, "The Development of three-dimensional wall jet", Proceedings of 48th Annual Conference of Canadian Aeronautics and Space Institute, Toronto.

[60] Sun, H. and Ewing, D., 1999, "Self-similar solutions in a three-dimensional wall jet", Proceedings of 8th CANCAM Conference, Hamilton.

[61] Swamy, N. V. C. and Bandyopadhyay, P., 1975, "Mean and turbulence characteristics of three-dimensional wall jets", Journal of Fluid Mechanics, Vol. 71, pp. 541-562.

[62] Tan-atichat, J. and George, W. K., 1996, "Use of computer data acquistion and processing ", Handbook of Fluid Dynamics and Fluid Machinery.

[63] Lakehal, D., Theodoridis, G. S. and Rodi, W., 1998, "Computation of film cooling of a flat plate by lateral injection from a row of holes", International Journal of Heat and Fluid Flow, Vol. 19, pp. 418-430.

[64] Tennekes, H. and Lumley, J. L., 1997, First Course in Turbulence, The MIT Press, Cambridge.

[65] Tutu, N. K. and Chevary, R., 1975, "Cross-wire anemometry in high intensity turbulence", Journal of Fluid Mechanics, Vol. 71, pp. 785-800.

[66] Townsend, A. A, 1976, Structure of Turbulent Shear Flow. CUP, Cambrodge.

[67] Viets, H. and Sforza, P. M., 1966, "An experimental investigation of a turbulent, incompressible, three-dimensional wall jet", PIBAL Report No. 968, AFOSR 66-0888.

[68] Weaver, H. J., 1989, Theory of Discrete and Continuous Fourier Analysis, John Wiley & Sons.

[69] Wygnanski, I. and Fiedler, H., 1969, "Some measurements in the self-preserving jet," Journal of Fluid Mechanics, Vol. 38, pp. 577-612.

[70] Yule, A. J., 1978, "Large-scale structure in the mixing layer of a round jet", Journal of Fluid Mechanics, Vol. 89, pp. 413-432.

[71] Zhou, M. D., Heine, C. and Wygnanski, I., 1996, "The effects of excitation on the coherent and random motion in a plane wall jet", Journal of Fluid Mechanics, Vol. 310, pp. 1-37.